



HAL
open science

Numerical simulation and thermal radiation analysis in sooted flames : impact of radiative properties description

Kévin Torres

► **To cite this version:**

Kévin Torres. Numerical simulation and thermal radiation analysis in sooted flames : impact of radiative properties description. Chemical and Process Engineering. Université Paris-Saclay, 2021. English. NNT : 2021UPAST079 . tel-03462471

HAL Id: tel-03462471

<https://theses.hal.science/tel-03462471>

Submitted on 1 Dec 2021

HAL is a multi-disciplinary open access archive for the deposit and dissemination of scientific research documents, whether they are published or not. The documents may come from teaching and research institutions in France or abroad, or from public or private research centers.

L'archive ouverte pluridisciplinaire **HAL**, est destinée au dépôt et à la diffusion de documents scientifiques de niveau recherche, publiés ou non, émanant des établissements d'enseignement et de recherche français ou étrangers, des laboratoires publics ou privés.

Numerical simulation and thermal radiation
analysis in sooted flames: impact of radiative
properties description

Thèse de doctorat de l'université Paris-Saclay

École doctorale n°579, Sciences mécaniques et
énergétiques, matériaux et géosciences (SMEMAG)
Spécialité de doctorat: Combustion
Unité de recherche : : Université Paris-Saclay, CNRS, CentraleSupélec,
Laboratoire EM2C, 91190, Gif-sur-Yvette, France.
Réfèrent : CentraleSupélec.

**Thèse présentée et soutenue à Paris-Saclay, Théâtre Rousseau,
le 05/07/2021, par**

Kévin TORRES MONCLARD

Composition du Jury

Pascale DOMINGO Directrice de recherche CNRS, CORIA	Présidente
Franck ENGUEHARD Professeur, Université de Poitiers, Institut PPrime	Rapporteur & Examineur
Jean-Louis CONSALVI Maître de conférences, Université d'Aix-Marseille, IUSTI	Rapporteur & Examineur
Guillaume LEGROS Professeur, Université d'Orléans, ICARE	Examineur
Jérôme YON Maître de conférences, INSA Rouen, CORIA	Examineur
Francis DUPOIRIEUX Directeur de recherche, ONERA	Examineur
Stéphane RICHARD Ingénieur Expert, Safran Helicopter Engines	Invité

Direction de la thèse

Olivier GICQUEL Professeur, CentraleSupélec, Université Paris-Saclay	Directeur de thèse
Ronan VICQUELIN Professeur, CentraleSupélec, Université Paris-Saclay	Co-Directeur de thèse

Remerciements

Je tiens à remercier tout d'abord l'ensemble des membres de mon jury pour leur bienveillance et les échanges constructifs et très intéressants que nous avons pu avoir lors de la soutenance de thèse. Je remercie Franck Enguehard et Jean-Louis Consalvi pour avoir accepté d'être rapporteurs de mon manuscrit et pour leur rapports et remarques pertinentes, et Pascale Domingo pour avoir accepté la présidence de ce jury. La séance de questions, bien que longue et éprouvante, a été extrêmement fructueuse et passionnante, grâce à l'intérêt qu'a porté l'ensemble du jury à ce travail. Un grand merci à Jérôme Yon, Guillaume Legros, Francis Dupoirieux d'avoir accepté d'être examinateurs de ma thèse et pour vos remarques pertinentes et échanges.

Tout ce travail n'aurait pas été possible sans l'indéfectible soutien de mes encadrants : Ronan et Olivier. Malgré toute la crise sanitaire et le confinement et les moments difficiles, vous n'avez jamais lâché prise et avez toujours été présents et investis dans ce travail. Merci d'avoir cru en moi et accompagné jusqu'au bout de cette aventure (même si elle n'est jamais vraiment terminée) ! Merci pour votre temps, vos discussions pertinentes, et parfois des échanges tardifs dans la nuit pour finir un papier ! J'espère que les bruits du canari sur Teams ne vont pas trop vous manquer...

Je tiens également à remercier le projet européen SOPRANO qui a financé ces travaux de recherches et qui m'ont aussi permis de voyager et d'échanger avec des industriels, des expérimentateurs de différents laboratoires et entreprises. Je remercie également le Grand équipement National en Calcul Intensif (GENCI), qui m'a donné accès à des ressources de calcul intensif sur le calculateur Occigen du Centre Informatique National de l'Enseignement Supérieur, le mésocentre commun à CentraleSupélec et l'école Normale ParisSaclay (calculateurs Fusion), financé par le CNRS et la région Île de France; et bien entendu le Centre National de la Recherche Scientifique (CNRS), cotutelle du laboratoire EM2C.

La thèse, c'est aussi faire partie d'une grande famille, et qui de mieux pour incarner nos "mamans" que Noi, Nathalie et Brigitte, qui sont toujours là pour nous, nous soutiennent ... et nous rappellent à l'ordre quand on ne fait pas ce qu'il faut ! (Désolé pour tous les ordres de missions fait au dernier moment, et

les compte d'heures pour Soprano ...). Merci pour votre présence, votre bonne humeur et votre soutien sans quoi le labo ne tiendrait pas plus d'une semaine. Merci également à Jean-Michel et Sébastien Turgis pour toute votre aide sur l'aspect informatique et la gestion des calculateurs. Je suis désolé d'avoir pu lancer des calculs sur la frontale de Fusion à l'époque ... mea culpa ! Merci à Franck Richecoeur, Aymeric Vié, Laurent Zimmer, Sean, Marie-Laurence Giorgi, Clément et Antoine pour m'avoir également permis de donner des cours à Centrale, qui a été une expérience très enrichissante. J'espère pouvoir réintervenir dans un futur proche dans ces cours !

Evidemment, une thèse ne se fait pas seul, et ne peut pas se faire seul. J'ai peut-être raconté beaucoup d'histoires aux doctorants du laboratoire, mais je connais également beaucoup de leurs histoires ! Tout d'abord, un énorme merci et soutien à la team du ED214 : Gsquare (Guilhem pour les non habitués), Constantin, Matteo, Corentin. C'est à vous de jouer maintenant, on se retrouve de l'autre côté des docteurs ! Ensuite, un énorme merci à Karl évidemment pour toutes nos pauses cafés, nos bières, et nos fous rires sur "le RV compilation test", qui est encore un secret actuellement, et aussi Luc, qui aurait pu être davantage au laboratoire ! Je remercie également Guillaume et Hernando qui sont déjà loin maintenant, Yacine, Victor, Victorien, David, Roxanne, et je vais en oublier alors je suis désolé ... Un grand merci à ceux que j'ai eu la chance de croiser avant qu'ils finissent leur thèse ou partent : Amanda, Leo, Théa, Davy, Jan et Pedro (à quand un verre de porto ?)

Le meilleur pour la fin, sans doute, car ils ont été là même s'ils étaient loin : pour absolument tout votre soutien, votre présence, l'amitié forte que j'ai pour vous et qui va durer, croyez-moi, je tiens à remercier Livia, Aurélien et mon Gillou. Je vous aime, sincèrement, merci ! Merci à tout les copains de Lille, de la "Petite", et même du Sud de m'avoir soutenu et encouragé dans les moments difficiles, merci pour tout ! J'embrasse enfin terminer toute ma famille, qui a fait le déplacement de très loin pour venir, pour le soutien depuis toutes ces années. Merci pour tout cet amour et votre présence !

Abstract

The evolution of environmental standards in the vicinity of airports has required engine manufacturers to determine the number and mass of particulate pollutants from aircraft engines. The introduction of such standards follows the recent awareness of the harmful impact of soot particle emissions. Controlling these emissions is now a major environmental and human issue.

Manufacturers are therefore required to design less polluting engines. The design of these engines must also enable the various materials to withstand thermal stresses. Soot can play an important role in thermal radiation and, consequently, in these constraints. Soot emits energy that can reach walls and create a significant flow. It is therefore important to determine these heat transfers accurately.

This thesis deals with sooted flames, and focuses in particular on soot thermal radiation. The latter must be modelled in order to calculate the heat transfer. There are many models in the literature, most of which are validated on simple configurations. In this thesis, a state-of-the-art soot particle radiation model called RDGFA is selected and applied to several complex and turbulent configurations. This model considers the complex morphology of soot particles that are aggregates, contrary to standard radiation models that assume spherical particles.

However, the implementation of such radiation simulations is complex, as there is a coupling between the flow and flame within the combustion chamber and radiative heat transfer. Indeed, the radiative transfers will modify the temperature of the flow, which will directly affect the flame and the species, and consequently, on the radiative transfers. In this thesis, a calculation taking into account the radiation/reactive-flow coupling is proposed.

The manuscript is divided into three parts. The first part focuses on developing a detailed model for the radiation of soot particles, making it sufficiently robust and fast to be included in complex flow simulations. This model is combined with the so-called Quasi-Monte-Carlo techniques, which allow for significant time savings in calculating radiative transfers. In a second part, these models

are applied to two complex turbulent configurations: a diffusion jet flame and a swirling non-premixed flame. In this second part, the impact of different parameters (pressure, particle size) on the radiative transfers is evaluated. In a third part, a coupled multi-physics calculation is performed on a laminar flame to capture the interactions between the flame, the thermal heat transfer within the burner, and thermal radiation. Soot and gas models are compared with experimental data on this laminar diffusion flame to identify the remaining uncertainties. Finally, soot particle diffusion signals are numerically reconstructed using the fields obtained from the multi-physics calculation on the laminar flame. When compared to the current experimental data, these images will allow a better understanding of the soot morphology and distribution within these laminar flames.

Résumé

L'évolution des normes environnementales au voisinage des aéroports a contraint les motoristes d'être capable de déterminer le nombre et la masse des particules polluantes issues des moteurs d'avions. La mise en place de telles normes fait suite à la récente prise de conscience de l'impact nocif des émissions de particules de suies. La maîtrise de ces émissions constitue aujourd'hui un enjeu majeur à la fois environnemental et humain.

Les constructeurs sont donc amenés à concevoir des moteurs moins polluants. Le dimensionnement de ces moteurs doit également permettre aux différents matériaux de résister à des contraintes thermiques. Les suies peuvent jouer un rôle important dans le rayonnement thermique et, par conséquent, dans ces contraintes. Les suies, émettent en effet de l'énergie qui peut atteindre des parois et ainsi y créer un flux important. Il est donc important déterminer avec précision ces transferts thermiques.

La simulation numérique permet d'estimer rapidement et à un coût raisonnable les transferts thermiques liées aux suies dans des configurations complexes. Les transferts radiatifs sont, dans cette thèse, calculés via une méthode précise de résolution de l'équation du rayonnement : la Méthode Monte-Carlo.

Cette thèse se focalise principalement sur des flammes suitées, et en particulier sur le rayonnement thermique des suies qui doit être modélisé afin de calculer les transferts thermiques. Il existe de nombreux modèles dans la littérature, qui sont pour la plupart validés sur des configurations simples. Dans le cadre de cette thèse, le modèle à l'état de l'art de rayonnement des particules de suies appelé RDGFA est retenu et est appliqué sur plusieurs configurations complexes et turbulentes. Ce modèle prend en compte la morphologie complexe des suies qui sont des agrégats, contrairement aux modèles standards de rayonnement qui supposent des particules sphériques.

La mise en place de tels calculs de rayonnement est toutefois complexe, car il existe un couplage entre l'écoulement au sein de la chambre de combustion et le rayonnement. En effet, les transferts radiatifs vont modifier la température de l'écoulement, ce qui va avoir un effet direct sur la flamme et les espèces, et

par conséquent, sur les transferts radiatifs. Dans cette thèse, un calcul prenant en compte le couplage rayonnement/écoulement est proposé.

Le manuscrit s'articule en trois parties. La première partie se concentre sur le développement d'un modèle détaillé pour le rayonnement des particules de suies, tout en le rendant suffisamment robuste et rapide pour être inclus dans des simulations d'écoulements complexes. Ce modèle se combine aux techniques dites Quasi-Monte-Carlo permettant un gain de temps appréciable sur les calculs de transferts radiatifs.

Dans une deuxième partie, ces modèles sont appliqués à deux configurations turbulentes complexes : une flamme jet de diffusion et une flamme non-prémélangée swirlée. Dans cette deuxième partie, l'impact de différents paramètres (pression, taille des particules ...) sur les transferts radiatifs est évalué.

Dans une troisième partie, un calcul couplé multi-physique est réalisé sur une flamme laminaire pour capturer les interactions entre la flamme, la thermique au sein du brûleur et le rayonnement. Les modèles de suies et de gaz sont comparés aux données expérimentales sur cette flamme de diffusion laminaire pour identifier les incertitudes restantes. Finalement, des signaux liés à la diffusion des particules de suies sont reconstruits numériquement à l'aide des champs obtenus via le calcul multi-physique sur la flamme laminaire. Ces images, une fois comparées aux données expérimentales en cours, permettront de mieux comprendre la morphologie des suies et leur distribution au sein de ces flammes laminaires.

Contents

Abstract	iii
Résumé	v
I Radiative heat transfer modeling	9
1 Radiative heat transfer and soot radiative properties	11
1.1 Fundamentals of Thermal Radiation modeling	12
1.2 Radiative properties for gaseous phase	19
1.3 Radiative properties of soot particles	26
1.4 Soot radiation in CFD simulations	55
1.5 Conclusion	60
2 Accounting for high-fidelity radiative properties in a Monte-Carlo solver	61
2.1 Monte-Carlo methods for the RTE	62
2.2 A Monte-Carlo code : RAINIER	67
2.3 Combining scattering treatment and Quasi-Monte-Carlo methods	69
2.4 Conclusion	83
II Characterization of soot radiation in turbulent flames with stand-alone Monte-Carlo simulations	85
3 Accurate quantification of soot scattering contribution in a turbulent jet flame	87
3.1 Modelling of thermal radiation in sooted flames	88
3.2 Computation of radiative heat transfer in a turbulent sooted jet flame	96
3.3 Global metrics to a priori assess the impact of scattering	108
3.4 Conclusion	112
4 Sensitivity analysis of radiative heat transfer in turbulent flames.	115

4.1	Introduction: Radiative heat transfer in High pressure systems . . .	116
4.2	Radiative heat transfer analysis on the DLR FIRST burner . . .	117
4.3	Impact of soot radiation modelling and morphology in the Sandia's turbulent jet flame.	125
4.4	Conclusion	135
III	Soot radiation in laminar flames	137
5	Inclusion of differential diffusion effects with the Flamelet Progress Variable approach	139
5.1	Original FPV and RFPV methods	140
5.2	Extension to non-unity Lewis numbers	145
5.3	Treatment of PAHs for sooty flames	161
5.4	Conclusion	165
6	Coupled simulation of an axisymmetric ethylene air-flame	167
6.1	Experimental and numerical set-up : Santoro's burner	168
6.2	Results and comparison with experimental data	179
6.3	Analysis of fuel preheating	194
6.4	Analysis of radiative heat transfer	200
6.5	Conclusion	209
7	Numerical synthesis of scattered Laser signals by soot particles	213
7.1	Description of the problem and numerical strategy	214
7.2	Application of peel-off technique to CFD fields from coupled calculations	226
7.3	Application of peel-off technique to CFD fields from detailed chemistry calculations	236
7.4	Conclusion	242
	Conclusion	245
A	Generalization of the peel-off method for non-collimated radiation	253
A.1	Parametrization of the problem	253
A.2	Derivation of the first condition of detection Source-Observer generalized	254
A.3	Derivation of the second condition of detection Source-Observer generalized	256
B	Synthèse de la thèse	259
B.1	Introduction et problématiques :	259
B.2	Objectifs de la thèse :	260

CONTENTS

ix

B.3 Plan du manuscrit :	260
References	281
Index	283

List of Tables

1.1	Synthesis of RTE resolution methods.	19
1.2	Values of m used in the litterature to study sooting flames	30
1.3	List of encountered models for single spherical particle. m is the optical index of soot particle, and x the size parameter.	32
2.1	Evolution of the convergence rate exponent in function of the maximum number of scattering events s_{max} used to build the Sobol sequence for the RQMC method. The retained convergence rate in Sec. 2.3.4.2 are emphasized in bold fonts.	82
4.1	Gaseous and soot contributions of emitted and asorbed radiative power for the reference field and the f_V increased field.	123
4.2	Gaseous and soot contributions of emitted and absorbed radiative power for the reference field and the f_V increased field.	125
6.1	List of boundary conditions used in the AVBP solver for the simulation of Santoro's non smoking flame.	173
6.2	Repartition of the CPU cores between the different codes for the coupled calculation.	175
6.3	Contributions of the terms I, II, III in the integrated heat release (HR) rate in W.	198
6.4	Detailed analysis of convective/radiative fluxes (in W) on the pipe walls.	199
6.5	Spectral integrated values of emitted and absorbed power for each case presented Figure 6.27.	204
7.1	Experimental data of the Laser considered in this study.	214
7.2	Experimental data of the observer considered in this study.	215
7.3	Radiation characteristics as a function of the source wavelength	225

List of Figures

1	Global Greenhouse Gas Emission contribution by Gas in 2015 (from United States Environmental Protection Agency website).	1
2	Evolution of the global fuel consumption over the years in function of the considered resource (from Our World in Data website).	2
3	Illustration of ICAO emissions certification at the vicinity of airports (extracted from ICAO website).	3
1.1	Schematic description of radiative mechanisms for the RTE.	13
1.2	Comparison between Monte Carlo and other techniques conventionally used for the RTE solutions (extracted from Modest (2003b)).	18
1.3	Schematic representation of the absorption coefficient evolution in a small band $\Delta\nu$. Extracted from Rodrigues (2018).	22
1.4	Comparison of soot complex index of refraction (from Modest (2003b)). 1 : Lee and Tien (1981) (polystyrene and plexiglas soot), 2 : Stull and Plass (1960) (amorphous carbon), 3 : Dalzell and Sarofim (1969) (propane soot), 4 : Howarth et al. (1966) (pyrographite at 300K), 5 : Chang and Charalampopoulos (1990) (propane soot), 6 : Felske et al. (1984a) (propane soot)	28
1.5	Scattering regime map as a function of the particle size parameter x and the soot volume fraction f_v . Extracted from Modest (2003b).	31
1.6	Comparison of $E(m)$ with excitation wavelength λ , extracted from Mouton (2014).	35
1.7	Comparison of the absorption coefficient obtained by Rayleigh scattering theory for different values of m .	36
1.8	Polar representation of the Rayleigh's phase function. Isotropic scattering is also displayed in dashed lines.	38
1.9	Contour error in terms of Q_{ext} . x is the size parameter and m the refractive index Kerker et al. (1963). Region I corresponds to an error of less than 10% between RDG and Mie's theory. Region II corresponds to an error less than 100%, region III corresponds to an error greater than 100%.	42

1.10	TEM characterization of soot aggregates for ethylene/air diffusion laminar flame. Both single sphere and aggregates are displayed in the TEM images (Okuyay (2016))	44
1.11	Comparison of ICP method, RDG standard and for fractal aggregates theories and equivalent sphere Mie method in terms of non-dimensionnal absorption (a) and scattering (b) coefficients. N is the number of soot particles in the aggregate.	49
1.12	Comparison of DDSCAT code using DDA and GMM method (from Comberg and Wriedt (1999)) in terms of intensity in a row parallel (left) and perpendicular (right) to an incident electromagnetic wave.	52
1.13	Illustration of soot morphology interactions : standard point-touch (a), overlapping (b) and necking (c) from Liu et al. (2016)	53
1.14	Influence of soot overlapping in extinction coefficient (Yon et al. (2015))	54
1.15	Discretization of the soot volume fraction density $q_i(v)$	58
2.1	Parametrization of the scattering problem	71
2.2	Wall emittance obtained in function of the albedo ω for two optical thickness τ_L and comparison with literature data from Siegel (1987).	76
2.3	Wall emittances obtained in function of the albedo ω for two optical thickness τ_L and for four different scattering treatments. Comparison with reference results from Siegel (1987) is also provided. Plain markers : $\tau_L = 0.2$, empty markers : $\tau_L = 0.5$	77
2.4	Relative standard deviation of computed wall emittance as a function of the total number of rays N for the five considered cases. Conditions: $\tau_L = 0.2$ and $\omega = 0.3$. Convergence rates are also displayed in dashed lines.	79
2.5	Relative standard deviation of computed wall emittance as a function of the total number of rays N for the five considered cases. Conditions: $\tau_L = 1$ and $\omega = 0.7$. Convergence rates are also displayed in dashed lines.	80
2.6	Relative standard deviation of computed wall emittance as a function of the total number of rays N for standard Monte Carlo case and Standard Forced Scattering and Fast-forced-scattering case. Conditions: $\tau_L = 0.1$ and $\omega = 0.9$. Convergence rate is also displayed in dashed lines.	80
2.7	Comparison of relative standard deviation for the computed wall emittance as a function of the total number of rays N for the cases <i>full-RQMC</i> and <i>full-RQMC-FFS</i> . Conditions: $\tau_L = 1$ and $\omega = 0.7$. Convergence rate is also displayed in dashed lines.	81

2.8	Comparison of relative standard deviation for the computed wall emittance as a function of the total number of rays N for the cases <i>full-RQMC</i> and <i>full-RQMC-FFS</i> . Conditions: $\tau_L = 0.1$ and $\omega = 0.9$. Convergence rate is also displayed in dashed lines.	82
3.1	Comparison of phase functions between Rayleigh theory (red dashed lines) and RDG-FA theory (blue line) for a given aggregate with 3 different primary particle diameters $d_p = 1$ nm (left), 10 nm (center) and 50 nm (right). The wavelength is fixed at 534 nm.	91
3.2	Comparison of phase functions between Rayleigh theory (red dashed lines) and RDG-FA theory (blue line) for a given aggregate with 3 different wavelengths $\lambda = 100$ nm (left), 775 nm (center) and 1000 nm (right).	92
3.3	Profile of radiative power along the domain composed of soot aggregates and comparison with Ref. Eymet et al. (2002)	94
3.4	Relative difference of spectral radiative power with and without scattering for both RDG-FA setups.	94
3.5	Spectral evolution of the albedo in the RDGFA validation case	95
3.6	Left: reference fields of temperature and soot volume fraction. Right: computed radiative power field.	97
3.7	Soot mass fraction and soot number density fields for the first and tenth sections.	97
3.8	Comparison of relative standard deviation fields in the turbulent jet flame. Top : <i>Standard-MC</i> . Bottom : <i>full-RQMC-FFS</i>	99
3.9	Relative standard deviation as a function of the number of rays N at the location of maximum soot volume fraction.	99
3.10	Comparison of the number of rays required to reach a given error on the Sandia's turbulent jet flame. Top : <i>Standard-MC</i> , Bottom : <i>full-RQMC-full</i>	100
3.11	Local efficiency between for the standard-MC computation in the turbulent jet flame.	101
3.12	Ratio of local efficiencies between full-RQMC-FFS and Standard-MC in the turbulent jet flame.	102
3.13	Comparison of radiative power profiles (left axis, solid and dashed lines) along the jet flame centerline. The plotted region corresponds to the peak in soot volume fraction (right-axis, dotted line).	103
3.14	Difference of radiative power along the centerline with and without scattering for RDG-FA (solid line) and Rayleigh (dashed line) theories. Error bounds corresponding to the results' standard deviation are shown in plain horizontal lines.	104
3.15	Spectral radiative power with/without scattering obtained at the peak location of soot volume fraction.	105

3.16	Difference in spectral radiative power obtained at the soot volume fraction peak location in wavenumber (top) and wavelength (bottom) space.	106
3.17	Evolution of the spectral asymmetry factor G_{glob} for the aggregate distribution at the maximum soot volume fraction location.	107
3.18	Evolution of the spectral albedo factor ω_λ for the aggregate distribution at the maximum soot volume fraction location.	107
3.19	Computed Albedo importance metric on the Sandia turbulent jet flame. The iso-contour of soot-volume fraction at 10 ppm is also displayed in black line.	109
3.20	Mean soot transmissivity $\bar{\tau}^{soot}$ for the studied turbulent jet flame field. The black line corresponds to an isocontour of Temperature equals to 1000 K. The characteristic length is chosen equals to 0.01 m.	110
3.21	Mean asymmetry factor \bar{G} for the studied turbulent jet flame field. The black line corresponds to an isocontour of temperature at 1000 K.	111
3.22	Computed effective albedo importance $\bar{\omega}^{eff}$ on the Sandia turbulent jet flame.	112
4.1	Comparison between instantaneous emitted radiative powers from gas and soot phases, extracted from P. Rodrigues PhD thesis Rodrigues (2018)	117
4.2	Burner geometry of the DLR configuration (from Geigle et al. (2015)).	118
4.3	Temperature, soot volume fraction and radiative power reference fields in the DLR First Burner.	119
4.4	Soot contribution to the mean transmissivity $\bar{\tau}^{soot}$ calculated using soot optical properties. The reference length is here chosen equals to 0.01 m. See Chapter 3 for more details on this metric.	119
4.5	Spectral emitted and absorbed radiative power integrated over the volume of the combustion chamber.	120
4.6	Computed Scattering Importance metric on the DLR FIRST Combustor chamber. The contour in white represents the zone where the NDF of the 17 th of the sectional model is maximum.	121
4.7	Spectral emitted and absorbed radiative power integrated over the volume of the combustion chamber, at P = 3 bars, and with a soot volume fraction multiplied by 10, 100 and 1000.	122
4.8	Spectral emitted and absorbed radiative power integrated over the volume of the combustion chamber at P = 30 bars, obtained with the reference f_V field.	124
4.9	Evolution of optical index component for soot particles with the wavelength.	126

4.10	Derivation of the surface-volume model (SV-1) based on numerical results obtained on 1D laminar premixed flames by Mueller et al. (2009), Salenbauch et al. (2015). Extracted from Rodrigues (2018)	128
4.11	Primary particle diameter (left) and number of primary particles per aggregate (right) obtained for two difference surface-volume relationships. Experimental data at different pressures are also provided in black squares.	129
4.12	Radiative power along the centerline of Sandia turbulent jet flame for the 4 considered soot radiative models. Soot volume fraction is represented with dot lines.	130
4.13	Difference of radiative power with and without scattering along the centerline for Sandia jet flame with the two morphological models presented Section 4.3.3. Soot volume fraction is represented with dot lines.	131
4.14	Number density function at maximum soot volume fraction location. Left : reference. Right : after increasing the particle size.	133
4.15	Impact along the centerline of the soot mean particle size on the radiative power with SV-model 2.	133
4.16	Mean effective albedo importance $\bar{\omega}^{eff}$ for the studied turbulent jet flame field with increased particle size.	134
4.17	Mean soot transmissivity $\bar{\tau}^{soot}$ for the studied turbulent jet flame field with increased particle size. The black line corresponds to an isocontour of Temperature equals to 1000 K. The characteristic length is chosen equals to 0.01 m.	134
4.18	Mean asymmetry factor \bar{G} for the studied turbulent jet flame field with increased particle size. The black line corresponds to an isocontour of Temperature equals to 1000 K.	135
5.1	Schematic "S-curve" representing the set of steady flamelet solutions (solid and dashed black lines), extracted from Pierce and Moin (2004).	141
5.2	Inclusion of heat loss effect with the RFPV technique by computing intermediate non-adiabatic flamelets (in red).	142
5.3	Comparison of 1D profiles of temperature with/without differential diffusion effects using detailed chemistry (KM2 mechanism) on a 1D counterflow diffusion flame for a strain rate $a = 100 \text{ cm}^{-1}$	147
5.4	Comparison of 1D profiles of acetylene mass fraction with/without differential diffusion effects using detailed chemistry (KM2 mechanism) on a 1D counterflow diffusion flame for a strain rate $a = 100 \text{ cm}^{-1}$	148

5.5	Comparison of 1D profiles of A4 PAH mass fraction with/without differential diffusion effects using detailed chemistry (KM2 mechanism) on a 1D counterflow diffusion flame for a strain rate $a = 100 \text{ cm}^{-1}$	148
5.6	Comparison of 1D profiles of soot volume fraction with/without differential diffusion effects using detailed chemistry (KM2 mechanism) on a 1D counterflow diffusion flame for a strain rate $a = 100 \text{ cm}^{-1}$	149
5.7	Comparison of 1D profiles of number density of soot particles with/without differential diffusion effects using detailed chemistry (KM2 mechanism) on a 1D counterflow diffusion flame for a strain rate $a = 100 \text{ cm}^{-1}$	149
5.8	Evolution of temperature in function of the mixture fraction for X-flamelet and Z-flamelet formulation in a 1D counterflow diffusion flame, accounting for differential diffusion effects.	152
5.9	Evolution of Y_C in function of Z for different 1D counterflow flamelets generated with the KM2 mechanism for ethylene. Differential diffusion is considered and 2 transported equations for Y_c and Z are additionally solved. Only the stable branch flamelets are represented.	153
5.10	Evolution of the transported enthalpy and the mixture enthalpy in function of Z for one of the 1D counterflow flamelets generated with the KM2 mechanism for the ethylene	154
5.11	Geometry of the counterflow problem	157
5.12	Obtained fields on the counterflow diffusion flame computed in AVBP. The strain rate is set at 120 s^{-1}	159
5.13	Comparison of profiles obtained in AVBP (tabulated chemistry) and in the flamelet solver REGATH with differential diffusion. The strain rate is set at 120 s^{-1}	160
5.14	Obtained fields on the sooty counterflow diffusion flame computed in AVBP. The strain rate is set at 120 s^{-1}	165
5.15	Comparison of the profiles obtained in AVBP and in the flamelet solver REGATH (sooting case). The strain rate is set at 120 s^{-1}	166
6.1	Schematic of Santoro's burner. Extracted from Santoro et al. (1987).	169
6.2	Soot formation mechanisms in a laminar diffusion coflow flame. Extracted and adapted from Intasopa (2011).	170
6.3	Visualisation of the computational domain and zoom on the pipe area.	172
6.4	Solid part sketch with corresponding length and mesh sizes. g_{ratio} is the growth rate applied.	173
6.5	Communication scheme between the three solvers with corresponding exchanged quantities.	175

6.6	Pipe response to a heat-flux perturbation : temperature of the solid.	177
6.7	Evolution of L2 error norms of temperature T and radiative power as a function of the fluid solver iteration N_{cpl}	179
6.8	Temperature, molar fractions of H_2O and CO_2 , soot volume fraction, and progress variable results from the coupled simulation. The contour $Z = 0.064$ is also displayed in black line.	180
6.9	Soot volume fraction, total particles number density and soot source terms (nucleation, surface growth, coagulation, oxidation and condensation for two sections.)	181
6.10	Mass fraction fields of three PAHs : A_3 , A_4 and A_7 . The nucleation source term is also displayed on the left.	183
6.11	Source term of the biggest PAH considered in this study (A_7) based on the relaxation model presented in Chapter 5.	184
6.12	Centerline profiles of temperature, axial velocity, soot volume fraction and N_{part} with comparison to experimental data : Santoro et al. (1983) (●), Köylü et al. (1997) (▼), McEnally et al. (1997) (★).	186
6.13	Integrated soot volume fraction distribution along the axis height above the burner : experimental data from Santoro et al. (1983) (●)	187
6.14	Comparison Coupled Calculation / optically thin assumption on the predicted soot volume fraction along the centerline and temperature. Experimental data ((●)) from Santoro et al. (1983).	188
6.15	Comparison of radial temperature profiles obtained for three different axial heights above the burner with experimental data from Santoro et al. (1983) (●)	189
6.16	Comparison of axial velocity profiles for six axial heights above the burner with experimental data from Santoro et al. (1983) (●).	190
6.17	Comparison of radial velocity profiles for six axial heights above the burner with experimental data from Santoro et al. (1983) (●).	191
6.18	Comparison of radial profiles mass fraction of C_2H_2 , OH and soot volume fraction with experimental data from Santoro et al. (1983) (●) at a fixed height above the burner exit.	192
6.19	Evolution of soot volume fraction, primary particle number and diameter along the flame wings, with comparison with experimental data from Santoro et al. (1983) (●).	193
6.20	Obtained wall temperature profiles for the inner, outer and lip walls, accounting for conjugate heat transfer.	195
6.21	Radial temperature profiles obtained at various locations along the pipe when accounting for fuel preheating (CHT). The referred positions are relative to the exit of the pipe.	195

6.22	Radial axial velocity profiles obtained at various locations along the pipe when accounting for fuel preheating (CHT). The referred positions are relative to the exit of the pipe.	197
6.23	Comparison between axial velocity profiles at the exit of the pipe, accounting for fuel preheating (CHT) or not. The pipe extends radially between 0 and 0.55 cm, while the coflow extends above 0.59 cm.	197
6.24	Convective and radiative wall fluxes profiles along the inner and outer pipe wall.	200
6.25	Participating gases and soot particles contributions to the total radiative power. An iso-contour of $f_V = 1ppm$ is also displayed on the gaseous phase contribution.	201
6.26	Emitted and absorbed radiative power due to soot and gaseous phase. The ratio between the absorbed and emitted power is also displayed on the right.	202
6.27	Spectral emitted and absorbed volume-integrated powers for the instantaneous representative solution. Results correspond to the reference case taking into account gas and soot particles emission and absorption and the four other studied cases: GEGA, GESA, SEGA and SESA.	203
6.28	Spectral transmissivity computed at $x = 4cm$ above the burner and comparison with experimental data (top), and detailed contribution of gas and soot particles (bottom).	205
6.29	Impact of soot optical index formulation on the computed transmissivities and comparison with experimental data.	206
6.30	Axial evolution of the vertical-vertical scattering coefficient (for an angle of $\theta_i = 90^\circ$ and a wavelength $\lambda = 513nm$. Experimental values with associated errors are also reported.	207
6.31	Axial evolution of the extinction coefficient at wavelength $\lambda = 513nm$. Experimental values with associated errors are also reported.	208
6.32	Reconstructed albedo of aggregates at various heights above the burner with experimental data comparison at 513nm. Errors bars are taken from Iyer et al. (2007).	209
6.33	Difference of radiative power due to scattering, effective albedo importance and mean asymmetry factor fields for the studied configuration.	210
7.1	Schematic of the studied problem: a Laser beam scattered and collected by an observer (2D view). The source and observer are actually much wider.	215

7.2	Traditional forward (left) and backward (right) Monte Carlo methods. In both cases, only the rays exchanged between O-S are needed. For the targeted application, both methods are inefficient in computing the radiative fluxes impinging the observer (O point) from the Laser (S point).	216
7.3	Principle of peel-off illustrated with a photon scattered three times (points A, B, C). At each scattered location, an additional ray is generated and is traced towards the source.	217
7.4	Parametrization used to compute the direct contribution Source-Observer (green line). The source is characterized by its center C_{source} , its radius R_{source} , a direction characterized by a normal vector \vec{n}_{source} , its power and the emission wavelength.	218
7.5	Parametrization used to compute the scattering contribution Source-Observer (green line). The real photon computed by Rainier is scattered at P_{scat} and goes to B. θ_{po} represents the angle between the initial direction and the direction pointing towards the source.	220
7.6	Peel-off validation case: uniform slab with absorption coefficient κ and albedo ω ; the source is defined on the left of the cube with an imposed surface flux; the observer elements are placed along the right face of the cube.	221
7.7	Radiative flux at the observer as function of the albedo for the ERM ((●)) and peel-off (★) methods in the case of an homogeneous and isotropic medium ($\kappa L = 0.01$).	222
7.8	Radiative flux direct (▲) and scattered (▼) contributions computed with the peel-off methods in the case of an homogeneous and isotropic medium ($\kappa L = 0.01$).	223
7.9	Relative standard deviation of the computed scattered flux as a function of the total number of rays N for the ERM ((●)) and the peel-off (★) methods. The fitted convergence rate is depicted by dashed lines.	223
7.10	Radiative flux at the observer as a function of the source wavelength for the ERM and peel-off methods in the case of anisotropic scattering due to soot particles.	225
7.11	Radiative flux direct (▲) and scattered (▼) contributions at the observer as a function of the source wavelength for the ERM and Peel-off methods in the case of anisotropic scattering due to soot particles.	226
7.12	Parametrization used to generate signals from the Santoro laminar diffusion flame. Left : side view, right : top view.	228
7.13	Synthetized image of total signal obtained on the observer. Wavelength: 405 nm. Angle: $\alpha_o = 0^\circ$	229
7.14	Synthetized image of scattered signal obtained on the observer. Wavelength: 405 nm. Angle: $\alpha_o = 0^\circ$	230

7.15	Synthesized image of scattered signal obtained on the observer. Wavelength: 405 nm. Angle: $\alpha_o = -40^\circ$ (left), $\alpha_o = 40^\circ$ (right).	231
7.16	Phase function given by the RDGFA model for an aggregate distribution localized at the maximum signal location in Figure 7.15. The phase function given by Rayleigh theory is indicated by the red dashed line.	232
7.17	Angular evolution of the integrated radiative flux on the observer. Wavelength : 405 nm.	232
7.18	Angular evolution of the integrated radiative flux on the observer for two wavelengths : 405 nm (black line) and 785 nm (gray line).	233
7.19	Phase function given by the RDGFA model for an aggregate distribution localized at the maximum signal location at 785 nm. The phase function given by Rayleigh theory is indicated by the red dashed line.	234
7.20	Spectral evolution of the scattered radiative flux on the center of the observer, for an angle $\alpha_o = 0^\circ$.	234
7.21	Considered ray for the study of the spectral optical thickness evolution.	235
7.22	Spectral evolution of soot radiative properties averaged on a characteristic optical path along the flame.	236
7.23	Spectral evolution of the factor $\sigma_{soot}e^{-\beta L}$ along the observer line-of-sight for $\alpha_o = 0^\circ$.	236
7.24	Fields of soot volume fraction and density of the number of particles from detailed chemistry calculations.	238
7.25	Synthesized image obtained on the observer : scattering of particles at 405 nm, $\alpha_o = 0^\circ$. Top : detailed chemistry, bottom : tabulated chemistry.	239
7.26	Comparison of the total density number of particles N_{part} between the coupled calculation performed in this thesis (left) and the detailed chemistry simulation (right).	240
7.27	Comparison of mean primary particles diameter between the thesis computation (left) and detailed chemistry simulation (right).	241
7.28	Comparison of integrated signals collected by the observer for both computations : thesis work (dashed lines), detailed chemistry (solid lines) at two different wavelengths (405 nm : black , 785 nm : gray).	241
7.29	Angular variation of normalized integrated signal. Computations: detailed chemistry (solid line); thesis work (dashed line)	242
7.30	Computation of phase functions for the thesis computation (left) and detailed chemistry simulation (right) in a polar diagram. The phase function predicted by Rayleigh theory is indicated by a red dashed line.	243
7.31	Flickering behaviour of the laminar flame investigated in Chapter 6 without including radiation.	249

7.32	Evolution of the heat-release rate in the case of the flickering flame.	250
7.33	Evolution of $\bar{\omega}$ (top), $\bar{\omega}^{eff}$ (middle) and \bar{G} (bottom) for various aggregate morphology. The four studied cases in this thesis are indicated with red stars.	252
A.1	Parametrization of the source for non-collimated radiation : the source is characterized by a deflexion angle Θ_s	254
A.2	Parametrization of the source-observer for non-collimated radiation. The observer is represented by the point O_1	254
A.3	Determination of the second condition for the computation of the direct contribution observer-source in a case of non-collimated radiation.	256

Introduction

Global context

The last five years have been marked by the raise of the environmental awareness, epitomized by Greta Thunberg's Speech at the U.N Climate Action Summit in 2019. In her speech, she pointed that the Paris Agreement, signed by 196 state parties in 2015, has not met yet expectations.

The goal of this Agreement is to keep the increase in global average temperature below 2 degrees before 2100. This temperature increase is due to the well known green-house effect. Such effect is caused by the emission of gases, mainly CO_2 (65 %) and CH_4 (16 %), as seen Figure 1.

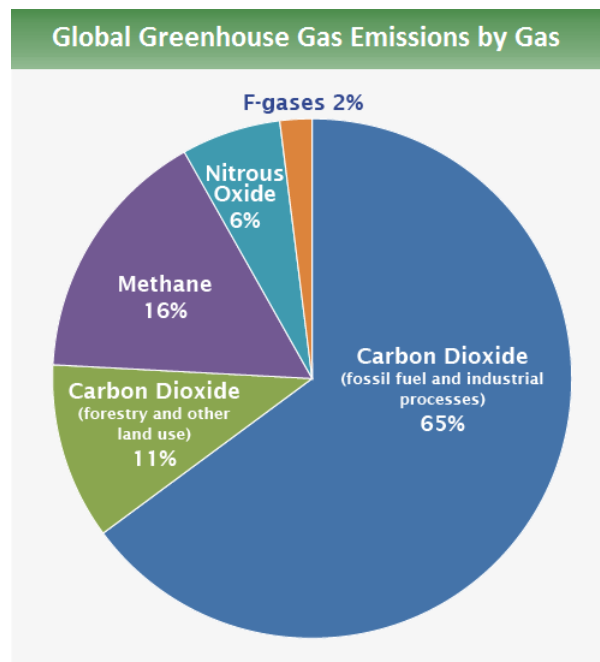


Figure 1: Global Greenhouse Gas Emission contribution by Gas in 2015 (from United States Environmental Protection Agency website).

The emission of CO_2 is mostly due to the fossil fuels, used to generate thermal

power as a source of energy. It can be observed that a large amount of power consumption is due to such fossil fuels (Figure 2) while renewable resources have a smaller contribution.

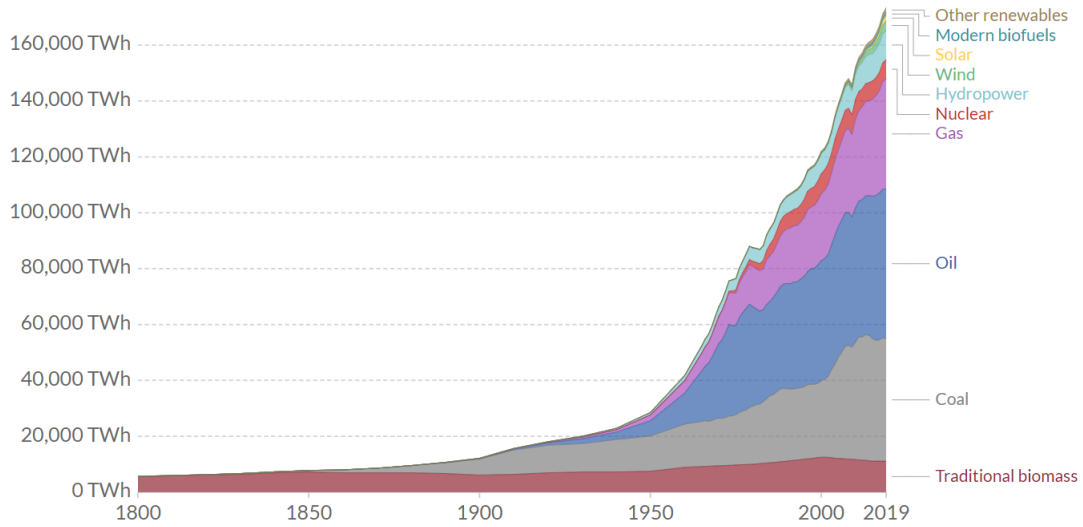


Figure 2: *Evolution of the global fuel consumption over the years in function of the considered resource (from Our World in Data website).*

Fossil fuel consumption has not only an effect on the global warming, but also on humans' health. Indeed, incomplete combustion products, such as carbon monoxide, nitrogen oxides, unburned hydrocarbons and soot particles have an important impact on environment and health diseases.

In this thesis, we are focusing on soot particles, which are issued from incomplete fuel rich combustion. The understanding and the prediction of such particles is of primal importance and is the main objective of the Soprano's European H2020 project.

This project aims at delivering more accurate experimental and numerical methodologies for predicting the soot emissions. This thesis, which is part of this project, is focusing on a numerical approach.

Industrial context

From an industrial point of view, environmental regulations exist to limit the pollutant emissions from aeronautical engines. Initially, these regulations were focusing on reducing the visibility of trails of smoke at the exit of engines. The smoke is correlated to the soot particles concentration and is measured in terms

of *Smoke Number*. Exhaust gases are passing through a smoke filter, which is opacified due to the presence of soot particles. An engine could be certified if the Smoke Number was sufficiently low.

However, due to the hazardous impact of such particles on humans' health, new environmental regulations have been developed by the ICAO (International Civil Aviation Organization), both in terms of number and mass. These limitations are applied for nvPM (non-volatile Particulate Matter) and have been adopted during the ICAO CAEP11 (Committee on Aviation Environmental Protection) in 2019 [OACI \(2020\)](#).

The engine certification is based on its pollutant emissions in the vicinity of airports, which are high density humans zones. The ICAO quotas have to be verified in 4 operating modes : the take-off, the climb, the approach and the taxi phases as illustrated Figure 3. Each phase is characterized by a duration time and a percentage of thrust level.

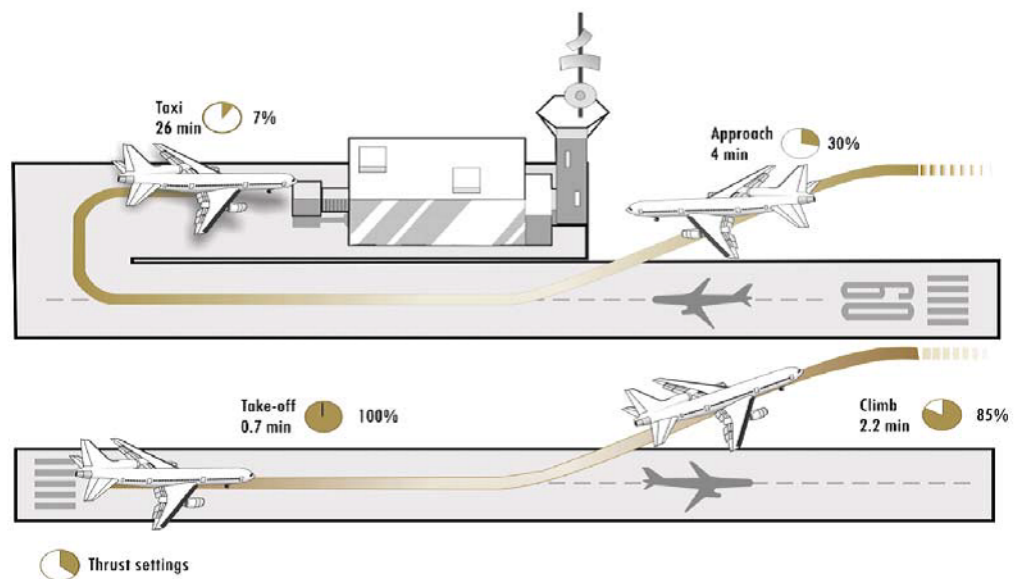


Figure 3: Illustration of ICAO emissions certification at the vicinity of airports (extracted from ICAO website).

Industrials are therefore running measurement campaigns on an engine with these different levels of thrust and are collecting information on the nvPM at the exit of the engine. Such an approach is extremely costly and can be performed a limited number of times.

In parallel, the numerical simulation is an interesting approach, since many op-

erating points, geometries, injection systems ... can be tested easily and their impact on the production of pollutants can be assessed at an affordable cost, with the development of accurate numerical methods such as the Large Eddy Simulation (LES).

Soot particles are due to the incomplete combustion of the fuel. These particles are formed in the combustion chamber. Predicting pollutants from the simulations of a combustion chamber remains a challenging task, since many uncertain parameters must be taken into account such as :

- **The chemical mechanism** : reactions occurring in the combustion chamber are described through a chemical mechanism which contains information on the species chemical kinetics, especially on the polycyclic aromatic hydrocarbons (PAHs). PAHs play an essential role in soot formation. The PAHs kinetics is described using an Arrhenius Law whose parameters are uncertain. Besides, the use of large chemical mechanism is impossible in practice, since many equations need to be solved (one for each species). This drastically increases the computational time of these simulations. Reduced models are considered instead and are discussed in Chapter 5.
- **Soot modelling** : several models are encountered in the literature which enable to compute soot related quantities such as the soot volume fraction f_V . This is one of the quantities of interest for environmental quotas and its accurate prediction is crucial. These models are usually accounting for five main phenomena which describe soot mechanisms. The first one is the *nucleation* (which is the collision between two big PAHs) and leads to the formation of the smallest soot particle. The second one is the *condensation* which is a collision between a PAH and a soot particle. The third one is the *coagulation* which is a collision between two soot particles. The fourth one is the *surface growth* and involves the acetylene (C_2H_2) which interacts at the surface of soot particles. The fifth one is the *oxidation*, which is responsible for the decrease of the total soot mass, mainly due to the action of O_2 and OH . The understanding of each of these mechanisms, especially for the surface-growth, are still nowadays ongoing.
- **Turbulence modelling** : in industrial applications, complex turbulent flows are encountered. Three classic approaches can be considered to deal with turbulent configurations. The Direct Numerical Simulation (DNS), which consists in solving all the temporal and spatial turbulence scales (which is unaffordable in practice), the Large Eddy Simulation, resolving only the most energetic scales of the turbulence, on the Reynolds Average Navier-Stokes approach (RANS) which models all turbulent length scales and solves averaged quantities on the flow. The LES offers a good trade off between CPU cost and accuracy and is retained in this thesis.

The three points above have been extensively studied in the literature and research on these topics is still very much active. This thesis focuses on a fourth point, which is **radiation modelling**. Thermal radiation plays a crucial role on the three previously mentioned points. Indeed, radiation acts on the temperature of the flow which has an impact on the PAHs kinetics, soot dynamics and modifies the flow topology. In the PhD thesis carried out by [Palluotto \(2019\)](#), it has been reported that including detailed radiation in the Oxytec chamber Flame A (a swirl-stabilised premixed non-sooted methane flame) modifies the flame topology.

Radiative heat transfer is classically split into two contributions: non-luminous radiation from participating burnt gases on the one hand, and luminous radiation from soot particles emitted in the visible spectral range on the other hand. It is known the latter is contributing to a non-negligible part of the wall fluxes in RQL technologies [Lefebvre \(1984\)](#). Accounting for detailed and accurate radiative models especially for sooty flames is therefore important.

Objectives of the thesis and manuscript organization

The objectives of this thesis are :

- Developing accurate and efficient methods too account for soot radiative models (Chapter 2)
- Applying these models to two turbulent configurations to emphasize key parameters that impact soot radiation (Chapters 3 and 4)
- Assessing the capability of these models to retrieve rich experimental data in a laminar sooted flame configuration (Chapters 5 and 6)
- Reconstructing experimental signals useful for optical diagnostics (Chapter 7)

The manuscript contains three part :

- **Part I** is focusing on radiative properties of soot particles. In Chapter 1, the fundamental radiative transfer equation (RTE) is presented. The different radiative mechanisms (emission, absorption, scattering) are presented and numerical strategies to solve the RTE are discussed. A review of gaseous and soot radiative properties is then detailed, and the retained models for gases (the ck-model) and soot (the Rayleigh Debye Gans for Fractal Aggregates - RDGFA - model) phases are chosen.

In Chapter 2, the Monte-Carlo RTE solver is presented. The code originally accounts for emission/absorption but not for scattering phenomena. Therefore, in Chapter 2, the implementation of scattering in a Monte-Carlo code is first discussed. Then, a strategy to combine scattering with

the Quasi-Monte-Carlo approach is detailed in order to speed-up the calculations.

- **Part II** is assessing the impact of the radiative properties in two turbulent sooted flames. In Chapter 3, an ethylene turbulent diffusion jet-flame at 1 bar is studied. This flame has been widely studied in the literature and scattering by soot particles was neglected. The argument invoked is based on the Rayleigh theory, applying for spherical particles, in which scattering is indeed negligible. However, soot particles are aggregates, whose radiative properties are described here using the RDGFA model. The impact of soot scattering with this state-of-the-art model is then assessed. In parallel, global metrics that can be computed *prior* any Monte-Carlo simulation are detailed to *a-priori* assess the impact of scattering in a given configuration.

In Chapter 4, several parameters such as the optical index of soot particles, the soot volume fraction, the pressure and the size of particles are investigated on the turbulent diffusion jet-flame and on a turbulent non-premixed swirled ethylene flame. This sensitivity study highlights which experimental data or numerical efforts are required to assess the importance of radiation at industrial operating points.

- **Part III** is focusing on the study of a coflow ethylene/air laminar diffusion flame. The advantage of such configuration is that a wide range of experimental data is available to assess the accuracy of the chosen radiative models. Moreover, the uncertainty related to the turbulence modelling is removed. In Chapter 5, the chemical modelling of the gaseous phase (species and PAHs) is discussed. In this work, a tabulated chemistry approach is retained which enables to reduce the number of equations that needs to be solved. This approach is originally used for turbulent flames (such as in Part II). In the laminar configuration, a more detailed species transport needs to be accounting for: the original approach is then modified accordingly. The strategy and the validation of this extended tabulated chemistry is detailed in Chapter 5.

In Chapter 6, a multiphysics simulation is performed in the chosen laminar configuration. This simulation enables to take into account several mechanisms that are not considered in a stand-alone CFD flow solver. The solver AVBP is then coupled with our Monte-Carlo radiative solver Rainier and conjugate heat transfer at the walls. Comparison with experimental data in terms of temperature, soot volume fraction, transmissivities, albedo, scattering coefficient are performed and the uncertainties of this computation are discussed.

Finally, in Chapter 7, signals collected by a Laser scattered due to soot particles are numerically synthesized using the fields obtained in Chapter 6. This situation reproduces an experimental set-up carried out at the Institut Jean Rond d'Alembert. The experimental measurements are currently ongoing. The impact on the intensity collected by sensor is investigated by modifying its position and the Laser wavelength and are compared with the experimental data.

Acknowledgement

The financial support within the EU Horizon 2020 Soot Processes and Radiation in Aeronautical Innovative Combustion (SOPRANO) project (Grant Agreement No. 690724) is gratefully acknowledged. The numerical work was performed using HPC resources from GENCI-CINES (Grant 2019-A0062B10159) as well as from the “Mésocentre” computing center of CentraleSupélec and École Normale Supérieure Paris-Saclay supported by CNRS and Région Île-de-France (<http://mesocentre.centralesupelec.fr/>).

Part I

Radiative heat transfer
modeling

Chapter 1

Radiative heat transfer and soot radiative properties

This chapter provides a global introduction on radiative heat transfer and its modeling. The radiative transfer equation and the associated physical mechanisms (emission, absorption, scattering) are first presented. Modeling strategies to solve this equation are then briefly introduced and compared.

Spectral radiative properties of participating gases are presented while an analysis for soot particles radiative properties is detailed. Two categories of radiative models are discussed whether soot is considered as a spherical particle or a complex aggregate. A brief review of soot radiative properties used in CFD calculations is finally given before presenting the soot sectional description.

The chapter allows to appreciate the timely combination of soot sectional model and RDGFA radiative property model investigated in the thesis.

Contents

1.1	Fundamentals of Thermal Radiation modeling . . .	12
1.1.1	The Radiative Transfer Equation (RTE)	12
1.1.2	Numerical resolution of the RTE	14
1.2	Radiative properties for gaseous phase	19
1.2.1	Line-by-line calculations- LBL	20
1.2.2	Spectral narrow-band models	20
1.2.3	Global models	24
1.3	Radiative properties of soot particles	26
1.3.1	Introduction	26
1.3.2	Soot complex refractive index m	27
1.3.3	Radiative properties for spherical soot particles . . .	29
1.3.4	Radiative properties for aggregates	42

1.3.5	Other methods : irregular geometries	49
1.3.6	Towards highly-detailed aggregates description : latest improvements of the RDG-FA method	52
1.4	Soot radiation in CFD simulations	55
1.4.1	State-of-the art in the literature	55
1.4.2	Soot sectional description retained in this thesis	57
1.5	Conclusion	60

1.1 Fundamentals of Thermal Radiation modeling

1.1.1 The Radiative Transfer Equation (RTE)

Thermal radiation consists in transferring energy through electromagnetic waves, which means that, contrary to heat conduction, radiation does not need a medium to occur. Such a property makes thermal radiation of a specific interest in applications such as atmospheric reentry where the pressure is extremely low (almost on the vacuum). Moreover, it is well known that radiation is proportional to the fourth power of temperature : in gas-turbines applications, especially in the combustion chamber, this heat transfer mode can be important, compared to conduction and convection, because of the high temperatures encountered. Another difference with conduction and convection relies in the length scales at stake. Conduction and convection occurs in relatively short length scales while radiation occurs at much higher length scales, so the entire medium needs to be taken into account to describe the local radiative exchanges.

Mathematically, this is traduced by an integro-differential equation called Radiative Transfer Equation (RTE). The RTE expresses the variations of the *radiative intensity* I_ν of an electromagnetic wave in a short distance ds and at a given wavenumber ν .

In order to understand the different mechanisms involved, let us consider a small domain, of a length ds , as sketch in Figure 1.1.

The medium can increase the radiative intensity carried by the electromagnetic waves through two mechanisms along optical path s : first, the emission from the medium, characterized by a coefficient κ_ν , then, the in-scattering, which corresponds to a deviation of a photon from another direction \vec{r}' to the direction of interest \vec{r} . The in-scattering is characterized by a scattering coefficient noted σ_ν . The medium can also be responsible of a loss of energy carried by the photons, via the absorption and the out-scattering mechanisms. Since we are assuming a local thermodynamic equilibrium (LTE), absorption and emission by the medium have the same probabilities : both phenomenon are then characterized by the same coefficient κ_ν named absorption (or emission) coefficient.

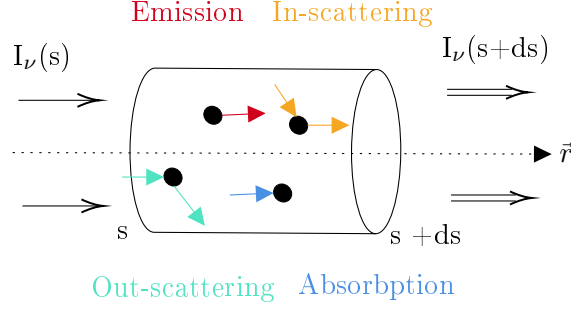


Figure 1.1: Schematic description of radiative mechanisms for the RTE.

The out-scattering mechanism is also characterized by the scattering coefficient σ_ν .

Assuming an optical index of the medium equals to 1, the Radiative Transfer Equation then writes :

$$\frac{dI_\nu(\vec{r}, s)}{ds} = -(\kappa_\nu + \sigma_\nu) I_\nu(\vec{r}, s) + \kappa_\nu I_{b\nu} + \frac{\sigma_\nu}{4\pi} \int_{4\pi} I_\nu(\vec{r}', s) \Phi_\nu(\vec{r}', \vec{r}, s) d\Omega' \quad (1.1)$$

In this equation, the radiative intensity at a given position I_ν is a function of the direction \vec{r} , the optical path s and the wavenumber ν . κ_ν and σ_ν are respectively the absorption and scattering coefficients, $d\Omega'$ the solid angle and $I_{b\nu}$ is the blackbody intensity. This blackbody intensity is given by the *Planck's law* :

$$I_{b\nu}(T) = \frac{2\pi h\nu^3}{c_0^2 \left[e^{\frac{h\nu}{k_b T}} - 1 \right]} \quad (1.2)$$

where h and k_b are respectively the Planck's and Boltzmann's constants, and c_0 the speed of light in vacuum.

The first term of the RTE right-hand side corresponds to a loss of intensity due to absorption and out-scattering. The second term accounts for the emission process. The last term represents the in-scattering contribution. This contribution depends on the scattering phase function $\Phi_\nu(\vec{r}', \vec{r}, s)$ which can be seen as the probability for a photon to be scattered from \vec{r}' to \vec{r} .

In practical applications, the radiative power and fluxes are the quantities of interest. They are defined from the radiative intensity I_ν from the RTE. The

radiative heat flux vector \mathbf{q}^R is defined by :

$$\begin{aligned}\mathbf{q}^R &= \int_{\nu=0}^{\infty} \mathbf{q}_{\nu}^R d\nu \\ &= \int_{\nu=0}^{\infty} d\nu \int_{4\pi} I_{\nu}(\vec{r}, s) \vec{r} d\Omega\end{aligned}\quad (1.3)$$

The radiative flux φ^R is obtained as:

$$\varphi^R = \mathbf{q}^R \cdot \mathbf{n} = \int_{\nu=0}^{\infty} d\nu \int_{4\pi} I_{\nu}(\vec{r}) \mathbf{n} \cdot \vec{r} d\Omega \quad (1.4)$$

where \mathbf{n} is the unity vector normal to the wall.

The radiative power P^R is defined by :

$$\begin{aligned}P^R &= -\nabla \cdot \mathbf{q}^R \\ &= - \int_{\nu=0}^{\infty} d\nu \int_{4\pi} \text{div} [I_{\nu}(\vec{r}) \vec{r}] d\Omega\end{aligned}\quad (1.5)$$

The expression of the radiative power is rewritten using Equation 1.1 :

$$P^R = - \int_{\nu=0}^{\infty} \left[\left(4\pi \kappa_{\nu} I_{b\nu} - \int_{4\pi} \kappa_{\nu} I_{\nu} d\Omega \right) \right] d\nu \quad (1.6)$$

1.1.2 Numerical resolution of the RTE

The RTE is an integro-differential equation of dimension 6 : 3 spatial coordinates, 2 angular coordinates (which defines the direction of the electromagnetic wave), and 1 spectral variable. The complexity of such equation requires specific methods to solve it. These methods are either based on a specific formulation of the radiative intensity or on the direct expression of the radiative power and/or fluxes which are the quantities of interest.

In this section, we consider the most common methods used in CFD simulations, from the less to more accurate : the Optically Thin Assumption (OTA), the Spherical Harmonic Method (SHM or PN-approximation), the Discrete Ordinate Methods (or SN-approximation), the Finite-Volume Method and the Monte-Carlo method. The Monte-Carlo approach is specifically detailed in Chapter 2. For other related methods (Discrete Transfer Methods, Ray Tracing among many others), the reader can find additional information in [Modest \(2003b\)](#).

1.1.2.1 The Optically Thin Assumption

This method assumes that the radiative power is reabsorbed neither by the participating gases nor soot particles. In this case, the radiative power can directly be expressed by :

$$P^R = -4\sigma(T^4 - T_\infty^4)(\sum_i (p_i \kappa_{P,i}) + \kappa_{P,soot}) \quad (1.7)$$

where $\sigma = 5.669 \cdot 10^{-8} \text{ W/m}^2\text{K}^4$ is the Stefan constant, T is the local temperature, T_∞ is the background temperature, p_i is the partial pressure of species i (expressed in atmospheres), $\kappa_{P,i}$ is the Planck mean absorption coefficient for species i (expressed in $\text{m}^{-1}\text{atm}^{-1}$) and $\kappa_{P,soot}$ for soot particles.

Two important remarks must be emphasized here. First, this model provides a direct expression of the radiative power, so the RTE does not need to be solved: it can directly be implemented in a CFD solver. Then, this model tends to strongly over-estimate the radiative losses since only emission is considered, and hence under-estimate the temperature predicted in CFD simulations.

1.1.2.2 The Spherical Harmonic Method - P_N approximation

The Spherical Harmonic Method has been originally developed in [Jeans \(1917\)](#) to study stars radiation. The P_N approximation decouples the spatial and directional variables of the radiative intensity by expressing it as a series of spherical harmonics :

$$I(\vec{r}, s) = \sum_{l=0}^{\infty} \sum_{m=-l}^l I_l^m(\vec{r}) Y_l^m(s) \quad (1.8)$$

This expression is a 2D generalized Fourier series, whose coefficients are I_l^m . These coefficients need to be determined to retrieve the radiative intensity. The directional parts, $Y_l^m(s)$ are called spherical harmonics and are expressed in terms of Legendre polynomials by :

$$Y_l^m(\theta, \psi) = \begin{cases} \cos(m\psi) P_l^m(\cos\theta), & \text{for } m \geq 0 \\ \sin(m\psi) P_l^m(\cos\theta), & \text{for } m < 0 \end{cases} \quad (1.9)$$

here, the direction s is characterized by a polar (θ) and azimuthal angles (ψ), and P_n^m are the Legendre polynomials.

In practical applications, the P_1 method is retained, even though some work has considered high order methods, such as the P_3 method ([Mengüç and Viskanta \(1985\)](#)) or the P_N method ([Ou and Liou \(1982\)](#)). For the P_1 method, the

complex RTE equation can be replaced by simultaneous first-order Partial Differential Equations much easier to solve, enabling to retrieve the coefficients I_l^m . However, this method fails to provide accurate results in the case of moderate anisotropic intensities, and increasing the order of the method leads to very complex mathematical formulations and implementation.

1.1.2.3 The Discrete Ordinate Methods - S_N approximation.

The DOM has been first introduced by in Chandrasekhar (1960) and is based on solving the RTE for N discrete angular directions spanning the whole solid angle range of 4π . Each direction \vec{r}_i is characterized by a set of directional cosines (usually noted μ_i, ν_i, ξ_i) and a weight w_i .

In the RTE, all the integrals over the solid angle are replaced by numerical quadratures. Any quantity f is then written :

$$\int_{4\pi} f(\mathbf{u})d\Omega \simeq \sum_{i=1}^N \omega_i f(\mathbf{u}_i) \quad (1.10)$$

The directional cosines corresponds to the projection of the i -th direction s_i onto the normal vector of a cell j :

$$\vec{r}_i \cdot \vec{n}_j = \mu_i n_{xj} + \nu_i n_{yj} + \xi_i n_{zj} \quad (1.11)$$

The RTE (equation 1.1) is hence approximated by a set of N partial differential equations :

$$\frac{dI_\nu(\vec{r}_i)}{ds_i} = -(\kappa_\nu + \sigma_\nu) I_\nu(\vec{r}_i) + \kappa_\nu I_{b\nu} + \frac{\sigma_\nu}{4\pi} \sum_{j=1}^N w_j I_\nu(\vec{r}_j) \Phi_\nu(\vec{r}_j, \vec{r}_i) d\Omega_j \quad (1.12)$$

The advantage of the DOM is that the intensity field can be found without any iterative procedure for simple problems (no scattering and no wall reflections) or, for more complex cases, with standard PDE-system resolution algorithms.

The choice of the angular discretization (*i.e* the choice of the directional cosines) is critical since it will directly affect the boundary conditions expression. Examples of discretization schemes can be found in Modest (2003b) and Joseph et al. (2009).

A good trade-off must be found between the accuracy of the angular discretization and the computational time, as it increases with the angular discretization refinement. Besides, the DOM suffers from discretization errors, known as the *false scattering*, corresponding to the spatial discretization error, and the *ray effect* (Coelho (2008)) corresponding to the angular discretization error. The

first effect can be reduced by using finer CFD mesh, but this tends to increase the ray effect. Here again, a good trade-off between the two errors must be found.

1.1.2.4 The Finite Volume Method

In the DOM method, ray effect and false scattering errors can be mitigated by controlling the mesh discretization and the angular discretization scheme. However, the fact that simple quadratures are used for angular discretization does not guarantee the conservation of the energy. Since Finite Volume Methods are already used for spatial discretization (and ensure the conservation of the mass, momentum), a natural extension of the DOM would be to consider the finite volume approach for angular discretization.

In the FVM, the solid angle $d\Omega$ is divided in small control volumes $\Delta\Omega^{CV}$. Each control volume is expressed in terms of polar (θ) and azimuthal angles (ϕ), such as :

$$\Delta\Omega^{CV} = \int_{\phi^{CV-}}^{\phi^{CV+}} \int_{\theta^{CV-}}^{\theta^{CV+}} \sin\theta d\theta d\phi \quad (1.13)$$

where θ^{CV-} and θ^{CV+} are the lower and upper values of the polar angle defining the solid angle control volume, and ϕ^{CV-} and ϕ^{CV+} the lower and upper values of the azimuthal angle. This formulation is directly applied to the RTE where integrals over the 4π range solid angle are replaced by integrals over the control volumes. A complete derivation of the RTE can be found in [Chai et al. \(1994\)](#). Several studies such as work of [Selçuk and Kayakol \(1997\)](#), [Liu et al. \(1997\)](#), [Coelho et al. \(1998\)](#) have shown that FVM is faster than the DOM approach, less sensitive to the ray effect. Moreover, as stated previously, the method is fully conservative, and there are less constraints in the choice of the discretization of the solid angles than in the DOM discretization schemes.

1.1.2.5 The Monte-Carlo method principle

The Monte-Carlo method is a *statistical approach* in which a mathematical quantity (integrals, equation ...) is solved using *sampling techniques* of the variables of the problem. Since the variables of the RTE are the position, the direction and the wavelength, the standard MC technique consists here to randomly pick a position, a wavelength and a direction values (which form a vector \mathbf{X}) and obtain a radiative intensity with these values. With this radiative intensity, we can retrieve the radiative flux and radiative power which are our quantities of interest.

Let us assume we have repeated this solving process N times, so we have obtained N values of the radiative intensity. We define the *estimator of the*

quantity of interest by :

$$Q_{est} \approx \frac{1}{N} \sum_{i=1}^N Q(\mathbf{X}_i) \quad (1.14)$$

The central limit theorem ensures that, for an infinite number of N repetitions, the *estimator* converges to the exact value of the quantity of interest Q (which is, again, either the radiative flux or the radiative power). *How* the estimator converges depends on the intrinsic standard deviation of the estimator, $\sigma_{intrinsic}$ defined by :

$$\sigma_{intrinsic} \equiv \sigma(Q) \approx \frac{1}{N-1} \sum_{i=1}^N (Q(\mathbf{X}_i) - Q)^2 \quad (1.15)$$

According to the central limit theorem, the standard deviation of the estimator samples $\sigma(Q_{est})$, which is a metric of the error between Q_{est} and Q , follows the following relation :

$$\sigma(Q_{est}) \approx \frac{\sigma_{intrinsic}}{\sqrt{N}} \quad (1.16)$$

This is an important result showing that the standard Monte-Carlo method convergence rate is in $\frac{1}{\sqrt{N}}$. This result does not depend on the complexity of the quantity that needs to be calculated. Such remark can be also interpreted in terms of CPU time as depicted Figure 1.2.

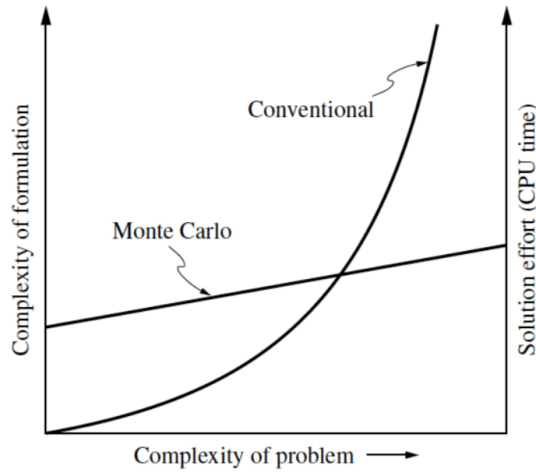


Figure 1.2: Comparison between Monte Carlo and other techniques conventionally used for the RTE solutions (extracted from *Modest (2003b)*)

Indeed, the convergence rate is the same regardless the complexity of the problem : for very simple problems, a conventional method might be more appropriate since the Monte-Carlo method is quite expensive. However, when more complex problems are involved, the CPU cost of MC does not increase too much contrary to conventional methods and becomes much more attractive. Moreover, it enables to obtain an estimation of the error, which can be reduced by increasing the number of realizations N .

1.1.2.6 Ray Tracing method

The most accurate method to solve the RTE is the deterministic ray tracing [Iacona et al. \(2019\)](#) where directions and wavelength are discretized, and photons are emitted for each direction and wavelength. The high CPU cost of such method limits it to academic configurations as in the work of [Coelho et al. \(2003\)](#).

1.1.2.7 Synthesis of the RTE resolution numerical methods

The different RTE methods with their advantages and drawbacks are presented in Table 1.1. In this work, the Monte-Carlo approach is retained because of its high accuracy.

Method	Accuracy	Cost
OTA	—	—
SHM	+	++
DOM	++	+
FVM	++	+
<u>MC</u>	+++	++
Ray Tracing	+++	++++

Table 1.1: *Synthesis of RTE resolution methods.*

1.2 Radiative properties for gaseous phase

The description of gaseous phase radiative properties received a specific attention because of the importance of hot burnt gases in the radiative heat transfer. Their emission and absorption spectrum exhibits strong erratic lines ([Rothman et al. \(2009\)](#)) which makes difficult to consider such properties in a CFD calculation. Several strategies have been developed to overcome these difficulties and are described in the next paragraphs, from the reference (the line-by-line method or LBL) to the more or less approximate ones.

1.2.1 Line-by-line calculations- LBL

The LBL calculations provides highly-detailed spectra resolution (down to 0.01 cm^{-1}) for the gaseous phase species. These calculations relies on spectroscopic databases such as HITRAN (Rothman et al. (2009)) and HITEMP (Rothman et al. (2010)) which accurately describe the spectral lines structure. A line is characterized by its strength (amplitude), position and width which are reported in the databases, along with line broadening effects.

Generally, the high resolution spectra calculation is not affordable in practical 3-D calculations. Indeed, due to the strong variations in the absorption coefficient, the spectral radiative transfer problem must be solved for up to one million wavenumbers. Several work have been conducted on two 2D-axisymmetric configurations : a methane-air jet flame (Wang et al. (2008), based on a LBL-MC method previously developed by Wang and Modest (2007)) and in a pre-mixed flame configuration (Ren and Modest (2019)) along with a Monte-Carlo method resolution for the RTE. Such studies show the capability of using LBL in CFD simulations, but the computational domain and the mesh resolution (around 10000 cells) is far from industrial configurations where the number of cells can exceed several millions of elements. For this reason, LBL calculations are used as a reference to validate more simplified models presented hereafter, or limited to academical configurations.

1.2.2 Spectral narrow-band models

Instead of performing a fully-resolved spectral calculation like in the line-by-line method, spectral narrow-band models rather divide the spectrum into several bands of a size $\Delta\nu$ sufficiently small (narrowed) to consider a constant value of the Planck's law inside each band.

1.2.2.1 Statistical Narrow Band models

Let us consider a very simple case, namely an homogeneous medium (constant temperature, gas partial pressures ...) surrounded by black walls. The radiative intensity at a given wavenumber ν can be written, along an straight optical path s :

$$I_\nu = I_{bw\nu}\tau_\nu(s) + I_{b\nu}\epsilon_\nu(s) \quad (1.17)$$

where $I_{bw\nu}$ is the blackbody intensity at the wall temperature.

Now, we are considering a small spectral band $\Delta\nu$ where the Planck's law (so the blackbody intensity) is almost constant. In this case, we can write the average value on the spectral band of the radiative intensity \bar{I}_ν :

$$\bar{I}_\nu = \frac{1}{\Delta\nu} \int_{\Delta\nu} I_\nu d\nu = I_{bw}\bar{\tau}_\nu(s) + I_{b\nu}\bar{\epsilon}_\nu(s) \quad (1.18)$$

The bar quantities referred to average values over the spectral band, and, by definition, the narrow-band averaged transmissivity and emissivities are equal to :

$$\bar{\tau}_\nu = \frac{1}{\Delta\nu} \int_{\Delta\nu} e^{-\kappa_\nu s} d\nu; \quad \bar{\epsilon}_\nu = \frac{1}{\Delta\nu} \int_{\Delta\nu} (1 - e^{-\kappa_\nu s}) d\nu \quad (1.19)$$

At this point, only the emissivities or transmissivities on the band need to be evaluated. In the literature, two statistical descriptions are classically encountered :

- The Elsasser's model which assumes that, in a band, spectral lines have the same amplitude and are equally spaced.
- The Malkmus model ([Malkmus \(1967\)](#)) which assumes that, in a band, spectral lines are randomly spaced. The amplitude is picked from a probability distribution which enables to account for weak and strong lines strength.

These two models lead to different expressions of the transmissivities/emissivities, which can be found in [Modest \(2003b\)](#). Finally, the radiative intensity can be found by performing an integration of $\bar{I}_{\nu(s)}$ over the spectrum. Although these models lead to accurate results (providing a good resolution of the spectral bands), they only provide line-of-sight emissivities and transmissivities, they are not then adapted to ray tracing methods (Monte-Carlo,...) and do not handle properly reflecting surfaces case.

1.2.2.2 ck-model

This approach is the one retained for the radiative calculations performed in this thesis. The starting point of the narrow-band k-distribution model is the same as SNB models : we consider a small spectral interval $\Delta\nu$ in which the Planck function remains constant.

Recalling Equation 1.17 obtained for homogeneous medium, the radiative intensity only depends on the absorption coefficient κ_ν . In Figure 1.3, a schematic example of the evolution of κ_ν is provided : it can be observed that, in this small interval, the absorption coefficient has the same values multiple times. In other words, the *same* radiative intensity would be calculated several times in the spectral band which is not efficient.

The idea is then to reorder the absorption coefficient so the radiative intensity would be only evaluated once on the spectral band. Then, integrals performed over the small band $\Delta\nu$ are replaced by calculations over the absorption coefficient values taken in this small band.

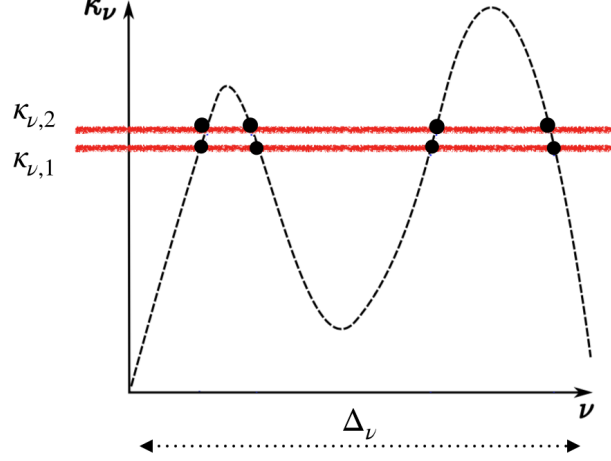


Figure 1.3: Schematic representation of the absorption coefficient evolution in a small band $\Delta\nu$. Extracted from [Rodrigues \(2018\)](#).

Any quantity averaged in the spectral band can be written in terms of a k -distribution $f(k)$ which is the fraction of $\Delta\nu$ for which the absorption coefficient takes values between k and $k + dk$. For example, the averaged transmissivity in the spectral band writes :

$$\bar{\tau}_\nu(X) = \frac{1}{\Delta\nu} \int_{\Delta\nu} e^{-\kappa_\nu X} d\nu = \int_0^\infty f(k) e^{-kX} dk \quad (1.20)$$

By definition $f(k)$ is the probability density function for the absorption coefficient ; over the spectral band, it is defined by :

$$f(k) = \frac{1}{\Delta\nu} \int_{\Delta\nu} \delta(k - \kappa_\nu) d\nu \quad (1.21)$$

with δ the Dirac function.

It is clear, looking at Equation 1.20, that only the knowledge of $f(k)$ is needed to compute our averaged quantities. In order to compute $f(k)$, the evolution of κ_ν must be quite smooth. However, for non-homogeneous media as encountered in the different cases studied in this work, spectral lines are very dynamic and such integration is complex. The difficulty is overcome by considering the cumulative distribution function $g(k)$ defined as :

$$g(k) = \int_0^k f(k') dk' \quad (1.22)$$

This quantity represents the probability that the absorption coefficient takes a value lower than k : in each band this quantity varies monotonically from 0 (no

probability) to 1 (certain). Hence, it is possible to have a unique value of the absorption coefficient knowing $g(k)$. Its integration is much easier carried and the average transmissivity along a band is approximated for a *non-homogeneous medium* by :

$$\bar{\tau}_\nu(X) \approx \int_0^1 \exp \left[- \int_0^l k(g, s) ds \right] dg \quad (1.23)$$

If the same methodology is applied to the radiative intensity, one obtains the expression of its averaged value on the spectral band \bar{I}_ν :

$$\bar{I}_\nu = \int_0^1 I(k(g, s)) dg \quad (1.24)$$

Finally, this integral is approximated using a Gaussian-quadrature, which yields to :

$$\bar{I}_\nu = \sum_{j=1}^N \omega_j I_{g_j} \quad (1.25)$$

where g_j and ω_j are the quadrature points and weights respectively, and N is the quadrature order. The intensity I_{g_j} for a quadrature point g_j verifies then:

$$\frac{\partial I_{g_j}}{\partial s} = k(g_j, s) [I_{b\nu} - I_{g_j}(\vec{r}, s)] - \sigma \left(I_{g_j} - \frac{1}{4\pi} \int_{4\pi} I_{g_j}(\vec{r}', s) \Phi(\vec{r}', \vec{r}, s) d\Omega' \right) \quad (1.26)$$

recalling that, in the small band considered, all radiative properties except the absorption coefficient are constant. Hence, knowing the values of k at the quadrature points, it is possible to evaluate the intensity (or any quantity of interest) at the quadrature points, and then find its averaged value over the spectral band.

In the case of combustion, several gaseous species are involved in radiation process and can absorb/emit simultaneously. In this case, it is assumed that the spectra of these species are uncorrelated over each narrow band and the mean transmissivity of a mixture column in a given narrow band can be approximated by the multiplication of the mean transmissivities of the species sharing the same narrow band. As a consequence, if we consider m species, a N^m -quadrature is needed to reconstruct the radiative intensity over the band.

In this work the *correlated k-model* (ck) is used. The term "correlated" refers to the k -distributions $g(k)$. If the quantity $g(k)$ is known at two locations in the non-homogeneous medium, it is possible to map the absorption coefficient from

one location to another (Goody and Yung (1995)). Only radiative properties from CO_2 and H_2O are considered as they are the main contributors to heat transfer. These properties are based on updated parameters from Rivière and Soufiani (2012) used for the ck-model.

These parameters have been generated for applications at atmospheric pressure in temperature range 300 K - 4000K . They are based on the CDSD-4000 database for CO_2 absorption spectra (Rothman et al. (2010)) and HITEMP 2010 for H_2O absorption spectra (Tashkun and Perevalov (2011)). For H_2O 44 spectral bands, with widths varying from 50 cm^{-1} to 400 cm^{-1} , are considered between 150 cm^{-1} and 9200 cm^{-1} . CO_2 absorbs radiation in only 17 of these bands. The cK database is made of 7 -points Gauss quadrature per band for each gaseous component, leading to 1022 pseudo-spectral points, since 49 quadrature points are used in the 17 overlapping bands.

1.2.3 Global models

The global models enable to compute spectral integrated quantities of interest. In this section we will limit to 2 global classic models : *the weighted-sum-of-gray-gases* (WSGG) and the *Full Spectrum k-distribution* (FSK) approaches.

1.2.3.1 WSGG model

The method has been first presented by Hottel and Sarofim (1967) for zonal methods of RTE resolution, but the method was limited to non-scattering media surrounded by black walls. The model has then been extended to any solution of the RTE in Modest (1991).

In the weighted-sum-of-gray-gases (WSGG), the nongray gases are replaced by a sum of fictitious gray gases. For each gray gas, the RTE is solved with weighted coefficients w_k , with k the k -th gray gas considered. This approach is equivalent to divide the spectrum in few bands in which the absorption coefficient κ_k is supposed constant, each band corresponding to a gray gas.

More specifically, the method approximates the total emissivity of a non-gray iso-thermal gas by :

$$\epsilon(T, s) = \sum_{k=0}^K \omega_k(T) (1 - e^{-\kappa_k s}) \quad (1.27)$$

T is the temperature and s the optical path length. Knowing the coefficients w_k and the corresponding values of κ_k the radiative intensity is found by :

$$I(s) = \sum_{k=0}^K I_k(s) = \sum_{k=0}^K \left[w_k I_{bw} e^{-\kappa_k s} + w_k I_b (1 - e^{-\kappa_k s}) \right] \quad (1.28)$$

This method leads to acceptable results, providing an accurate calculation of the coefficients $w(k)$ based either on old experimental data [Modest \(1991\)](#), or on more recent HITEMP databases ([Dorigon et al. \(2013\)](#), [Bordbar et al. \(2014\)](#), [Centeno et al. \(2016\)](#), [Centeno et al. \(2018\)](#)). However, this method assumes gray scattering and surfaces properties.

1.2.3.2 FSK model

As for the WSGG model, the FSK method [Modest and Zhang \(2002\)](#) approach assumes that all the radiative properties except the absorption coefficient do not vary across the spectrum. This *global* method is also inspired from a *spectral* model already discussed : the narrow-band k-distribution. In the spectral model, the absorption coefficient is reordered on a small spectral band in which the Planck function is assumed constant. Then, since the obtained function is noisy, we considered the cumulative distribution g of the reordered absorption coefficient.

As a *global* model, the FSK approach applies the same principle but over the *whole* spectrum : in this case, a fractional Planck function $i(T, \nu)$ itself is reordered all over the spectrum :

$$i(T, \nu) = \frac{1}{I_b(T)} \int_0^\nu I_{b\nu} d\nu \quad (1.29)$$

By definition, the total transmissivity of a gas column can be written as :

$$\bar{\tau}(X) = \int_{i=0}^{i=1} e^{(-\kappa_\nu(i)X)} di \quad (1.30)$$

One may notice that, knowing the value of i , only one value of κ_ν is possible. Following the development of the ck-model, we proceed to a change of variable, replacing i by k which is the value taken by the absorption coefficient for a given value of i . The total transmissivity is then :

$$\bar{\tau}(X) = \int_{i=0}^{i=1} e^{(-\kappa_\nu(i)X)} di = \int_0^\infty e^{-kX} f(T, k) dk = \int_0^1 e^{-k(T,g)X} dg \quad (1.31)$$

where g is the cumulative distribution of reordered the fractional Planck function f , introduced because the obtained reordered fractional Planck function is erratic.

The major difference with the ck-model is that the transmissivity obtained is not defined on a spectral band. Besides, it can be observed that k is depending on the temperature. This is due to the fact that i depends on the temperature as well. A solution to overcome this difficulty is to move the temperature

dependence into a base function determined using LBL calculations. Discrete values of the radiative intensities are then evaluated from a set of discrete values of k and the total radiative intensity is reconstructed using quadrature methods.

The FSK method is an exact method for homogeneous medium and its accuracy depends only on the quadrature method used. In the case of non-homogeneous medium, the FSK is also exact if the absorption coefficient is *scaled* : the coefficient is evaluated at a reference state (widely chosen) and applied to evaluate the different functions needed to compute the global transmissivity. Extensions of the FSK method based on this scaling approach have been developed : full-spectrum scaled-k approach (FSSK) and full-spectrum correlated-k (FSCK) (Modest (2003a)).

1.3 Radiative properties of soot particles

1.3.1 Introduction

Considering radiative properties of particulate media is a challenging task as complex phenomena must be taken into account : scattering, morphology of the particles, size distributions, clearance between particles ... Historically, radiation by particles has been first considered in astrophysics and especially in interstellar dust interactions (Mattila (1970) , Witt (1977)). Hence, most of models currently used in CFD calculations and especially for soot particles are based on these pioneering works.

Soot radiation depends on three parameters Modest (2003b) :

- **Optical properties** characterized by the complex optical index m , introduced in the next section, and developed in the review of Mullins and Williams (1987) ,
- **Soot morphology** : a common assumption made is to consider soot particles as spherical. However, experimental studies (Megaridis and Dobbins (1989), Köylü and Faeth (1993), Tian et al. (2004)) have emphasized the aggregates nature of soots, formed by nearly spherical primary particles. Consequently, the absorption and scattering of light by soot aggregates cannot be treated by simplified electromagnetic theories for single spheres,
- **Interaction with medium and other particles** : soot during their aging process can overlap Yon et al. (2015) or mix with organic species (coating phenomenon), studied by Schnaiter et al. (2006), Bond and Bergstrom (2006) and recently in Liu et al. (2016), which modifies their absorbing and scattering properties.

The following sections aim at discussing on these three dependencies.

1.3.2 Soot complex refractive index m

When an electromagnetic wave interacts with a medium containing soot particles, the radiative intensity may be changed by absorption and/or scattering. How much and into which direction a particle scatters an electromagnetic wave passing through its vicinity depends on the complex optical index m , defined as :

$$m = n + ik \quad (1.32)$$

with n the refractive index and k the absorptive index. k represents how quickly the electromagnetic wave is absorbed by the particle. Knowledge of the in-situ soot optical properties and morphology is necessary to reduce uncertainty when making optical measurements of soot volume fraction or size distributions in flames. Optical measurements such as **LII** (Laser Induced Incandescence), **LE** (Laser Extinction) or **LS** (Laser scattering) rely on the choice of the complex optical index m . Therefore, experimental and numerical studies on this index have received a specific attention.

In the study of [Foster and Howarth \(1968\)](#), the authors provided experimental measurements for the complex index of refraction of soot. A plane polarised light reflection technique has been used on a series of carbons. The measurement of the quantity ρ defined as :

$$\rho^2 = \frac{I_p}{I_s} \quad (1.33)$$

where I_p and I_s are the intensities of the light parallel and perpendicular to the incident plane, enable to retrieve n and k .

In their study, the values of n and k for pure carbon (graphite) is assumed to be same as for soot. However, they did not take into account the influence of ratio H/C of the specimen. For soot, approximatively 97 percent of the mass is carbon ([Dombrovsky and Baillis \(2010\)](#)), while the remaining is hydrocarbons, hence the soot optical constants may differ from the graphite optical constants.

In 1969, [Dalzell and Sarofim \(1969\)](#) confirmed the influence of H/C ratio by collecting soot on cooled plates from laminar diffusion flames. In their study, it appears the values of n and k for acetylene soot were higher in the infrared range than the ones for propane soot. This has been explained by the ratio H/C higher in propane soot than in acetylene. [Pagni and Bard \(1979\)](#) pointed these data may be in error because the soot in the plate is actually a mix of soot and air.

In order to bypass this issue, Lee and Tien (1981) proposed a model based on dispersion theory and obtained soot optical properties from in situ flame transmission. The advantage of this model is its dependency on temperature. It also appears that the values obtained are independent of the ratio H/C of soots. However, this model relies on Lorenz-Mie scattering theory which only applies for spherical soot particles. Thus, these results can be used with confidence for such geometries.

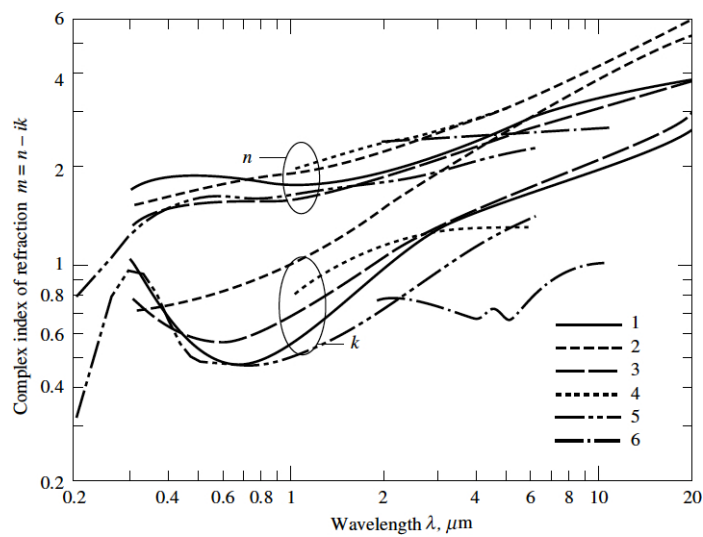


Figure 1.4: Comparison of soot complex index of refraction (from Modest (2003b)). 1 : Lee and Tien (1981) (polystyrene and plexiglas soot), 2 : Stull and Plass (1960) (amorphous carbon), 3 : Dalzell and Sarofim (1969) (propane soot), 4 : Howarth et al. (1966) (pyrographite at 300K), 5 : Chang and Charalampopoulos (1990) (propane soot), 6 : Felske et al. (1984a) (propane soot)

In Fig.1.4, an important uncertainty in these measurements can be observed, which may be an artifact of the differential experimental techniques employed in obtaining these data. It could also be related to different chemical and physical properties of the materials studied. These studies provide a range for n and for k , from 0.8 to 2 and from 0.3 to 1 respectively.

Following these experiments, analytical expressions of the complex index of refraction of soot particles have been derived. In the literature, three models are usually encountered.

Blokh's model :

A first expression, provided in Blokh (1988), relates the complex index m to

the wavelength λ :

$$m = 1,6 + 0,3\lambda - i\lambda^{0,6} \quad (1.34)$$

This relation is valid for wavelengths between 1 and 6 μm . This simple expression is not adapted to soot radiation studies, since soot are emitting mostly in the visible wavelength and near infrared.

Chang and Charalampopoulos' model :

Another classical expression is provided for n and k ,in the range of interest, in [Chang and Charalampopoulos \(1990\)](#). This expression is widely used in experimental studies of laminar and turbulent flames, and is given by :

$$\begin{aligned} n &= 1.811 + 0.1263 \ln \lambda + 0.027 \ln^2 \lambda + 0.0417 \ln^3 \lambda \\ k &= 0.5821 + 0.1213 \ln \lambda + 0.2309 \ln^2 \lambda + 0.01 \ln^3 \lambda \end{aligned} \quad (1.35)$$

This formulation is valid for wavelengths up to 20 μm , which is adapted to study soot radiation.

Constant formulation :

In practical applications, the use of the first two models is quite difficult. Indeed, these models are *spectral* formulations so *spectral evaluations* of the RTE must be considered which can lead to an increase of CPU time. As reviewed in [Smyth and Shaddix \(1996\)](#), the combustion community uses a constant value of $\mathbf{m} = \mathbf{1.57-0.56i}$ instead of considering a wavelength dependency.

Table 1.2 gathers the different values of m used in some recent numerical and experimental studies found in the literature dealing with soots optical properties.

The numerous values used for m show the difficulty to obtain a standard value of the soot refractive index. According to the table, two values of m are retained for the study :

- A constant value of $m = 1.57 - 0.56i$ since this value is widely used for the study of sooting diffusion flames
- The wavelength dependent formulation provided by [Chang and Charalampopoulos \(1990\)](#)

1.3.3 Radiative properties for spherical soot particles

In this section, different models of soot radiative properties are detailed. We first introduce a series of definitions useful in the derivation of soot radiative models. Then, the exact *Mie* theory for a single sphere is presented. Approximate models belonging to the *Rayleigh's* model family are then detailed and

Study	Value of m
Santoro et al. 1983 Santoro et al. 1987 Smyth et al. 1985 Snelling et al. 1999 Guo 2002 Arana 2004 Yon 2008 Zhang 2009 Yon 2015	$m = 1.57 - 0.56i$
Puri et al. 1993 Lee and Tien 1981 Iyer 2007	$m = 1.90 - 0.55i$
Liu 2008 Fuentes et al. 2013	Chang formulation
Kahnert 2010	$1.77 - 0.63i$
Doner 2017 Mulholland et al. 1994	$1.77 - 0.56i$

Table 1.2: Values of m used in the literature to study sooting flames

compared to the Mie's solution reference. In this section, soot particles are assumed to be **spherical**.

1.3.3.1 Basic definitions

Radiative properties of a spherical particle depend on three non-dimensionnal parameters (Modest (2003b)) :

- the complex refractive index m , introduced in the previous section,
- the non-dimensionnal size parameter $x = \frac{\pi d}{\lambda}$ with d the diameter of the spherical particle,
- the ratio of the mean distance of soot particles with the wavelength $\frac{a}{\lambda}$ with a being the distance between the center of two particles.

This latter ratio characterizes two types of scattering :

- if the ratio is smaller than 1, then the scattering by one particle can be affected by the other particles since they are close to each other : this is the dependent scattering regime,
- if the ratio is greater than 1, then each particle is far enough from the others to absorb and scatter as if the other particles do not exist : this is the independent scattering regime.

Figure 1.5 presents different regimes of scattering in function of the particle volume fraction and the size parameter. For a medium size particle, let us assume

the following values for respectively its diameter, the wavelength (infra-red here) and soot volume fraction : $d = 20 \text{ nm}$, $\lambda = 534 \text{ nm}$, $f_V = 10^{-6}$. One obtains a size parameter $x \approx 0.1$ which is a good order of magnitude of such parameter for soot particles. In Figure 1.5 the corresponding zone is within the independent scattering regime. More details on dependent scattering regimes, either obtained for bigger particles or volume fraction are provided in the review of Baillis and Sacadura (2000).

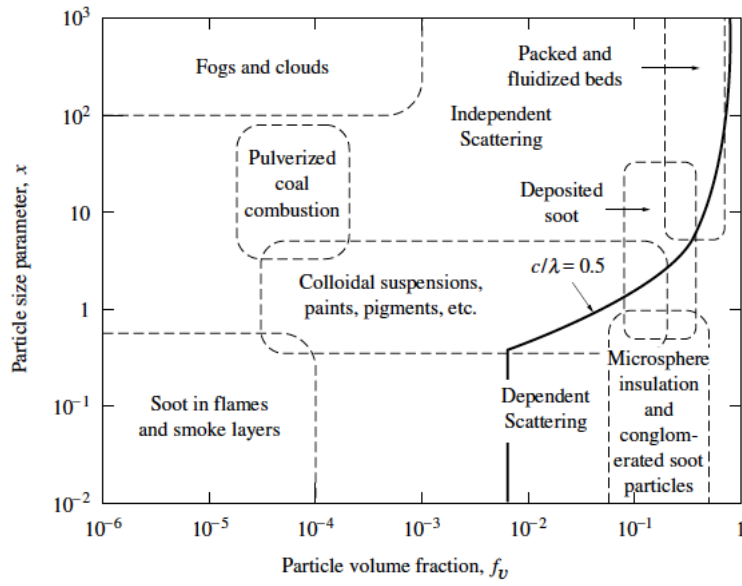


Figure 1.5: Scattering regime map as a function of the particle size parameter x and the soot volume fraction f_v . Extracted from Modest (2003b).

Radiative models presented hereafter are expressed in terms of efficiency factors, accounting for absorption, scattering and extinction. These quantities are respectively defined as :

$$\begin{aligned} Q_{abs} &= \frac{4C_{abs}}{\pi d^2} \\ Q_{scat} &= \frac{4C_{scat}}{\pi d^2} \\ Q_{ext} &= \frac{4C_{ext}}{\pi d^2} \end{aligned} \tag{1.36}$$

Coefficients C_{abs} , C_{scat} , $C_{ext} = C_{abs} + C_{scat}$ are the absorption, scattering and extinction cross-sections. From these quantities, one can retrieve the radiative absorption and the scattering coefficients, under some assumptions :

- the particles have the same optical properties,

Model	Assumptions	Shape of particle
Mie scattering theory	Exact	Spherical particle
Rayleigh scattering	$x \ll 1$ and $ m x \ll 1$	
Rayleigh-Gans scattering	$ m-1 \ll 1$ and $2x m-1 \ll 1$	
Geometrical optics approximation	$x \gg 1$ and $2x(m-1) \gg 1$	
Anomalous Diffraction	$x \gg 1$ and $ m-1 \ll 1$	

Table 1.3: List of encountered models for single spherical particle. m is the optical index of soot particle, and x the size parameter.

- the particles are within the independent scattering regime,
- the particles are described by a particle size distribution $n(R)$.

The absorption coefficient and the scattering coefficient of soot particles $\kappa_{\lambda,soot}$ are usually expressed in terms of wavelength λ . They are given by :

$$\kappa_{\lambda,soot} = \int_0^{+\infty} C_{abs}(R)n(R) dR \quad (1.37)$$

$$\sigma_{\lambda,soot} = \int_0^{+\infty} C_{sca}(R)n(R) dR \quad (1.38)$$

Finally, we define the *phase function* as the probability that a electromagnetic wave is scattered at a given angle θ . By definition, it corresponds to the fraction of intensity scattered into a direction θ :

$$\Phi(\theta) = \frac{I_{scattered}(\theta)}{I_{incoming}}. \quad (1.39)$$

The phase function is often normalized such as :

$$\frac{1}{4\pi} \int_{4\pi} \Phi(\theta) d\Omega \equiv 1 \quad (1.40)$$

The expression of the phase function depends on the considered model.

Hence, to fully characterize soot radiative properties, we need to determine the two cross-sections coefficients and the phase function expression. Several models can be encountered to treat radiation by spherical particles, under some assumptions gathered in Table 1.3. Geometrical optics and anomalous diffraction theories will not be considered here as soot particles are not fulfilling the required assumptions of such approaches.

1.3.3.2 Mie's theory

Mie's theory is the exact solution of the scattering problem of an electromagnetic wave train traveling through a medium with a single sphere. A complete review of this theory can be found in [Bohren and Huffman \(1983\)](#). The theory is based on the resolution of Maxwell's equations.

In this case, the efficiency factors of scattering and extinction are expressed in the form of the following series :

$$\begin{aligned} Q_{ext} &= \frac{2}{x^2} \sum_{n=1}^{+\infty} (2n+1) \Re(a_n + b_n) \\ Q_{sca} &= \frac{2}{x^2} \sum_{n=1}^{+\infty} (2n+1) (|a_n|^2 + |b_n|^2) \end{aligned} \quad (1.41)$$

where a_n and b_n are the Mie scattering coefficients, obtained using Riccati-Bessel functions $\psi_n(x)$ and $\zeta_n(x)$, and expressed as [Van De Hulst \(1957\)](#):

$$\begin{aligned} a_n &= \frac{\psi'_n(mx)\psi_n(x) - m\psi_n(mx)\psi'_n(x)}{\psi'_n(mx)\zeta_n(x) - m\psi_n(mx)\zeta'_n(x)} \\ b_n &= \frac{m\psi'_n(mx)\psi_n(x) - \psi_n(mx)\psi'_n(x)}{m\psi'_n(mx)\zeta_n(x) - \psi_n(mx)\zeta'_n(x)} \end{aligned} \quad (1.42)$$

with m the complex refractive index defined in the previous section. One may notice the absorption factor is obtained as a difference of $Q_{ext} - Q_{sca}$. Once these coefficients have been calculated, efficiency factors and corresponding absorption and scattering coefficients are derived using powerful algorithms ([Mätzler \(2002\)](#)).

The model also provides a formulation for the scattering phase function. A simplified expression, provided by [Chu and Churchill \(1955\)](#) is using Legendre polynomials whose coefficients are directly related to a_n and b_n .

Several studies ([Deirmendjian et al. \(1961\)](#), [Kattawar and Plass \(1967\)](#), [Wiscombe \(1980\)](#)) pointed limitations of this theory in terms of computational efficiency. Efficiency of calculation decreases for increasing n which causes complete failure of the methodology for large size particles, since many terms must be calculated in the series.

Due to the high computational cost of such method, it is not affordable in a context of CFD calculations. In practice, approximate models are used instead. Among them, the widely used Rayleigh's theory that applies for small particles is presented hereafter.

1.3.3.3 Rayleigh's theory

Optical properties of some small particles can be predicted on the basis of the so-called Rayleigh theory. Rayleigh's theory applies if the following conditions are verified :

$$\begin{aligned} x &\ll 1 \\ |m|x &\ll 1 \end{aligned} \quad (1.43)$$

The first condition is true for particles of a very small radius in comparison with the wavelength, which is verified for soot particles. The second condition gives a limitation for the optical properties of particle. The constant formulation of m introduced in Section 1.3.2 leads to a value $|m|$ around 1.5. In Figure 1.5, the value of x for soot in flames is around 0.1 , hence the second condition is satisfied as well.

Rayleigh theory appears as the Mie's theory asymptotic solutions as x becomes very small comparing to the unity. In this case the scattering and absorption efficiencies are:

$$\begin{aligned} Q_{sca} &= \frac{8}{3} \left| \frac{m^2 - 1}{m^2 + 2} \right|^2 x^4 \\ Q_{abs} &= -4\Im \left(\frac{m^2 - 1}{m^2 + 2} \right) x \end{aligned} \quad (1.44)$$

where x is the size parameter, m the refractive index and \Im the imaginary part operator.

In this expression, scattering by Rayleigh particles is very much less important than absorption, since $x \ll 1$.

The knowledge of the efficiency factors enables to derive the absorption and scattering coefficient needed for the radiative transfer equation.

Absorption coefficient for soot particles :

$$\kappa_{\lambda,soot} = \int_0^{+\infty} C_{abs}(R)n(R) dR \quad (1.45)$$

$$= - \int_0^{+\infty} 8\pi^2 R^3 n(R) \frac{1}{\lambda} \Im \left(\frac{m^2 - 1}{m^2 + 2} \right) dR \quad (1.46)$$

introducing the volume fraction f_V , defined as :

$$f_V = \int_0^{+\infty} \frac{4}{3}\pi R^3 n(R) dR \quad (1.47)$$

one obtains :

$$\kappa_{\lambda,soot} = -\Im \left(\frac{m^2 - 1}{m^2 + 2} \right) \frac{6\pi f_V}{\lambda} \quad (1.48)$$

A refractive index function $E(m)$ is commonly employed in the literature to describe soot properties :

$$E(m) = -\Im \left(\frac{m^2 - 1}{m^2 + 2} \right) \quad (1.49)$$

Since m is a function of λ , the index function $E(m)$ depends also on the wavelength. Optical diagnostics have been made to obtain measurements of $E(m)$ and therefore provided values of absorption coefficient for soot in Rayleigh's regime. These experiments were carried for different types of flames (diffusion, premixed laminar or turbulent) using several techniques : thermometry CARS (Snelling et al. (1999)), extinction measurements (Lee and Tien (1981)) or LII (Liu et al. (2004)). A comparison between the different studies is provided in Mouton (2014).

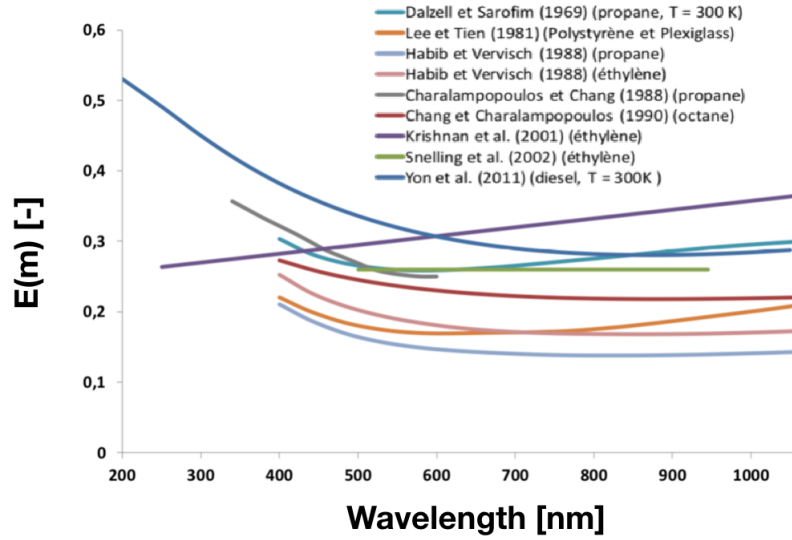


Figure 1.6: Comparison of $E(m)$ with excitation wavelength λ , extracted from Mouton (2014).

In our work, we consider only two formulations (constant and spectral) for the optical index m , which leads to only two formulations of $E(m)$. Using a value of $m = 1.57 - 0.56i$, the obtained absorption coefficient expression is $\kappa_{\lambda,soot} = 4.89 f_v / \lambda$. Let us emphasize that this expression states that absorption

by soot particles is proportional to the soot volume fraction and increases as λ is lower.

However, in an important number of studies, a choice of $\kappa_{\lambda,soot} = 5.5f_v/\lambda$ is retained (Liu et al. (2003), Saji et al. (2008), Zhang et al. (2009), Demarco et al. (2013)). This result is from the study of Buckius and Tien (1977) who reported average absorption coefficients for particules, in a non-homogeneous medium. However, these measurements were made on polymers as Polystyrene, plexiglas and Delrin which makes their use in laminar flame studies questionable.

In order to assess the impact of the optical index formulations, These two expressions of κ are compared with the one obtained using Equation 1.3.2 in Figure 1.7, for a soot volume fraction of 10 ppm, corresponding to a classic value found in experimental studies on coaxial diffusion laminar flames with etylene (Santoro et al. (1983)).

The absorption coefficient expressions obtained with Buckius and Tien (1977) and Smyth and Shaddix (1996) present similar values in the whole range of wavelength considered comparing to Chang and Charalampopoulos formulation. However, it can be observed that for the lowest and highest wavelengths, disparities occurs, which justifies the interest in considering a spectral formulation for the optical index m in this study.

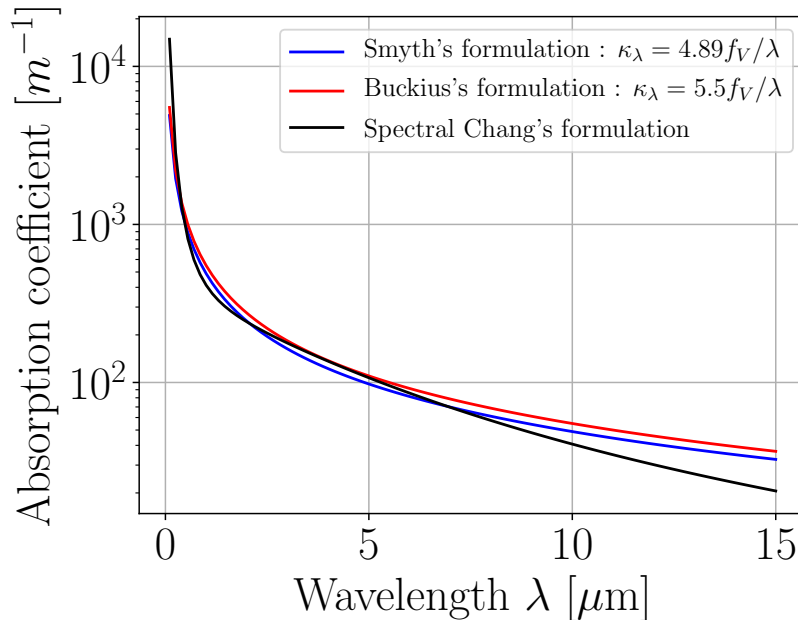


Figure 1.7: Comparison of the absorption coefficient obtained by Rayleigh scattering theory for different values of m .

Scattering coefficient for soot particles:

$$\begin{aligned}\sigma_{\lambda,soot} &= \int_0^{+\infty} C_{sca}(R)n(R) dR \\ &= F(m) \frac{32\pi^4}{\lambda^4} \int_0^{+\infty} V(R)n(R)R^3 dR\end{aligned}$$

in this expression, another refractive index function commonly employed $F(m)$ is introduced :

$$F(m) = \left| \frac{m^2 - 1}{m^2 + 2} \right| \quad (1.50)$$

Finally, $V(R)$ is the volume of the spheric soot particle of radius R . The main advantage of Rayleigh scattering theory is to provide a simple expression of the absorption coefficient which is directly proportional the volume fraction. A little effort must be done to retrieve the scattering coefficient : the **particle size distribution $n(\mathbf{R})$** is needed and the integral must be evaluated numerically in the general case of polydispersion in the soot particle size.

Phase function for soot particles :

Finally, the phase function is obtained by taking the limit of Mie's theory expression for $x \ll 1$ and $|m|x \ll 1$, which yields to :

$$\Phi(\Theta) = \frac{3}{4} (1 + \cos^2 \Theta) \quad (1.51)$$

This phase function presents several interesting features due to the approximation of Rayleigh's model :

- the phase function is symmetric,
- the phase function does not depend neither on the size of the particle nor the wavelength

A common way of displaying the phase functions is using a polar representation as shown Figure 1.8. In the case of isotropic scattering, the phase function is a circle, which shows the equiprobability to scatter in a given direction.

The interest in such a representation is that it exhibits whether preferential scattering is performed in a given angle : the left part of the polar plot represents a *backward scattering area* while the right part is *forward scattering area*. For single and small spheres, it can be seen that scattering presents a moderate anisotropy.

The previous results have also been obtained for other geometrical form such as ellipsoids and finite cylinders (Bohren and Huffman (1983) Van De Hulst (1957)) which not limits the Rayleigh theory to single spherical spheres. It is

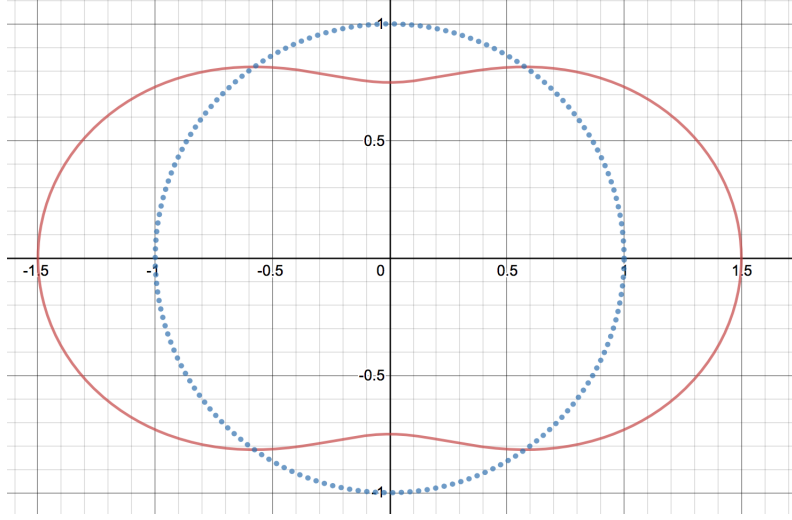


Figure 1.8: Polar representation of the Rayleigh's phase function. Isotropic scattering is also displayed in dashed lines.

worthwhile to notice that the Rayleigh approximation is usually inapplicable when the size parameter x is greater than 0.3 (Dombrovsky and Baillis (2010)). To extend its range of capability, Penndorf (1962) and later Caldas and Semião (2001) have accounted for high order terms of the Mie series, considering again x small compared to unity.

1.3.3.4 Planck-mean soot absorption coefficient based on Rayleigh theory

Another frequently invoked simplification is the gray-gas model. In this case, spectral properties such as emittance are independent of the wavelength. Hence, the spectral dependence of the optical properties of the medium can be expressed by mean values which are averaged in the entire spectrum.

Two useful parameters are defined according to the optical thickness of the domain : the Planck mean absorption coefficient κ_P (for optically thin cases) and the Rosseland mean absorption coefficient κ_R (for optically thick cases).

$$\kappa_P = \frac{\int_0^{+\infty} \kappa_{\nu,soot} I_{b\nu}(T) d\nu}{\int_0^{+\infty} I_{b\nu} d\nu} \quad (1.52)$$

$$\frac{1}{\kappa_R} = \frac{\int_0^{+\infty} \frac{1}{\kappa_{\nu,soot}} \frac{dI_{b\nu}}{dT} d\nu}{\int_0^{+\infty} \frac{dI_{b\nu}}{dT} d\nu} \quad (1.53)$$

In the expressions above $I_{b\nu}$ is the blackbody intensity at a given wavenumber ν . For the sake of clarity, the absorption coefficient is noted $\kappa_{\nu,soot}$ to emphasize its dependency to the wavenumber.

Felske et al. (1984b) derive the expressions of these coefficients for particles in the Rayleigh regime, under the Milne-Eddington assumption. It assumes that the absorption coefficient can be written as a product of two functions : $\kappa_{\nu,soot}(T) = f(\nu)g(T)$. Since in the Mie theory (and in the Rayleigh regime), the absorption coefficient $\kappa_{\nu,soot}(T)$ is proportional to ν , the function f is assumed to be ν . The two obtained coefficients are expressed by :

$$\kappa_P = 3.83C_0f_VT/C_2 \quad (1.54)$$

$$\kappa_R = 3.60C_0f_VT/C_2 \quad (1.55)$$

where C_0 must be determined from the optical properties of the soot particles, and C_2 the Planck's second constant ($C_2 = 1.4388 \cdot 10^{-2}$ m.K).

Because of the limited domain of application of the coefficients κ_P and κ_R (respectively for optically thin and thick media), Tien and Felske (1977) suggested to use an average value to calculate radiative power for different media.

$$\kappa_{mean} = 3.72C_0f_VT/C_2 \quad (1.56)$$

Assuming the particles are in the Rayleigh regime, and that the optical index m is independent of λ , the expression of C_0 is given by

$$C_0 = \frac{36\pi nk}{(n^2 - k^2 + 2)^2 + 4n^2k^2} \quad (1.57)$$

1.3.3.5 Rayleigh-Debye-Gans theory

For particles which a non-regular geometry, solving the radiative problem is extremely complex, especially when scattering is taken into account. The *general Rayleigh-Debye* theory is based on division of an *arbitrary shape* into volume elements, each element is then treated as a Rayleigh scatterer excited by the incident field. It also assumes that particles have a small refractive index m with respect to that of ambient medium. With these hypotheses, it is possible to derive somewhat complex expressions to fully determine the scattering field (Bohren and Huffman (1998)) without any limitation of particle shape. Particles with such optical index property has been considered in the book of Mobley (1994) for organic particles in water.

Gans rederived the scattering formula for an homogeneous *sphere*, adding another assumption, relative to the size parameter x . This leads to the RDG theory for an homogeneous sphere and presented after :

$$\begin{aligned} |m - 1| &\ll 1 \text{ (Rayleigh - Debye general theory)} \\ 2x|m - 1| &\ll 1 \text{ (Rayleigh - Debye - Gans theory)} \end{aligned} \quad (1.58)$$

These conditions show that neither the particle size nor the relative refractive index can become too large.

The scattering and absorption cross-sections coefficients for the RDG theory are given in Kerker et al. (1963) and summarized hereafter.

Efficiency factor and absorption coefficient for RDG theory :

The expression of the cross-section coefficient is the same as in the Rayleigh theory, which leads then to the same formulation for the absorption coefficient presented in Section 1.3.3.3 :

$$Q_{abs} = -4\mathfrak{J} \left(\frac{m^2 - 1}{m^2 + 2} \right) x \quad (1.59)$$

$$\kappa_{\lambda,soot} = -\mathfrak{J} \left(\frac{m^2 - 1}{m^2 + 2} \right) \frac{6\pi f_V}{\lambda} \quad (1.60)$$

This behaviour is expected since RDG theory divides the domain into Rayleigh particles acting independently.

Efficiency and scattering coefficient for RDG theory :

The RDG theory provides a more complex expression for the scattering cross-section efficiency, and is given by :

$$Q_{sca} = |m - 1|^2 x^4 \int_0^\pi G^2(u) (1 + \cos(\Theta))^2 \sin(\Theta) d\Theta \quad (1.61)$$

with $G(u)$ given by :

$$G(u) = \frac{2}{u^3} (\sin(u) - u \cos(u)) \quad u = 2x \sin\left(\frac{\Theta}{2}\right) \quad (1.62)$$

Obviously, once Q_{sca} is known, the scattering coefficient σ_λ is determined using Equation 1.38. The quantity G is known as the form factor : it represents the

modification of the intensity due to the size of the particle.

Phase function for RDG theory :

The scattering function is here more complex. Its general expression is given by :

$$\Phi(\Theta) = \frac{2G^2(u)(1 + \cos^2 \Theta)}{\int_0^\pi G^2(u)(1 + \cos^2 \Theta) \sin \Theta d\Theta} \quad (1.63)$$

The previous results are only valid for homogeneous spheres, with a refractive index close to the unity, and is at the basis of more complex theories as we will discuss in Section 1.3.4.

1.3.3.6 Validity of the RDG theory for spherical particles

The previous models in their construction rely on assumptions on the size of the particle and/or the optical index m . The latter point is probably one of the most complex as a strong uncertainty on this parameter exists. Moreover, because of their dependency to the wavelength λ , it is possible to encounter cases where such assumptions are no longer verified.

Farone and Robinson (1968) have studied the range of validity of Rayleigh-Debye-Gans theories in function of the value of the size parameter x and the optical index m . They considered a case of a single sphere hit by an electromagnetic wave and compared each theory with the exact Mie theory. The results of this study are displayed in Figure 1.9.

The contours numbers show the relative error between both theories, with the area noted I corresponding to the lowest errors applied on the efficiency factor Q_{scat} (Equation 1.61). Three distinct areas can be observed : the zone I, confined to values of m close to the unity and extending to high values of x represents the range of validity of this theory. This is expected since the main assumption of RDG theory is to consider m close to 1. As m increases, the maximum value of x drops quickly which is also pointed in the RDG section : the size parameter x cannot be too large.

In Section 1.3.2, a constant value of m is chosen and gives a module of 1.5 approximatively for soot particles. In Figure 1.9, for standard values of x for soot particles (around 0.1) one may observe a poor agreement between the two methods as we are in the area noted II. It is important to reckon that this study only considers spherical particles, which is a drastic simplification for soot.

Indeed, soot particles are known to be aggregates (Köylü and Faeth (1993)). Therefore, it has been necessary to develop other approaches in order to take into account complex soot morphology, as presented in the next section.

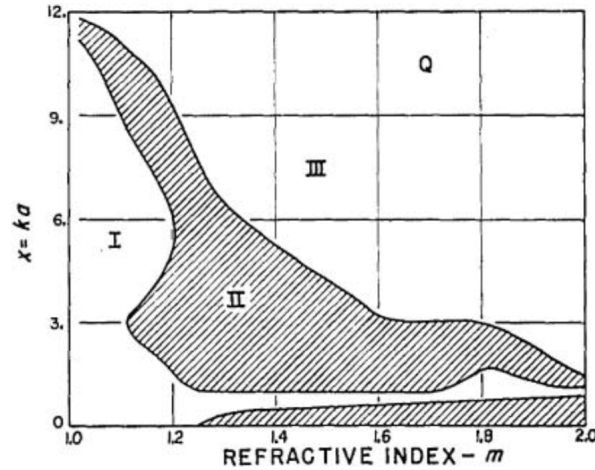


Figure 1.9: Contour error in terms of Q_{ext} . x is the size parameter and m the refractive index *Kerker et al. (1963)*. Region I corresponds to an error of less than 10% between RDG and Mie's theory. Region II corresponds to an error less than 100%, region III corresponds to an error greater than 100%.

1.3.4 Radiative properties for aggregates

Before presenting the theories and models describing soot aggregates, we briefly introduce experimental findings on soot aggregate structure these models rely on.

1.3.4.1 Experimental characterization of soot aggregates: diagnostics and morphology

Experimental diagnostics :

Because of the small soot particles size, classic techniques as mass spectroscopy cannot be used to determine soot volume fraction, particle size distribution and morphology properties. We mainly find two type of experimental diagnostics used for soot particles :

- In-situ measurements which exploit the interaction of light with particles in the combustion environment. In general, these techniques are non-intrusive. These techniques are important for the determination of soot volume fraction, particle nucleation and growth kinetics.
- Ex-situ measurements which are intrusive and gives a better information on the structure and the morphology of soot.

The light extinction technique is a first example of in-situ measurement and is based on computing the light beam transmission via soot particles. This

technique assumes that scattering is negligible, so the transmittance is directly linked to the absorption coefficient which enables to determine the soot volume fraction f_V , providing an expression for the optical index m . If scattering cannot be neglected, studies as [Yang et al. \(2005\)](#) are using correction factors in the relation. This factor depends on the measured flame and varies along its axis, and is measured using Light scattering technique.

Light scattering technique or laser diffraction is very similar to the Laser extinction technique, but the measurement is not performed in the axis of the incoming light. The particle size distribution is here obtained by measuring the angular variation in intensity of light scattered as a laser beam passes through the flame. By analyzing the scattering patterns, it is possible to determine the size of soot particles : this shows the primal importance of scattering to have access to soot morphology properties.

More recent in-situ techniques have been developed as the **Laser Induced Incandescence or LII**. The particles are hit by a laser and quickly heated to about 4000K. After the laser pulse, by heat conduction, the particles are cooling back to their initial temperature. Particles are then emitting radiation, which provides information on soot volume fraction and particle size distribution. As highlighted in [Liu et al. \(2006\)](#), the LII signal detected is actually biased by the scattering and the absorption of the radiation by the particles. This technique also needs a calibration by a Laser Extinction method, which depends on the refractive index m chosen, and also adds uncertainty in the LII.

With these three techniques, obtained data are analysed considering spherical particles (Rayleigh theory) and lead to errors in radiative properties determination. Optical diagnostic techniques such as Laser Extinction and Laser Scattering are used to measure soot volume fraction but are limited on soot morphology information and can only monitor soot formation and growth.

[Megaridis and Dobbins \(1988\)](#) proposed a non-intrusive technique based on thermophoretic sampling. Soots aggregates from an ethylene laminar flame are observed in an electronic microscope. This technique have been improved by more recent studies ([Tian et al. \(2004\)](#) and [Tian et al. \(2006\)](#), [Okyay \(2016\)](#)). One main advantage of this technique is that no calibration is required contrary to the other ones.

In [Figure 1.10](#), the aggregates structure of soot is appreciable, composed of nearly spherical primary particles. Notable effects such as the overlapping of primary particles are occurring and must be taken into account in radiative models for aggregates.

Aggregate description :

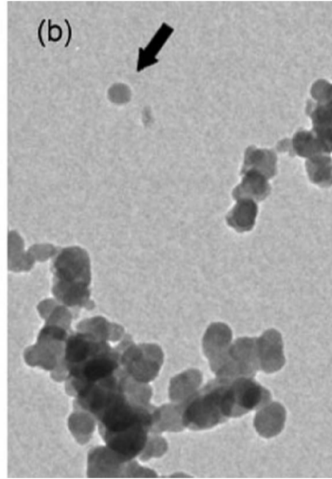


Figure 1.10: TEM characterization of soot aggregates for ethylene/air diffusion laminar flame. Both single sphere and aggregates are displayed in the TEM images (Okuyay (2016))

The application of the previously presented diagnostics enables to emphasize the aggregate structure of soot particles. These aggregates are characterized by a number of primary particles n_P with a diameter d_P .

Characterization of the diameter and number of primary particles has received an important interest. Very recent work conducted in Joo et al. (2018) and Gigone et al. (2019) has been focusing on collecting soot samples for different pressures in laminar diffusion flames, up to 16 bars. It has been shown that the maximum primary particle diameter reached was about 80 nm, regardless the pressure. However, the evolution of the number of primary particle with the diameter is strongly dependent on the pressure and the height above the burner.

The diameters of the primary particles follow a normal distribution as studied for acetylene and ethylene buoyant turbulent diffusion flames by Köylü and Faeth (1992). This statement is widely accepted and still in use in the latest studies (Liu et al. (2016), Doner and Liu (2017)). However, recent studies have been carried by Tian et al. (2006) on coflow laminar ethylene/air diffusion flame using TEM images on thousands of aggregates to obtain a statistical distribution of particles. The comparison of the experimental distribution with a log-normal law showed the inability of the model to reproduce the experimental results, a double lognormal model has been proposed instead to improve accuracy of future calculations.

The number of primary particles depends on the flame structure : in premixed flames, aggregates are formed by few tens of particles, unlike in turbulent flames where this number can go up to thousands of particles. However, regardless

the flame structure, an universal and well admitted empirical law describes the number of particles (Samson et al. (1987), Dobbins and Megaridis (1990), Puri et al. (1993), and used in many other studies) as :

$$n_p = k_f \left(\frac{R_g}{r_p} \right)^{D_f} \quad (1.64)$$

with n_p the number of primary particles, R_g the radius of gyration, r_p the radius of the primary particles, the fractal dimension D_f and the prefactor k_f . There is a common agreement in the values used for the fractal dimension, as explained in Okyay (2016), who compared the values of the empirical law used for several studies. Most of D_f values range between 1.6 and 1.9, whereas k_f ranges between 1.2 and 3.5. These differences are due to more complex measurement of k_f which depends on the experimental conditions, particle overlapping ... while D_f is universal to the measurement method.

1.3.4.2 Aggregates with spherical primary particles - RDG-FA model

In this section, the extension of Rayleigh-Debye-Gans theory for Fractal-Aggregates (RDG-FA) is considered. The RDG-FA approach relies on Rayleigh's theory for single spherical particles. This model, proposed by Dobbins and Megaridis (1991) considers absorption and scattering for fractal aggregates. Because of its computational simplicity and relatively low cost, this method is used in many studies in order to assess aggregate's influence in optical measurements (Murphy and Shaddix (2005), Liu et al. (2006), Yon et al. (2015), Liu et al. (2016)).

The main assumptions of original RDG-FA model are recalled here :

- Soot is a fractal aggregate whom primary particles verifies Equation 1.64,
- Each primary particle is supposed to verify the RDG constraints (Equations 1.58) and the Rayleigh hypothesis,
- No internal scattering is considered within an aggregate,
- Phenomena such as particle overlapping, necking and coating are neglected.

The model provides then an expression for the absorption and scattering coefficients, and the phase function.

Absorption coefficient for an aggregate :

Since there is no multiple scattering, we have the following result (Dobbins and Megaridis (1991)):

$$C_{abs,agg} = n_p C_{abs,p} \quad (1.65)$$

In this equation, the subscript *agg* refers to the aggregate while *p* refers to the primary particle. n_p is the number of primary particle of the aggregate.

Using Rayleigh's theory (which gives $C_{abs,p}$), the absorption cross-section of the aggregate is written as

$$C_{abs,agg} = -n_p \Im \left(\frac{m^2 - 1}{m^2 + 2} \right) \frac{4\pi x_p^3}{k'^2} \quad (1.66)$$

with x_p the size parameter of the primary particle, n_p the number of primary particles, and $k' = \frac{2\pi}{\lambda}$ the wave number. Recalling the definition of the absorption coefficient, we have :

$$\begin{aligned} \kappa_{\lambda,soot} &= \int_0^{+\infty} C_{abs,agg}(d)n(d)dd \\ &= \int_0^{+\infty} n_p C_{abs,p}(d)n(d)dd \\ &= - \int_0^{+\infty} 6\pi/\lambda \Im \left\{ \frac{m^2 - 1}{m^2 + 2} \right\} \underbrace{n_p \pi (d_p)^3 / 6}_{v(d)} n(d)dd \\ &= -6\pi/\lambda \Im \left\{ \frac{m^2 - 1}{m^2 + 2} \right\} \int_0^{+\infty} v(d)n(d)dd \\ &= -6\pi/\lambda \Im \left\{ \frac{m^2 - 1}{m^2 + 2} \right\} f_V \\ &= \frac{6\pi E(m) f_V}{\lambda} \end{aligned} \quad (1.67)$$

It appears that the expression of the absorption coefficient remains unchanged compared to the classic Rayleigh theory for a single sphere. In other words, the absorption coefficient in the RDGFA model does not depend on the morphology or size of the particle. This is a strong assumption, and leads to incorrect evaluation of the absorption coefficient (corresponding to an error of 10% in the absorption coefficient (Sorensen et al. (2018))). Recent improvements have been done to correct such coefficient and are presented in Section 1.3.6.

Scattering coefficient for soot aggregates :

The RDG-FA theory states that the scattering cross-section coefficient of an aggregate, $C_{sca,agg}$ is related to the scattering cross-section coefficient of a single particle $C_{sca,p}$ (given by the classic Rayleigh theory) by the following relation :

$$C_{sca,agg} = n_p^2 C_{sca,p} g \quad (1.68)$$

g is a corrective factor which takes into account the fractality of soot particles

and is given by :

$$g = \left(1 + \frac{4k'^2 R_g^2}{3D_f} \right)^{-D_f/2} \quad (1.69)$$

As previously mentioned for classic Rayleigh's theory for single sphere, there is not a simple expression for the scattering coefficient : the scattering coefficient is evaluated numerically via its integral form (Equation 1.38).

Phase function for an aggregate :

The phase function for an ensemble of aggregates can be defined by an integral formulation involving the number density function $n(V)$:

$$\Phi_{glob}(\theta) = \int_V \Phi_{agg}(\theta) n(V) dV \quad (1.70)$$

The scattering-phase function of a particular aggregate is defined by :

$$\Phi_{agg}(\theta) = \frac{4\pi}{C_{sca,agg}} \frac{C_{vv,agg}(\theta) + C_{hh,agg}(\theta)}{2} \quad (1.71)$$

where θ is the angle of scattering, $C_{vv,agg}$ and $C_{hh,agg}$ are the differential scattering cross-sections. In the RDG-FA theory, these two cross-sections are given by :

$$\begin{aligned} C_{vv,agg}(\theta) &= n_P^2 C_{vv,part} f(qR_g) \\ C_{hh,agg}(\theta) &= n_P^2 C_{hh,part} f(qR_g) \\ C_{vv,part} &= \frac{C_{hh,part}}{\cos(\theta)^2} = \frac{x_p^6 F(m)}{k'^2} \end{aligned} \quad (1.72)$$

The structure factor f can be seen as a parameter describing the angular dependency of the scattering. The scaling approach theory also enables to provide a formulation for the structure factor f which depends on the value taken by the product qR_g (with $q = 4\pi \sin(\frac{\theta}{2}) \frac{1}{\lambda}$ and R_g the gyration radius already introduced) :

$$\begin{aligned} f(qR_g) &= \exp\left(\frac{-(qR_g)^2}{3}\right) \text{ for } (qR_g)^2 \leq 1.5D_f \text{ (Guinier regime)} \\ f(qR_g) &= \left(\frac{\exp(1)(qR_g)^2}{1.5D_f}\right)^{(-D_f/2)} \text{ for } (qR_g)^2 > 1.5D_f \text{ (Power-law regime)} \end{aligned}$$

$$(1.73)$$

Such form factor is not universal, and several expressions can be encountered in the literature (Dobbins and Megaridis (1991), Köylü and Faeth (1994) or Yang, Hu, and Koylu (2005)). Liu et al. (2013) have studied different expressions of the form factor and compared results from the RDG-FA theory with an accurate theory called Generalized Multi-Mie model (briefly presented in Section 1.3.5) at a given wavelength. It appears that the up-to-date expression from Yang et al. (2005) is the most accurate. It will be retained in this work :

$$f = \left(1 + \frac{8(qR_g)^2}{3D_f} + (qR_g)^8 \right)^{-D_f/8} \quad (1.74)$$

By combining equations 1.68 and 1.72 and inserting into Eq. 1.71, one obtains the general expression of the phase function for one aggregate :

$$\Phi_{agg}(\theta) = \frac{3f(qR_g)(1 + \cos^2(\theta))}{4g(k', R_g)} \quad (1.75)$$

In the case of $f = g = 1$, the expression of the phase function is strictly equal to the one obtained in the classic Rayleigh theory for a sphere. Therefore, the ratio $\frac{f}{g}$ can be seen as a corrective factor taking into account the aggregate morphology of soot particles on how the light is scattered.

Comparison of RDG-FA method with exact solutions for aggregates

The ICP exact method developed by Iskander et al. (1989) is based on the volume integral equation and the method of moments. It calculates scattering from a cluster of chained spheres. Hence the aggregate is divided in spherical cells with uniform electromagnetic fields. A control volume analysis converts the governing equations to a set of linear algebraic ones. A complete study of this method has been provided by Nelson (1989).

It is also possible to define an equivalent sphere from the aggregate and use Mie's theory with the same volume as the aggregates. This method is known as *Mie scattering for an equivalent sphere*. (Sorensen (2001))

A comparison of these three methods in terms of scattering cross section have been studied by Köylü and Faeth (1993) and Farias et al. (1995) and is displayed in Figure 1.11.

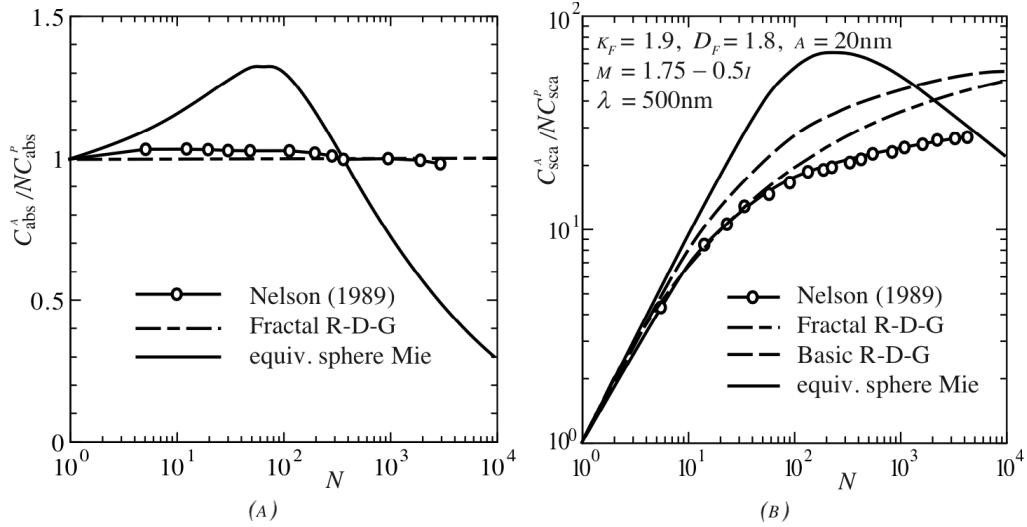


Figure 1.11: Comparison of ICP method, RDG standard and for fractal aggregates theories and equivalent sphere Mie method in terms of non-dimensional absorption (a) and scattering (b) coefficients. N is the number of soot particles in the aggregate.

On Figure 1.11, ICP model (corresponding to the dotted line) and RDG-FA approximation gives similar results for absorption and scattering cross-section coefficient. Equivalent sphere Mie theory gives significant error for a large number of primary particles for absorption coefficient underpredicting by a factor 2 the normalized absorption cross-section. This limit shows the necessity for considering fractal models when dealing with aggregates. The accuracy of RDG-FA comparing to the ICP technique has also been emphasized in the study of [Farias et al. \(1995\)](#).

The RDG-FA method offers a good trade-off between accuracy and computational time and is relatively easy to implement. For these reasons, this approach is retained in our work.

1.3.5 Other methods : irregular geometries

The previous methods (ICP, RDG-FA, Equivalent Mie theory) are valid for aggregates with monodisperse spherical primary particles. More sophisticated theories have been developed for irregular geometries and are used to assess the accuracy of the retained RDG-FA model and improves it.

[Kahnert \(2003\)](#), [Okuyay \(2016\)](#) and [Mishchenko et al. \(2010a\)](#) provided a review of the different methods available when dealing with random aggregates geometry. Additional information can be found in these three papers. These methods can be classified in two main categories :

- *Methods based on partial derivative equations* which calculate the scatter-

ing field by solving the Maxwell equation. SVM (Seperation of Variable method in [Asano and Yamamoto \(1975\)](#)), FDTD (Finite Differences Time Domain in [Yang et al. \(2000\)](#)), FEM (Finite Element Method in [Coccioli et al. \(1996\)](#)), PMM (Point-Matching Method in [Wriedt and Comberg \(1998\)](#)) are some examples of such methods,

- *Methods based on integration over volume or surface of equations* derived from the Maxwell equations, in which T-Matrix methods, Generalized Multiparticle Mie method presented hereafter are part of.

The next sections aim to present briefly the two exact methods based on Surface and Volume equations. Since these methods suffer from a high computational cost, an approximate method named Discrete Dipole Approximation have been developed and is also discussed hereafter.

T-Matrix method

T-Matrix is a surface based method dealing with irregular aggregates, as proposed by [Waterman \(1971\)](#). In the T-matrix method, the incident and scattering fields (given by the Maxwell's equations) are expressed in the form of a series of spherical vector wave functions. This approach is named the T-matrix method when the expansion coefficients of the incident wave and the scattering wave are connected by a linear transformation called T-matrix. The matrix contains all the information on the particle's optical properties for a given wavelength : directionnal scattering is then provided and can be used for optical diagnostics such as LII or LS. However, this method suffers from stability issues for irregular grains, high aspect ratio or large aggregates ([Okyay \(2016\)](#) and references therein). Its computation time depends also on the number and size parameter of primary particles. Since Maxwell's equation are linear, the superposition principle enables to obtain scattering information on aggregates of sphere ([Mishchenko et al. \(2010b\)](#)). However, this method is restricted to clusters of which the enclosing spheres of the individual spheroids do not overlap ([Comberg and Wriedt \(1999\)](#)). Overlapping properties will be discussed in the next section and must be taken into account to predict radiative properties accurately.

Generalized Multiparticle Mie method (GMM)

This method is an extension of the analytical Mie solution, applied on aggregates, and presents similar features with the T-Matrix method. More information can be found in the development of this method by [Xu \(1995\)](#). This extension is mainly applied for aggregates of spherical particles, since it is related to Mie's solution for spheres, however, the theory is applicable to nonspherical ones ([Lin Xu and Gustafson \(2001\)](#), [Jacquier and Gruy \(2007\)](#)).

This method as the T-Matrix presents a high computational cost. Approxi-

ated methods have therefore been developed and compared with GMM theory (Jacquier and Gruy (2010)) such as the Effective Refractive Index method.

Discrete Dipole Approximation (DDA)

The DDA technique was originally developed by Purcell and Pennypacker (1973) and extended by Draine (1988) and Enguehard (2009). It enables to calculate the electromagnetic field diffused by an object with random shape, subject to an incidence electromagnetic wave. Radiative properties are then derived from the electromagnetic field calculated.

It consists on discretizing the object into N oscillating dipoles, which must verify two conditions : the characteristic size of the dipole should be smaller compared to the attenuation length of the incident wave inside the material and the path difference of the incident electromagnetic field inside the volume must be smaller than 2π . Draine unifies these conditions to : $|m|ka < 1$.

Enguehard (2009) compared the results of DDA and Mie theory on silice nanoparticles. The results are similar for high values of λ . As the wavelength becomes smaller, DDA predicts significantly inferior extinction coefficients which are in agreement with experimental values.

To perform a simulation using DDA for soot particles, it is first necessary to generate a soot aggregate geometry. Two methods are widely used : particle-cluster aggregation (PCA, in which aggregation is done only between isolated particles and clusters) and Cluster-Cluster aggregation (CCA, in which aggregate between clusters are allowed). Because of the range of fractal diameter considered for soots (between 1.6 and 1.8), Okyay (2016) stated the DLCCA algorithm is more suitable for soots study.

DDA method has been compared with exact methods in many studies (Hovenier et al. (1996), Wriedt and Comberg (1998), Yurkin et al. (2007), and more recently by Okyay (2016)) and discussed in the review of Yurkin and Hoekstra (2007).

Comberg and Wriedt (1999) compared the DDA method with the GMM method presented in the previous section, simulating clusters of few spheres. Intensity are compared in Figure 1.12 for two spheres in the parallel and perpendicular rows to the incident wavelength.

The DDA approach gives comparable results to the GMM exact method. Therefore, this approach is used as a reference when assessing the capability of the RDGFA method to take into account more detailed phenomena, as shown in the next section.

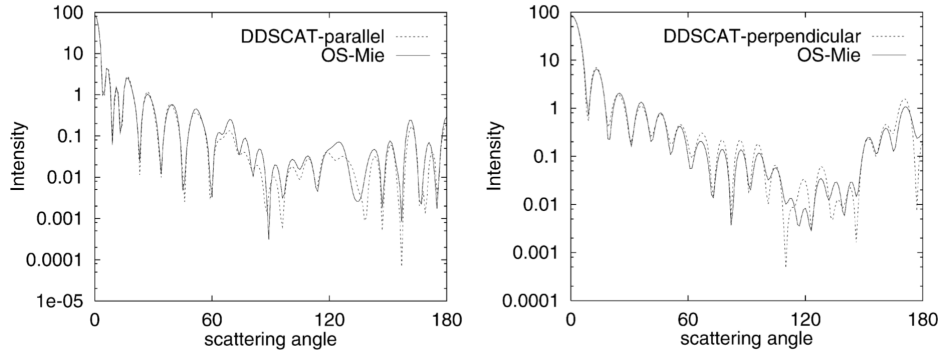


Figure 1.12: Comparison of DDSCAT code using DDA and GMM method (from *Comberg and Wriedt (1999)*) in terms of intensity in a row parallel (left) and perpendicular (right) to an incident electromagnetic wave.

1.3.6 Towards highly-detailed aggregates description : latest improvements of the RDG-FA method

In this section, state-of-the-art RDG-FA improvements are presented and discussed. Aggregates are numerically generated and reference values are computed using the DDA approach.

Four main features corresponding to the 4 main limitations of the original RDG-FA theory are discussed :

- the internal multiple-scattering within an aggregate,
- the overlapping of primary particles,
- the necking or ageing of primary particles,
- the polydispersity of primary particles

Multiple-scattering effects :

The inclusion of multiple-scattering effects (*Nelson (1989)*) in the RDG-FA theory has been studied by Yon and coworkers, first for a given wavelength (*Yon et al. (2008)*) and then for a whole range of wavelengths (*Yon et al. (2014)*). The motivation is to include such effects on Light Scattering experimental diagnostics, which rely on the RDG-FA theory to determine aggregates parameters and particle size. The principle of the method is to introduce corrective parameters which are derived by fitting results of high-accuracy calculations. Namely, the form factor from the original RDG-FA theory was a two-form expression depending on the values of qR_g (see Equation 1.73). The cut-off value Ξ is $1.5D_f$ with D_f the fractal dimension. In the new model, it is now expressed

by :

$$\Xi = \frac{3C}{2B} \quad (1.76)$$

where C and B are function of the wavelength, the fractal parameters k_f and D_f introduced Equation 1.64, and coefficients obtained by fitting DDA results. The classic expression of the absorption coefficient is modified by introducing a parameter h also based on DDA calculations :

$$C_{abs,agg} = hN_p C_{abs,p} \quad (1.77)$$

Because of such an expression, the absorption coefficient cannot be written as simple as the classic formulation of Equation 1.67. The effect of multiple-scattering (MS) is complex as it strongly depends on the wavelength and the size of the aggregates. It tends to increase absorption effects for small aggregates and high wavelengths. MS also impacts scattering since the structure factor f is impacted : the amount of scattering light increases when aggregates are bigger and for lowest wavelengths. On the contrary, for smallest aggregates and highest wavenumbers, this amount decreases.

Overlapping and necking :

So far, soot aggregates without interaction have been considered. However, as shown on the tomography in figure 1.10, primary particles do interact with each other. These interactions are of two natures : between primary particles (characterized by two phenomenon : overlapping and necking as displayed figure 1.13) and with the environment, characterized by the coating phenomenon.

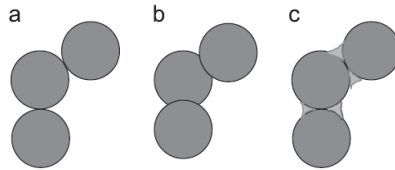


Figure 1.13: *Illustration of soot morphology interactions : standard point-touch (a), overlapping (b) and necking (c) from Liu et al. (2016)*

Overlapping has received a very recent attention (Johnsson et al. (2013),Yon et al. (2015), Doner and Liu (2017)) since this phenomenon is not taken into account in CCA algorithms. This phenomenon is characterized by a non-dimensional overlapping number introduced in Brasil et al. (1999), C_{ov} varying between 0 (no overlap) and 1 (complete overlap : the center of the two particles are in the same position). The studies have reported that the overlapping

globally reduces the absorption coefficient (for the smallest wavelengths) and makes the scattering more isotropic.

Figure 1.14 shows the influence of overlapping in extinction coefficient studied by Yon et al. (2015) using a DLCA algorithm to generate overlapping. It appears that overlapping decreases the coefficient for small wavelengths (around 10 %) but increase it (around 5 %) for higher wavelengths.

In the recent study by Doner and Liu (2017), overlapping is simulated by enlarging the diameter of originally point-touch primary particles. Overlapping causes a decrease of the volume of the aggregate, which causes a decrease in absorption coefficient as observed in both studies. It causes also in the infrared an important increase of scattering coefficient which is consistent with the findings by Yon et al. (2015) as shown in Figure 1.14. This increase is due to the enhancement of multiple scattering taken into account when considering overlapping.

The necking effect between primary particles is simulated by adding necking material around the contact area, using a 3D level-set function. Similar results as those for overlapping have been underlined, more information are provided in the studies by Bescond et al. (2013) and Yon et al. (2015).

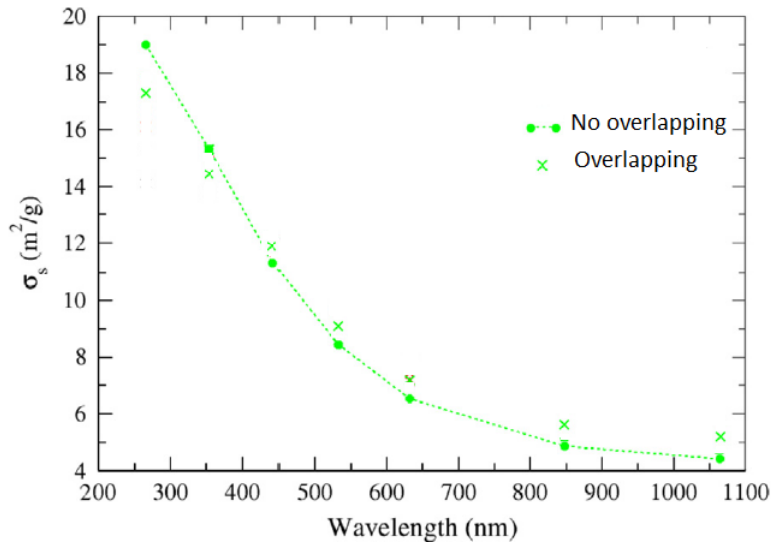


Figure 1.14: Influence of soot overlapping in extinction coefficient (Yon et al. (2015))

Coating :

After emitted from a combustion device, soot during their aging process interact with its environment and can become coated by organic aerosols, water, ...

The coating phenomenon has been studied by [Liu et al. \(2016\)](#), generating aggregates using a DLCA algorithm, adding overlapping and necking (via the 3D level-set function defined above) and adding to these realistic aggregates a weakly absorbing material (WAM) coating.

It appears that coating increases both scattering and absorbing coefficient. The increase in absorption coefficient have been observed in experimentations and is known as a lensing effect ([Lack et al. \(2013\)](#)). In the study, results from DLCA algorithms and equivalent Mie sphere have been compared. Mie's theory also predicts the increase of scattering and absorbing coefficients but tends to over-estimate the obtained values . If more detailed techniques as DDA are required in order to predict with accuracy soot radiative properties and complex phenomena (coating, necking, overlapping), the RDG-FA theory is also able to take into account such mechanisms using appropriate corrective factors.

Polydispersity of the primary particles:

The RDG-FA theory assumes that each soot aggregate is composed of n_p primary particles with the same diameter d_p . However, experimental work has shown that primary particles diameters within an aggregate can vary following a log-normal distribution ([Liu et al. \(2006\)](#), [Bescond et al. \(2014\)](#)). In the study by [Liu et al. \(2015\)](#), the T-matrix method presented in Section 1.3.5 is considered to assess the impact of polydispersity on radiative properties of soot aggregates and were compared with the original RDG-FA method. The effect of polydispersity is found to be small for absorption but important for scattering.

A very recent study conducted in [Yon et al. \(2019\)](#) aimed at including polydispersity of the aggregates in the RDG-FA theory. Using DDA algorithm as a reference, corrections on parameter introduced in the extended RDG-FA theory for multiple-scattering have been proposed to take into account such effects.

1.4 Soot radiation in CFD simulations

1.4.1 State-of-the art in the literature

On the one hand, the models described in the previous section have been validated and challenged using numerically generated aggregates with great details. On the other hand, radiation as a heat transfer mechanism has an impact on temperature and needs to be taken into account in CFD simulations to properly estimate thermal fields. The objective of this paragraph is then to give a short review of CFD simulations carried out for laminar and turbulent flames considering soot radiation.

Historically, pioneer work on soot radiation in CFD has been considered using

Optically Thin Assumption (OTA) (Kennedy et al. (1996), McEnally et al. (1998), Smooke et al. (2004)) for laminar coflow diffusion flames, mostly for computational constraints. In these studies, a sectional approach for soot dynamics description was retained, but only information on soot volume fraction was provided. Such studies used relatively large mechanisms such as the GRI mechanism (more than 40 species and 200 reactions) and showed that radiation has an important impact on temperature and soot volume fraction values : neglecting radiation increases the peak temperature predicted of around 100K. However, using OTA underpredicts the thermal values obtained in the simulations and tends to underpredict the soot volume fraction (around a factor 3 in the study by Smooke et al. (2004)). These studies also point the need for accurate modelling of the burner lip as it will lead to a different flame attachment and then have an impact on temperature.

The effect of more detailed gas and soot properties in laminar flames have been studied by Liu et al. (2002), Liu et al. (2004), and more recently by Dorey et al. (2011) with 1D laminar premixed flames and Demarco et al. (2013) considering different gravity conditions. These studies are considering spectral properties for soot and gas phases, with DOM/MC resolution of the RTE, but soot particles dynamics are described using a 2 equations semi-empirical formulation. Moreover, the scattering by soot particles is not accounting for. Here again, the impact on temperature of the different radiative models is noticeable (around 100K for different fuels : ethylene, methane) and predicted soot volume fraction peaks are in a good agreement with experimental data. In the study by Liu et al. (2004), temperature predicting along the centerline is under-estimated by around 100K. This is attributed to the fuel pre-heating effect (the flame anchored at the lip will heat the pipe which in turn heats the fuel) neglected or the use of a simplified soot 2 equations model. Such a model transports the soot mass fraction and the soot number density.

The increase in computational resources have led to an increasingly number of studies of turbulent sooting flames considering radiation. Historically, most of the studies on soot radiation for turbulent flames have been carried out using RANS formulation (Tessé et al. (2002), Wang et al. (2005), Pal et al. (2015)) with simplified soot description. Such studies have conducted coupled calculations with, respectively, MC, SHM and DOM methods for the RTE resolution. More detailed descriptions for soot dynamics have been recently considered with the moment method (Mehta et al. (2010)) and the sectional method (Rodrigues et al. (2019)). On these turbulent flames, scattering by soot particles is neglected as well.

These studies are carried at atmospheric pressure, far from operating conditions encountered in many industrial engines.

In IC-engines, operating at pressures up to 200 bars, it is known that radiation can go up to 50% of the total heat losses (Borman and Nishiwaki (1987)). These engines are faced with regulations on particulate and NOx emissions and need to be accurately predicted. In Abraham and Magi (1997), the Discrete-Ordinate-Method has been used to quantify radiative heat transfer and its impact on NOx emissions: Accounting for soot radiation reduces the NOx emissions, and similar conclusions have been found in Yoshikawa and Reitz (2009). Recently, coupled calculations with more accurate models for gaseous radiation (FSK method) and considering a spectral Rayleigh model for soot particles have been carried out (Paul et al. (2017), Paul et al. (2019)).

In gas-turbines applications, there is little data on soot particle fields. Several numerical studies (Felden et al. (2018), Teng et al. (2019), Rodrigues (2018)) have been carried out on the DLR FIRST combustion chamber test rig Geigle et al. (2015) to study a pressurized sooty flame at 3 bars with numerous experimental data available for validation.

Nowadays, detailed information on soot particles (soot volume fraction f_V , particle size distribution, morphology) can be obtained in CFD studies thanks to the progress done on soot dynamics modelling. However, state-of-the-art studies accounting for soot radiation are only considering spectral Rayleigh model without scattering, which only requires the knowledge of f_V .

1.4.2 Soot sectional description retained in this thesis

In this work, the RDGFA model is considered to describe soot radiative properties. Recalling the expressions of the absorption, scattering and phase functions, the values of f_V (the soot volume fraction) and $n(V)$ (the number density function) is required.

In this work, f_V and $n(V)$ are obtained via a soot sectional method, previously developed and validated in Rodrigues (2018). The next paragraphs aims at introducing briefly the approach and show it is combined with the RDGFA model.

1.4.2.1 Principle and definitions

The sectional approach consists in dividing the Particle Size Distribution (PSD) into different classes called "**sections**". These sections are corresponding to a given range of volume in which soot related quantities are calculated.

In this work, the discretization of the sections is the same as in the original method developed in Rodrigues et al. (2017), and is given, for a total number

of sections N_{sect} , by :

$$v_i^{max} = v_1^{max} \left(\frac{v^{MAX}}{v_1^{max}} \right)^{\left(\frac{i-1}{N_{sect}-1} \right)} \quad (1.78)$$

with $i \in \llbracket 2, N_{sect} - 1 \rrbracket$, v_1^{max} and v^{MAX} the maximum volume of the first section and the biggest volume of a soot particle, respectively.

The numerical accuracy of the method depends on the number of sections used for the PSD discretization.

In each section, the PSD is assumed constant. The total soot volume fraction can then be calculated in the section i , noted $Q_{s,i}$ is defined as :

$$Q_{s,i} = \int_{v_i^{\min}}^{v_i^{\max}} q_i(v) \quad (1.79)$$

where $q_i(v)$ is the soot volume fraction density of the section i which is constant and equals to $q(v_i^{mean})$, with $v_i^{mean} = (v_i^{\min} + v_i^{\max})/2$. Figure 1.15 gives a representation of the discretization of the soot volume fraction density.

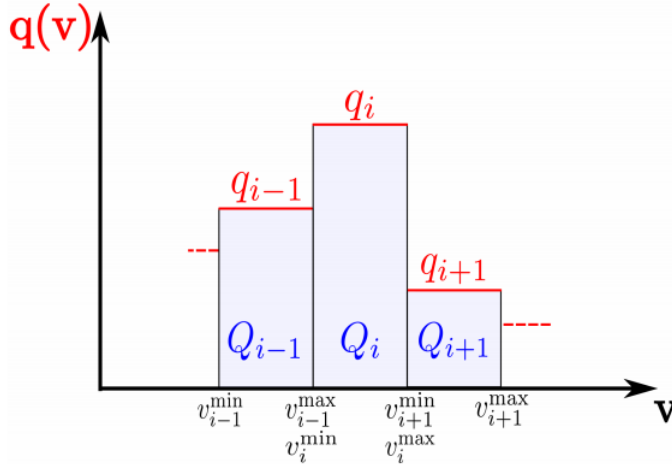


Figure 1.15: Discretization of the soot volume fraction density $q_i(v)$.

An important quantity, which is used in the RDGFA model, is the particle number density $n(v)$. This quantity is, for a section i evaluated for a volume v (between v_i^{\min} and v_i^{\max}), given by :

$$n(v) = q_i(v)/v \quad (1.80)$$

1.4.2.2 Link between the sectional method and RDGFA inputs

The objective of this section is to establish the link between the RDGFA inputs, f_V and the sectional method.

Population Balance Equation solved by the sectional approach

The sectional approach solves the Population Balance Equation (PBE), for each section, which can be written in terms of $Q_{s,i}$:

$$\frac{\partial Q_{s,i}}{\partial t} + \nabla \cdot ((\mathbf{u} + \mathbf{v}_T) Q_{s,i}) = \nabla \cdot (D_{s,i} \nabla Q_{s,i}) + \dot{Q}_{s,i} \quad (1.81)$$

where \mathbf{u} is the gas velocity, \mathbf{v}_T the thermophoretic velocity, and $\dot{Q}_{s,i}$ the source term.

In practice, the equation is solved in terms of $Y_{s,i}$, the mass fraction relative to the section i , which is linked to $Q_{s,i}$ by :

$$Q_{s,i} = \frac{\rho}{\rho_s} Y_{s,i} \quad (1.82)$$

Hence, the PBE equation can be written with an additional simplification as

$$\frac{\partial \rho Y_{s,i}}{\partial t} + \nabla \cdot (\rho (\mathbf{u} + \mathbf{v}_T) Y_{s,i}) = \nabla \cdot (\rho D_{s,i} \nabla (Y_{s,i})) + \rho_s \dot{Q}_{s,i} \quad (1.83)$$

The source term, $\dot{Q}_{s,i}$, describes the different mechanisms related to soot particles' dynamics. These mechanisms are : the nucleation (which is the collision of two big PAHs), the condensation (which is the collision between a big PAH and a soot particle), the coagulation (the collision between two particles), the surface growth and the oxidation.

The corresponding expressions can be found in [Rodrigues et al. \(2017\)](#).

In practice, the sectional method gives the values of $Y_{s,i}$ for each section i , which enables to calculate $Q_{s,i}$.

Soot volume fraction

The total soot volume fraction f_V is defined by :

$$f_V = \int_0^\infty q(v) dv \quad (1.84)$$

which can be also written as :

$$f_V = \sum_{i=1}^{N_{\text{sect}}} Q_{s,i} = \sum_{i=1}^{N_{\text{sect}}} q_i (v_i^{\text{max}} - v_i^{\text{min}}) \quad (1.85)$$

since $q_i(v)$ is constant within each section. Hence, the soot volume fraction f_V is deduced from $Q_{s,i}$ given by the PBE resolution.

Number Density Function

Once $Q_{s,i}$ is known via the PBE for each section, the soot volume fraction density $q(v)$ can be found by : $Q_{s,i} = q_i(v_i^{\max} - v_i^{\min})$.

Then, $n(v)$ is obtained using Equation 1.80.

1.5 Conclusion

In this chapter, several methods of resolution of the RTE have been detailed and their assets/drawbacks emphasized.

In this thesis, the RTE is chosen to be solved with a Monte-Carlo solver : it is nowadays affordable for accurate simulations, with highly-detailed gas and soot phases radiative properties. The narrow-band ck model is retained for CO_2 and H_2O radiative properties, while the RDG-FA approach is retained for soot particles, since it enables to take into account the complex aggregate shape of soot at an affordable cost with analytical expressions.

In CFD studies accounting for soot radiation, scattering is neglected by invoking the Rayleigh theory, which applies only for spherical particles and strongly underestimates scattering. Therefore, the scattering impact must be reevaluated using the RDG-FA theory.

In this work, soot dynamics is described by the sectional method. This model provides information on particle size distribution and morphology, which are both inputs needed to compute scattering using the RDG-FA model.

The next step is then to combine the sectional method used in CFD with the state-of-the-art soot radiative model RDGFA to accurately compute soot radiative transfer in several configurations. The implementation of the scattering treatment in the radiative Monte-Carlo solver is discussed in Chapter 2. The application of RDGFA model in a turbulent configuration is detailed in Chapter 3. It is important to keep in mind that, nowadays, uncertainties remain in soot properties and formation mechanisms, which can impact predictions of soot dynamics and radiation.

Chapter 2

Accounting for high-fidelity radiative properties in a Monte-Carlo solver

In Chapter 1, we have presented different radiative property models that need to be considered to solve the RTE. Among the different RTE resolution methods, the Monte-Carlo (MC) approach is retained for its high accuracy. The objective of this chapter is now to present how such soot radiative properties can be taken into account in a Monte-Carlo (MC) solver. In a first part, we briefly introduce the existing Monte-Carlo approaches: forward, backward methods before presenting the in-house Monte-Carlo code RAINIER with its features in a second part. The MC approach, despite its high accuracy, has a slow convergence rate: acceleration techniques such as the Quasi-Monte Carlo method (QMC) have then been considered up to now for non-scattering media in RAINIER. In a third part, we extend QMC methods to scattering media. This third part has been accepted for publication in the International Journal of Heat and Mass Transfer.

Contents

2.1	Monte-Carlo methods for the RTE	62
2.1.1	Non-reciprocal formulations : Forward and Backward Monte-Carlo methods	62
2.1.2	Reciprocity principle and Emission Reciprocity Method	63
2.1.3	Probability density functions for the ERM	66
2.2	A Monte-Carlo code : RAINIER	67
2.2.1	Presentation of the original code	67
2.2.2	Contributions of this thesis in the RAINIER code . .	68
2.3	Combining scattering treatment and Quasi-Monte-Carlo methods	69

2.3.1	Introduction	69
2.3.2	Monte Carlo resolution of the RTE with scattering. .	70
2.3.3	Randomized Quasi-Monte Carlo treatment of scattering	73
2.3.4	Validation and assessment of convergence properties in a homogeneous gray medium	75
2.4	Conclusion	83

2.1 Monte-Carlo methods for the RTE

Two categories of Monte-Carlo solvers are discussed in this Section, depending on whether they are based on a non-reciprocal or reciprocal formulation.

2.1.1 Non-reciprocal formulations : Forward and Backward Monte-Carlo methods

In such methods, the radiation computational domain is discretized into N_v and N_f isothermal finite cells of volume V_i and faces of area S_i , respectively. Forward (**FM**) and backward (**BM**) methods differ in the way of describing the radiative power.

Forward Monte-Carlo :

In this method, a series of photons is emitted from a point of the computational domain and their history is traced until the photon is either absorbed, reflected or leaves the domain. The radiative power in any cell i is written as the sum of the part of the emission of all the other cells j or faces absorbed by the cell i (P_{ji}^{ea}) minus the emitted power from the cell i (P_i^e) :

$$P_i^{FM} = \sum_{j=1}^{N_v+N_f} P_{ji}^{ea} - P_i^e \quad (2.1)$$

In the case where j is a cell, P_{ji}^{ea} is expressed by:

$$P_{ji}^{ea} = \int_{\nu=0}^{+\infty} P_{\nu,ji}^{ea} d\nu = \int_{\nu=0}^{+\infty} 4\pi\kappa_\nu(T_j) I_{b\nu}(T_j) dV_j \times \left(\frac{dA_i}{4\pi r^2} \right) \times \tau_{\nu,r} \times \kappa_\nu(T_i) ds_i d\nu \quad (2.2)$$

where $I_{b\nu}(T_j)$ is the equilibrium spectral intensity at temperature T_j , r the distance between the two volume cells, κ_ν the spectral absorption coefficient and $\tau_{\nu,r}$ the transmissivity of the column between dV_i and dV_j . The photon is characterized by an initial location, a direction of propagation and a spectral

frequency. These values are randomly picked according to probability distribution (see Section 2.1.3).

Backward Monte-Carlo :

The Forward Monte-Carlo method is inefficient if only information on a small portion of the domain (areas of interest) is needed. Indeed, most of the photons emitted from the other cells j will not reach the cells within a small portion of the domain. Hence, an important number of samples are needed to achieve a statistically meaningful result. The Backward Monte-Carlo (**BM**) addresses such issue by generating optical paths from the desired location (cell i). Then, the radiative power of our cell of interest i is computed by considering the radiative power emitted by the other cells j that crossed the photon leaving i minus the emission of the cell i :

$$P_i^{BM} = \sum_{j=1}^{N_v+N_f} P_{ji}^{ea} - P_i^e \quad (2.3)$$

The expression of the radiative power at the cell i is the same as the one obtained for the Forward Monte-Carlo approach, but the optical paths are only issued from the cell i of interest.

2.1.2 Reciprocity principle and Emission Reciprocity Method

The non-reciprocal methods are not adapted in optically thick media cases. Indeed, photons emitted in such media are quickly absorbed before reaching a wall preventing the calculation of heat-fluxes at the wall. A second limitation is encountered for quasi-isothermal media: in this case, the values of emitted and absorbed power are quite similar. It implies that the calculation of the radiative power (the difference between emitted/absorbed power) can be strongly affected if the absorption part is affected by statistical error.

To face such issues, [Cherkaoui et al. \(1996\)](#) developed a method called Reciprocal Monte-Carlo which is based on the reciprocity principle.

Reciprocity Principle

The radiative power of a cell i can be written as the sum of the exchanged powers P_{ij}^{exch} between i and all the other cells or faces j :

$$P_i = \sum_{j=1}^{N_v+N_s} P_{ij}^{exch} = - \sum_{j=1}^{N_v+N_s} P_{ji}^{exch} \quad (2.4)$$

For volume cells, for instance, P_{ij}^{exch} is defined as:

$$P_{ij}^{exch} = P_{ji}^{ea} - P_{ij}^{ea} = \int_0^\infty \left(P_{\nu,ji}^{ea} - P_{\nu,ij}^{ea} \right) d\nu \quad (2.5)$$

where $P_{\nu,ij}^{ea}$ is the spectral radiative power emitted by volume i and absorbed by volume j .

The Reciprocity Principle can be written as :

$$\frac{P_{\nu,ij}^{ea}}{I_{b\nu}(T_i)} = \frac{P_{\nu,ji}^{ea}}{I_{b\nu}(T_j)} \quad (2.6)$$

The reciprocity principle enables to rewrite the exchanged power $P_{\nu,ij}^{exch}$ as a difference of radiative intensities :

$$P_{\nu,ij}^{exch} = \tau_{\nu,r} \kappa_\nu(T_i) \kappa_\nu(T_j) ds_j \left[I_{b\nu}(T_j) - I_{b\nu}(T_i) \right] dV_i d\Omega_i \quad (2.7)$$

Finally, since we need P_{ij}^{exch} to calculate the radiative power at the cell i P_i (Eq 2.4), Equation 2.7 is integrated over all the frequencies and directions emitted from i :

$$P_{ij}^{exch} = \int_0^{+\infty} \kappa_\nu(T_i) \left[I_\nu^\circ(T_j) - I_\nu^\circ(T_i) \right] \int_{V_i} \int_{4\pi} A_{ij\nu} d\Omega_i d\nu \quad (2.8)$$

where $A_{ij\nu}$ accounts for all the paths between emission from the cell i and absorption in any point of the cell j , after transmission, scattering and possible wall reflections along the paths:

$$A_{ij\nu} = \sum_{m=1}^{N_p} \tau_\nu(BF_m) \alpha_{jm\nu} \quad (2.9)$$

where N_p is the total number of crossing pf the cell j by a given optical path issued from the cell i , $\tau_\nu(BF_m)$ is the spectral transmissivity between the source point B in the cell i and the inlet point F_m of the cell j , while $\alpha_{jm\nu}$ is the spectral absorptivity defined as:

$$\alpha_{jm\nu} = 1 - \exp \left[-\kappa_\nu(T_j) l_{jm} \right] \quad (2.10)$$

In this equation, l_{jm} is the length traveled by the photon within the cell j during its m -th crossing. The knowledge of the exchanged power between the cell i and j enables to compute the radiative power P_i of a cell i :

$$P_i = \sum_{j=1}^{N_{ij}} P_{ij}^{exch} \quad (2.11)$$

Similarly, the radiative heat-fluxes integrated on the surface area S_i , Φ_i , can be computed using :

$$\Phi_i = \sum_{j=1}^{N_{ij}} \Phi_{ij}^{\text{exch}} \quad (2.12)$$

where the exchanged flux Φ_{ij}^{exch} between a surface cell i of surface S_i and a volume cell j is given by:

$$\Phi_{ij}^{\text{exch}} = \int_0^{+\infty} \epsilon_{i\nu} \left[I_\nu^\circ(T_j) - I_\nu^\circ(T_i) \right] \int_{S_i} \int_{4\pi} A_{ij\nu} \cos(\theta_i) d\Omega_i dS_i d\nu \quad (2.13)$$

where θ is the angle of the optical path with the normal of the surface.

In the Emission Reciprocity Method **ERM**, optical paths are generated from the desired location of the radiative power, and information based on reciprocity principle is taken into account. Such method presents the benefits of the backward Monte-Carlo method as only the points of interest need to be computed. This method is the one retained in this thesis. Let us note there is an equivalent of the Forward Method using the reciprocity principle, named the Absorption Reciprocity Method (**ARM**) (see [Tessé et al. \(2002\)](#) for more details on this method).

In the **ERM**, following the reciprocity principle derivation (Equation 2.11), the statistical estimation of the radiative power on the cell q of interest can be expressed by :

$$\widehat{P}_q^{\text{ERM}} = \sum_{j=1}^{N_v+N_f} \widehat{P}_{qj}^{\text{exch}} \quad (2.14)$$

Such estimation is obtained by summing the contributions of the N_q photon emitted from our point of interest, which leads to the following expression :

$$\widehat{P}_q^{\text{ERM}} = \frac{P_q^e}{N_q} \sum_{n=1}^{N_q} \sum_{m=1}^{M_n} \left[\frac{I_{\nu_n}^\circ(T_m)}{I_{\nu_n}^\circ(T_q)} - 1 \right] \tau_{\nu_n} (\text{BF}_m) \alpha_{j m \nu} \quad (2.15)$$

where m is the index corresponding to the number of cells crossed by one photon (hence, $m = 1$ is the cell q , $m = M_n$ is the last cell crossed by the photon). N_q is the total number of photons emitted, and P_q^e is the emitted power from the cell q . One may notice that, the radiative power exchanged between two cells at the same temperature is equal to 0, while this is only statistically verified with the FM/BM methods.

Such a property, added to the CPU efficiency of this method (as only points of interests needs to be considered) results in an accurate, efficient method which is retained in this work.

2.1.3 Probability density functions for the ERM

In order to compute such radiative power, a propagation direction Δ and a wavenumber ν needs to be stochastically picked according to probability density functions.

Recalling the equation for the exchanged power between the cell i and the other cells j (Equation 2.8), the expression can be rewritten :

$$\begin{aligned} P_{ij}^{\text{exch}} &= P_i^e(T_i) \int_{\nu=0}^{\infty} \left[\frac{I_{\nu}^{\circ}(T_j)}{I_{\nu}^{\circ}(T_i)} - 1 \right] \int_{4\pi} \frac{\kappa_{\nu}(T_i) I_{\nu}^{\circ}(T_i)}{P_i^e(T_i)} A_{ij\nu} d\Omega_i d\nu \\ &= P_i^e(T_i) \int_{\nu=0}^{\infty} \left[\frac{I_{\nu}^{\circ}(T_j)}{I_{\nu}^{\circ}(T_i)} - 1 \right] \int_{4\pi} A_{ij\nu} f_i(\Delta, \nu) d\Omega_i d\nu \end{aligned} \quad (2.16)$$

where P_i^e is the volumetric power emitted in the cell i , $f_i(\Delta, \nu)$ is the desired PDF. More specifically, since the direction and the wavenumbers are two independent events, we can split such PDF expression :

$$\begin{aligned} f_i(\Delta, \nu) d\Omega_i d\nu &= f_{\Delta_i}(\Delta) d\Omega_i f_{\nu_i}(\nu) d\nu \\ \text{with: } \begin{cases} f_{\Delta_i}(\Delta) = 1/(4\pi) \\ f_{\nu_i}(\nu) = \frac{\kappa_{\nu}(T_i) I_{\nu}^{\circ}(T_i)}{\int_0^{\infty} \kappa_{\nu}(T_i) I_{\nu}^{\circ}(T_i)} \end{cases} \end{aligned} \quad (2.17)$$

In practice, the spherical coordinates parametrization is suitable to determine the direction Δ which is replaced by two angles : the polar angle θ and the azimuthal angle ψ with their respective PDF :

$$\begin{aligned} f_{\theta_i}(\theta_i) &= \sin(\theta_i)/2 \\ f_{\psi_i}(\psi_i) &= 1/(2\pi) \end{aligned} \quad (2.18)$$

Finally, the determination of the wavenumber, the polar and azimuthal angles of the photon is done by picking three random numbers between 0 and 1 (respectively R_{ν} , R_{θ} and R_{ψ}), which leads to the following relations to inverse to determine ν , θ and ψ :

$$R_{\nu} = \int_0^{\nu} f_{\nu}(\nu') d\nu' \quad (2.19)$$

$$R_{\theta} = \int_0^{\theta} f_{\theta}(\theta_i) d\theta_i = \frac{1 - \cos(\theta)}{2} \quad (2.20)$$

$$R_\psi = \int_0^\psi f_\psi(\psi_i) d\psi_i = \frac{\psi}{2\pi} \quad (2.21)$$

It is worthwhile to notice that no random number for the initial location is in fact picked up : the radiative power is actually directly computed at the node j of the radiative mesh.

2.2 A Monte-Carlo code : RAINIER

2.2.1 Presentation of the original code

RAINIER is a Monte-Carlo solver for the RTE developed at EM2C (Zhang et al. (2018), Palluotto et al. (2019), Rodrigues et al. (2019), Armengol et al. (2020)). In the original code, only non-scattering media were treated. The radiative power can be computed either using ERM or Optimized-ERM technique (or OERM) (Zhang et al. (2018)). The OERM consists in modifying the spectral PDF to enhance convergence in regions where absorption dominates emission. Quasi-Monte Carlo methods are also implemented in RAINIER in order to improve the convergence of the Monte-Carlo method, but are limited for non-scattering medium (Palluotto et al. (2019)).

One advantage of the ERM method is the capability to compute only the points of interest (called "probes") or specific regions where the radiative power or fluxes are needed. The independent treatment of these points allows for a high degree of scalability and ensures a high performance of the solver.

In Section 2.1.3, the expression of the exchanged radiative power and the sampling of random numbers to generate a ray (without scattering) have been presented. The path that the ray follows is treated with the energy partitioning method or path-length method (Farmer and Howell (1998)). The ray is gradually attenuated along its path by a factor $e^{-\kappa\Delta l}$ after each cell's crossing, where Δl is the path length through one cell, and after each wall reflection. In practice, a stopping criterion is given: the bundle is traced until it carries certain percentage of its initial energy τ_{min} .

In order to estimate the error in the Monte Carlo simulations, the total number of ray samples N is divided into M packs, yielding M subtrials. For a given pack i , the Monte Carlo trial $Q_i(P)$ is computed, with $P = N/M$ the number of rays in the pack. The Monte Carlo estimate from the total number of rays $Q(N)$ is then given by :

$$Q(N) = \frac{1}{M} \sum_{i=1}^M Q_i(P) \quad (2.22)$$

In practice, Q designates either the radiative power or radiative flux. The knowledge of $Q(N)$ and $Q_i(P)$ enables to estimate the standard deviation of $Q(N)$ as

$$\sigma[Q(N)] \approx \left(\frac{1}{M(M-1)} \sum_{i=1}^M [Q_i(P) - Q(N)]^2 \right)^{1/2} \quad (2.23)$$

The accuracy of the Monte Carlo results is controlled thanks two convergence criteria based on the standard deviation $\sigma[Q(N)]$:

- Relative error: it is defined as the ratio of the local standard deviation to the local quantity of interest (radiative power or flux).
- Absolute error: the standard deviation is checked to be lower than a prescribed threshold, typically set equal to a given percentage of the estimated maximum value of the quantity of interest.

Once one of these criterion is attained, the ray tracing is interrupted.

Two models for gaseous properties are implemented : either gray-gas (with a constant absorption coefficient κ) or the ck-model for H_2O and CO_2 . In this case, when a wavenumber is picked, the corresponding band is then considered to evaluate gaseous radiative properties. For soot particles, only the absorption coefficient given by the Rayleigh model for spherical particles is implemented.

2.2.2 Contributions of this thesis in the RAINIER code

During this thesis, several implementations have been realized in the RAINIER code :

- Development of stochastic scattering approach accounting for isotropic or anisotropic scattering
- Implementation of the complete Rayleigh, RDG and RDG-FA models.
- Implementation of importance sampling techniques for the scattering
- Implementation of Randomized QMC approach extended to scattering medium
- Extension of Rainier to axisymmetric cases
- Coupling framework accounting for scattering exchanges between Rainier and other codes (see Chapter 6)
- Monochromatic solver
- Development of numerically synthesized signals due to scattering (see Chapter 7)

2.3 Combining scattering treatment and Quasi-Monte-Carlo methods

2.3.1 Introduction

The radiative contribution to wall fluxes must be determined in many engineering systems, particularly in combustion chambers which feature high temperatures. In such applications, radiative heat transfer is classically split into two contributions: non-luminous radiation from participating burnt gases on the one hand, and luminous radiation from soot particles emitted in the visible spectral range on the other hand. Both contributions need to be accurately quantified in order to properly predict the radiative fluxes and radiative power in the combustion chamber.

From a numerical point of view, the computation of the radiative power is based on solving the Radiative Transfer Equation (RTE) accounting emission, absorption, and scattering phenomena. In this work, the Monte-Carlo solver RAINIER is considered. However, as emphasized in Section 2.2, scattering is not taken into account and needs to be implemented in a first step.

Combining scattering and Monte Carlo resolution is done in other research fields such as stellar observation (Peest et al. (2017), Cashwell and Everett (1960), Min et al. (2009)) or medical approaches (Fredriksson et al. (2009)). In these studies, several techniques of Monte Carlo convergence improvements have been employed, since the variance due to the scattering was important. One of these techniques is known as the Forced Scattering (Cashwell and Everett (1960)) and are using the idea of biasing: the random numbers are generated from a probability density function (PDF) $q(x)$ instead of the original one $p(x)$. The weight of the Monte Carlo ray is then corrected by a factor $1/q(x)$. This enables to reduce the variance of the Monte Carlo estimate and then have a better estimation of the radiative power or flux. However, since a Monte Carlo cubature method is used, the convergence rate law is known to be proportional to $N^{-1/2}$ with N the total number of rays, which can keep the calculations costly.

Considering high-fidelity simulations of turbulent reactive flows with a Monte Carlo method and detailed soot radiative properties including scattering has never been done before. It would remain, however, very costly if the scattering effects to outline are small. Additional efforts are needed to make such computations more affordable. Several strategies can be encountered in the literature. When the origin of penalized convergence is identified, variance reduction techniques (Feldick et al. (2011), Juvela (2005), Buras and Mayer (2011), De Lataillade et al. (2002)), which Forced Scattering is a part of, are of great interest. Recently, an alternative sampling mechanism for numerical integration known as Quasi-Monte Carlo (QMC) has been applied to radiative

energy transfer in participating media (Palluotto et al. (2019), Farmer and Roy (2020)). Such a methodology, which can be combined with any other variance reduction techniques, improves significantly the convergence rate of the Monte Carlo simulation. In particular, Palluotto et al. (2019) have used a Randomized QMC (RQMC) that enables the statistical estimation of the results accuracy, and have demonstrated its increased efficiency in several cases. RQMC simulations of thermal radiation have been retained in recent coupled simulations: direct numerical simulation of a turbulent jet (Armengol et al. (2019)) and large-eddy simulation of a sooted jet flame (Rodrigues et al. (2019)).

Therefore, the next sections are focusing on :

- The implementation of scattering in our Monte-Carlo code,
- The improvement of the scattering treatment via the Randomized Quasi-Monte Carlo technique and importance sampling.

2.3.2 Monte Carlo resolution of the RTE with scattering.

2.3.2.1 Standard stochastic treatment of scattering

The Rainier solver did not account for scattering in previous works. The implemented stochastic treatment of scattering combined with energy partitioning for absorption and ERM follows the PhD work of Tessé (2001). The method does not modify the radiative power expression, and scattering events only corresponds to a modification of the direction of the ray.

To clarify the ideas, let us consider the problem sketched in Figure 2.1. An incoming ray displayed in red enters the cell from a point K. Without any scattering, the ray exits the cell through the point K'. The point S represents the location of the scattering event, and θ_s the scattering angle. (The sketch represents a 2D configuration, for practical 3D cases, one need to add the polar angle ϕ_s).

The objective is know to determine when the ray is scattered or not, the location of the scattering event (point S) and the angles which define the change of the direction.

Optical thickness for scattering

In the Monte Carlo method, each ray follows the standard ERM until a given distance determined by the attributed scattering optical thickness is reached. A scattering event is then computed. The optical thickness (for scattering) of each ray is based on a random number sampled uniformly between 0 to 1 that corresponds to a value of a cumulative probability distribution function (*c-pdf*). The scattering *pdf*, indicating the probability that a ray changes its direction

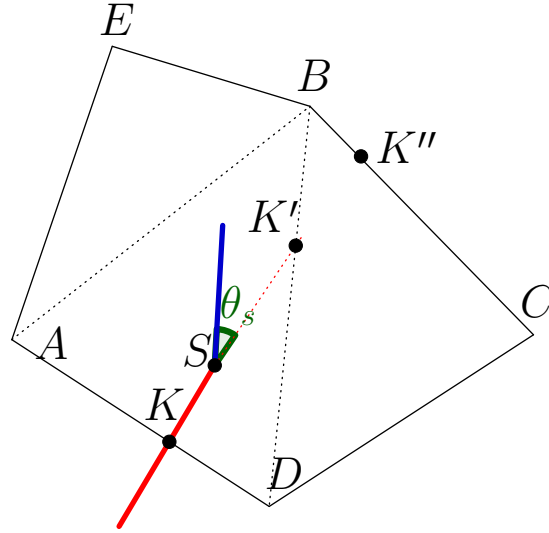


Figure 2.1: *Parametrization of the scattering problem*

between s and $s + ds$, is equal to :

$$f_s(s)ds = \exp \left[- \int_0^s \sigma_\nu(s') ds' \right] \sigma_\nu ds \quad (2.24)$$

Then, the cumulative probability function (*c-pdf*) F_s is defined by :

$$F_s(s) = \int_0^s f_s(s') ds' = 1 - \exp \left[- \int_0^s \sigma_\nu(s') ds' \right] \quad (2.25)$$

One can define an optical thickness for scattering $\tau_s = \int_0^s \sigma_\nu(s') ds'$, and a random number R_s (corresponding again to a value of F_s) given by :

$$\tau_s = -\ln(R_s) \quad (2.26)$$

Determination of the scattering location

Let N_c be the number of cells crossed by the ray, and l_i the length crossed by the ray in the i -th cell. The scattering event occurs in the cell N_c if $\sum_{i=0}^{N_c} \sigma_{i,\nu} l_i > \tau_s$.

The length l_s from the cell entry point at which the scattering takes place is determined by

$$l_s = \frac{\sum_{i=1}^{N_c} \sigma_{i,\nu} l_i - \tau_s}{\sigma_{N,\nu}} \quad (2.27)$$

The knowledge of l_s enables to retrieve the position of the scattering event S. The radiative power exchanged between the ray origin and the cell N_c is calculated using the distance l_s .

Determination of the new direction

At this point, the new direction is unknown and needs to be determined. The scattered ray is parametrized by two new angles θ_s and ϕ_s defined in respect to the ray direction. Two new random numbers R_θ and R_ϕ are sampled accordingly. Their definition depends on the scattering phase function Φ . In this study, isotropic scattering and the RDG-FA model for soot particles are considered.

- Isotropic scattering

$$\begin{aligned} \phi_s &= 2\pi R_\phi \\ \cos(\theta_s) &= 1 - 2R_\theta \end{aligned} \quad (2.28)$$

- Anisotropic scattering with RDG-FA. Φ is only a function of θ (cf. Equation 1.75).

$$\begin{aligned} \phi_s &= 2\pi R_\phi \\ R_\theta &= \frac{\int_0^{\theta_s} \Phi(\theta) \sin(\theta) d\theta}{2} \end{aligned} \quad (2.29)$$

Once the new direction is known, a new scattering optical thickness is sampled and the ray tracing continues.

2.3.2.2 Improvement of the methodology with forced-scattering

One issue with this standard methodology is that the scattering criterion $\sum_{i=0}^N \sigma_{i,\nu} l_i > \tau_s$ can be rarely verified in areas with a low scattering optical thickness. Consequently, to achieve a statistically meaningful number of scattering events in these regions, a significant number of sampling would be required, leading to an increase in CPU cost.

The idea of forced-scattering (Cashwell and Everett (1960)) is to limit the value taken by τ_s to guarantee that a ray is scattered along its path. Equation 2.26 is then modified and becomes

$$\tau_s = -\ln(R_s(1 - e^{\tau^*})) \quad (2.30)$$

with τ^* the total optical depth along a ray's path from the emitted point to a wall of the domain. Since the physics has been biased, the exchanged power after scattering is corrected accordingly by a factor $\frac{1}{1-e^{\tau^*}}$.

The quantity τ^* is pre-computed at the point of emission before the usual ray tracing begins to determine the radiative power or flux: after the initial direction is randomly generated, the quantity $\tau^* = \sum_{i=0}^N \sigma_{i,\nu} l_i$ is calculated until the ray reaches a wall. Although this technique improves convergence, it increases the CPU cost due to this additional ray generation.

To overcome this difficulty, an approximation of the quantity τ^* is done, by prescribing $\tau_{fast}^* \approx \sigma_{emit,\nu} L_{max}$ where L_{max} is a quantity explicitly chosen before any computation. In practice, it is set to be equal to the maximum length of the domain. $\sigma_{emit,\nu}$ corresponds to the value of the scattering coefficient at the emission point. This technique will be referred to *fast forced-scattering* method in the following.

Once a ray is scattered, as explained in the previous part, a new random optical thickness is computed. In this case, the above procedure is repeated by computing τ^* or τ_{fast}^* from the scattering point.

2.3.3 Randomized Quasi-Monte Carlo treatment of scattering

2.3.3.1 Quasi-Monte Carlo

The Quasi-Monte Carlo (QMC) methodology has been implemented and validated in the Rainier solver (Palluotto et al. (2019)) for a non-scattering medium. The QMC technique relies on the use of low-discrepancy sequences instead of usual random number generators. This enables to improve the rate of convergence of the iterative method. The construction of the low-discrepancy sequence requires to know beforehand the stochastic dimension of the problem, which matches the dimension of the sequence. The stochastic dimension corresponds here to the number of different random variables to initialize and trace a ray. This requirement for the construction is fundamentally different from the classical use of a single random generator that provides (with a given quality) independent and identically distributed (i.i.d.) samples for all needed random variables. In this work, a Sobol sequence is used. Its construction algorithm follows the algorithm described in Sobol (1976). The stochastic dimension, *i.e.* the number of different random variables, is in general unknown in Monte Carlo simulations addressing radiative heat transfer. This issue is common to all QMC methods and has not been studied in scattering media.

2.3.3.2 Stochastic dimension and scattering

For a non-scattering medium with diffuse wall reflections, the sequence dimension is here equal to $d = 3 + 2r_{max}$. The number 3 corresponds to the initial random numbers picked up for the ray (wavenumber ν , direction angles θ and

ϕ). r_{max} is the maximum number of diffuse reflections of a ray which can be determined as a function of the wall properties (Palluotto et al. (2019)): $\frac{\ln(\tau_{min})}{\ln(1-\epsilon_{min})}$ where τ_{min} and ϵ_{min} are the stopping ray criterion and the minimal wall emissivity encountered in the simulation, respectively. Finally, for each reflection, 2 random numbers are sampled to define the reflected direction.

In the case of a scattering medium, determining beforehand the number of scattering events of a ray is difficult or, at best, cumbersome: the different fields (temperature, species, soot) are not homogeneous and time-varying in coupled simulations involving DNS or LES. However, this knowledge is required before any computation to build the corresponding low-discrepancy sequence. Let us denote s_{max} the prescribed maximum number of scattering events for a ray. The dimension of the sequence is then equal to $4+2r_{max}+3s_{max}$ when accounting for scattering. Four random variables are now needed at the beginning of the computation with the added scattering optical thickness to sample. After each scattering event, three random numbers are sampled.

Since the user choice of s_{max} could be underestimated, one can run out of samples in the QMC sequence. Two strategies are then considered to deal with scattering:

- *Hybrid-RQMC* method: QMC samples are considered for emission and wall reflections only ($d_{QMC} = 3 + 2r_{max}$); scattering is fully treated with a standard Monte Carlo approach.
- *Full-RQMC* method: the QMC method is used for emission, wall reflections and scattering up to s_{max} events ($d_{QMC} = 4 + 2r_{max} + 3s_{max}$); when s_{max} is reached, additional sampling switches to a standard random generator, *i.e.* a Monte Carlo method instead of QMC.

The RQMC concept which extends the QMC method is introduced below. In the first strategy (*Hybrid-RQMC*), QMC only benefits to the first part of the rays tracing where the stochastic dimension is known with certainty. In the second strategy (*Full-RQMC*), QMC sampling is used up to the initially fixed full stochastic dimension. Beyond s_{max} , we choose not to interrupt the ray tracing not to bias the computed results, and the solver relies then on a standard MC sampling.

2.3.3.3 Accuracy monitoring

Compared to Monte Carlo simulations and the associated central limit theorem, the QMC method uses deterministic sequence whose points are not independent anymore. Consequently, QMC does not provide a way to estimate the error, which prevents any accuracy control of the computations. In order to have access to the error, the low-discrepancy sequences can be randomized (L'Ecuyer and Lemieux (2016)), resulting in Randomized QMC (or RQMC approach).

In this approach, M trials of low-discrepancy sequences are built, each composed of P realizations. Each sequence is a randomized version of the original low-discrepancy sequence, which ensures the independency between each of them. This enables, following equations 2.22 and 2.23 to have access to the standard deviation of the RQMC estimator of our quantity of interest, by :

$$\sigma \left[Q^{\text{RQMC}}(N) \right]^2 \approx \frac{1}{M(M-1)} \sum_{i=1}^M \left[Q_i^{\text{QMC}}(P) - Q^{\text{RQMC}}(N) \right]^2 \quad (2.31)$$

where $N = MP$ is the total number of realizations, $Q^{\text{RQMC}}(N) = \frac{1}{M} \sum_{i=1}^M Q_i^{\text{QMC}}(P)$ is the RQMC estimator of the quantity of interest. When considering Quasi-Monte Carlo simulations in the following, only RQMC computations are actually carried out. This is of great interest in practical simulations where on-the-fly control of the accuracy is desired. Finally, the convergence rates of the different methods can be quantified identically based on the evolution of the estimate's standard deviation with the total number of samples N .

Looking at equation 2.31, the choice of the number of trials M is important, as it must be large enough to provide a statistical meaningful error. In the literature, a minimum value of M admitted in 10 (Lemieux (2009)). However, it has been shown in Palluotto et al. (2019) that RQMC methods converges with a $M^{-1/2}P^\beta$ with $\beta > \beta_{MC} = 1/2$. Therefore, it is more interesting to increase the number of realizations P instead of M to achieve a better convergence rate. The choice of P and M are then not trivial. For each case presented in this work, values of M , P and N are then mentioned.

2.3.4 Validation and assessment of convergence properties in a homogeneous gray medium

2.3.4.1 Test case

All the calculations carried out in this section assume uniform gray radiative properties and isotropic scattering. Other validation cases encountered in the literature have mostly been realized in these conditions.

The chosen validation case is taken from the study of Siegel (1987). A 1D domain with a uniform temperature of 1000 K and gray radiative properties is considered. Two black walls at 300 K surround the domain. The medium is characterized by an extinction optical thickness $\tau_L = (\kappa + \sigma)L$ with L the domain length, and an albedo $\omega = \frac{\sigma}{\kappa + \sigma}$. Knowing these two quantities, the radiative properties of the medium are completely described by $\sigma = \frac{\omega\tau_L}{L}$ and $\kappa = \frac{\tau_L}{L} - \sigma$.

The wall emittance is defined as the ratio $\frac{\varphi_r}{\varphi_{black}}$ with φ_r the wall radiative heat flux and φ_{black} the corresponding black body wall flux at the given wall temperature. Siegel (1987) has reported emittance values that allows for validating the present implementation of scattering in the Rainier solver.

2.3.4.2 Validation of the standard scattering treatment

The standard Monte Carlo treatment of scattering described in Sec. 2.3.2.1 and added in the Rainier solver is here assessed on a 3D cubic domain $L_x \times L_y \times L_z$ with $L_x = L_y = L_z = 0.2$ m. The x -axis corresponds to the wall-normal direction. The domain is discretized on a structured mesh: $N_x = 100$, $N_y = 100$, $N_z = 10$. The MC backward method enables the computation of the points of interest located at the left and right walls. Periodic boundaries are applied to the four other walls.

The error control is set such that the relative error on the computed flux is 1%. Since the error is fixed here, the number of rays is allowed to vary until the error is reached. For this validation case, the number of packs M is set to 100. Scattering is here treated with the *Hybrid-RQMC method*. The results obtained with the Rainier solver are compared with the study of Siegel in Figure 2.2.

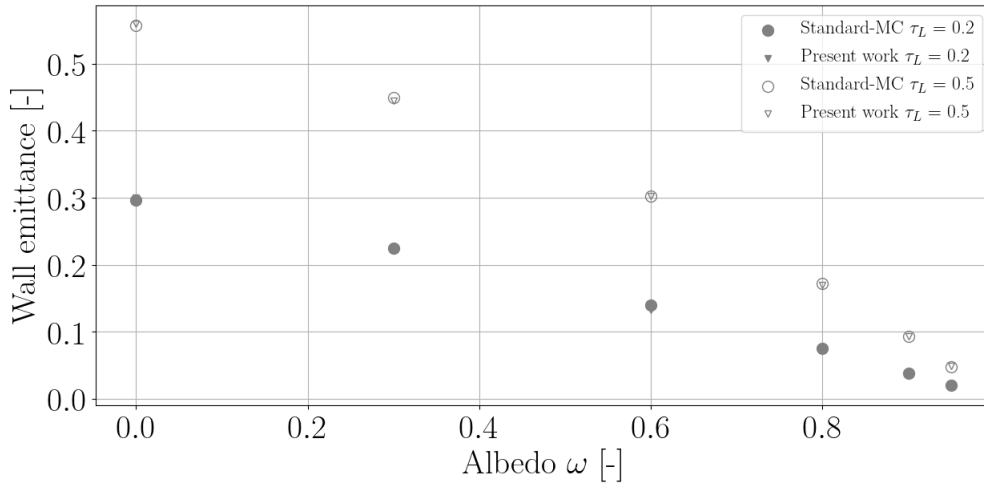


Figure 2.2: Wall emittance obtained in function of the albedo ω for two optical thickness τ_L and comparison with literature data from Siegel (1987).

It can be observed that the amount of heat flux impinging the wall diminishes as the albedo increases. Indeed, the medium scatters more energy, which, after absorption, does not reach the wall. When the total optical thickness increases, the normalized heat flux increases because the medium emits more energy. The obtained results are in excellent agreement with Siegel's work, which validates the implemented methodology to deal with a scattering in the radiation solver.

2.3.4.3 Comparison of different methods

In the previous section, a controlled error has been prescribed. The objective of this section is to apply several techniques to compare the convergence of the calculations. The CPU time is directly related to the number of rays required

to achieve the prescribed accuracy.

2.3.4.3.1 Validation

The following methods are considered:

- The *hybrid-RQMC* case used for the validation of standard scattering in Section 2.3.4.2 (RQMC for absorption and emission, MC for the scattering)
- The *Standard forced-scattering* (SFS) case. In order to assess the validity of the method, absorption, emission and scattering are treated with a standard MC approach.
- The *Fast-forced-scattering* (FFS) case, with a maximum length is prescribed to $L_{max} = 0.2$ m, which corresponds to the size of the domain. A classical MC approach is also used here for the random number generation.
- The *full-RQMC* case where scattering is also treated using RQMC. For this computation, a value of $s_{max} = 50$ is chosen in order not to affect the obtained results. This choice yields a Sobol sequence dimension of 154.

The number of trials M is set to 100, and the same convergence criteria are prescribed to all cases for the absolute and relative standard deviation. The obtained results are shown in Figure 2.3. The different methodologies give identical results, which is expected with the controlled error. This validates their implementation.

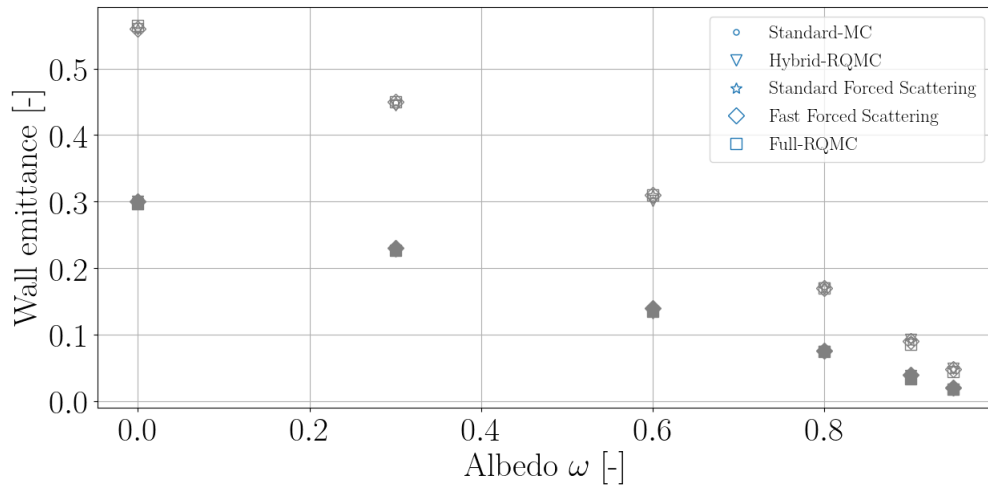


Figure 2.3: Wall emittances obtained in function of the albedo ω for two optical thickness τ_L and for four different scattering treatments. Comparison with reference results from Siegel (1987) is also provided. Plain markers : $\tau_L = 0.2$, empty markers : $\tau_L = 0.5$.

2.3.4.3.2 Convergence performance : tests with fixed number of rays

In the previous section, the number of rays was allowed to vary since an error criterion was prescribed. The different methods do not take the same computational time. Additional computations are performed by calculating the error of all the methods for a fixed number of rays to assess the improved methods' convergence performance. The error is assessed with each method's standard deviation for their estimation of the wall radiative flux.

The case with optical thickness $\tau_L = 0.2$ and albedo $\omega = 0.3$ is first considered. The four methods compared in Section 2.3.4.3.1 are considered. The number of trials M is fixed at 100 for a correct estimation of the standard deviation. $s_{max} = 50$ is set for the *full-RQMC* computation. An additional method where emission, absorption, and scattering (standard treatment) are all treated via a traditional Monte Carlo approach is also exhibited for reference. This method is referred to as *Standard-MC*.

In Figure 2.4, the methods exhibit different curves of relative standard deviation as a function of the total number of rays N . For large values of N , the asymptotic convergence law is outlined. Three trends can be observed in Figure 2.4. For the cases with a standard Monte Carlo treatment, *Standard-MC*, *SFS* and *FFS* cases, the classical $N^{-1/2}$ convergence law of MC methods is retrieved. One can note that the errors achieved for these cases are similar here. This is attributed to the chosen conditions (optical thickness and albedo) where scattering is not dominant: *SFS* and *FFS* do not increase the convergence in this case.

When a *full-RQMC* treatment is considered, the convergence rate is greatly improved (up to 0.8), and the lowest error is obtained with this method. Typically, if one requires a relative standard deviation of 10^{-3} , approximately 10^4 rays need to be computed for the RQMC method, while 10^5 rays are required for the standard MC method, which saves an important CPU time. The difference increases as the desired error are lowered. With a hybrid-approach (*Hybrid-RQMC*), the error and corresponding convergence law are in-between the *Standard-MC* and *full-RQMC* cases.

The power-law exponent is slightly affected here by the standard MC treatment of scattering, limiting the achieved error.

A second case with $\tau_L = 1$ and the albedo $\omega = 0.7$ is considered to see how the previous results are affected. The number of maximum scattering has been increased to $s_{max} = 250$ for the *full-RQMC* method not to affect the convergence law results. Results are presented in Fig. 2.5.

Here again, *Standard-MC*, *SFS* and *FFS* methods exhibit a $1/2$ -convergence-

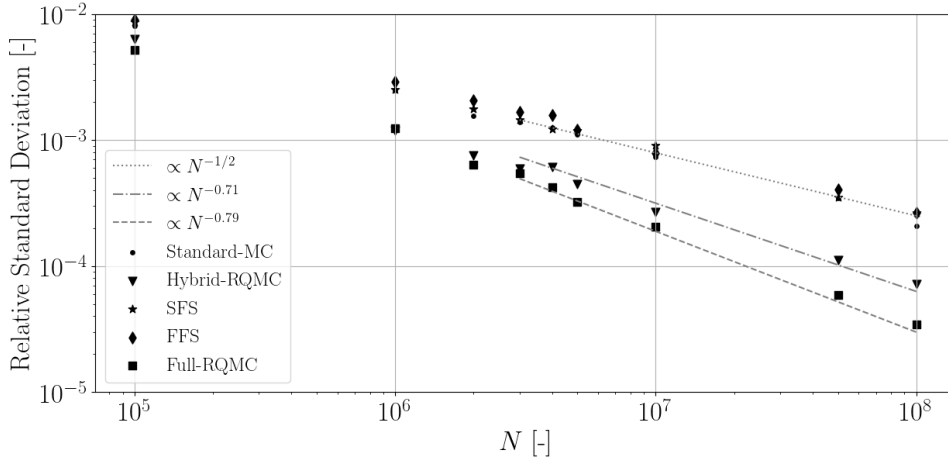


Figure 2.4: Relative standard deviation of computed wall emittance as a function of the total number of rays N for the five considered cases. Conditions: $\tau_L = 0.2$ and $\omega = 0.3$. Convergence rates are also displayed in dashed lines.

rate law. *SFS* and *FFS* methods perform slightly better than the *Standard-MC* method when looking at the obtained relative standard deviation.

In this configuration, the scattering phenomenon is dominant but occurs often. Hence, forcing the ray to scatter has a little impact on the error than the *Standard-MC* method without forced-scattering. The *full-RQMC* convergence rate is barely affected compared to the case with an albedo equals to 0.3 and still outperforms all the methods.

Finally, the *Hybrid-RQMC* convergence rate becomes closer to $1/2$, which confirms that the MC scattering treatment limits the convergence rate of the hybrid method. The *full-RQMC* approach appears more interesting as its convergence properties are less sensitive to the weight of scattering.

A third case is finally considered to emphasize the effects of fast-forced-scattering by considering an optical thickness $\tau_L = 0.1$ and an albedo $\omega = 0.9$. In this configuration, the radiative wall flux strongly depends on scattering, while the scattering event probability is low. Hence, the forced-scattering technique is expected to lessen the relative standard deviation in such a case significantly. This is indeed observed in Fig. 2.6.

Almost ten times more realizations are needed for the standard MC computation to achieve a 10^{-4} relative error, demonstrating the benefits of the fast forced-scattering (FFS) technique in such conditions. It can be observed that the standard forced-scattering technique (SFS), gives similar results than the FFS, but with an increased CPU time due to the generation of τ^* as explained in Section 2.3.2.2.

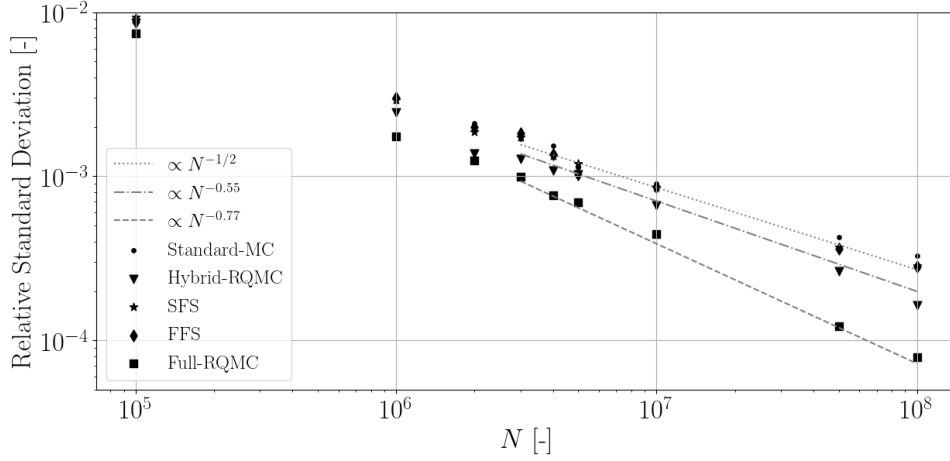


Figure 2.5: Relative standard deviation of computed wall emittance as a function of the total number of rays N for the five considered cases. Conditions: $\tau_L = 1$ and $\omega = 0.7$. Convergence rates are also displayed in dashed lines.

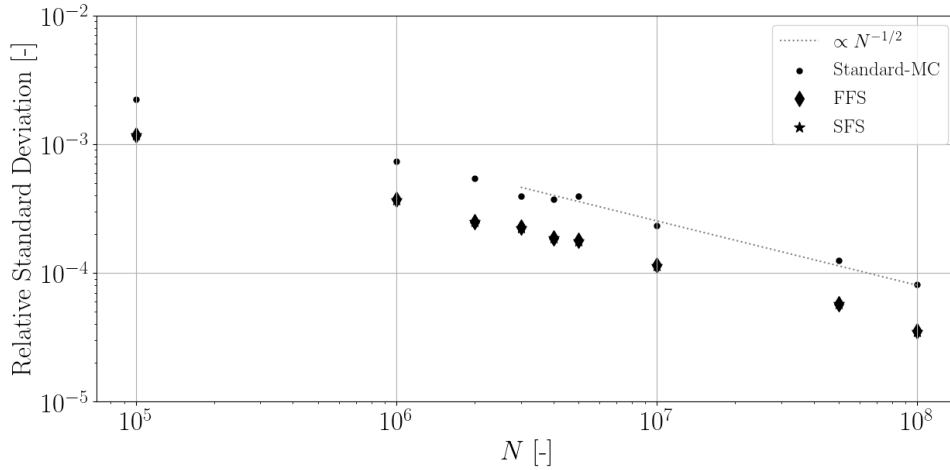


Figure 2.6: Relative standard deviation of computed wall emittance as a function of the total number of rays N for standard Monte Carlo case and Standard Forced Scattering and Fast-forced-scattering case. Conditions: $\tau_L = 0.1$ and $\omega = 0.9$. Convergence rate is also displayed in dashed lines.

2.3.4.3.3 Convergence performance : combination of methods

Previous sections have shown the efficiency of the *full-RQMC* approach. It is here combined with forced-scattering to assess the impact on the convergence rate. Results for three cases are compared: the previous *Standard-MC* and *full-RQMC* cases, and the full-RQMC computation combined with fast forced-scattering technique referred as *full-RQMC-FFS*.

Figure 2.7 compares the results for the three cases for the conditions $\tau_L = 1$ and $\omega = 0.7$. It can be observed that the *full-RQMC-FFS* case is the most accurate: applying the variance reduction technique to favor scattering events on the *full-RQMC* case shifts the relative standard deviation to lower values. Besides, the power-law coefficient of the convergence rate for *full-RQMC* and *full-RQMC-FFS* cases is similar. In other words, using variance reduction techniques along with the RQMC method preserves its benefits and lessens the number of realizations required.

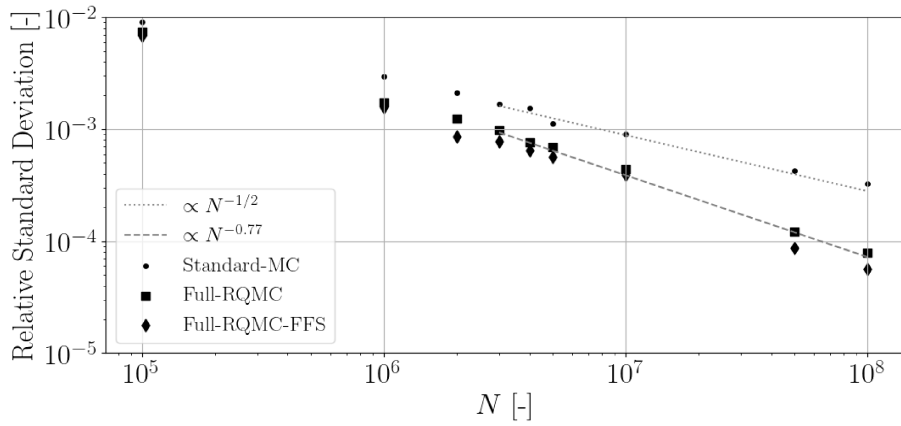


Figure 2.7: Comparison of relative standard deviation for the computed wall emittance as a function of the total number of rays N for the cases *full-RQMC* and *full-RQMC-FFS*. Conditions: $\tau_L = 1$ and $\omega = 0.7$. Convergence rate is also displayed in dashed lines.

The benefits from the fast-forced-scattering technique is quite low since scattering already occurs often in this condition ($\tau_L = 1$, $\omega = 0.7$). Hence, the three methods are also considered with $\tau_L = 0.1$, $\omega = 0.9$ in order to emphasize FFS effects, and are presented Fig. 2.8. It is observed that the RQMC technique enables again to enhance the convergence rate. For the studied condition, combining RQMC with the FFS technique achieves a greater improvement than in the aforementioned conditions. The results in Fig. 2.8 are shifted downwards, and the convergence rate exponent is similar to the one obtained in the *Full-RQMC* case.

2.3.4.4 Impact of the value of s_{max} on the performance of the full-RQMC method

In the previous section, the performance of the *full-RQMC* case has been assessed for different conditions with appropriate values of s_{max} . This part's objective is to *a-posteriori* justify the chosen values by studying the obtained convergence rate for several values of s_{max} . The Monte Carlo computational

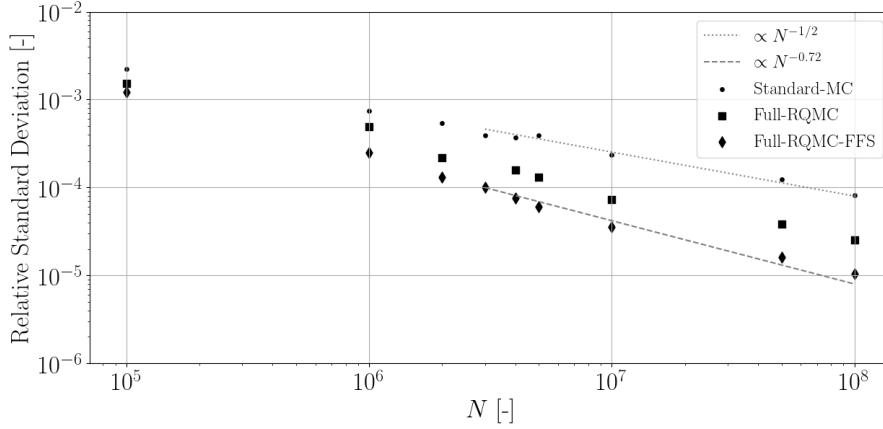


Figure 2.8: Comparison of relative standard deviation for the computed wall emittance as a function of the total number of rays N for the cases full-RQMC and full-RQMC-FFS. Conditions: $\tau_L = 0.1$ and $\omega = 0.9$. Convergence rate is also displayed in dashed lines.

parameters are identical as those defined in Sec. 2.3.4.3.2, only s_{max} is allowed to vary. Only the *full-RQMC* case (without forced-scattering) is considered to isolate the impact of the Sobol sequence dimension.

Table 2.1 shows the evolution of the convergence rate obtained for the various considered cases.

Number of max. scattering s_{max}	Convergence rate exponent		
	$\tau_L = 0.2, \omega = 0.3$	$\tau_L = 1, \omega = 0.7$	$\tau_L = 0.1, \omega = 0.9$
1	0.504	0.502	0.501
3	0.53	0.503	0.505
10	0.58	0.53	0.51
20	0.61	0.58	0.53
30	0.7	0.6	0.59
50	0.8	0.68	0.64
100	0.804	0.768	0.71
250	0.805	0.77	0.72

Table 2.1: Evolution of the convergence rate exponent in function of the maximum number of scattering events s_{max} used to build the Sobol sequence for the RQMC method. The retained convergence rate in Sec. 2.3.4.2 are emphasized in bold fonts.

For a low Sobol dimension corresponding to a low s_{max} value, the convergence rate is identical to the expected Monte Carlo convergence rate. This is explained by the fact that, once the number s_{max} of scattering events is reached, the solver switches from the RQMC cubature rule to a standard Monte Carlo sampling. When s_{max} increases, the convergence rate is improved until it reaches a given

value indicating the final numerical result's sensitivity to the number of scattering events. The plateau is reached for different values depending on the albedo and the optical thickness. Then, one should be aware of such property to maximize RQMC efficiency. *A priori* evaluation of s_{max} should be considered before carrying out any expansive RQMC simulations with scattering. The three previous values considered for s_{max} correspond to the convergence rate law's converged values. The previously reported RQMC convergence rates are not notably affected by choice of a higher number of scattering events.

2.4 Conclusion

The increase in computational resources and advances in numerical algorithms enables accurate Monte Carlo methods to solve radiative heat transfer in 3D configurations. In this Chapter, the Rainier Monte-Carlo solver for the RTE retained in this thesis has been presented. Such methods can even be used nowadays in coupled simulation workflows where thermal radiation, turbulence, and combustion are solved simultaneously. These computations remain expansive and benefit strongly from any improvements to the Monte Carlo solver. In particular, the Quasi-Monte Carlo cubature provides a very interesting methodology to accelerate the convergence of Monte Carlo estimates.

Originally developed for non-scattering media, a methodology has been proposed to take into account scattering events in the solver. The treatment of scattering with a randomized Quasi-Monte Carlo (RQMC) method has been therefore investigated. Different variants have been derived and assessed in homogeneous slabs with various conditions of optical thickness and albedo. A significant improvement in the convergence rate has been demonstrated. It was shown that the accuracy is increased by considering a maximum number of scattering events in the RQMC sampling and by combining the approach with forced-scattering. The latter property outlines that the RQMC method is independent of any variance reduction techniques: it can benefit from the large set of Monte Carlo acceleration techniques to be further improved.

In the next chapter, our methodology is applied on a turbulent jet flame in order to quantify with accuracy soot scattering in a complex 3D configuration.

Part II

Characterization of soot radiation in turbulent flames with stand-alone Monte-Carlo simulations

Chapter 3

Accurate quantification of soot scattering contribution in a turbulent jet flame

*In the previous chapter, a methodology accounting for scattering combined with a Quasi-Monte-Carlo approach has been exposed and validated on homogeneous slabs. The objective of this chapter is to apply this approach to an heterogeneous configuration : a turbulent sooty jet flame. In a first part, the retained soot radiative modeling (RDG-FA) is validated and compared in a simple 3D domain with literature data. In the second part, the methodology is applied to instantaneous fields of the turbulent jet flame. These fields have been obtained from a previous coupled calculation with a Large Eddy Simulation solver. Improvements in terms of convergence rate and number of realizations required to reach a given error are emphasized. The impact of scattering in this configuration is then investigated. Finally, global metrics are developed to *a-priori* evaluate the impact of scattering in a given configuration.*

Contents

3.1	Modelling of thermal radiation in sooted flames . . .	88
3.1.1	Gaseous radiative properties	88
3.1.2	Soot radiative properties	88
3.1.3	Validation of RDG-FA scattering computation	93
3.2	Computation of radiative heat transfer in a turbulent sooted jet flame	96
3.2.1	Reference fields	96
3.2.2	Quasi-Monte Carlo performance tests	98
3.2.3	Impact of scattering	101
3.2.4	Interpretation of scattering impact: spectral analysis	103

3.3	Global metrics to a priori assess the impact of scattering	108
3.4	Conclusion	112

3.1 Modelling of thermal radiation in sooted flames

This section introduces the radiative models used in the calculation of the turbulent sooting jet flame presented in Section 3.2.

3.1.1 Gaseous radiative properties

Only the radiative properties of CO₂ and H₂O are considered. The cK model, based on updated parameters from Rivière and Soufiani (2012), is used to describe the gas radiative properties. For H₂O, 44 spectral bands are considered up to 9200 cm⁻¹. CO₂ absorbs radiation in 17 of these bands. For each gaseous component, a 7-point Gauss quadrature is used per band. In the 17 overlapping bands, 49 quadrature points are used. The cK database is then made of 1022 pseudo-spectral points.

3.1.2 Soot radiative properties

A total of 93 spectral bands up to 29 000 cm⁻¹ are added into the cK-model. Soot radiative properties depend on their optical properties and their morphology. In this study, the interaction phenomenon between primary particles of an aggregate such as overlapping or necking (Yon et al. (2015)) are neglected.

3.1.2.1 Soot optical properties

The complex index of refraction of soot particles, noted $m = n - ik$, characterizes soot optical properties. The real part n is the refractive index, and the imaginary part k is the absorptive index. In the literature, two models are mostly encountered for n and k : a constant formulation as proposed in Smyth and Shaddix (1996) and a wavelength dependency. The second model is here retained, given by Chang and Charalampopoulos (1990):

$$\begin{aligned} n(\lambda) &= 1.811 + 0.1263 \ln \lambda + 0.027 \ln^2 \lambda + 0.0417 \ln^3 \lambda \\ k(\lambda) &= 0.5821 + 0.1213 \ln \lambda + 0.2309 \ln^2 \lambda + 0.01 \ln^3 \lambda \end{aligned} \tag{3.1}$$

3.1.2.2 Soot morphology

The retained model for soot morphology considers soot particles as spherical below a given volume V_{LIM} and as aggregates otherwise. These aggregates are

characterized by a number of primary spherical particles n_P of diameter d_P . These two quantities are given by the following relations :

$$\begin{aligned} n_P &= \frac{S^3}{36\pi V^2} \\ d_P &= \frac{6V}{S} \end{aligned} \quad (3.2)$$

where S is the aggregate surface, and V its volume. In order to close these relations a relation between the surface and the volume of an aggregate is required. The same law as in [Rodrigues \(2018\)](#) is retained : the model has been derived by fitting numerical results obtained on 1D laminar premixed ethylene flames ([Salenbauch et al. \(2015\)](#), [Mueller et al. \(2009\)](#)), leading to

$$S = \begin{cases} (V/V_{C_2})^{2/3} S_{C_2} & \text{for } V < V_{LIM} \\ (V/V_{C_2})^{\theta(V)/3} S_{C_2} & \text{for } V > V_{LIM} \end{cases} \quad (3.3)$$

with $S_{C_2} = 0.372 \text{ nm}^2$ and $V_{C_2} = 0.021 \text{ nm}^3$ the surface and volume of a molecule composed by two atoms of carbon. The limit volume V_{LIM} is equal to $10^{2.6} \text{ nm}^3$. $\theta(V)$ is given by :

$$\theta(V) = 3.0 \cdot \frac{(\log(V/V_{LIM})) + 2/3 \cdot (\log(V_{LIM}/V_{C_2}))}{\log(V/V_{C_2})} \quad (3.4)$$

3.1.2.3 Rayleigh-Debye-Gans theory for Fractal Aggregates

The Rayleigh-Debye-Gans theory (RDG-FA) derived in [Dobbins and Megaridis \(1991\)](#) and [Köylü and Faeth \(1994\)](#) extends the Rayleigh theory for spherical particles by assuming an aggregate shape for soot. An aggregate is composed of an ensemble of monodisperse spherical primary particles. The model assumes that the soot optical refraction index $m = n - ik$ is close to unity and that the size parameter $x_P = \frac{\pi d_P}{\lambda}$ is smaller than unity. Although these assumptions are questionable, especially for low values of λ , RDG-FA yields to a reasonable description of scattering properties as discussed in [Chapter 1](#).

Soot absorption coefficient

The absorption coefficient is computed using [Equation 1.67](#). The optical index m is calculated via [Equation 3.1](#).

Soot scattering coefficient

The soot scattering coefficient is defined by the following expression:

$$\sigma_{\lambda}^{soot} = \int_0^{+\infty} C_{scat,agg}(V)n(V) dV \quad (3.5)$$

The computation of $C_{scat,agg}$ is done following Equation 1.68.

D_f and k_f are the fractal parameters, fixed in the simulations, respectively to 1.8 and 1.3, such as in the RDG-FA theory (Dobbins and Megaridis (1991)).

Soot scattering phase function

The phase function is computed using Equation 1.75 for an aggregate. The phase function for an assembly of aggregates is then given by the integral formulation (Equation 1.75).

3.1.2.4 Discussion on phase function patterns for an aggregate

Figure 3.1 compares the phase functions obtained with the RDG-FA model, using Eq. 1.75 (blue line) and the Rayleigh model (red line). The considered aggregate is composed of $n_P = 256$ primary particles, with three different diameters d_P : 1 nm (left), 10 nm (center), 50 nm (right), at a fixed wavelength of 534nm. These conditions correspond to a size parameter x respectively equals to 0.006 , 0.06 and 0.3. Let us notice that the RDG-FA assumption is valid since the size parameter is lower than 1 for the three cases considered.

As expected, the discrepancy between the two models increases with the size of the primary particle diameter. The polar representation exhibits the behavior of the scattering phase function, *i.e.* the probability to be scattered in a given direction.

The RDGFA model for the biggest particles tends to predict a strong forward scattering. For smaller particles encountered, the scattering phase function pattern tends to be similar to the one obtained with the simple Rayleigh regime.

A common parameter to describe the forward/backward scattering of one aggregate is the asymmetry factor G , defined by :

$$G = \frac{1}{4\pi} \int_{4\pi} \Phi_{agg}(\theta) \cos \theta d\Omega \quad (3.6)$$

In the case of RDG-FA, this asymmetry factor can be written as :

$$G = \frac{1}{2} \int_{\pi} \Phi_{agg}(\theta) \sin \theta \cos \theta d\theta \quad (3.7)$$

This factor varies between -1 (pure backward scattering) to +1 (pure forward scattering). For each cases, the values of G are respectively :

- Case 1 ($d_p = 1$ nm) : $G_{Rayleigh} = 0$ (symmetric pattern for Rayleigh regime) and $G_{RDGFA} = 0.004$.
- Case 2 ($d_p = 10$ nm) : $G_{RDGFA} = 0.031$
- Case 3 ($d_p = 50$ nm) : $G_{RDGFA} = 0.76$

The evolution of the asymmetry factor with the diameter G is consistent with the increase of the forward-scattering behavior. Such forward-scattering has also been observed experimentally (Weinert et al. (2003)), and with aggregates numerically generated (Liu et al. (2013)).

The overall effect of scattering is not only linked to the phase function and the asymmetry factor but also to the scattering coefficient σ . Because the expressions between Rayleigh and RDGFA differs for the scattering cross-section, the resulting σ is different. An interesting metric to quantify such effect is the albedo, defined as : $\omega = \frac{\sigma}{\kappa + \sigma}$. For the three patterns presented Figure 3.1, the albedo is respectively :

- Case 1 ($d_p = 1$ nm) : $\omega_{Rayleigh} = 3 \times 10^{-4}$ and $\omega_{RDGFA} = 0.1$
- Case 2 ($d_p = 10$ nm) : $\omega_{Rayleigh} = 4 \times 10^{-2}$ and $\omega_{RDGFA} = 0.6$
- Case 3 ($d_p = 50$ nm) : $\omega_{Rayleigh} = 0.8$ and $\omega_{RDGFA} = 0.95$

These values have been calculated using a soot volume fraction value of $f_V = 10^{-5}$. It can be observed that, although the scattering patterns are similar (case 1 and 2), the albedo strongly differs to the the difference of scattering cross-section expressions, therefore, the impact of scattering can be important.

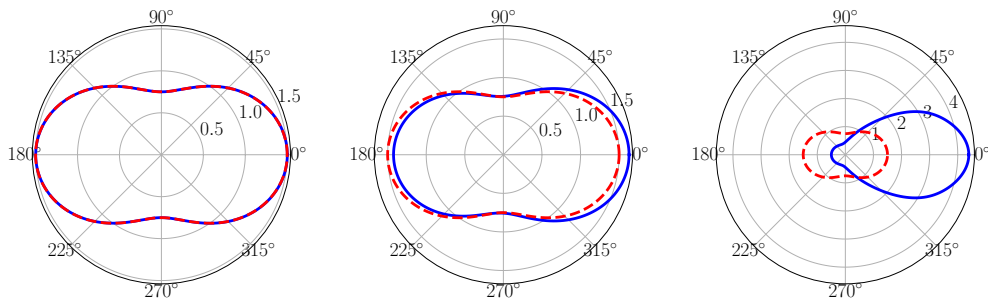


Figure 3.1: Comparison of phase functions between Rayleigh theory (red dashed lines) and RDG-FA theory (blue line) for a given aggregate with 3 different primary particle diameters $d_p = 1$ nm (left), 10 nm (center) and 50 nm (right). The wavelength is fixed at 534 nm.

Let us recall that the previous discussion is carried out at a fixed wavelength. However, the phase function is also strongly dependent on the wavelength.

In Figure 3.2, phase functions are compared at a fixed diameter of primary particles $d_P = 10\text{nm}$ at $\lambda = 100, 775$ and 1000 nm. Although the case at 100 nm is unrealistic in practice, it is considered as a "limit" situation where scattering becomes very important.

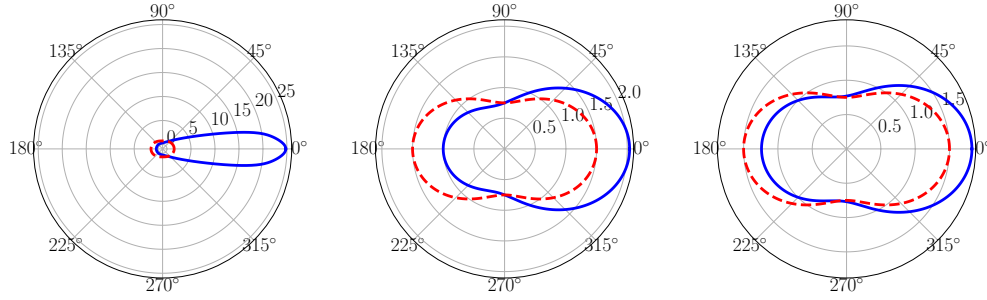


Figure 3.2: Comparison of phase functions between Rayleigh theory (red dashed lines) and RDG-FA theory (blue line) for a given aggregate with 3 different wavelengths $\lambda = 100$ nm (left), 775 nm (center) and 1000 nm (right).

It can be observed that RDGFA tends to the Rayleigh pattern when the wavelength is increased (as the size parameter $x = \frac{\pi d_P}{\lambda}$ is becoming small (from left to right : $x = 0.314, x = 0.04, x = 0.03$). For each case, the asymmetry factor is given by :

- Case 1 ($\lambda = 100$ nm) : $G_{Rayleigh} = 0$ (symmetric pattern for Rayleigh regime) and $G_{RDGFA} = 0.9$.
- Case 2 ($\lambda = 775$ nm) : $G_{RDGFA} = 0.21$
- Case 3 ($\lambda = 1000$ nm) : $G_{RDGFA} = 0.11$

Here again, the values of G well describes the strong forward scattering observed for low wavelengths.

Finally, the albedo is calculated for each case :

- Case 1 ($\lambda = 100$ nm) : $\omega_{Rayleigh} = 0.97$ and $\omega_{RDGFA} = 0.98$
- Case 2 ($\lambda = 775$ nm) : $\omega_{Rayleigh} = 0.09$ and $\omega_{RDGFA} = 0.12$
- Case 3 ($\lambda = 1000$ nm) : $\omega_{Rayleigh} = 0.04$ and $\omega_{RDGFA} = 0.05$

Contrary to the previous case at λ fixed , the values reached by the albedo for both models are quite similar. Indeed, for $\lambda = 100$ nm, the scattering coefficient is very important in both RDGFA and Rayleigh cases and the albedo is almost equals to 1 : in this case, scattering is much more important than absorption. For the other wavelengths, the absorption strongly dominates scattering regardless the model employed, therefore, albedos are small for both models.

Such an example shows the importance of taking into account both the asymmetry factor and the albedo in the analysis of phase function patterns.

3.1.3 Validation of RDG-FA scattering computation

The implementation of the RDG-FA theory in RAINIER is validated against published numerical results of radiative heat transfer obtained with a Discrete Ordinates Method calculation (Eymet et al. (2002)).

The computational domain is a 3D cubic box with a length of $L = 1$ m, with 100x100x10 points in the direction x, y and z, respectively. The black walls temperature are set to $T_w = 300$ K while the domain is set to $T_{dom} = 2000$ K. The domain is composed of homogeneous soot aggregates with $n_p = 256$ primary particles and $d_p = 50$ nm. The soot volume fraction is set to $f_V = 10^{-6}$. Small changes from the previously described setup are considered to be consistent with the model for soot radiative properties retained in Eymet et al. (2002).

The optical index of soot particles m is chosen with a spectral dependency whose parameters are taken from Dalzell and Sarofim (1969). The form factor expression f is taken from the original RDG-FA model (Equation 1.73, which differs from Equation 1.74. This set-up is referred to "**Original set-up**" in the following.

The Monte Carlo simulations are carried out using the *full-RQMC-FFS* method that combines RQMC and fast-forced-scattering. s_{max} is fixed at 200, and the maximum length for the fast-forced-scattering method is set to $L_{max} = 1$ m. The controlled error is set to 0.5% for relative standard deviation. Such a fine accuracy is required to capture scattering effects correctly. The obtained radiative power profile is displayed in Figure 3.3.

Results are in excellent agreement with the discrete ordinate methods calculation. However, it appears that the effects of scattering are small in this configuration. To achieve a thorough validation of the scattering formulation, the predicted spectral radiative power difference with and without scattering is compared. The relative difference $\frac{P_{scattering} - P_{no-scattering}}{P_{no-scattering}}$ is computed and averaged for several points on the mid-plane of the domain.

It is shown in Fig. 3.4 as a function of the spectral wavelength. The figure illustrates the known effect of soot scattering, which increases drastically for small wavelengths. Both numerical results are very close. The error bars (0.5%) associated with the simulation with scattering are also shown around the predicted curve. For high wavelength, scattering effects diminish, which requires an accurate control to be captured. Negligible differences between the predicted profile and results in Eymet et al. (2002) are attributed to remaining statistical noise in the present results outlined by the error bars, and numerical errors in the Discrete Ordinates Method calculation of the original study.

It is important to recall that the form-factor and optical index m expressions considered in the following are not the same as the ones used in the validation case. In Figure 3.4, results are also computed with the retained set-up (which is referring to **Retained set-up**). The difference in optical soot properties and form-factor quantitatively affects the spectral profile throughout the whole range of wavelengths.

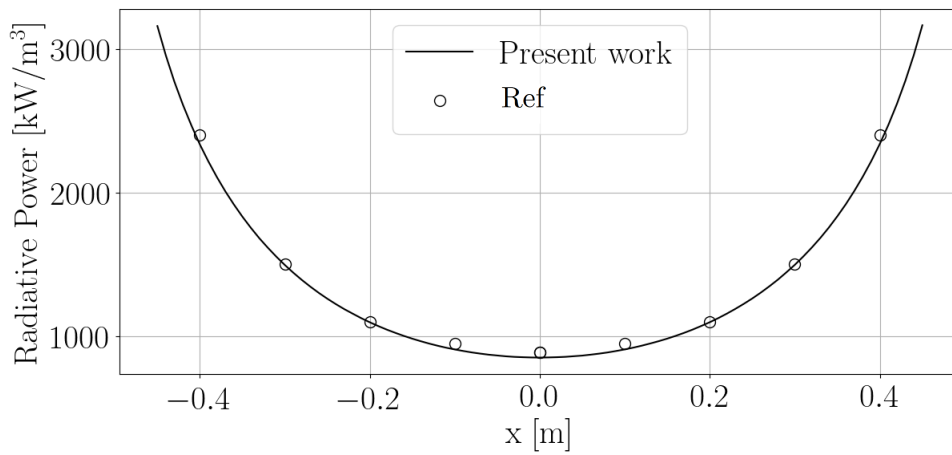


Figure 3.3: Profile of radiative power along the domain composed of soot aggregates and comparison with Ref. *Eymet et al. (2002)*.

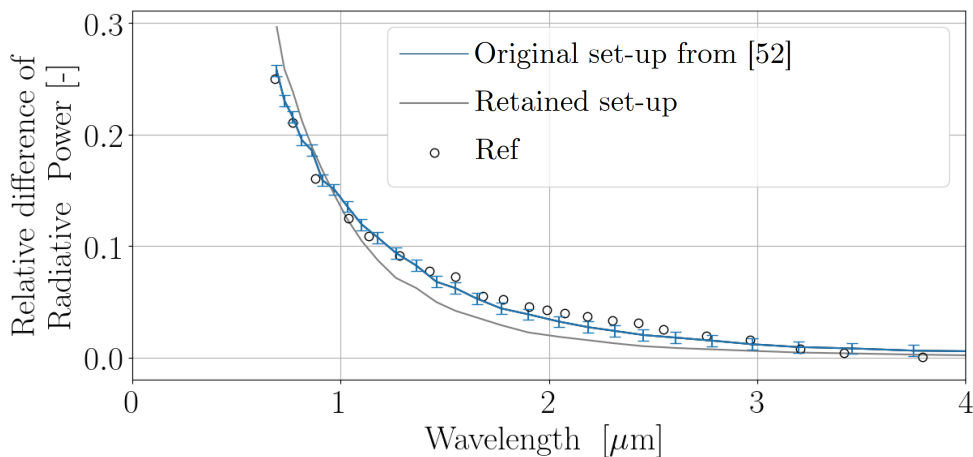


Figure 3.4: Relative difference of spectral radiative power with and without scattering for both RDG-FA setups.

Overall, the effect of scattering in this configuration is small. This can be

understood by computing the spectral albedo

$$\omega_\lambda = \frac{\sigma_\lambda}{\kappa_\lambda + \sigma_\lambda}. \quad (3.8)$$

For soot aggregates of a specific size as considered here, it yields

$$\omega_{agg,\lambda} = \frac{C_{sca,agg}}{C_{abs,agg} + C_{sca,agg}} \quad (3.9)$$

where $C_{abs,agg}$ and $C_{sca,agg}$ are respectively the absorption and the scattering cross-section coefficient for an aggregate. This albedo can be an interesting metric in the case where the domain is characterized by a monodisperse population of aggregates (they have all the same volume). Recalling the definitions given by the RDG-FA theory of the cross-sections coefficients (Equations 1.66 and 1.68), the albedo for an aggregate can be written:

$$\omega_{agg,\lambda} = \frac{2/3 F(m)/E(m) (\frac{2\pi}{\lambda} d_p)^3 n_p g}{1 + 2/3 F(m)/E(m) (\frac{2\pi}{\lambda} d_p)^3 n_p g} \quad (3.10)$$

where $F(m)$ and $E(m)$ are quantities depending on the soot optical index m , d_p and n_p are respectively the diameter and the number of primary particles, g the corrective factor introduced in the RDG-FA model.

$\omega_{agg,\lambda}$ for the present case is plotted in Fig. 3.5. The evolution of the spectral albedo appears indeed correlated to the relative difference of radiative power computed in Figure 3.4. Since low albedo values are reached in this configuration, the scattering contribution is small.

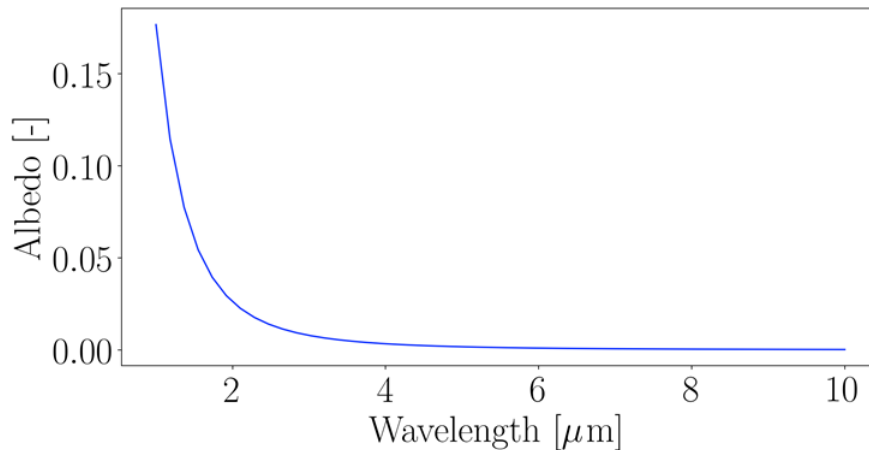


Figure 3.5: Spectral evolution of the albedo in the RDGFA validation case

3.2 Computation of radiative heat transfer in a turbulent sooted jet flame

In this section, all Monte Carlo calculations are performed using the RDG-FA model presented in Sec. 3.1.2.3.

3.2.1 Reference fields

The studied configuration is the turbulent jet diffusion flame experimentally studied at Sandia (ISF3 (2017)). It is a diffusion, non-confined turbulent jet flame under standard atmospheric conditions. The fuel pipe is fed with pure ethylene. This configuration corresponds to a turbulent jet with Reynolds number $Re_D = 20\,000$, based on the fuel injector of the main jet $D = 3.2$ mm. The corresponding bulk velocity is $v_{fuel} = 54.7$ m/s. The main jet tube presents an outer diameter of 4.6 mm and is surrounded by another tube with an inner diameter of 15.2 mm, and an outer diameter of 19.1 mm. The mesh contains 10 million cells/1.7M nodes, and the typical cell size at the jet exit is $\Delta x \approx 0.20$ mm and increases up to 5 mm further downstream.

The reference fields considered for the present study are taken from previous works on this flame : Rodrigues et al. (2019) carried out a coupled large-eddy simulation (LES) to study soot formation and radiation. In their work, the soot formation modeling relies on a sectional method (Rodrigues et al. (2018)), which gives here access to the soot number density function $n(V)$ and the soot volume fraction $f(V)$, as explained in Chapter 1.

LES fields are provided to the Monte Carlo solver to compute radiative fields while accounting for scattering, which was neglected in the previous numerical study. The objective is here to quantify this assumption accurately. Figure 3.6 presents the temperature, soot volume fraction fields used in this study, and the corresponding radiative power field computed by the Rainier solver.

In most parts of the domain, the radiative power is governed by hot participating gases. Soot particles are present where the mixture is rich, and the temperature is high before oxidized. In this zone, the high instantaneous soot volume fraction (25 ppm) strongly impacts the radiative power.

The following solution data are given to the Rainier solver: pressure, molar fractions of CO_2 and H_2O , soot volume fraction f_v , and the soot number density function $n(V)$ discretized in 25 sections. Figure 3.7 presents for two sections the corresponding soot mass fraction Y_s and the soot number density $n(v)$ given by the sectional method presented Chapter 1. It can be observed that each field is located in a different part of the flame, depending on the section considered. The information of the plotted quantities for each section enables to compute the soot radiative properties for a distribution of aggregates : this shows the benefits of using the sectional approach in this work.

For all Monte Carlo computations, the inlet and the outlet of the domain are

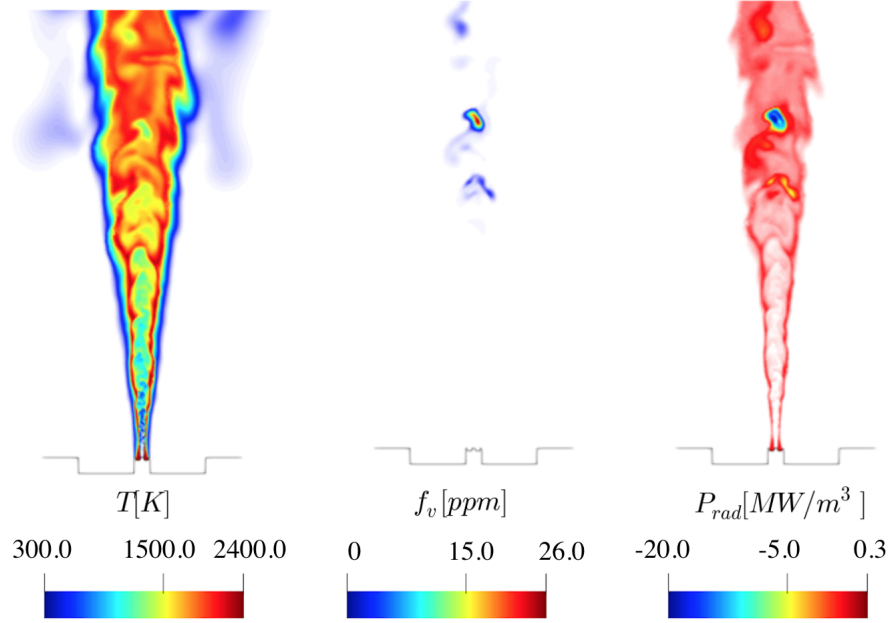


Figure 3.6: Left: reference fields of temperature and soot volume fraction. Right: computed radiative power field.

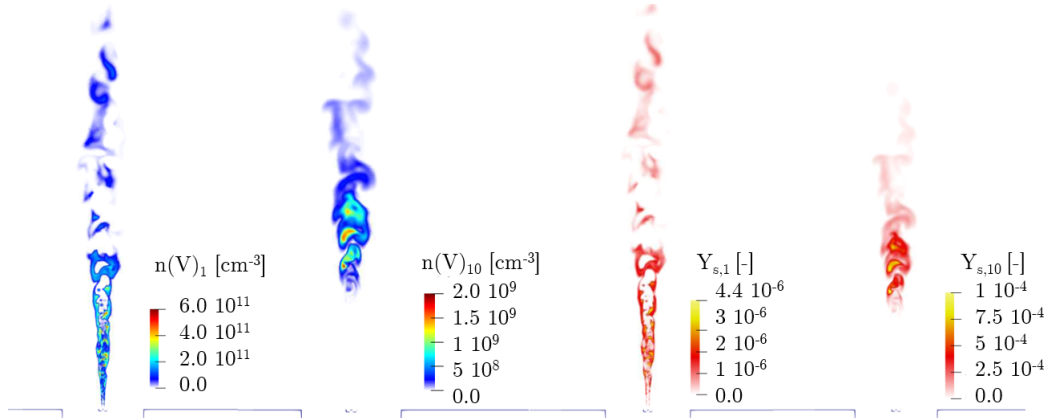


Figure 3.7: Soot mass fraction and soot number density fields for the first and tenth sections.

considered as non-reflective walls. The same mesh and geometry as in [Rodrigues et al. \(2019\)](#) are employed.

3.2.2 Quasi-Monte Carlo performance tests

Convergence properties of the RQMC method derived to take into account scattering are first presented. Two different tests are carried out on the turbulent jet flame configuration. The first test consists of imposing the same total number of rays N , introduced in Section 2.3.3.3 with the same number of trials $M = 100$, at all the points where the radiative power is computed. The achieved error measured by the relative standard deviation of the result is checked at every node. In the second test, convergence criteria are imposed on the desired standard deviation: 0.1% for the relative value, and 0.1% of the maximum radiative power for the absolute value. In this case, the number of rays is not fixed and will vary in the domain. Two computations are compared: the *Standard-MC* and *full-RQMC-FFS* cases. The latter case should achieve fast convergence by combining fast forced-scattering and RQMC cubature applied to emission, absorption and scattering ($s_{max} = 300$).

3.2.2.1 Test 1: fixed number of rays

This test indicates which zones are easily converged or not. The accuracy for the prescribed number of rays in both computations is characterized by the local relative standard deviation of the radiative power. Results for *Standard-MC* and *full-RQMC-FFS* cases are compared in Fig. 3.8. Different convergence properties at each node yields an inhomogeneous error field. The relative standard deviation is the highest in low-temperature regions where the radiative power is small, which is not critical. This is also a known shortcoming of the considered ERM Monte Carlo method that convergences weakly in cold regions dominated by absorption. It can be seen nonetheless that the computation based on RQMC gives a smaller error field throughout the domain, indicating a faster convergence for this case.

The convergence rate is studied further by considering the evolution of the standard deviation of the number of rays at a given point. Since we are focusing on the scattering by soot particles, we choose the location where the soot volume fraction is maximum ($x = 0.4$ m). The convergence plot similar to the ones presented in Sec. 2.3.4 is shown in Fig. 3.9. As expected, the asymptotic convergence law is proportional to $N^{-1/2}$ for the *Standard-MC* case while Quasi-Monte Carlo achieves a faster convergence rate whose exponent coefficient is close to 0.73. Hence, reaching a relative error of 10^{-3} requires approximatively 10 times more rays for the standard MC approach.

3.2.2.2 Test 2: controlled error

In Figure 3.8, an inhomogeneous convergence is observed. Some zones can be considered too accurate, while others suffer from poor convergence. Performing a simulation with a controlled error enables more efficient computation of the radiative power. The fields of the number of rays required to achieve the

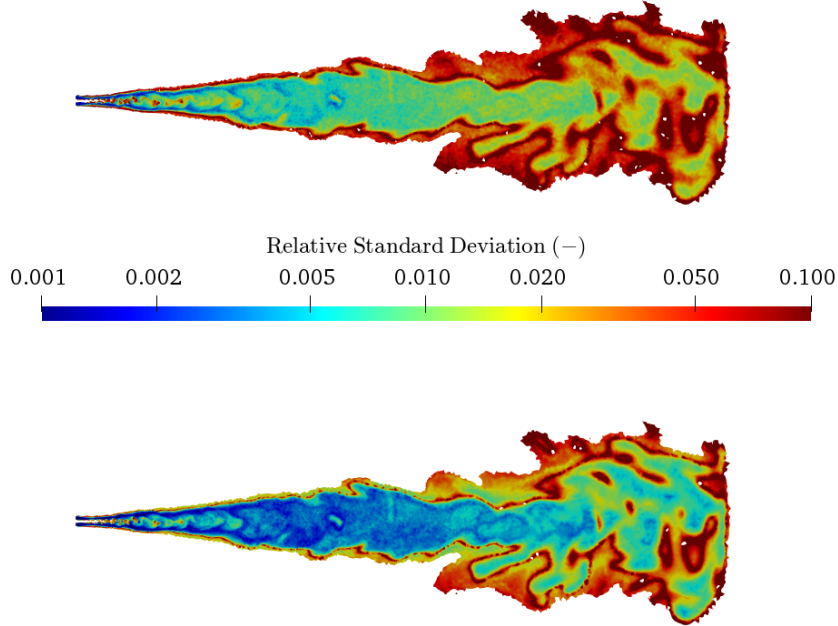


Figure 3.8: Comparison of relative standard deviation fields in the turbulent jet flame. **Top:** Standard-MC. **Bottom:** full-RQMC-FFS.

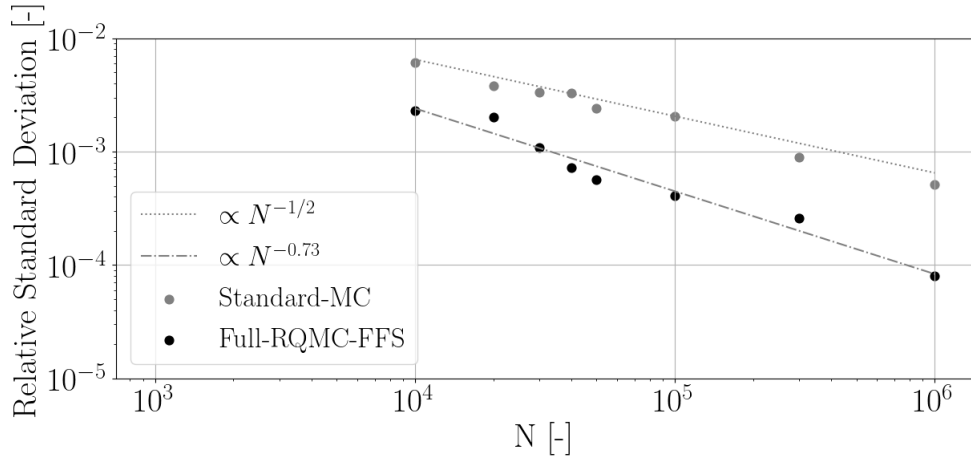


Figure 3.9: Relative standard deviation as a function of the number of rays N at the location of maximum soot volume fraction.

accuracy criteria in Test 2 are displayed in Fig. 3.10. Thanks to the absolute error criterion, ill-converged regions of the negligible contribution surrounding the flame are disregarded. In both cases, the regions where soot particles are

present, and the temperature is low is where the required number of rays is the highest. Clearly, with the QMC methodology combined with forced scattering, the number of rays required to achieve the prescribed error is much lower than with the *Standard-MC* case. In terms of CPU time, the *Standard-MC* case requires 850 seconds on 96 CPUs to achieve the prescribed error while the *full-RQMC-FSS* case takes 415 seconds. A twofold speed-up factor is then obtained, which is a significant improvement in computational time.

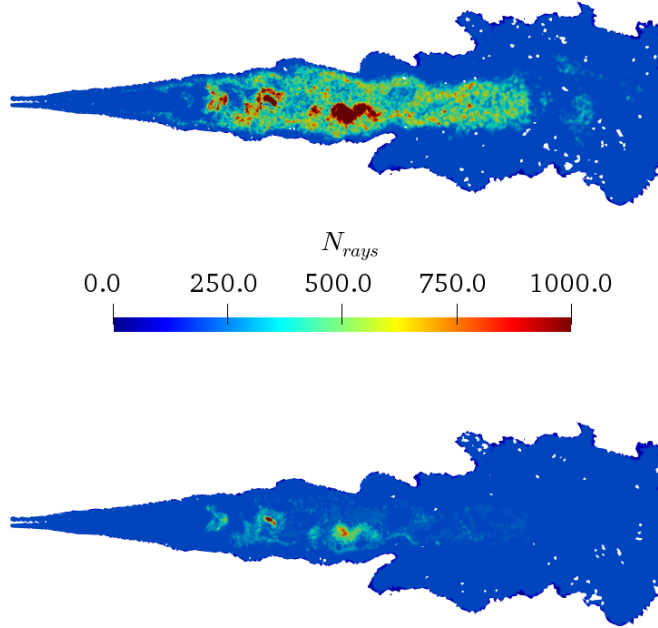


Figure 3.10: Comparison of the number of rays required to reach a given error on the Sandia's turbulent jet flame. **Top** : *Standard-MC*, **Bottom** : *full-RQMC-full*.

3.2.2.3 Efficiency

In the previous section, we have emphasized the fact that, for a given error, the required CPU time to compute the radiative power is reduced with the full-RQMC-FFS methodology. Instead of considering a global metric, a local one performed in Palluotto et al. (2019) is considered. This local efficiency noted η_i is computed via the following formula :

$$\eta_i = \frac{1}{\sigma_i^2 [Q(N)] T_i^{CPU}} \quad (3.11)$$

In this equation, σ_i is the relative standard deviation of the quantity of interest,

T_i^{CPU} is the local computational time. This term is equals to :

$$T_i^{CPU} = \frac{nb_{int,i} T_{CPU}}{nb_{int,tot}} \quad (3.12)$$

where $nb_{int,i}$ is the number of intersections experienced by a ray traced from point i , T_{CPU} is the total CPU cost of the simulation, and $nb_{int,tot}$ is the total number of intersections experienced in the simulation.

A property of the standard MC computation is that the local efficiency is almost constant. This point is verified in Figure 3.11.

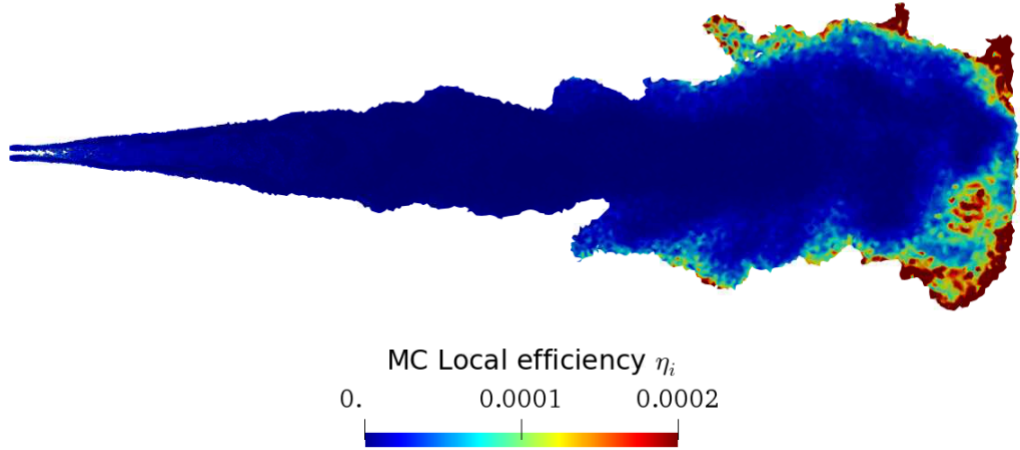


Figure 3.11: Local efficiency between for the standard-MC computation in the turbulent jet flame.

In Figure 3.12, the ratio of local efficiencies between the RQMC-FFS case and the standard MC case is displayed. Efficiencies higher than 1 means that the RQMC approach requires less CPU time to converge in this zone. It can be observed that the metric is correlated with the number of realizations displayed Figure 3.10. Globally, a speed up greater than 2 can be observed in the zones where the radiative contribution is the most important. This metric shows that the speed-up contribution already mentioned in Section 3.2.2.2 is not uniform along the computational domain.

3.2.3 Impact of scattering

As previously mentioned, scattering was neglected in the coupled calculations performed on this turbulent jet flame (Rodrigues et al. (2019)). Such an assumption is based on the scattering coefficient's expression using the Rayleigh

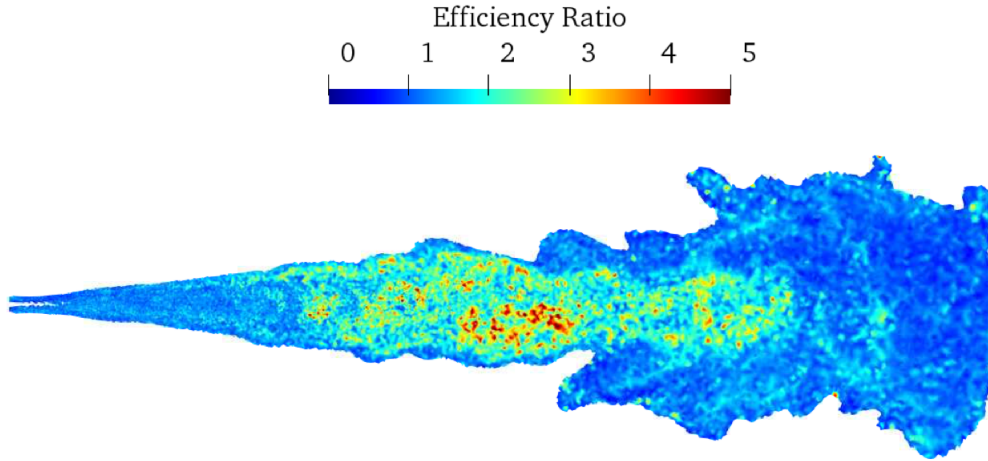


Figure 3.12: Ratio of local efficiencies between *full-RQMC-FFS* and *Standard-MC* in the turbulent jet flame.

theory: the absorption coefficient is proportional to x , the size parameter, while the scattering parameter is proportional to x^4 . Since $x \approx 0.1$ here, one expects that absorption strongly dominates scattering. However, when considering the RDG-FA theory, the scattering coefficient is related to the square of the number of primary particles n_p^2 that can be large (n_p is around several hundred). Therefore, accurate computation of scattering effects with the developed RQMC method and state-of-the-art soot radiative properties is required to assess *a posteriori* the hypothesis previously used in the coupled computation. The previously assessed *full-RQMC-FSS* method is used to achieve high accuracy at an affordable cost.

The scattering impact in the jet flame configuration is assessed with two computations: one accounting for scattering and another without. Since the scattering effect is expected to be low, the calculations need to be extremely accurate. The prescribed accuracy is based on local relative and absolute standard deviations that are then equal to 0.1% and 0.1 % of the maximum radiative power.

The radiative power along the centerline for the two cases is presented in Fig. 3.13. Only the zone with the soot volume fraction peak is displayed. Both computations with and without scattering give similar results. For both profiles, a decrease in radiative power magnitude is observed at the soot volume fraction peak. This is due to the corresponding lower temperature at this position coming from the considered fields issued from coupled simulations: the local temperature is reduced due to soot radiation, which, in turn, diminishes the magnitude of heat losses. Both cases differ only slightly, confirming a small

effect of soot scattering in the studied flame.

The decrease in absorbed power at the location of the soot volume fraction peak is attributed to an increase of the optical thickness due to the scattering; the radiative power emitted from the other cells is then absorbed before reaching this location.

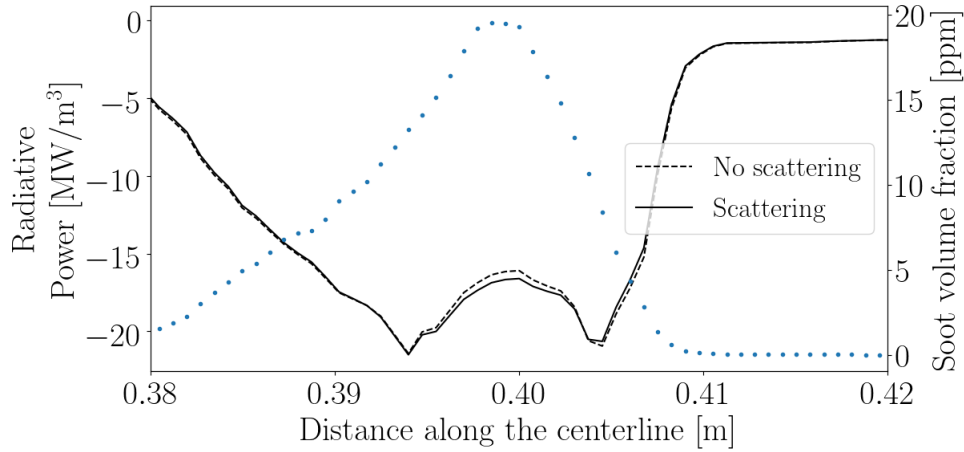


Figure 3.13: Comparison of radiative power profiles (left axis, solid and dashed lines) along the jet flame centerline. The plotted region corresponds to the peak in soot volume fraction (right-axis, dotted line).

Monte Carlo simulations need to be very accurate to capture such effects. The difference between both radiative power profiles in Fig. 3.13 is plotted Fig. 3.14. The error bounds, which here fulfill the accuracy condition based on 0.1 % of the maximum radiative power, outline that the results can be interpreted confidently. The statistical noise is lower than the observed difference. The same computation has been carried out with the standard Rayleigh model. The corresponding difference between the case with and without scattering is also shown in Fig. 3.14. The scattering contribution with the Rayleigh model is so small that it is not distinguished in the statistical noise. Indeed, the Rayleigh model applied to soot aggregates strongly underestimates scattering compared to RDG-FA theory. Hence, relying on Rayleigh’s theory to a priori exclude soot scattering is not safe. The present study has allowed quantifying such effects in the investigated flame that amounts here to a few percent of the local radiative power.

3.2.4 Interpretation of scattering impact: spectral analysis

It has been observed, Figure 3.13, that the inclusion of scattering leads to a decrease in the radiative power (or absorbed power since the emitted power is the same in both cases). This result gives only information on the radiative

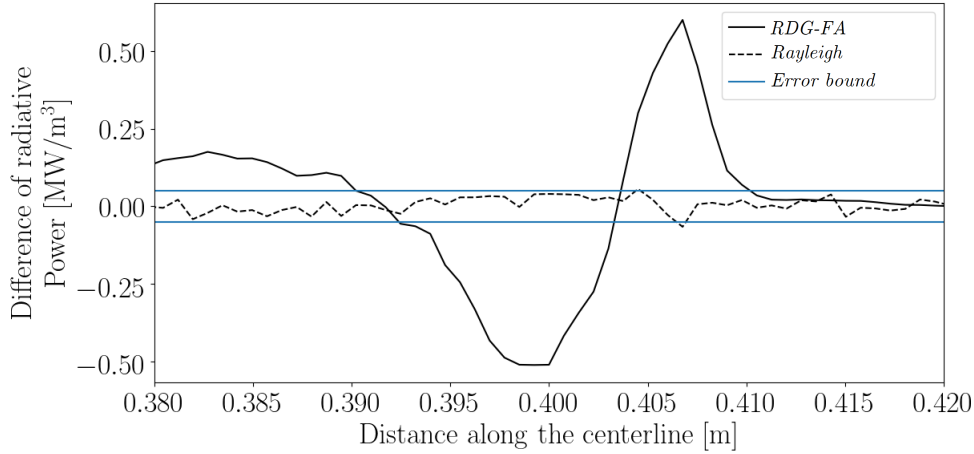


Figure 3.14: Difference of radiative power along the centerline with and without scattering for RDG-FA (solid line) and Rayleigh (dashed line) theories. Error bounds corresponding to the results' standard deviation are shown in plain horizontal lines.

power integrated over the wavenumber spectrum.

However, as previously mentioned (see the discussion in Sec. 3.1.2.4), the behavior of the scattering phase function highly depends on the wavelength. Thus, spectral analysis can be performed to assess which wavenumber is the most impacted by scattering.

The evolution of the spectral radiative power for the cases with and without scattering is presented Figure 3.15. Contributions in each band of the discretized spectrum are determined by the Monte Carlo solver at the peak location of soot volume fraction.

The difference of spectral radiative powers between both cases is shown in Figure 3.16 either as a function of the wavenumber ν or the wavelength λ . The scattering mainly affects wavenumbers around 5000 cm^{-1} (or $2 \mu\text{m}$), which corresponds to the part of the soot spectrum with the maximum emitted power. Looking at the values obtained in Figures 3.16 compared to Figure 3.15, it can be observed that the differences due to scattering represents less than 1% of the spectral radiative power.

The difference of radiative power computed in Figure 3.14 is retrieved by performing an integration of the spectrum over the whole range of wavenumbers. At the maximum soot volume fraction location ($x = 0.4 \text{ m}$), the difference is negative, which is consistent with the spectrum displayed Figure 3.15, where only negative values are obtained.

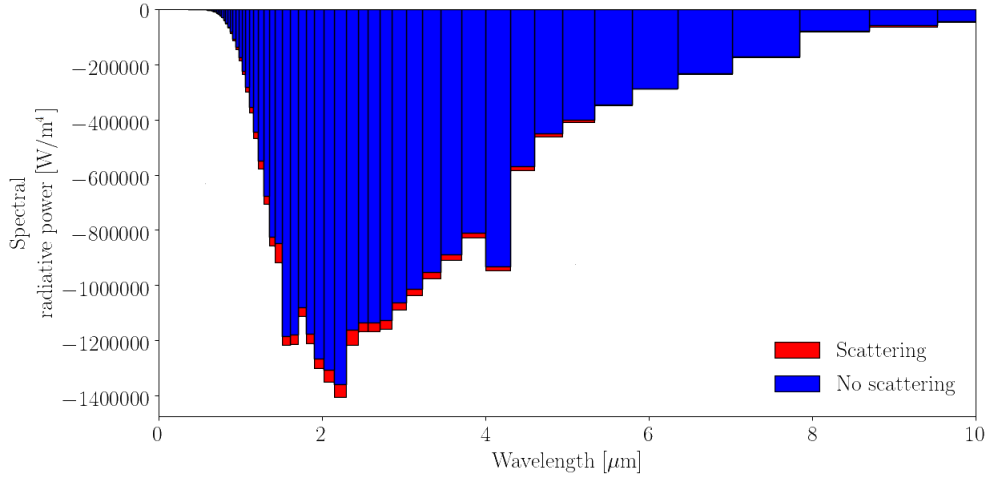


Figure 3.15: Spectral radiative power with/without scattering obtained at the peak location of soot volume fraction.

The impact of scattering on the spectral radiative power can be further analysed by computing the asymmetry factor G_{glob} as a function of wavelength λ at the peak location of soot volume fraction. Equation 3.7 valid for one aggregate is extended to an aggregate distribution using the global phase function Φ_{glob} (Equation 1.70) :

$$G_{glob}(\lambda) = \frac{1}{2} \int_{\pi} \Phi_{glob}(\theta, \lambda) \sin \theta \cos \theta d\theta \quad (3.13)$$

The spectral evolution of G_{glob} is reported in Figure 3.17. It can be observed that only positive values are obtained, which means that a forward-scattering behaviour predominates. For very small wavelengths, the asymmetry factor tends towards unity. The phase function becomes narrower and centered to 0° , which means that the rays, even scattered, almost do not change in direction. Hence, the scattering has a smaller impact for these wavelengths. In the region where the differences in spectral radiative power are the most important (around 1-5 μm), the asymmetry factor takes values between 0.2 and 0.6. For such values, a relatively large range of scattering angles is possible : contrary to a pure-forward phase function, the scattering allows a stronger impact on the radiative power.

The analysis is completed by computing the spectral albedo shown in Figure 3.18. It is defined for an aggregate distribution as

$$\omega_\lambda = \frac{\int_0^{+\infty} C_{sca,agg}(V)n(V)dV}{\int_0^{+\infty} [C_{sca,agg} + C_{abs,agg}](V)n(V)dV} \quad (3.14)$$

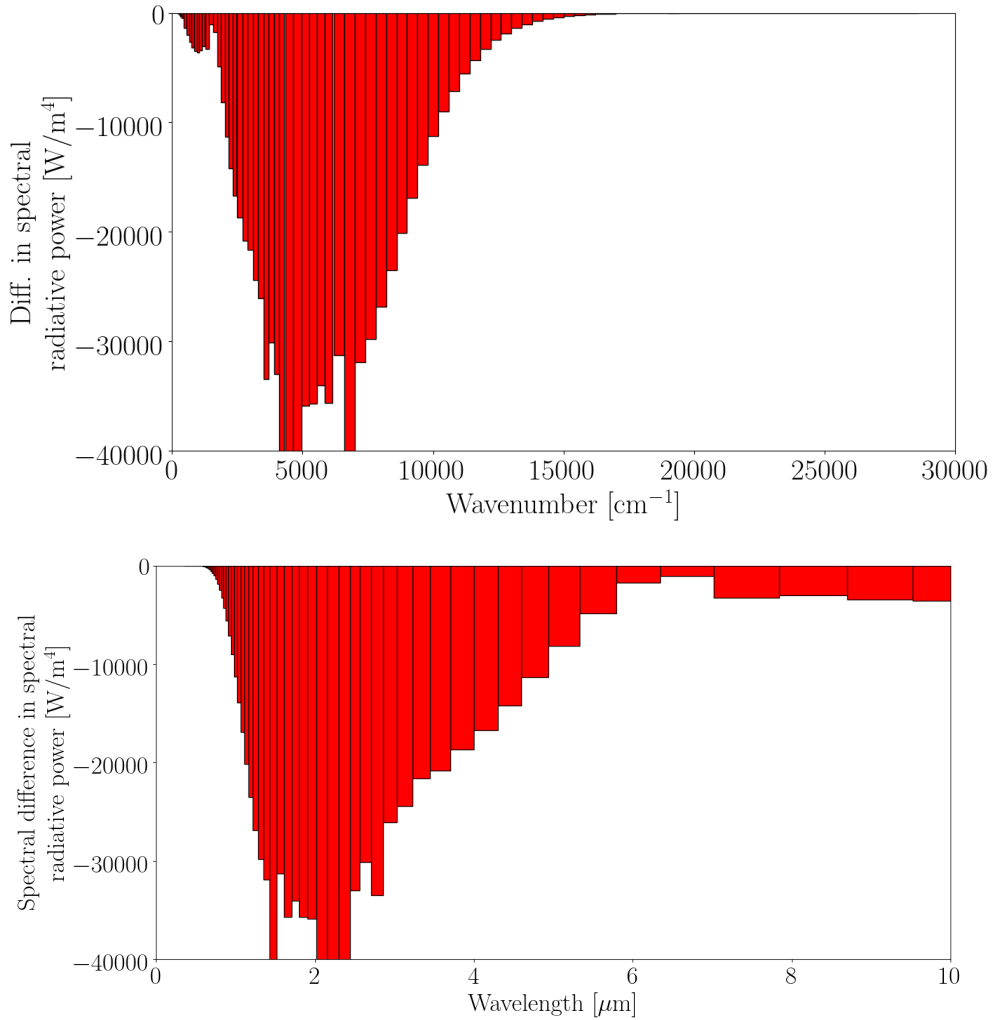


Figure 3.16: *Difference in spectral radiative power obtained at the soot volume fraction peak location in wavenumber (top) and wavelength (bottom) space.*

where $C_{sca,agg}$ and $C_{abs,agg}$ are the scattering and absorption cross-sections coefficients defined in the RDGFA model, $n(V)$ is the number density function distribution at the maximum soot volume fraction location.

The values obtained for the albedo are relatively small throughout the range of investigated wavelengths. The highest albedo values are reached for the smallest wavelengths ($< 1 \mu\text{m}$) but, due to a high asymmetry factor, the impact of scattering on the radiative power is very small. For albedos around 0.2 and small asymmetry factor (~ 0.4 around $2 \mu\text{m}$), the scattering impact is maximum, as seen in Figure 3.16. However, the small albedo limits the impact

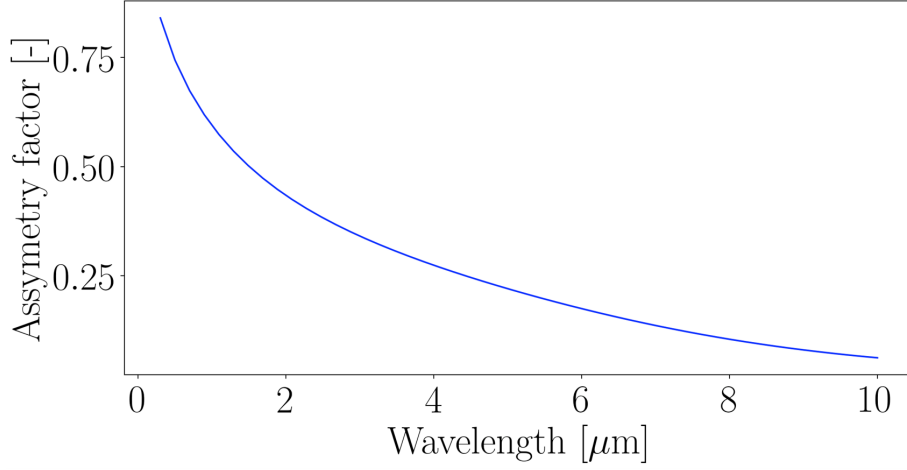


Figure 3.17: Evolution of the spectral asymmetry factor G_{glob} for the aggregate distribution at the maximum soot volume fraction location.

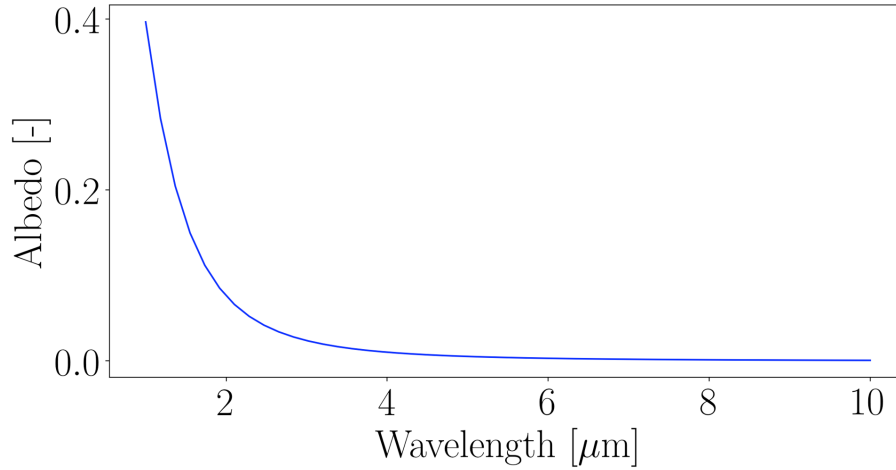


Figure 3.18: Evolution of the spectral albedo factor ω_λ for the aggregate distribution at the maximum soot volume fraction location.

of scattering at such wavelength, as seen in Fig. 3.15. The minor impact of scattering extends beyond $2 \mu\text{m}$ while the albedo becomes smaller and smaller. This is attributed to the predominant spectral range of emitted photons one can picture from Fig. 3.15. The impact of scattering is also related to the amount of spectral energy.

The combination of albedo, asymmetry factor and spectral emission is then required to understand in which extent the scattering may or may not impact the computed radiative power.

3.3 Global metrics to a priori assess the impact of scattering

The study carried out on the Sandia's turbulent jet flame has shown that the scattering impact is presently small. This validates *a-posteriori* the previous coupled calculation carried out by P. Rodrigues without soot scattering. The previous spectral analysis has shown that the scattering impact is related to several factors. The objective of this section is to derive global metrics which enables to *a-priori* assess the impact of the scattering in any CFD configuration.

The spectral albedo compares the scattering attenuation length scale $\ell_{scat} = \sigma_\lambda^{-1}$ to the total extinction length scale $\ell_{ext} = (\kappa_\lambda + \sigma_\lambda)^{-1}$, yielding $\omega_\lambda = \sigma_\lambda / (\kappa_\lambda + \sigma_\lambda)$. The quantity varies in the spectrum and the net effect of scattering also depends on the spectral range where the incoming radiative intensity is important. It is then reasonable to consider weighting the coefficients defining the albedo by a relevant intensity. Without solving the heterogeneous intensity field, it is practical to choose the local blackbody intensity to define a global metric we named **Albedo Importance**:

$$\bar{\omega} = \frac{\int_0^{+\infty} \sigma_\lambda I_{b\lambda} d\lambda}{\int_0^{+\infty} (\sigma_\lambda + \kappa_\lambda) I_{b\lambda} d\lambda} \quad (3.15)$$

At equilibrium, $\bar{\omega}$ properly accounts for the fraction of intensity attenuation or augmentation due to scattering:

$$\bar{\omega} \sim \frac{\text{Total out-scattering}}{\text{Total extinction}} \quad \text{or} \quad \frac{\text{Total in-scattering}}{\text{Total emission} + \text{in-scattering}} \quad (3.16)$$

Equation 3.15 is evaluated by integrating over each spectral band the spectral scattering and absorption coefficients that are themselves computed from the soot volume fraction and particle size distribution provided by the sectional model. This yields a metric which can be computed locally without any Monte-Carlo computations.

The albedo importance $\bar{\omega}$ is evaluated on the turbulent jet flame field obtained from the coupled simulation and is displayed in Figure 3.19. The metric values are small, which shows that scattering does not have a major impact on the studied turbulent configuration, as expected. In the RDGFA validation case studied in Sec. 3.1.3, the albedo importance is equal to 0.05 which here again shows that, in this case, a small scattering impact is observed.

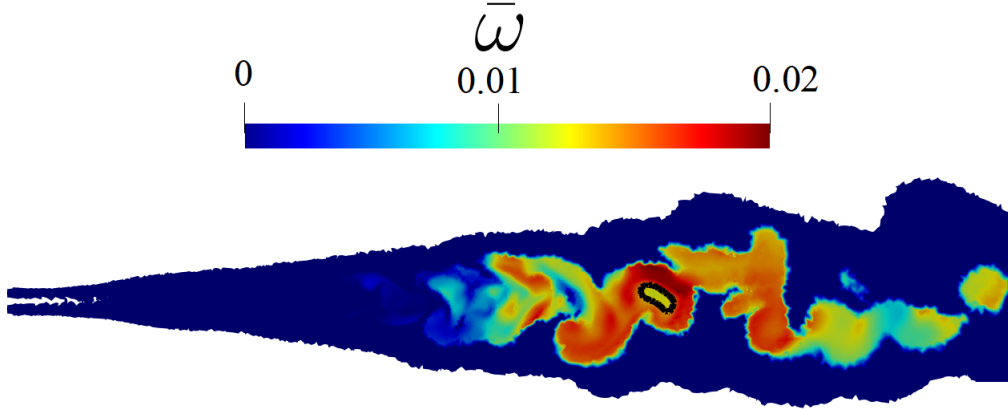


Figure 3.19: *Computed Albedo importance metric on the Sandia turbulent jet flame. The iso-contour of soot-volume fraction at 10 ppm is also displayed in black line.*

It is important to emphasize that the metric does not take into account the complex heterogeneous radiative exchanges since only the blackbody intensity at the local temperature is considered. It still gives a good order of magnitude of the impact of scattering and can be considered prior any detailed computation.

The metric can be completed with two other parameters defined in a similar way to Equation 3.15 :

- A mean transmissivity $\bar{\tau}$ based on the extinction coefficient β_λ to assess the optical thickness of the medium.
- A mean asymmetry factor \bar{G} to synthesises the detailed phase function information which can tamper scattering effects.

A mean and effective transmissivity is defined by the following equation :

$$\bar{\tau} = \frac{\int_0^{+\infty} \tau_\lambda \kappa_\lambda I_{b\lambda} d\lambda}{\int_0^{+\infty} \kappa_\lambda I_{b\lambda} d\lambda} = \frac{\int_0^{+\infty} e^{-\beta_\lambda l} \kappa_\lambda I_{b\lambda} d\lambda}{\int_0^{+\infty} \kappa_\lambda I_{b\lambda} d\lambda} \quad (3.17)$$

where τ_λ is the transmissivity at a given wavelength and at a given position, $I_b(T)$ the blackbody intensity at the local temperature. Note that the local emission $\kappa_\lambda I_{b\lambda}$ is considered to weight the spectral transmissivity to yield a mean transmissivity truly representative of the nature of thermal radiation where the medium actually participates. A characteristic length must be prescribed in order to compute τ_λ , which is chosen here equal to 0.01 m. Let us note $\bar{\tau}^{soot}$ the mean transmissivity computed only with soot radiative properties.

A mean asymmetry factor is defined as

$$\bar{G} = \frac{\int_0^{+\infty} G_{glob}(\lambda) I_{b\lambda} d\lambda}{I_b(T)} \quad (3.18)$$

where $G_{glob}(\lambda)$ is the asymmetry factor of the assembly of aggregates defined by Equation 3.13.

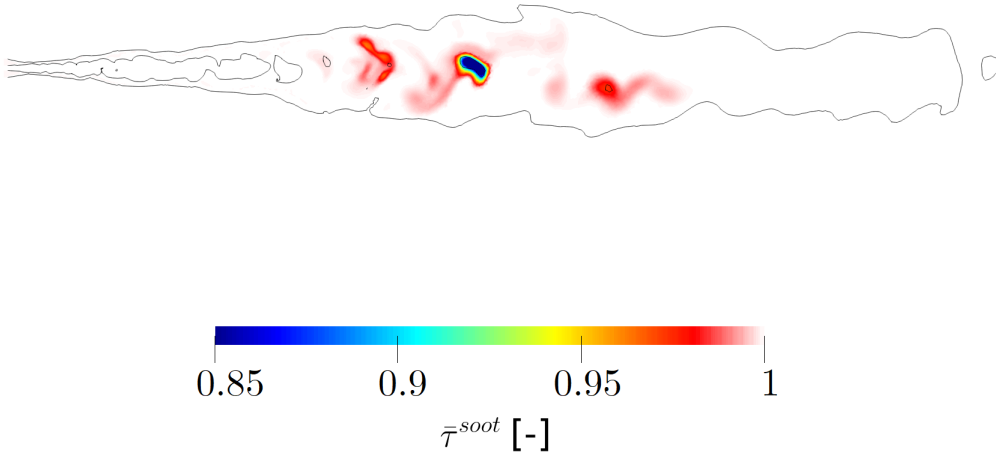


Figure 3.20: Mean soot transmissivity $\bar{\tau}^{soot}$ for the studied turbulent jet flame field. The black line corresponds to an isocontour of Temperature equals to 1000 K. The characteristic length is chosen equals to 0.01 m.

$\bar{\tau}^{soot}$ and \bar{G} are displayed in Figs. 3.20 and 3.21, respectively. The values of $\bar{\tau}^{soot}$ are high, around 0.95 except in the high f_V soot pocket where they go down to 0.85. Soot radiation in this case is then approximatively in an optically thin regime. Given the small albedo importance, the mean soot transmissivity is dominated by absorption which is then minor given $\bar{\tau}^{soot}$ values. A larger absorption optical thickness would have enhanced any increase of optical paths associated with scattering.

The mean asymmetry factor (Fig. 3.21) evolves throughout the flame : it goes from small values close to 0 to larger values around 0.4. This evolution is correlated with the size of particles which are increasing along the flame. For small particles, the phase function predicted by RDGFA tends to the symmetric pattern given by the Rayleigh model, which explains a quasi-null asymmetry factor. At higher locations, particles are bigger. For such particles, the RDGFA model predicts strong forward-scattering as previously seen (see Figure 3.1) which is

traduced by a positive asymmetry factor.

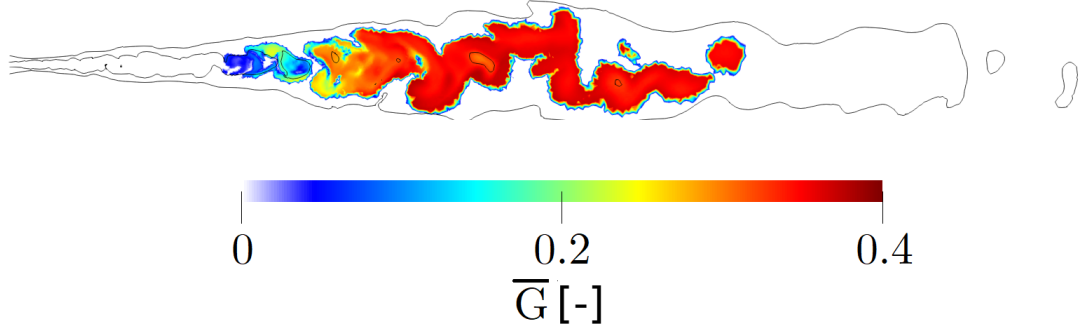


Figure 3.21: Mean asymmetry factor \bar{G} for the studied turbulent jet flame field. The black line corresponds to an isocontour of temperature at 1000 K.

The analysis of \bar{G} allows for refining the conclusion based on the albedo importance $\bar{\omega}$ that does not include any information on the phase function. It would be interesting to derive a metric that combines both information, the albedo and asymmetry factor, since they both quantify the scattering behaviour. A global length scale ℓ_g associated with the radiative flux can be introduced (see Sec. 6.3.5 in [Taine et al. \(2012\)](#)) :

$$\ell_g = \frac{1}{\kappa_\lambda + \sigma_\lambda (1 - G_{glob}(\lambda))}. \quad (3.19)$$

ℓ_g is an effective length scale that accounts for attenuation by absorption/out-scattering and augmentation by in-scattering while keeping directional information on the latter phenomenon with the appearing asymmetry factor $G_{glob}(\lambda)$. With scattering alone, the length scale is $\ell_{g,scat} = \frac{1}{\sigma_\lambda(1-G_{glob}(\lambda))}$. A spectral effective albedo is then defined as $\ell_g/\ell_{g,scat}$:

$$\omega_\lambda^{eff} = \frac{\sigma_\lambda (1 - G_{glob}(\lambda))}{\kappa_\lambda + \sigma_\lambda (1 - G_{glob}(\lambda))} = \frac{\omega_\lambda (1 - G_{glob}(\lambda))}{1 - G_{glob}(\lambda)\omega_\lambda} \quad (3.20)$$

For a symmetric phase function, $\omega_\lambda^{eff} = \omega_\lambda$ is retrieved. On the other hand, for purely forward scattering ($G_{glob}(\lambda) = 1$), the effective albedo is null, which is consistent with a zero net effect of scattering on heat transfer in this situation. Equation 3.20 is identical to the "transport" albedo obtained by the transport approximation [Dombrovsky and Baillis \(2010\)](#) where the phase function

is split into an isotropic part and forward peak. The corresponding radiative transport equation is re-expressed with a transport scattering coefficient $\sigma_\lambda^{tr} = \sigma_\lambda (1 - G_{glob}(\lambda))$ and a transport extinction coefficient $\beta_\lambda^{tr} = \beta_\lambda - \sigma_\lambda G_{glob}(\lambda)$.

Similarly to the albedo importance, we average over the spectrum and define an **Effective Albedo Importance** as

$$\bar{\omega}^{eff} = \frac{\int_0^\infty \sigma_\lambda (1 - G_{glob}(\lambda)) I_{b\lambda} d\lambda}{\int_0^\infty (\kappa_\nu + \sigma_\nu (1 - G_{glob}(\lambda))) I_{b\lambda} d\lambda} \quad (3.21)$$

At equilibrium, $\bar{\omega}^{eff}$ accounts for the following ratio:

$$\bar{\omega}^{eff} \sim \frac{\text{Total out-scattering and in-scattering}}{\text{Total extinction (absorption + out-scattering) and in-scattering}} \quad (3.22)$$

This new metric is displayed for the Sandia flame configuration in Figure 3.22. The effective albedo importance presents lower values than the initially derived albedo importance (Fig. 3.19), which is consistent with the mean asymmetry factor. $\bar{\omega}^{eff}$ allows to incorporate several pieces of spectral information ($\bar{\omega}$, $G_{glob}(\lambda)$, $I_{b\lambda}$) to better estimate the net effect of scattering on heat transfer. Again, this metric is compute locally without the need for any computation of the radiative transfer equation.

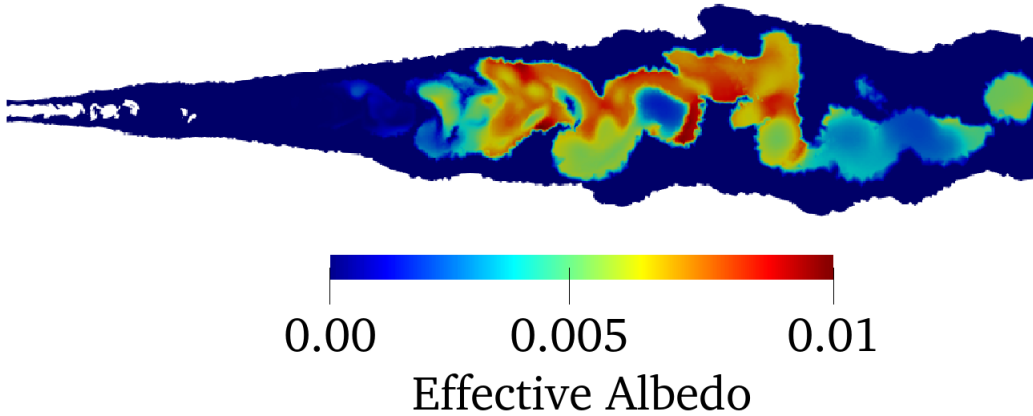


Figure 3.22: Computed effective albedo importance $\bar{\omega}^{eff}$ on the Sandia turbulent jet flame.

3.4 Conclusion

A methodology accounting accurately for scattering by soot particles has been applied to a sooted turbulent jet flame. Large-eddy simulation fields from a coupled computation, where soot scattering was neglected, are considered. Such

a hypothesis has always been retained so far in CFD studies accounting for soot radiation. However, the proposed justification relies on Rayleigh's theory, which is not valid for soot aggregates. An up-to-date description of soot scattering properties with RDG-FA theory has then allowed to quantify correctly such effects in the studied flame. The derived RQMC method estimates this contribution accurately and efficiently as it appears small. Such observation a-posteriori justifies the choice to neglect the scattering in previous calculations of this configuration.

The convergence rate analysis in this turbulent flame configuration also confirms the new Monte Carlo method's significant improvement. Indeed, at the soot volume fraction peak location, the same error can be achieved locally with approximatively 10 times fewer rays than the standard MC method. The improvement in terms of CPU time is finally evaluated using the local efficiency metric, which shows a speed-up of a factor higher than two in this study where very small error threshold is prescribed.

Finally, a metric referred as "Albedo Importance" $\bar{\omega}$, has been considered to *a-priori* assess the impact of scattering in a given configuration. This metric is able to give similar conclusions than a detailed Monte-Carlo solver. It takes into account the soot morphology and particle size distribution via the non-gray coefficient σ_λ . The Albedo Importance alone does not fully characterise the nature of radiative heat transfer and is therefore completed with two other parameters: a mean transmissivity $\bar{\tau}$, which assess the optical thickness of the medium, and a mean asymmetry factor \bar{G} , which details the scattering process in terms of the forward/backward behaviour of the particles phase function. A final metric $\bar{\omega}^{eff}$, referred as Effective Albedo importance, has been proposed to combine the asymmetry factor and the albedo information together. This allows to correct the $\bar{\omega}$ with directional awareness of the phase function.

While soot scattering effects are small in the investigated case, let us outline that RDG-FA theory is highly sensitive to the soot morphology and particle size distribution. Larger effects could then be encountered in other operating conditions. A sensitivity study is presented in the next chapter. The derived global metrics will be reported for these other investigated cases to assess the impact of soot scattering impact.

Chapter 4

Sensitivity analysis of radiative heat transfer in turbulent flames.

The Rayleigh-Debye-Gans for Fractal Aggregates theory has been implemented, validated and applied on a turbulent jet flame in Chapter 3 operating at atmospheric pressure. The objective of this chapter is to quantify the radiative exchanges due to soot and gas phases at operating conditions closer to those encountered in gas turbines. In a first part, the radiative heat transfer is investigated in a high-pressure turbulent non-premixed ethylene flame, with the same numerical set-up employed in Chapter 3 (gas and soot radiative properties). The impact of increasing soot volume fraction and pressure closer to industrial configurations is assessed by quantifying each phase contribution to the total radiative power. Exchanges between soot and gas phases are also quantified to highlight the correlation between both phases. In a second part, the impact of soot morphology description and radiative properties is quantified in the Sandia turbulent jet flame.

Contents

4.1	Introduction: Radiative heat transfer in High pressure systems	116
4.2	Radiative heat transfer analysis on the DLR FIRST burner	117
4.2.1	Impact of soot volume fraction in the DLR FIRST burner	120
4.2.2	DLR FIRST burner: Impact of Pressure	123
4.3	Impact of soot radiation modelling and morphology in the Sandia's turbulent jet flame.	125
4.3.1	Soot optical index m	126
4.3.2	Absorption coefficient formulations	126

4.3.3	Soot morphology description	127
4.3.4	Impact of absorption expression and optical index	129
4.3.5	Impact of mean soot particle size	132
4.4	Conclusion	135

4.1 Introduction: Radiative heat transfer in High pressure systems

Investigation of radiative heat transfer in high-pressure systems has received an increasing interest. In IC-engines, operating at pressures up to 200 bars, it is known that radiation can go up to 50% of the total heat losses (Borman and Nishiwaki (1987)). These engines are faced with regulations on particulate and NOx emissions and need to be accurately predicted. In Abraham and Magi (1997), the Discrete-Ordinate-Method has been used to quantify radiative heat transfer and its impact on NOx emissions: Accounting for soot radiation reduces the NOx emissions, and similar conclusions have been found in Yoshikawa and Reitz (2009). Recently, Paul et al. (2017) and Paul et al. (2019) coupled calculations are performed with more accurate models for gaseous radiation using an FSK method and considering the classic Rayleigh model for soot particles.

In parallel, global models, less costly, are gaining popularity to determine gaseous properties. However, these models were limited to gaseous phase description. Recent work (Cassol et al. (2014), He et al. (2021)) aimed at extending these models to sooty media. One of the main hypothesis of this model is that soot and gas phases are not correlated, *i.e* their interactions are small.

In gas-turbines applications, there is little data on soot particle fields. Several numerical studies (Felden et al. (2018), Teng et al. (2019)) have been carried out on the DLR FIRST combustion chamber test rig (Geigle et al. (2015)) to study a pressurized sooty flame at 3 bars with numerous experimental data available for validation. This laboratory-scale combustor exhibits several complexities representative of the turbulent reactive flow in a gas turbine.

A previous study, carried out by Rodrigues (2018) has shown that in the DLR configuration, the impact of soot particles in radiative heat transfer is small, as displayed Figure 4.1. In these instantaneous snapshots, it can be observed that soot particles contribute locally up to 10 % of the radiative power. One of the factor that explains such a behaviour is the low soot volume fraction encountered in this configuration.

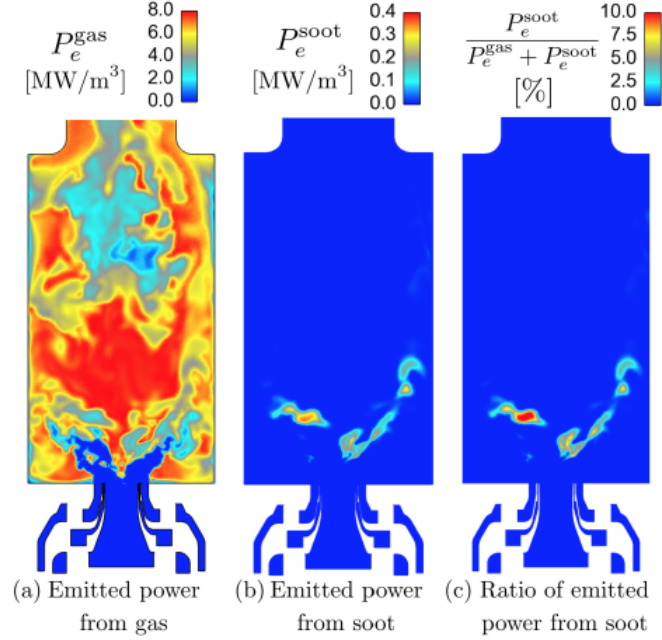


Figure 4.1: Comparison between instantaneous emitted radiative powers from gas and soot phases, extracted from P. Rodrigues PhD thesis [Rodrigues \(2018\)](#).

Assessing the impact of detailed soot and gaseous radiative properties at a realistic operating pressure point for gas turbines is crucial to understand how radiative heat transfer takes place in such industrial engines.

It will then be interesting to increase the soot volume fraction/pressure up to realistic levels encountered in gas turbines. This study is addressed in Sections 4.2.1 and 4.2.2.

4.2 Radiative heat transfer analysis on the DLR FIRST burner

The studied configuration is the FIRST burner experimentally investigated at DLR ([Geigle et al. \(2015\)](#)). The burner geometry is displayed Figure 4.2. The gaseous ethylene is injected between two concentric swirling air flows into the combustor chamber with a height of 120 mm. Secondary air injection is located at a height of 80 mm. The chamber operates at 3 bars with a global power of 38 kW.

The considered instantaneous solution is extracted from coupled calculation with conjugate and radiative heat transfer ([Rodrigues \(2018\)](#)). Radiative boundary conditions from [Rodrigues et al. \(2019\)](#), which account for the quartz wall semi-transparency, are prescribed.

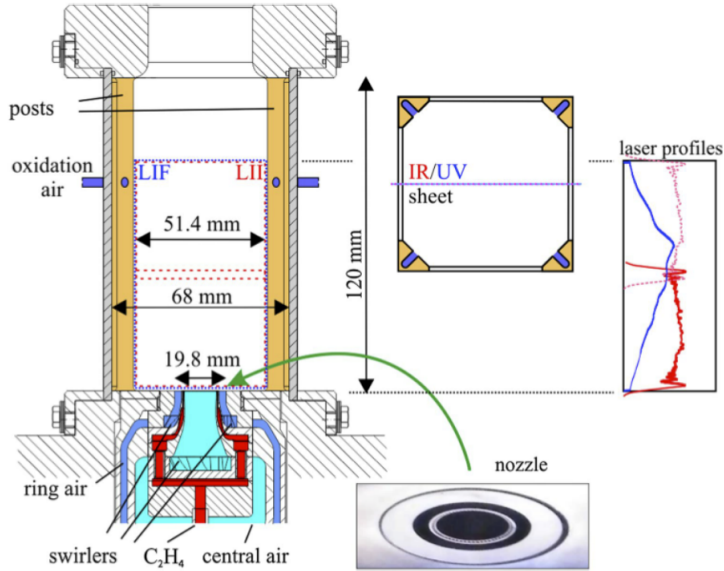


Figure 4.2: Burner geometry of the DLR configuration (from Geigle et al. (2015)).

In order to compute the radiative properties of gas and soot particles, fields of molar fraction of CO_2 and H_2O , temperature, pressure, soot volume fraction f_V and particle size distribution $n(V)$ are extracted.

The instantaneous solution used for the study (Temperature, soot volume fraction, and radiative power) are presented in Figure 4.3. In the zone between the primary and secondary injections, hot gases are reaching high temperatures, leading to high emitted power. Due to the secondary injection, the burnt gases are cooled down and can reabsorb energy emitted from the hot gases downstream: this explains the positive radiative power observed in this region.

Figure 4.5 presents the spectrum of the volume-integrated emitted and absorbed power. The spectrum can be divided into two parts: for wavenumbers lower than 10000 cm^{-1} , a highly dynamic spectrum dominated by hot burnt gases radiation, and for wavenumbers higher than 10000 cm^{-1} , a continuous spectrum dominated by soot radiation. The medium at the wavenumbers of the highest peak can be considered as optically thick since almost 90% of the emitted power is reabsorbed. Such behavior shows the inadequacy of the optically thin assumption for gases.

Concerning soot radiation, due to the low level of soot volume fraction (f_V), the emitted power due to soot is small compared to hot burnt gases. A comparison of absorbed and emitted radiative power also shows that soot radiation can be considered as optically thin. This point is also shown Figure 4.4 where the soot

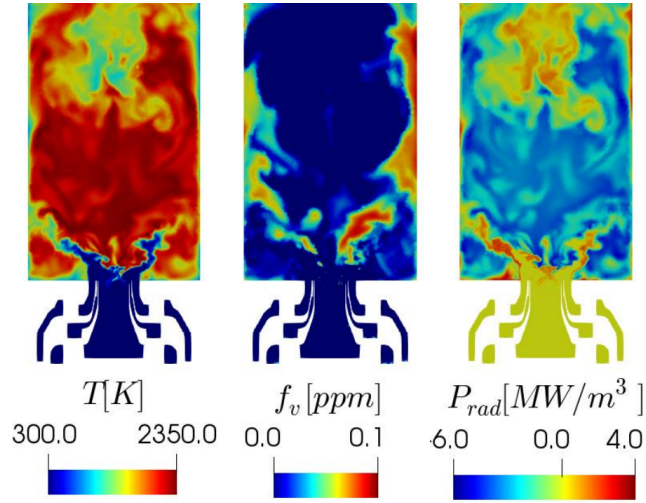


Figure 4.3: *Temperature, soot volume fraction and radiative power reference fields in the DLR First Burner.*

contribution to the mean transmissivity $\bar{\tau}^{soot}$ is displayed : values close to 1 are obtained which confirms the optically thin behaviour.

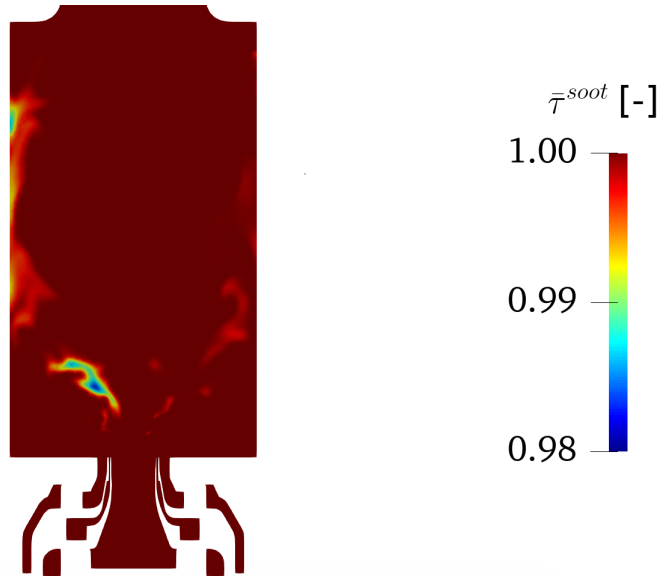


Figure 4.4: *Soot contribution to the mean transmissivity $\bar{\tau}^{soot}$ calculated using soot optical properties. The reference length is here chosen equals to 0.01 m. See Chapter 3 for more details on this metric.*

Computations with and without scattering not presented here also show that the scattering effect is negligible in this configuration. The metric derived in

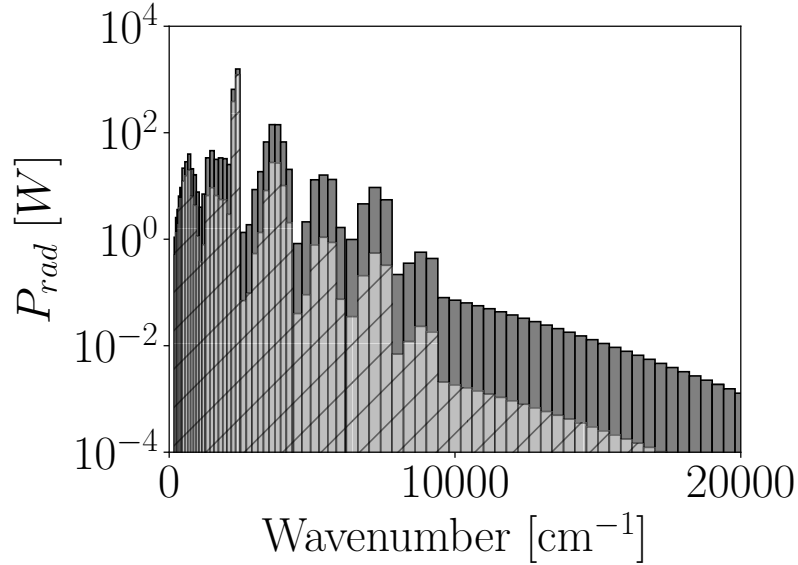


Figure 4.5: *Spectral emitted and absorbed radiative power integrated over the volume of the combustion chamber.*

Chapter 3, see Equation 3.15, has been computed on the DLR configuration and displayed Figure 4.6. An iso-contour of the 17th soot section is also displayed. In the present calculation, the soot volume distribution is divided in 25 sections, therefore, the 17th section corresponds to relatively big particles.

It can be observed that very low values are reached showing that the scattering is negligible in this configuration. The maximum location of the metric is localized where the biggest particles are located. Therefore, not only the size but also the number of particles is taken into account in this metric. Here again, the metric is able to a-priori assess the low impact of scattering in this configuration.

4.2.1 Impact of soot volume fraction in the DLR FIRST burner

Due to the relatively low values of soot volume fraction in the DLR FIRST burner, soot radiation represents only a small contribution to the total radiative power, which is not representative of realistic industrial cases.

In order to investigate the impact of soot volume fraction on radiative heat transfer, f_V is increased to more realistic levels found in more sooty flames, *i.e.* by a factor 10, 100 and 1000. The corresponding maximum f_V instantaneous level is 1 ppm, 10 ppm and 100 ppm respectively.

In such conditions, soot emission will tend to have the same order of magnitude as gaseous emissions enhancing soot-gas interactions. The spectral emitted and

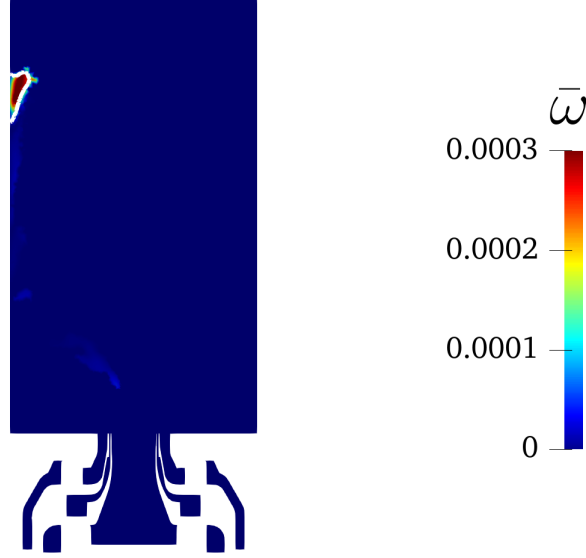


Figure 4.6: *Computed Scattering Importance metric on the DLR FIRST Combustor chamber. The contour in white represents the zone where the NDF of the 17th of the sectional model is maximum.*

absorbed radiative powers computed for the three cases is shown Figure 4.7. When comparing Figures 4.5 and 4.7, it can be observed that the magnitudes of the bands for the highest wavenumbers has increased of several order of magnitude, depending the case. As shown in [Rodrigues \(2018\)](#), these continuous band correspond to soot contribution to the radiative power. Between 7500 and 10000 cm^{-1} , the increase of soot volume fraction has also modified the radiative power. The peak structure previously observed at these locations (due to the participating gases) is smoothen and becomes more continuous. The interaction between gas and soot particles has therefore been impacted, especially for the cases $f_V \times 1000$.

To quantify these observations, four additional Monte-Carlo simulations have been carried out, one considering only gas emission and gas absorption (**GE GA**), one considering only gas emission and soot absorption (**GES A**), one considering only soot emission and gas absorption (**SE GA**) and one considering only soot emission and absorption (**SE SA**). In the **Total** case, soot and gas are both taken into account. As the role of soot particles and $\text{CO}_2, \text{H}_2\text{O}$ are not symmetric in **SE GA** and **GES A**, the ERM is not suitable and a classic backward Monte-Carlo method is used.

Table 4.1 presents the different contributions of gas and soot radiation for the reference and the cases where f_V is increased by a factor 10, 100 and 1000.

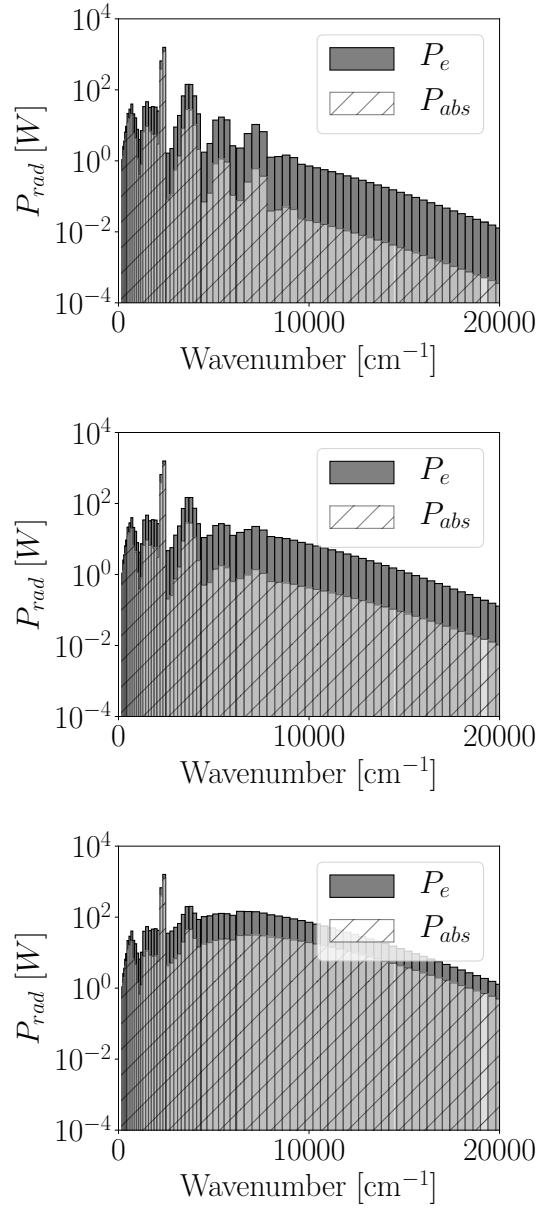


Figure 4.7: Spectral emitted and absorbed radiative power integrated over the volume of the combustion chamber, at $P = 3$ bars, and with a soot volume fraction multiplied by 10, 100 and 1000.

As seen in the first column of Table 4.1, the increase in soot volume fraction by a factor 10 has a small impact on the total emitted and absorbed radiative power. Indeed, the total emission increases only by 3 %, and absorption is barely affected. When increasing f_V by a factor 100, the total emission increases by 10% and absorption by 2%. For the case $f_V \times 1000$, the total emission is

	Case	Total	GEGA	GESA	SESA	SEGA
X1	P_{emit} [W]	3,053	3,050	3,050	3.1	3.1
	P_{abs} [W]	2,200	2,200	0.2	0.02	0.03
	P^R [W]	-853	-850	-3,050	-3.08	-3.07
X10	P_{emit} [W]	3,081	3,050	3,050	31	31
	P_{abs} [W]	2,201	2,200	1	0.2	0.6
	P^R [W]	-880	-850	-3,049	-30.8	-30.4
X100	P_{emit} [W]	3,360	3,050	3,050	310	310
	P_{abs} [W]	2,243	2,200	11	2	30
	P^R [W]	-1,117	-850	-3,049	-308	-280
X1000	P_{emit} [W]	6,150	3,050	3,050	3,100	3,100
	P_{abs} [W]	2,797	2,200	105	150	342
	P^R [W]	-3,353	-850	-2,945	-2,950	-2,758

Table 4.1: Gaseous and soot contributions of emitted and asorbed radiative power for the reference field and the f_V increased field.

increased by 100%. At these levels, soot emission reaches the same level as the gases. However, a small fraction (around 5%) of the soot emission is reabsorbed by soot (**SESA** case), while around 78 % of the radiative power emitted by the gaseous phase is reabsorbed (**GEGA**). Therefore, soot radiation has a major impact on the net radiative power obtained for the case $f_V \times 1000$.

In **GESA** and **SESA** simulations, only soot are supposed to absorb. In both cases, the absorbed power is small, which confirms that optically thin assumption for soot is valid. Finally, on the **SEGA** case, as the soot volume fraction increases, the gaseous phase absorbs more and more emitted power from the solid phase, but this part remains small. In other words, the interaction between soot and gas phases is still small. Finally, **SEGA** and **GESA** cases show that the interaction between soot and gaseous phases is small.

4.2.2 DLR FIRST burner: Impact of Pressure

In this section, the pressure field is artificially enhanced to 30 bars while keeping other fields fixed to estimate high-pressure radiative fields with a corresponding cK-database at 30 bars (values reached during the take-off phase).

The same analysis as in the previous section is carried out by either taking into account soot radiation, gas radiation ,or both for a different level of soot volume fraction: the reference f_V , $f_V \times 10$, $f_V \times 100$ and $f_V \times 1000$.

The effect of the increasing pressure can be assessed by looking again at the emitted and absorbed spectra for the reference f_V field displayed in Figure 4.8. Therefore, Figures 4.5 and 4.8 only differs by the pressure considered.

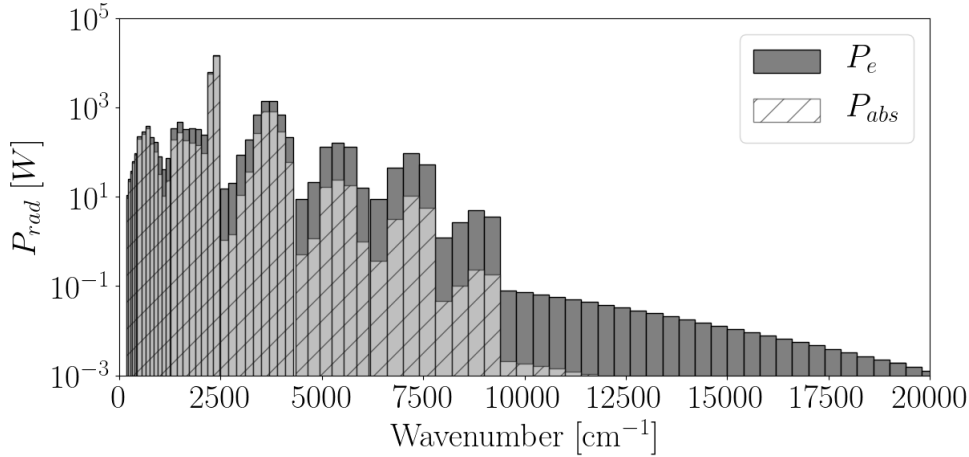


Figure 4.8: Spectral emitted and absorbed radiative power integrated over the volume of the combustion chamber at $P = 30$ bars, obtained with the reference f_V field.

It can be observed that the right part of the spectrum, corresponding to soot contribution is not modified : this is due to the fact that the soot radiative properties do not depend explicitly on the pressure (changes in pressure are artificially emulated by multiplying the soot volume fraction later on in this section). For the gaseous phase, both emitted and absorbed power have increased. It is important to notice that the absorptivity (the capacity of a gas to absorb energy) has increased, especially for the bands around 2500 cm^{-1} , corresponding to CO_2 contribution, where almost all the emitted power is re-absorbed.

Gas and soot contributions to the obtained radiative power is assessed by performing the 4 additional Monte-Carlo simulations (**GEGA**, **GESA**, **SESA** and **SEGA**) presented earlier. The results are reported in Table 4.2.

A strong increase in gaseous emission and absorption compared to the 3 bar computation is expected and observed by looking at the total and **GEGA** cases. Gaseous phase reabsorption goes from 78% at 3 bar to 85% at 30 bar. The **SESA** case, which only involves soot radiation, is identical to the 3-bar case since the absorption of soot particles does not depend on pressure.

As observed in the column **GESA**, the interaction between gas-emission and soot absorption is still negligible for all the investigated cases (for $f_V \times 1000$, less than 1% of the gas emission is reabsorbed by soot).

However, on the **SEGA** case, a notable increase in soot-gas interaction is observed compared to the reference case at 3 bar: almost 60% of the emitted power by soot particles is reabsorbed by the gaseous phase for the $f_V \times 100$ case. This amount goes up to 70% for the $f_V \times 1000$ case, while for the refer-

	Case	Total	GEGA	GESA	SESA	SEGA
X1	P_{emit} [W]	29,643	29,640	29,640	3.1	3.1
	P_{abs} [W]	24,548	24,548	0.2	0.02	0.3
	P^R [W]	-5,095	-5,092	-29,640	-3.08	-2.8
X10	P_{emit} [W]	29,671	29,640	29,640	31	31
	P_{abs} [W]	24,562	24,548	3	0.2	11
	P^R [W]	-5,109	-5,092	-29,637	-30.8	-20
X100	P_{emit} [W]	29,950	29,640	29,640	310	310
	P_{abs} [W]	24,774	24,548	26	2	198
	P^R [W]	-5,176	-5,092	-29,614	-308	-112
X1000	P_{emit} [W]	32,740	29,640	29,640	3,100	3,100
	P_{abs} [W]	27,028	24,548	280	150	2150
	P^R [W]	-5,712	-5,092	-29,360	-2,950	-950

Table 4.2: Gaseous and soot contributions of emitted and absorbed radiative power for the reference field and the f_V increased field.

ence case, it represents only 10%. Pressure has then increased the absorptivity of hot burnt gases, which has lead to enhanced interactions between the soot phase and the gaseous phase.

This shows that global models, which assume that the interactions between soot and gas phases are small, might not be adapted for high pressurized systems. Finally, the relative impact of soot radiation on the net radiative power has decreased because of the enhanced gaseous contribution at higher pressure for fixed fields of soot volume fraction. For both pressure cases, the gas-soot interactions have a small net impact on the volume-integrated fields.

Obviously, experimental data values for high-pressurized systems are required to draw definitive conclusions to this *a-posteriori* analysis. However, it shows the capability of Monte-Carlo methods to isolate and quantify the contribution of the different phases and emphasize their correlations.

4.3 Impact of soot radiation modelling and morphology in the Sandia's turbulent jet flame.

The same reference fields as the one considered in Chapter 3 are considered for the sooted Sandia jet flame. The radiative properties presented also Chapter 3 will be the reference numerical set-up. The impact on radiative heat transfer of three parameters is investigated in this section :

- The soot optical index m formulation
- The absorption coefficient formulation
- The soot morphology

These three parameters are presented and detailed in the following Sections

before carrying out the study on the turbulent jet flame.

4.3.1 Soot optical index m

The optical properties of soot particles are characterized by its complex index of refraction m . In this work, a spectral formulation $m(\lambda) = n(\lambda) - ik(\lambda)$, whose parameters are expressed as polynomials of the wavelength λ up to 20 μm , is used (Chang and Charalampopoulos (1990)). In Figure 4.9, the spectral formulation is compared with a classic model from the literature, which assumes a constant complex index (Smyth and Shaddix (1996)). As shown in Figure 4.9, a strong disparity exists between the two formulations. In spite of uncertainties, the spectral formulation is expected to be more accurate since it captures the spectral evolution of soot optical properties.

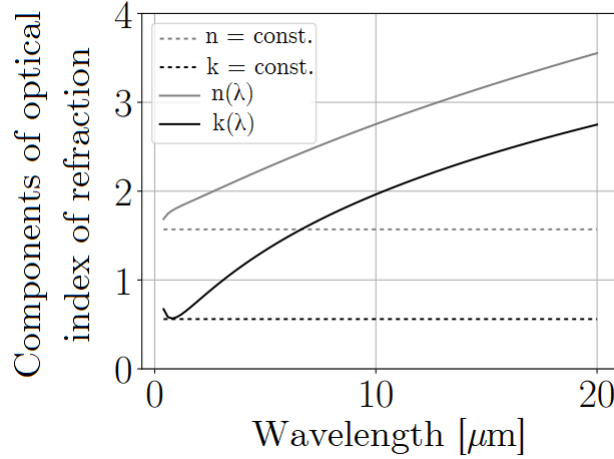


Figure 4.9: Evolution of optical index component for soot particles with the wavelength.

4.3.2 Absorption coefficient formulations

The RDG-FA model, which is considered as the reference, writes the absorption coefficient $\kappa_{\nu}^{\text{soot}}$ as :

$$\kappa_{\nu}^{\text{soot}} = \int_0^{+\infty} C_{\text{abs,agg}}(V)n(V) dV = C_0 f_{\text{V}} \nu \quad (4.1)$$

where $C_{\text{abs,agg}}$ is the absorption cross-section coefficient of the aggregate, V the volume, ν is the wavenumber (in m^{-1}), $n(V)$, the particle number density in m^{-6} , f_{V} is the soot volume fraction and C_0 is given by the complex index of refraction:

$$C_0 = \frac{36\pi nk}{(n^2 - k^2 + 2)^2 + 4n^2 k^2} \quad (4.2)$$

It is worthwhile to notice that the soot absorption coefficient of an aggregate given by RDG-FA is equivalent to the one obtained from Rayleigh's theory : the morphology of the particle does not appear explicitly on κ_{ν}^{soot} .

In the literature, simplified models assuming that soot particles can be considered as gray (*i.e* their radiative properties does not depend on the wavelength) with absorption coefficients calculated using mean values averaged all over the wavelength can be found (Widmann (2003)). In order to characterize the impact of a spectral dependency of the soot absorption coefficient, a gray model is considered. In the case of a constant index m , the Planck mean soot absorption coefficient is (Modest (2003c)) :

$$\kappa_P^{mean} = \frac{\int_0^{+\infty} \kappa_{\nu,soot} I_{\nu}^{\circ}(T) d\nu}{\int_0^{+\infty} I_{\nu}^{\circ}(T) d\nu} = 3.83 \frac{C_0 f_{\nu} T}{C_2} \quad (4.3)$$

with $C_2 = 1.4388 \text{ cm.K}$ and T the temperature.

These two formulations are therefore considered in this study.

4.3.3 Soot morphology description

The characterization of soot radiative properties from their morphology has shown an increasing interest (Joo and Gülder (2011), Amin et al. (2019), Steinmetz et al. (2016), Gigone et al. (2019)) since these properties have an impact on the radiative transfer properties (Liu et al. (2013), Köylü and Faeth (1993), Köylü et al. (1995)) but also on soot growth mechanisms. Soot particles are known to form aggregates of n_P primary particles with quasi constant primary particle diameter d_P . In practice, such a complex geometry is considered as a fractal structure. Although their shape varies irregularly, empirical laws have been proposed to describe these clusters. The law proposed by Samson et al. (1987) expresses the relationship between n_P and d_P as $n_P = k_f \left(\frac{2R_g}{d_P} \right)^{D_f}$ with k_f and D_f the fractal parameters introduced in Chapter 1.

In this work, soot particles are not always considered as spherical, but its morphology depends on their size. Beyond a given volume, a soot particle is considered as an aggregate characterized by a number of primary spherical particles n_p of diameter d_p . n_p and d_p are given by the aggregate surface S and volume V by : $n_p = \frac{S^3}{36\pi V^2}$ and $d_p = \frac{6V}{S}$.

A first surface-volume relationship (**s-v Model 1**) has been obtained by fitting numerical results obtained on 1D laminar premixed ethylene-flame (Mueller et al. (2009), Salenbauch et al. (2015)), as shown in Figure 4.10.

This surface-volume relationship is the one considered in Chapter 3 yielding to Equations 3.4.

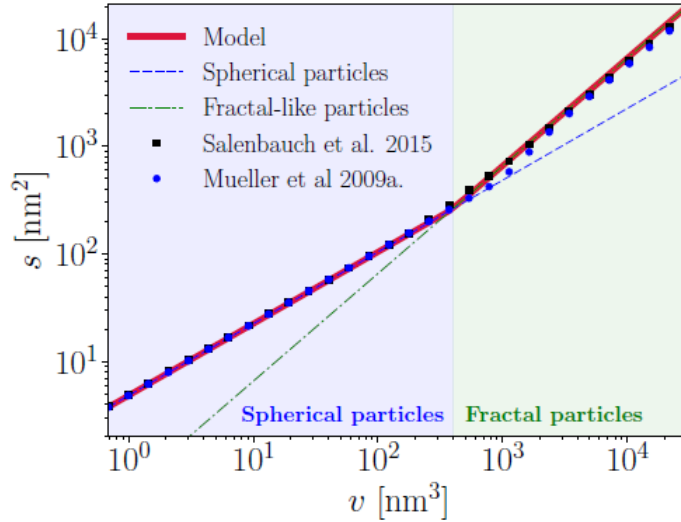


Figure 4.10: Derivation of the surface-volume model (SV-1) based on numerical results obtained on 1D laminar premixed flames by Mueller et al. (2009), Salenbauch et al. (2015). Extracted from Rodrigues (2018)

The n_p and d_p results of the model are presented in Figure 4.11 in dashed lines for different size of the soot particles. For large aggregates, n_p reach non-physical values, highlighting an incorrect behavior of the formulation. In fact, the prescribed surface-volume relationship limits d_p to 10 nm although recent work on laminar flames showed that d_p can go up to 80 nm (Steinmetz et al. (2016), Amin and Roberts (2017)).

A second formulation (**s-v Model 2**) for d_p and n_p is then proposed and shown in Figure 4.11 in plain lines: a linear extrapolation of d_p from 10 nm to 80 nm is performed, n_p is then reconstructed knowing the diameter and the volume of the aggregate. Comparison with experimental n_p obtained for various pressures shows a fair improvement using the second formulation. Both ad-hoc formulations are considered later.

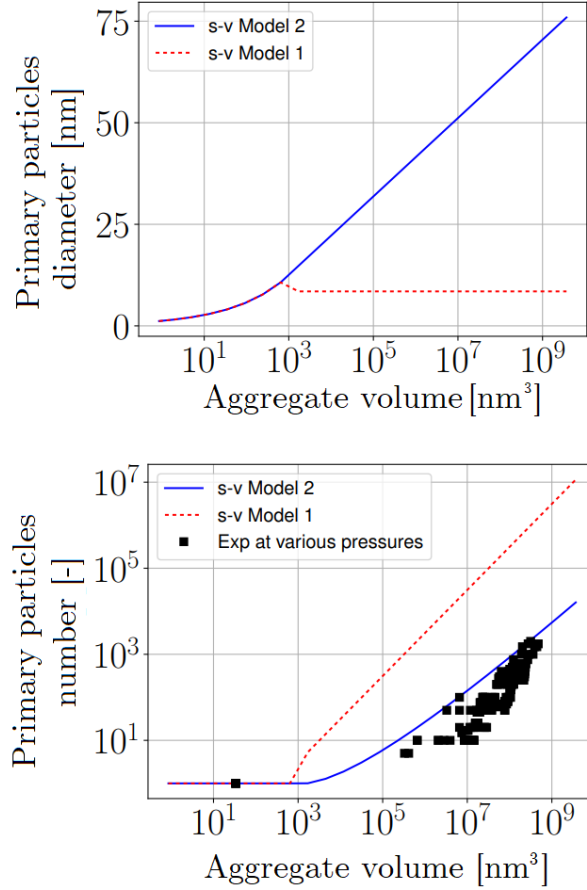


Figure 4.11: Primary particle diameter (left) and number of primary particles per aggregate (right) obtained for two different surface-volume relationships. Experimental data at different pressures are also provided in black squares.

4.3.4 Impact of absorption expression and optical index

An analysis of radiative heat transfer without scattering in Sandia’s jet flame has already been performed in [Rodrigues et al. \(2019\)](#). In this configuration, soot radiation accounts for 20% of the total radiative power and can be significant locally. A constant optical index m was retained, and a Rayleigh model with neglected scattering was considered. The objective of this section is twofold: first, assessing the impact of soot absorption modeling (spectral versus gray formulation) on the radiative power ; then, investigate the effect of the optical index formulation.

The accuracy of the Monte-Carlo simulation can be controlled locally: the relative one is set to 0.1%, and the absolute one is set to 0.1% of the maximum value of the mean radiative power. The accuracy is chosen to be consistent with the previous calculations carried out on Chapter 3 accounting for scattering

effects.

Four different soot radiative models are considered:

- . **MEAN_C**: a gray assumption where κ_P^{mean} is calculated with constant optical index, and no scattering,
- . **ABS_C**: κ_ν^{soot} calculated with a constant optical index noted, and no scattering,
- . **ABS_S**: κ_ν^{soot} calculated with a spectral optical index denoted, and no scattering,
- . **RDGFA_S**: κ_ν^{soot} and σ_ν^{soot} calculated with a spectral optical index, which is the one presented Chapter 3.

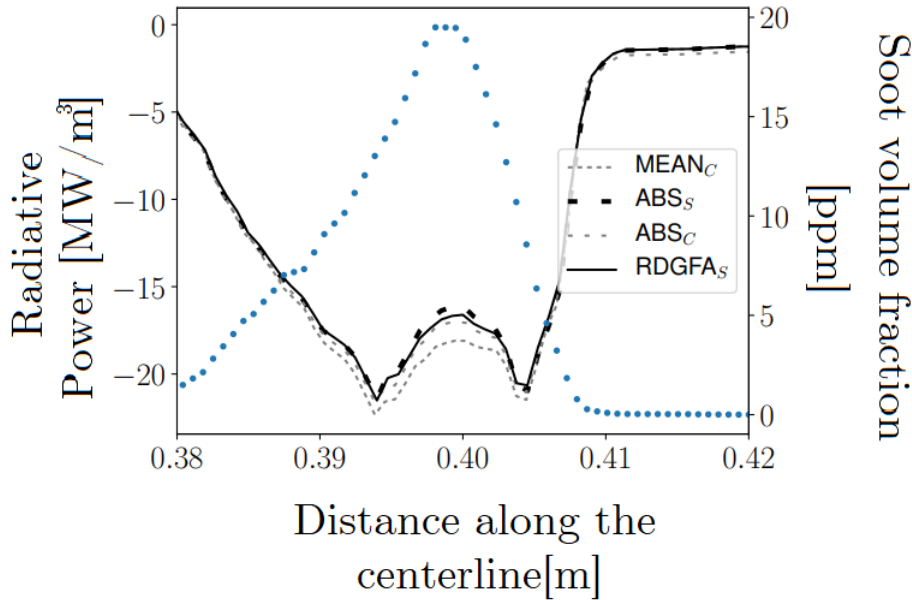


Figure 4.12: Radiative power along the centerline of Sandia turbulent jet flame for the 4 considered soot radiative models. Soot volume fraction is represented with dot lines.

The radiative power along the centerline for the four models is presented in Figure 4.12. Qualitatively, the models give similar results. At the location of the peak in soot volume fraction, a slight decrease in radiative power magnitude is observed: this is due to the corresponding lower temperature at this position coming from the considered fields issued from coupled simulations. The locally reduced temperature due to soot radiation diminishes then the magnitude of heat losses. It can be observed, for this instantaneous solution, that the comparable models **ABS_C** and **MEAN_C** are similar with a maximum difference of 10% in the computed radiative power is observed. This is due to the present soot radiation, which can be considered mainly optically thin, as already seen in Chapter 3, see Figure 3.20. This makes a gray soot model reasonable. However, increasing the level of soot by 10 enhances the difference between **ABS_C**

and \mathbf{MEAN}_C which then differ by 40 %. The gray model is not valid as soon as soot absorption is not small.

The comparison between \mathbf{ABS}_C and \mathbf{ABS}_S shows a small difference. This can be explained by the fact that both formulations are, in the range of wavelengths of interest (lower than 10 μm), very similar.

It can be observed that the case accounting for scattering (\mathbf{RDGFA}_S) tend to decrease the radiative power comparing to the calculation without scattering \mathbf{ABS}_C .

In order to quantify more precisely the impact of scattering, the difference in radiative power between \mathbf{ABS}_S and \mathbf{RDGFA}_S cases is displayed in Figure 4.13 for the two soot morphology models introduced Section 4.3.3. As scattering changes only the direction of the propagating ray, the emitted power at a node i is not modified between the two computations. Hence, the difference of radiative power can be interpreted directly as a difference in absorbed power, since $P^R = P_{abs} - P_{emit}$.

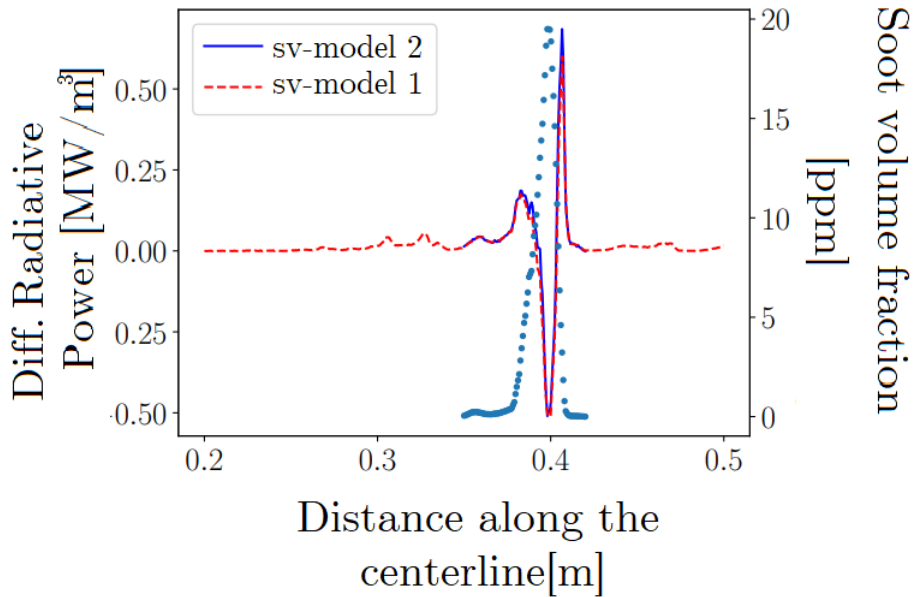


Figure 4.13: *Difference of radiative power with and without scattering along the centerline for Sandia jet flame with the two morphological models presented Section 4.3.3. Soot volume fraction is represented with dot lines.*

The two morphological models give very similar results for this case: this is attributed to the fact that most of the particles are localized on the smallest volume sections where both models are identical. The impact of the biggest sections on the scattering is here negligible.

The objective of the next section is then to enhance scattering effect by increas-

ing the soot particle size.

4.3.5 Impact of mean soot particle size

In this section, the impact of the aggregate size on the Sandia jet flame is studied. Soot volume fraction is nonetheless left unchanged: the absorption coefficient of soot particles is the same. Only scattering effects are modified by prescribing a different number density function (NDF) for the same f_V .

An arithmetic mean diameter of soot particles is calculated at the maximum soot volume fraction location, which gives a value of 3 nm. In order to increase this diameter to approximately 50 nm, a modification of the volume discretization in the sectional model is performed. On the original sectional mesh, the volume space is discretized as a geometrical progression (Rodrigues et al. (2018)). The geometrical progression is replaced by the following law:

$$v_i^{max} = v_1^{max} \left(\frac{v^{MAX}}{v_1^{max}} \right)^{\left(\alpha \frac{i-1}{N_{sect}-1} \right)} \quad (4.4)$$

with $i \in \llbracket 2, N_{sect} - 1 \rrbracket$, v_1^{max} and v^{MAX} the maximum volume of the first section and the biggest volume of a soot particle, respectively. α is a dilatation factor chosen to shift the number density function (NDF) in order to obtain the target mean diameter. The NDF is finally uniformly scaled to retrieve the same total soot volume fraction. The original and modified number density function are displayed in Figure 4.14 with their corresponding mean equivalent diameters. Only the second surface-volume model (**s-v model 2**) is considered since the original one yields unreasonable aggregates for the modified soot particle size distribution.

The mean aggregate diameter here is an equivalent diameter, computed from the volume of the aggregate. The original NDF presents a bimodal shape at this location. The first mode corresponds to the smallest nucleated particles. The second mode corresponds to the larger particles due to the competition of surface growth, coagulation, condensation, and oxidation processes. Hence, the applied shift is equivalent to consider a greater impact of the three previous mechanisms compared to the oxidation phenomenon, to achieve the same local soot volume fraction, but with larger aggregates. This transformation is applied locally to the full 3D field.

The radiative power along the centerline for the two cases (original and modified NDF) is presented in Figure 4.15. With the modified NDF, the radiative power is halved at the maximum soot volume fraction location. For the same f_V , the increase in optical thickness due to the larger aggregates leads to a significant effect of soot scattering with the modified NDF. It is then important

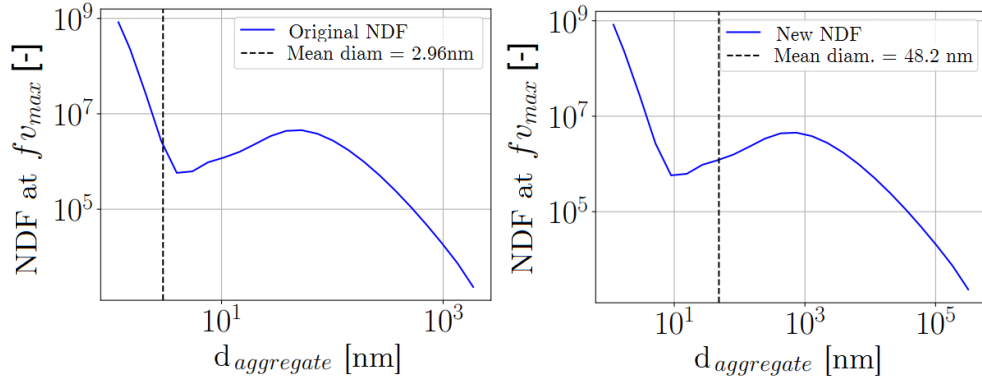


Figure 4.14: Number density function at maximum soot volume fraction location. Left : reference. Right : after increasing the particle size.

to note that, without changing the soot volume fraction, the morphology of soot aggregates and their size distribution can, therefore, strongly impact the radiative fields. Depending the soot particle size, the scattering effect might not be negligible. Modeling not only f_V but also this detail information appears then necessary to correctly estimate the scattering contribution in luminous radiation.

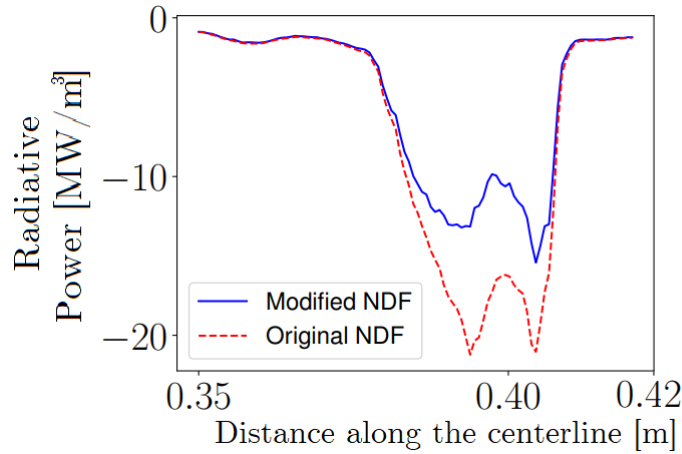


Figure 4.15: Impact along the centerline of the soot mean particle size on the radiative power with SV-model 2.

This effect can also be interpreted using the metrics developed in Chapter 3 : the fields of effective albedo importance $\bar{\omega}^{eff}$, soot mean transmissivity $\bar{\tau}^{soot}$ and mean asymmetry factor \bar{G} are reported in Figures 4.16, 4.17 and 4.18, respectively.

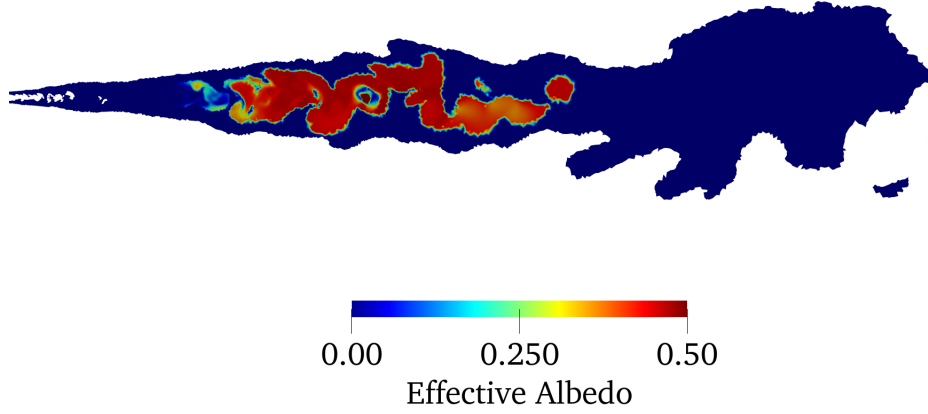


Figure 4.16: Mean effective albedo importance $\bar{\omega}^{eff}$ for the studied turbulent jet flame field with increased particle size.

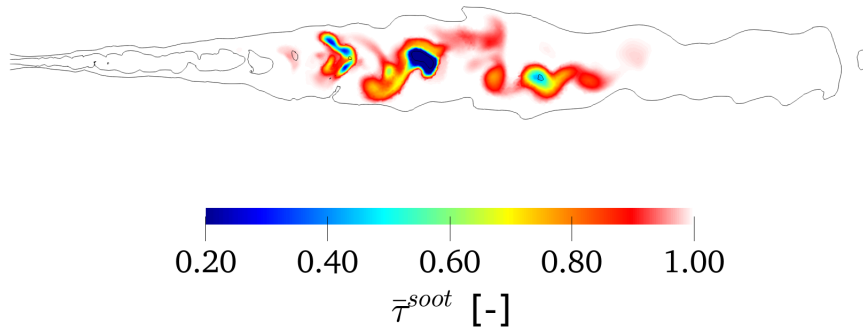


Figure 4.17: Mean soot transmissivity $\bar{\tau}^{soot}$ for the studied turbulent jet flame field with increased particle size. The black line corresponds to an isocontour of Temperature equals to 1000 K. The characteristic length is chosen equals to 0.01 m.

Since soot particles are bigger, a strong forward-scattering is observed, which corresponds to higher values of \bar{G} . The increase in size also yields to high values of the effective albedo $\bar{\omega}^{eff}$. Despite the pronounced forward phase function, this indicates that the scattering impact must be important, which has been confirmed in Fig. 4.15. Finally, the scattering enhancement increases the optical thickness of the domain (corresponding to a diminution of $\bar{\tau}^{soot}$).

The evolution of these three metrics ($\bar{\omega}^{eff}$, $\bar{\tau}^{soot}$, \bar{G}) compared to the ones reported in Chapter 3 (see Figures 3.19, 3.20, 3.21) confirms the significant magnitude of scattering in the present configuration, which outline their role of a-priori indicators of the scattering impact.

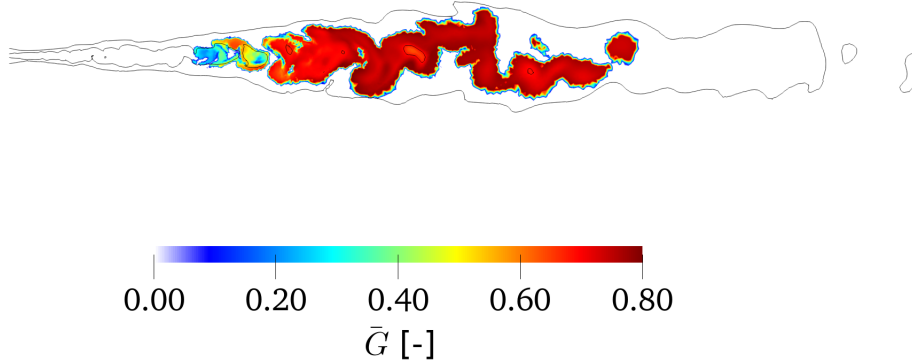


Figure 4.18: Mean asymmetry factor \bar{G} for the studied turbulent jet flame field with increased particle size. The black line corresponds to an isocontour of Temperature equals to 1000 K.

4.4 Conclusion

Computations with detailed radiative gas and soot properties have been carried out on two turbulent flames. Gas radiation is described by the cK narrow band model, while luminous radiation from soot particles is modeled by the RDG-FA theory. Fields from large-eddy simulations based on a sectional method are used in the analysis as a reference. Several effects on radiative heat transfer have been investigated with an accurate Monte-Carlo solver: soot volume fraction, pressure, soot optical properties and particle size.

The increase of the soot volume fraction and pressure in the DLR FIRST combustion chamber directly affects soot and gases emitted radiation. At 3 bars, for the case $f_V \times 1000$, soot and gas emissions have the same levels. However, the nature of radiative energy transfer is quite different in both phases: a large part of the emitted power from gases is self-absorbed while soot particles only reabsorbed a small fraction of their emitted power.

At 30 bars, the net impact of soot radiation is reduced because of the strong increase in gaseous emission. The increase of pressure also enhances interactions between both solid and gaseous phases. For high f_V levels (around 100 ppm local maximum in the DLR configuration) and at 30 bars, 70 % of the soot emission is reabsorbed by the participating gases.

In the Sandia turbulent jet flame, the impact of spectral soot optical properties $m = n - ik$ on radiative heat transfer is found weak: a constant value consistent with the spectral range of interest in soot radiation is adequate. Accounting for a spectral description in the MC approach is nonetheless costless.

Finally, soot morphology description is a critical point to assess scattering effects, which are already the key phenomenon in some optical diagnostics. In Chapter 3, observed scattering effects were negligible on heat transfer in the simulated conditions. The results are, however, very sensitive to the soot size distribution and the surface-volume relationship of soot aggregates. For large aggregates, the impact of soot scattering on heat transfer in gas turbines could become noticeable. Given the unknown fields of soot size distribution and morphology within industrial gas turbine combustors, the role of scattering in such systems remains undetermined. More data are then necessary to characterize soot radiation with realistic soot level and morphology in high-pressure systems.

Part III

Soot radiation in laminar flames

Chapter 5

Inclusion of differential diffusion effects with the Flamelet Progress Variable approach

In this chapter, the chemistry model used for the simulations of an axisymmetric laminar flame is presented. The chosen approach is a tabulated chemistry method, which relies on the generation of 1D flamelets: the flamelet progress variable model (FPV). The original FPV and its extension accounting for heat losses methods are introduced in a first part. These models have been implemented in a compressible reactive flows solver AVBP using the Tabulated Chemistry for Compressible flows (TTC) which is briefly introduced. The flamelet generation originally assumes that all the species have a unity Lewis number. As differential diffusion effects are important in laminar flames, especially here for the considered ethylene flame, this assumption needs to be corrected. In a second part, a new model accounting for differential diffusion is then derived and validated in the AVBP solver. The methodology and the new equations of the TTC method are also presented. In a third part, the model is extended for sooting flames by considering PAHs precursors.

Contents

5.1	Original FPV and RFPV methods	140
5.1.1	Introduction	140
5.1.2	Flamelet database	141
5.1.3	Look-up table parameters for laminar flames	142
5.1.4	Application of FPV-RFPV in compressible codes : TTC approach	144
5.2	Extension to non-unity Lewis numbers	145
5.2.1	Introduction	145

5.2.2	FPV-RFPV extension and modification of TTC formalism	150
5.2.3	Validation of the extended FPV methodology in AVBP	157
5.3	Treatment of PAHs for sooty flames	161
5.3.1	Limitation of FPV/RFPV method with PAHs	161
5.3.2	Multi-PAH model and extension to differential diffusion	161
5.3.3	Validation in AVBP and comparison with REGATH	164
5.4	Conclusion	165

5.1 Original FPV and RFPV methods

5.1.1 Introduction

When performing CFD simulations of reactive flows, the accuracy of the calculation relies, among others, on the use of an accurate chemical mechanism. Laminar axisymmetric flames are often combined with detailed mechanism since these calculations can be performed with an affordable CPU time. [Cuoci et al. \(2013\)](#) has considered the POLIMI mechanism in an axisymmetric ethylene laminar flame, while recent work carried by [Escudero \(2019\)](#) has chosen a modified mechanism of the DLR [Dworkin et al. \(2011\)](#) to study the same flame. Both mechanisms have respectively 170 and 94 species, which drastically increases the number of equations, and hence, the CPU time of these simulations.

The basic idea behind the FPV ([Pierce \(2001\)](#)) and RFPV methods ([Ihme and Pitsch \(2008\)](#)), which are tabulated chemistry based approaches, is to replace this large number of equations by a set of reduced parameters. This is done by generating a collection of 1D counterflow diffusion flame also named flamelets. In turbulent flames, unity Lewis numbers for each species are considered. These parameters, such as the mixture fraction, are then transported in any CFD code instead of transporting a large number of species equations.

Tabulated chemistry models lead then to a tremendous reduction of CPU time and such approaches have been widely considered in turbulent non-premixed flames simulations ([Mueller and Pitsch \(2012\)](#), [Chong et al. \(2018\)](#), [Rodrigues et al. \(2019\)](#), [Tardelli et al. \(2019\)](#)). Others tabulated methods were at first developed and applied for turbulent premixed configurations such as FPI ([Domingo et al. \(2005\)](#), [Hernandez-Perez et al. \(2011\)](#)) or FGM ([Oijen and Goey \(2000\)](#)).

The FPV/RFPV formulations are originally developed for turbulent flames. The objective here is to use these formulations for laminar flames simulations : first, to keep consistency with the analysis carried out in Chapters 3 and 4, then, to save CPU time in such simulations.

5.1.2 Flamelet database

The flamelet database is a collection of 1D counterflow diffusion flames which are computed using an in-house code REGATH (Franzelli et al. (2013), Rodrigues et al. (2017)). In our work, the flamelets are generated with the KM2 kinetic mechanism (with 202 species) (Wang et al. (2013)).

A flamelet is characterized by its **strain rate** ϵ , which corresponds to the transverse velocity gradient along the transverse direction.

A collection of flamelets is generated by varying the strain rate. The representation of the maximum temperature in function of ϵ is called the S-curve. An example of S-curve is represented in Figure 5.1. Note that the curve is parametrized by the scalar dissipation rate which is proportional to the strain rate.

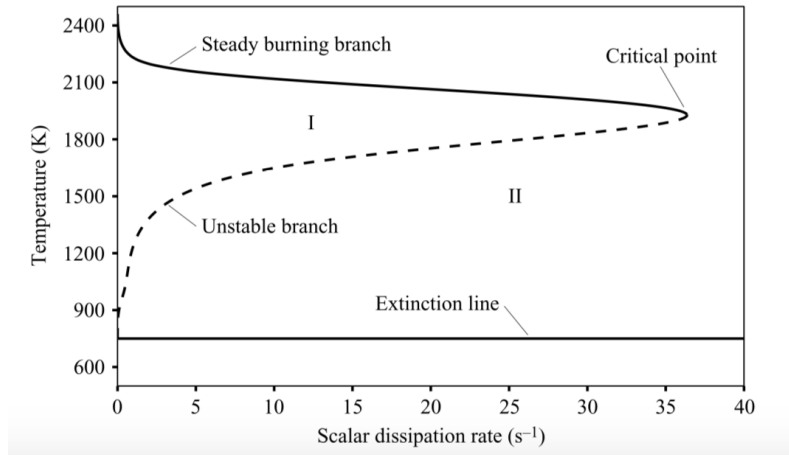


Figure 5.1: Schematic "S-curve" representing the set of steady flamelet solutions (solid and dashed black lines), extracted from Pierce and Moin (2004).

This curve is composed of three parts or branches : the stable and unstable burning branches and the extinction line. On the steady burning branch, the maximum temperature decreases with increasing dissipation rate (or strain rate) due to a competition between mixing time and chemical time. When the temperature starts being too low, the reactions cannot occur and the flame extinguishes. The extinction line corresponds to the state where fuel and oxidizer are purely mixed.

The unsteady branch corresponds to an intermediate state between the extinction line and the stable branch. The extrema of this branch corresponds to two quenching points. These points can be found using the continuation technique, which uses the curve's curvilinear abscissa to parametrize the curve instead of the strain-rate. This branch enables to capture quenching and reignition phe-

nomena in the database used to generate our flamelets.

The generation of this S-curve is the principle of the **FPV technique**. One of the main limitation is that the generated flamelets are adiabatic: heat losses are not then be taken into account. The **RFPV technique** (Ihme and Pitsch (2008)) considers non-adiabatic flamelets and the resulting database is constructed as follows :

- A collection of adiabatic flamelets is generated : this corresponds to an initial state in the stable branch.
- For each adiabatic flamelet, we add a radiative source term based on the optically thin assumption accounting for CO_2 , H_2O and soot absorption coefficients and solve the unsteady flamelet equations. The optically thin model allows for covering a wide range of possible heat losses.
- Between the adiabatic state and the converged non-adiabatic flamelet, we store intermediate solutions to enhance the database of flamelets (see Figure 5.2

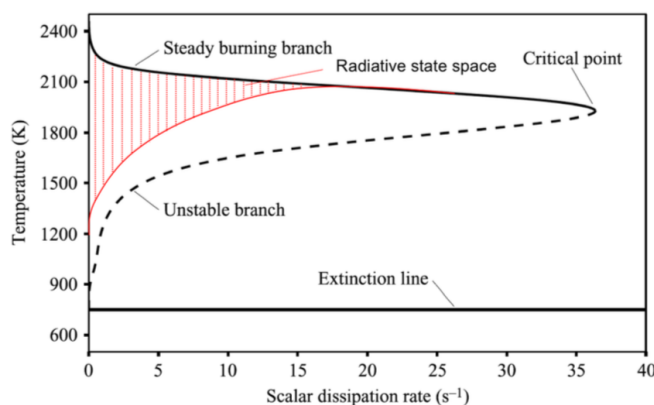


Figure 5.2: Inclusion of heat loss effect with the RFPV technique by computing intermediate non-adiabatic flamelets (in red).

Since only laminar flames are considered, only the parameters used to generate the look-up table for such cases are considered. For turbulent configurations, more informations can be found in Pierce (2001) and Ihme and Pitsch (2008).

5.1.3 Look-up table parameters for laminar flames

The previously generated database can be composed of several hundreds of flamelets : we then need a reduced set of parameters which enables to identify each flamelet.

In the FPV/RFPV method for laminar flames, flamelets are characterized by 2/3 parameters : the mixture fraction, the normalized progress variable and,

for the RFPV approach, the enthalpy.

Mixture fraction Z :

The mixture fraction Z is by definition a passive scalar, equals to 0 in the oxidizer stream and 1 in the fuel stream. In our work, Z is defined in terms of the N_2 species :

$$Z = \frac{Y_{N_2} - Y_{N_2|ox}}{Y_{N_2|fuel} - Y_{N_2|ox}} \quad (5.1)$$

The definition of Z with Equation 5.1 ensures that :

- The mixture fraction is a passive scalar (since N_2 is a passive scalar : NO_x formation is not considered),
- Z value is between 0 and 1,
- The diffusion properties of the scalar Z are consistent with the other species (since all the species have a Lewis number equal to 1, and their diffusion law is described using the Fick's formulation).

Normalized Progress Variable C :

The construction of this variable is a bit more complex as a flamelet needs to be identified without any ambiguity. In a first step, the flamelet is characterized by the progress variable, Y_C , defined as linear combination of species. In the case of a counterflow flame with ethylene, a following definition has been proposed [Rodrigues \(2018\)](#):

$$Y_C = \frac{Y_{H_2O}/W_{H_2O} + Y_{CO_2}/W_{CO_2} + Y_{CO}/W_{CO} - 3Y_{CH_4}/W_{CH_4}}{1/W_{H_2O} + 1/W_{CO_2} + 1/W_{CO} + 3/W_{CH_4}} \quad (5.2)$$

where Y_k is the mass fraction of the k species (H_2O , CO_2 , CO and CH_4) and W_k are the molecular weight of the k species.

This definition ensures that the couple (Z, Y_C) is bijective for the studied condition : a unique flamelet can be identified with these two parameters.

In practice, the table is parametrized by the normalized progress variable C , defined by:

$$C = \frac{Y_C - Y_C^f(Z)}{Y_C^{eq}(Z) - Y_C^f(Z)} \quad (5.3)$$

where Y_C is the progress variable, Y_C^f and Y_C^{eq} are the value of the progress variable of a flamelet in the extinction line and at the equilibrium, respectively. Here again, some important remarks can be noticed :

- The bijectivity ensured by the couple (Z, Y_C) enables to ensure the bijectivity of (Z, C)
- C varies between 0 (in non-reactive flow) to 1.

Enthalpy defect H :

When considering heat losses, an additional parameter is needed to uniquely identify a flamelet. This is done by considering the enthalpy h in the look-up table. Similarly to what has been done for the progress variable, the normalized enthalpy H is used as the new parameter :

$$H = \frac{h - h^{rad}(Z, C)}{h^{adiab}(Z, C) - h^{rad}(Z, C)} \quad (5.4)$$

in this equation, h^{adiab} is the enthalpy of the flamelet at a given strain-rate (which is equivalent to a given couple (Z, C)) without heat-losses and h^{rad} with the maximum heat-losses due to radiation. Hence, H varies between 0 (non-adiabatic flamelet) to 1 (adiabatic flamelet). An important remark is that H is related to the enthalpy of the mixture and then shares the same diffusion properties as the species (again since Lewis numbers equal to 1).

Finally, any transport or thermodynamic quantity of the flamelet database G can be stored and written $G(Z, C, H)$.

5.1.4 Application of FPV-RPFV in compressible codes : TTC approach

Once the table is generated, the CFD code needs to retrieve thermodynamical quantities via the knowledge of Z , C and H that need to be determined through transport equations. In the code, Z , Y_c and h are transported:

$$\frac{\partial \rho Z}{\partial t} + \frac{\partial}{\partial x_i} (\rho u_i Z) = \frac{\partial}{\partial x_i} \left(\rho D_Z \frac{\partial Z}{\partial x_i} \right) \quad (5.5)$$

$$\frac{\partial \rho Y_C}{\partial t} + \frac{\partial}{\partial x_i} (\rho u_i Y_C) = \frac{\partial}{\partial x_i} \left(\rho D_{Y_c} \frac{\partial Y_C}{\partial x_i} \right) + \rho \dot{\omega}_{Y_c} \quad (5.6)$$

$$\frac{\partial \rho h}{\partial t} + \frac{\partial}{\partial x_i} (\rho u_i h) = \frac{\partial}{\partial x_i} \left(\rho D_h \frac{\partial h}{\partial x_i} \right) + P^R \quad (5.7)$$

where $\dot{\omega}_{Y_c}$ is the source term of the progress variable, which is calculated using the source terms of the species of Equation 5.2 and P^R the radiative power.

In the previous section, we emphasized that all the parameters share the same diffusion properties than the k species of the chemical mechanism : $D_Z = D_H = D_{Y_c} = D_k = \frac{\lambda}{c_p \rho}$ since unity Lewis numbers are assumed. This ensures the consistency between the transported equations and the table parameters.

The collection of flamelets is generated at constant pressure which is not compatible with compressible flow solvers such as the one used, AVBP, where acoustics needs to be taken into account. In other words, mass density, temperature and energy cannot be taken from the table. The density and the energy are transported in AVBP by their own equation and then are not read in the table. The effect of compressibility in the temperature has been derived by [Vicquelin et al. \(2011\)](#):

$$T = T^{tab}(Z, C, H) + \frac{e - e^{tab}(Z, C, H)}{C_v^{tab}(Z, C, H)} \quad (5.8)$$

where the superscript tab refers to tabulated values.

The AVBP code uses characteristic boundary conditions (NSCBC formalism [Poinsot \(1992\)](#)) are used to prescribe the boundary conditions. This formalism has been modified consistently with the TTC approach in the AVBP code (see [Vicquelin et al. \(2011\)](#) for more details).

Finally, since the table is generated with Unity Lewis number species and a Fick's diffusion law, the total energy balance e_t equation can be expressed by :

$$\frac{\partial \rho e_t}{\partial t} + \frac{\partial}{\partial x_j} (\rho u_j e_t) = \frac{\partial}{\partial x_j} \left(\frac{\lambda}{c_p} \frac{\partial h}{\partial x_j} \right) + \frac{\partial}{\partial x_j} (\sigma_{ij} u_i) + \dot{Q} + P^R \quad (5.9)$$

with $\sigma_{i,j}$ the stress tensor, \dot{Q} a source or sink term. The advantage of this equation is to explicitly link the transported enthalpy h and the total energy e_t .

5.2 Extension to non-unity Lewis numbers

5.2.1 Introduction

In the original FVP method, the assumption of species Lewis number equal to 1 ensures a consistent definition between the table parameters and the transported quantities in the CFD code. It is also appropriate in turbulent flames where the turbulent transport is much more efficient than the molecular diffusion. However, in laminar flames, differential diffusion effects can be important and must be taken into account ([Liu et al. \(2006\)](#)).

5.2.1.1 Differential diffusion modeling

The general species balance equations, which include diffusion transport are written :

$$\frac{\partial \rho Y_k}{\partial t} + \frac{\partial}{\partial x_j} (\rho u_j Y_k) = - \frac{\partial}{\partial x_j} (\rho V_{k,j} Y_k) + \rho \dot{\omega}_k \quad (5.10)$$

where Y_k is the considered species, $V_{k,j}$ the diffusion velocity of the k^{th} species, and $\dot{\omega}_k$ the species chemical production rate.

The general equation (neglecting thermophoresis) which gives $V_{k,j}$ is given by :

$$\nabla X_k = \sum_{j=1}^N \left(\frac{X_k X_j}{D_{kj}} \right) (\mathbf{V}_j - \mathbf{V}_k) + (Y_k - X_k) \left(\frac{\nabla P}{P} \right) \quad (5.11)$$

where X_k is the molar fraction of the species, $D_{k,j}$ the binary diffusion coefficients for species k and j , and P the pressure. This equation is very expensive to solve and is replaced using the Curtiss-Hirschfelder ([Hirschfelder and Curtiss \(1949\)](#)) approximation:

$$V_{k,j} X_k = -D_k \frac{\partial X_k}{\partial x_j} \quad (5.12)$$

where D_k is the species diffusion coefficient in the mixture. In practice, this coefficient is calculated using the mixture-averaged approximation:

$$D_k = (1 - X_k) / \sum_{j \neq k} (X_j / D_{kj}) \quad (5.13)$$

Finally, in order to ensure the mass conservation, a corrective diffusive velocity $V_{c,j}$ is introduced such as:

$$V_{k,j} Y_k = -D_k \frac{W_k}{W} \frac{\partial X_k}{\partial x_j} + V_{c,j} Y_k \quad (5.14)$$

with

$$V_{c,j} = \sum_{k=1}^N D_k \frac{W_k}{W} \frac{\partial X_k}{\partial x_j} \quad (5.15)$$

Therefore, using the Curtis-Hirschfelder approximation and the mixture-averaged approximation, the species balance equation becomes:

$$\frac{\partial \rho Y_k}{\partial t} + \frac{\partial}{\partial x_j} \left(\rho (u_j + V_{c,j}) Y_k \right) = \frac{\partial}{\partial x_j} \left(\rho D_k \frac{W_k}{W} \frac{\partial X_k}{\partial x_j} \right) + \rho \dot{\omega}_k \quad (5.16)$$

Finally, the total energy e_t balance equation is written in its general form:

$$\frac{\partial \rho e_t}{\partial t} + \frac{\partial}{\partial x_j} (\rho u_j e_t) = -\frac{\partial q_j}{\partial x_j} + \frac{\partial}{\partial x_j} (\sigma_{ij} u_i) + \dot{Q} + P^R \quad (5.17)$$

where q_j is the heat diffusion flux. Using the Fourier's law, it is expressed as:

$$q_j = -\lambda \frac{\partial T}{\partial x_j} + \rho \sum_{k=1}^N h_k V_{k,j} Y_k \quad (5.18)$$

where $V_{k,j}$ is given by Equation 5.14.

5.2.1.2 Impact of differential diffusion on 1D flamelets

In the REGATH solver, 1D flamelets are computed accounting for differential diffusion effects or not (Unity Lewis numbers).

Figures 5.3 and 5.4 display the temperature and the acetylene evolution in a 1D counterflow diffusion flame, where the fuel is composed by ethylene at 300K and the oxidizer by air at the same temperature, for the two chemistry models. The strain-rate is here imposed at 100 s^{-1} . It can be observed that differential diffusion effects tend to decrease the temperature and increase the concentration of acetylene. Since acetylene is known to have a major role in the formation of soot particles, impact on the PAHs and hence on the soot volume fraction can be expected.

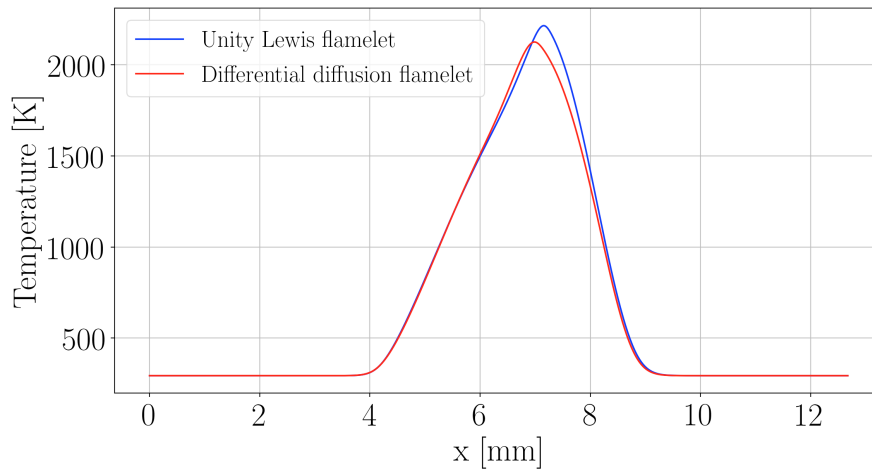


Figure 5.3: Comparison of 1D profiles of temperature with/without differential diffusion effects using detailed chemistry (KM2 mechanism) on a 1D counterflow diffusion flame for a strain rate $a = 100 \text{ cm}^{-1}$.

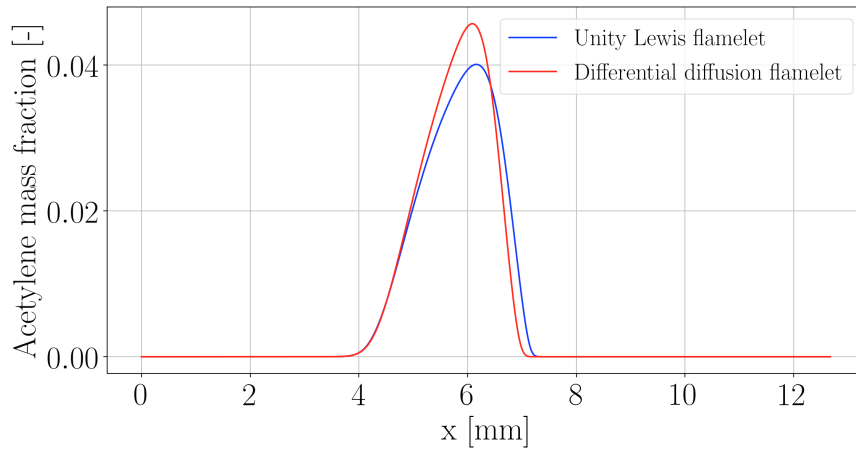


Figure 5.4: Comparison of 1D profiles of acetylene mass fraction with/without differential diffusion effects using detailed chemistry (KM2 mechanism) on a 1D counterflow diffusion flame for a strain rate $a = 100 \text{ cm}^{-1}$.

PAHs concentrations are strongly affected by the differential diffusion, as displayed Figure 5.5 for the A4 mass fraction. It can be observed that differential diffusion increases PAHs by a factor 10. Thus, including differential diffusion effects is of primary importance in flames driven by these effects (such as laminar flames).

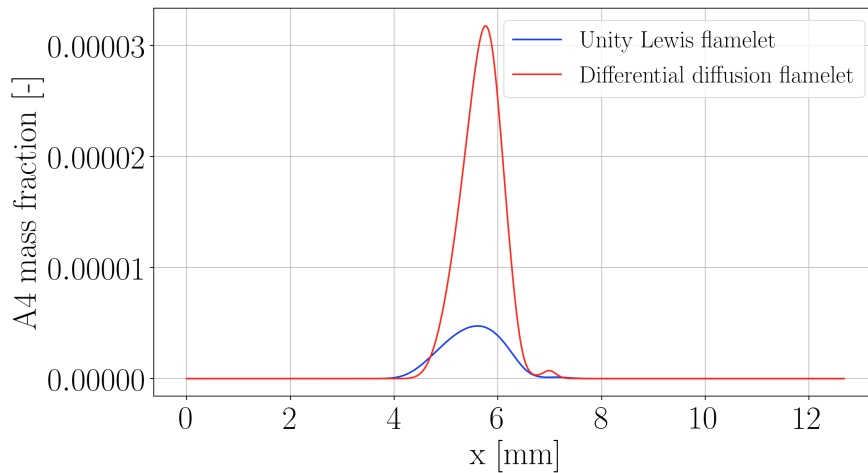


Figure 5.5: Comparison of 1D profiles of A4 PAH mass fraction with/without differential diffusion effects using detailed chemistry (KM2 mechanism) on a 1D counterflow diffusion flame for a strain rate $a = 100 \text{ cm}^{-1}$.

The effect of soot differential diffusion can also be quantified for soot particles in terms of volume fraction f_V (Figure 5.6) and number density of particles

(Figure 5.7), since these quantities are provided by the sectional method used to describe the soot phase.

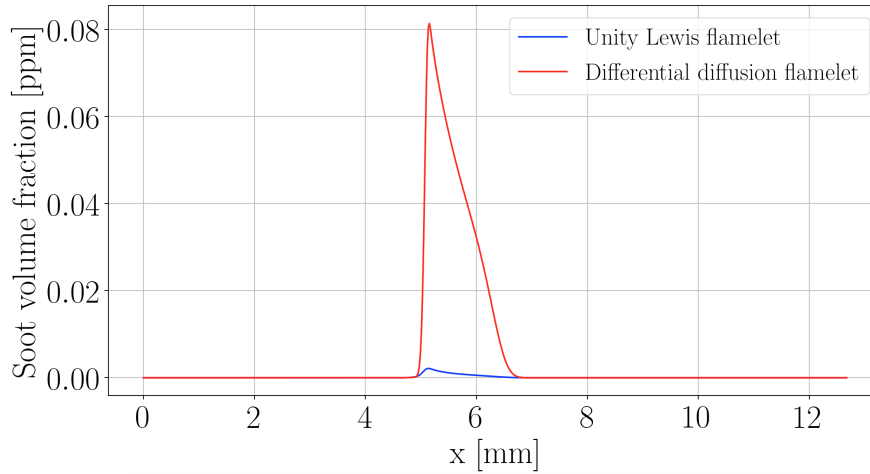


Figure 5.6: Comparison of 1D profiles of soot volume fraction with/without differential diffusion effects using detailed chemistry (KM2 mechanism) on a 1D counterflow diffusion flame for a strain rate $a = 100 \text{ cm}^{-1}$.

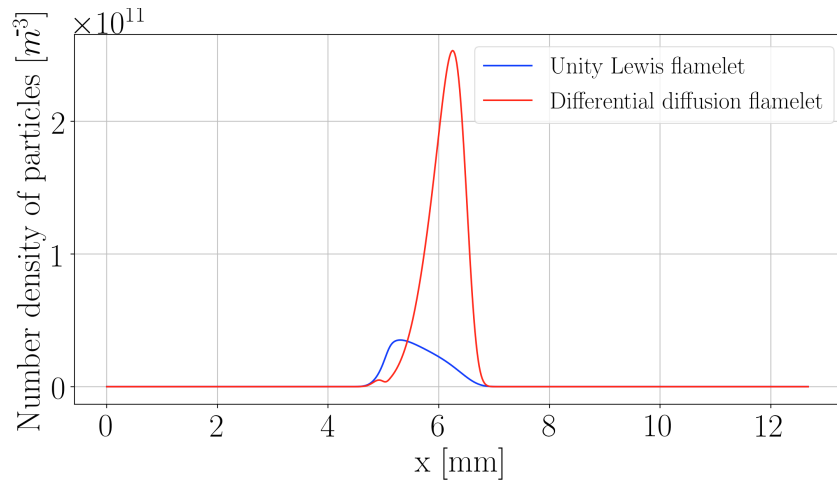


Figure 5.7: Comparison of 1D profiles of number density of soot particles with/without differential diffusion effects using detailed chemistry (KM2 mechanism) on a 1D counterflow diffusion flame for a strain rate $a = 100 \text{ cm}^{-1}$.

It can be observed that soot volume fraction is greatly increased due to differential diffusion effects, of a factor 10, which is consistent with the evolution of PAHs. Moreover, the number of particles is impacted of a factor 5. These results are of primal importance when they are interpreted in terms of soot

radiative properties with the RDG-FA model : the absorption coefficient is strongly increased since it is directly proportional to f_V , while the scattering explicitly depends on the number density function and will also be enhanced.

These results highlight the need for considering differential diffusion effects in laminar flames to accurately retrieve the good level of soot volume fraction, which has a direct impact on soot radiative contribution. The following sections are organized as follows : first, an extension of FPV/RFPV model is derived and validated in the AVBP compressible code. In a second part, PAH contributors to soot formation are taken into account and also validated.

5.2.2 FPV-RFPV extension and modification of TTC formalism

5.2.2.1 accounting for differential diffusion in flamelet models

Among the existing flamelet models, the Flamelet Generated Manifolds (FGM) method has been initially developed and applied for turbulent premixed configurations. A collection of flamelets is generated and these 1D flames are parametrized in terms of mixture fraction Z and progress variable Y_c (unlike the FPV method where the strain rate is used instead). In [Verhoeven et al. \(2012\)](#), the FGM approach is extended to laminar non-premixed flames. Differential diffusion effects are taken into account by generating a database of flamelets with different species Lewis numbers and by transporting two equations for the mixture fraction Z and the progress variable Y_c . The results of the flamelet approach are compared with a detailed chemistry on a laminar methane-air flame. One of the main issue emphasized is that multi-dimensionnal effects are not taken into account in the database generation, which leads to significant deviations of species prediction. Including these curvature effects in the FGM remains however a challenging task ([van Oijen et al. \(2007\)](#), [Nguyen et al. \(2010\)](#)).

In the FPV approach, pioneer work has been conducted in [Pitsch and Peters \(1998\)](#) to include differential diffusion effects. In their work, the mixture fraction Z is no longer defined as a passive scalar, but via its own transport equation, with an appropriate Lewis number. The model has been applied to a turbulent non-premixed hydrogen flame ([Pitsch et al. \(1998\)](#)) which yields to good results. The use of this extended FPV approach for laminar flames remains difficult ([Carbonell et al. \(2009\)](#)). In the study of [Liu et al. \(2006\)](#), an axisymmetric coflow ethylene-air diffusion flame was computed using the FPV model with differential diffusion and compared with detailed chemistry. Similarly to the FGM method, the inclusion of curvature effects remains essential to predict downstream the flame the major species and flame topology. Recent work ([Schlup and Blanquart \(2019\)](#)) aims at including these curvature effects

but are so far limited to premixed configurations.

One issue arises from the definition of Y_c , which is usually based on the species Y_k : indeed, since the Lewis number of each species Y_k is no longer equal to 1, the definition of an equivalent Lewis number for Y_c is not straightforward. In parallel, the transport of the Y_k species in the code would be too cumbersome. Therefore, the objective is, in a first time, to propose a definition of Y_c which accounts for differential diffusion effects, following the work of Pitsch and Peters, by defining Y_c by its own transport equation. Then, heat losses are taken into account by adding another parameter to Z and Y_c .

5.2.2.2 New definition of look-up table parameters

Definition of Mixture fraction Z : The proposed extension is based on pioneer work of [Pitsch and Peters \(1998\)](#) who included differential diffusion effects in a flamelet formulation. In this approach, the mixture fraction Z is no longer defined as a passive scalar via species, but via its own transport equation, namely :

$$\rho \frac{\partial Z}{\partial t} + \rho \mathbf{v} \cdot \nabla Z - \nabla \cdot (\rho D_Z \nabla Z) = 0 \quad (5.19)$$

In this equation, the diffusion coefficient D_Z can be arbitrarily chosen. Boundary conditions on Z ensures that Z equals 0 in pure oxidizer and 1 in the fuel. It is then possible to replace the equations of the flamelets expressed in spatial coordinates (the classic mass, species and temperature equations) by an equation expressed in this new mixture fraction coordinates ([Pitsch and Peters \(1998\)](#)).

In the following, flamelets generated respectively with the spatial and mixture fraction coordinates will be referred respectively as **X-flamelets** and **Z-flamelets**.

The transport equation 5.19 has been implemented in the flamelet solver. A **X-flamelet** is generated as in the classic FPV methodology, but an additional equation for Z is considered.

In order to validate such implementation, a simple 2-step mechanism is considered. The test case is a 1D counterflow diffusion flame, with fuel side composed by pure methane CH_4 at 300K and 1 bar and the oxidizer side is a mixture O_2/N_2 with $Y_{O_2} = 0.27$ and $Y_{N_2} = 0.27$, at 300K and 1 bar. The Lewis number of each species are 0.97 for CH_4 , 1.35 for CO , 1.07 for CO_2 , 1.06 for H_2O , 0.78 for N_2 and 1.04 for O_2 . The strain rate is 100 s^{-1} . Figure 5.8 the temperature profile as a function of mixture fraction for:

- The **Z-flamelet** formulation (the complete equation proposed in [Pitsch and Peters \(1998\)](#) is solved),
- The temperature obtained using the **X-flamelet** formulation and the transported mixture fraction via Equation 5.19. The diffusion coefficient for Z , D_Z , is chosen equal to $\frac{\lambda}{\rho c_p}$
- The **X-flamelet** using the definition of Z as a passive scalar.

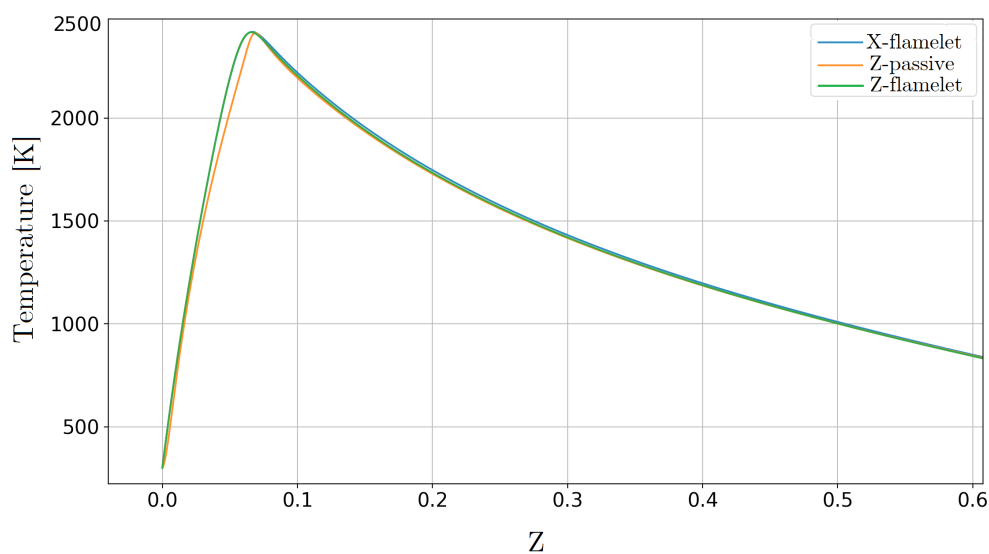


Figure 5.8: Evolution of temperature in function of the mixture fraction for X-flamelet and Z-flamelet formulation in a 1D counterflow diffusion flame, accounting for differential diffusion effects.

In Figure 5.8, the transported mixture fraction formulation is able to reproduce the exact general solution of the flamelet equations. When considering Z as a passive scalar, a noticeable mismatch in temperatures is observed, especially for low Z values. This shows that such formulation is not suitable when accounting for differential diffusion effects.

This validates the implementation of the transport equation of Z in the flamelet solver. However, additional parameters are required to build the look-up table : the progress variable and the enthalpy defect. Following the philosophy of the Z-flamelet formulations, these two parameters are no longer defined as function of species but by their own transport equation with appropriate boundary conditions.

Definition of Progress Variable Y_c : The progress variable Y_c is defined by :

$$\rho \frac{\partial Y_c}{\partial t} + \rho \mathbf{v} \cdot \nabla Y_c - \nabla \cdot (\rho D_{Y_c} \nabla Y_c) = \dot{\omega}_{Y_c} \quad (5.20)$$

In this equation, D_{Y_c} is arbitrary chosen. In the present work, the diffusion coefficient is chosen such as $Le_{Y_c} = 1$. This choice enables to keep the formulations of the transported variable in the CFD solver identical to Equation 5.7). The choice of $\dot{\omega}_{Y_c}$ is done such as the couple (Z, Y_c) is bijective (if we consider only adiabatic flamelets). In practice, the Y_c source term is written as a sum of weighted species source terms. However, Y_c follows its own transport description and is not a sum of species anymore. For the ethylene flame studied in the next chapter, the following definition is retained :

$$\dot{\omega}_{Y_c} = 0.396\dot{\omega}_{CO} + 0.252\dot{\omega}_{CO_2} + 0.616\dot{\omega}_{H_2O} - 2.079\dot{\omega}_{CH_4} \quad (5.21)$$

As an example, Figure 5.9 presents the evolution of Y_c in function of Z for different flamelets used to generate the look-up table for the simulations presented in the following chapters. The flamelets are generated using the KM2 mechanism and ethylene/air are considered as fuel/oxidizer compositions.

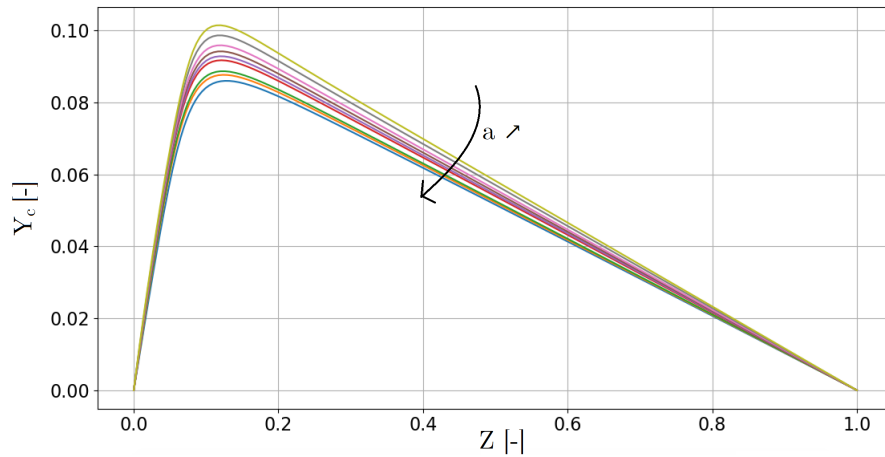


Figure 5.9: Evolution of Y_c in function of Z for different 1D counterflow flamelets generated with the KM2 mechanism for ethylene. Differential diffusion is considered and 2 transported equations for Y_c and Z are additionally solved. Only the stable branch flamelets are represented.

Definition of a "fictive" enthalpy h' : Heat losses are accounting for by introducing a fictive enthalpy h' , which follows its own transport equation:

$$\rho \frac{\partial h'}{\partial t} + \rho \mathbf{v} \cdot \nabla h' - \nabla \cdot (\rho D_{h'} \nabla h') = P^R \quad (5.22)$$

It is important to note that the parameter h' is not directly related to the real mixture enthalpy h . It enables to parametrize the table in order to take into account heat losses without ambiguity on the definition of the diffusion coefficient.

Here again, the diffusion coefficient is chosen arbitrary such as $Le_{H'} = 1$. In order to validate the implementation of this parameter, we can verify that, in absence of heat losses ($P^R = 0$), Z and h' are proportional. Such property is due to the fact that both parameters are transported with $Le = 1$. On the contrary, the real enthalpy of the mixture h is not linear since differential diffusion effects are included. The two parameters are plotted in Figure 5.10 as a function of Z for one of the flamelets in Figure 5.9.

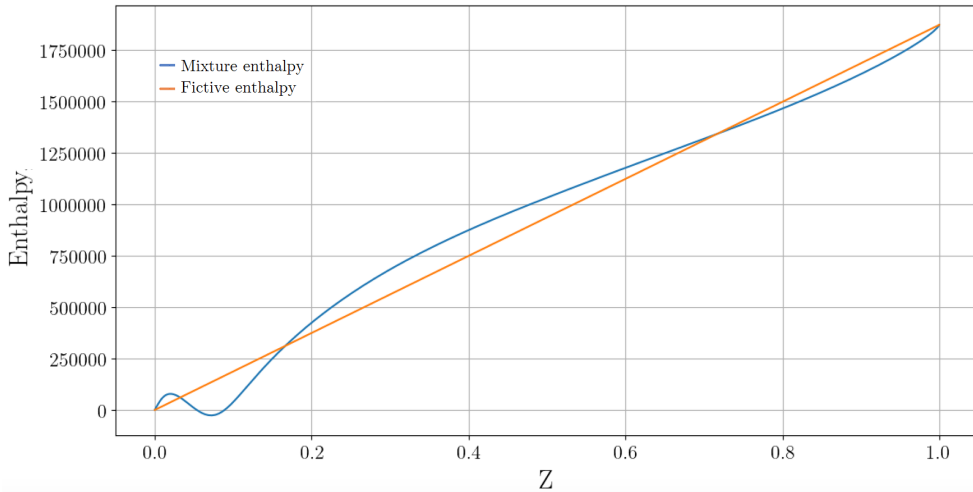


Figure 5.10: Evolution of the transported enthalpy and the mixture enthalpy in function of Z for one of the 1D counterflow flamelets generated with the KM2 mechanism for the ethylene

In Figure 5.10, the extremum values of both enthalpies are respectively the enthalpy of air (for $Z = 0$) and ethylene ($Z = 1$). The strongest non-linearities of the enthalpy of the mixture are located near the stoichiometric mixture fraction values.

The thermodynamic quantities are finally stored in a look-up table, parametrized by Z , C (obtained by normalizing the progress variable) and the normalized

h' .

5.2.2.3 Modification of the heat flux expression

An extra equation for the real energy in addition to the one for the parameter h' is considered in different situations. In a low-Mach solver, the real thermodynamic variables can be stored in the flamelet database. Alternatively, one could prefer to keep track of the real energy or enthalpy by solving its transport equation and deduce the temperature from it. In a compressible flow solver, as the AVBP code, compressible effects must be taken into account, as done in the TTC formalism, by keeping the reference energy.

The expression of the "real" energy equation (see Equation 5.9) originally used in TTC formalism is however no longer valid, since its derivation assumes unity-Lewis numbers.

The general expression of the heat flux vector q_j is (see Section 5.2.1.1) :

$$q_j = -\lambda \frac{\partial T}{\partial x_i} + \sum_{k=1}^N \rho h_k Y_k V_{k,i} \quad (5.23)$$

with :

$$\rho Y_k V_{k,i} = -\rho D_k \frac{W_k}{W} \frac{\partial X_k}{\partial x_i} + \rho Y_k \sum_{j=1}^N D_j \frac{W_j}{W} \frac{\partial X_j}{\partial x_i} \quad (5.24)$$

The expression involves the N species of the mechanism. In order to be transported in the CFD solver, we need to express the heatflux vector as a function of the N_{fic} "fictive" species (namely the parameters Z, Y_c, h'). To do so, we first need to rewrite the expression of the heat flux vector :

$$\begin{aligned} q_i &= -\lambda \frac{\partial T}{\partial x_i} + \sum_{k=1}^N \left(-\rho h_k D_k \frac{W_k}{W} \frac{\partial X_k}{\partial x_i} + \rho h_k Y_k \sum_{j=1}^N D_j \frac{W_j}{W} \frac{\partial X_j}{\partial x_i} \right) \\ &= -\lambda \frac{\partial T}{\partial x_i} - \sum_{k=1}^N \rho h_k D_k \frac{W_k}{W} \frac{\partial X_k}{\partial x_i} + \left(\sum_{k=1}^N \rho h_k Y_k \right) \left(\sum_{j=1}^N D_j \frac{W_j}{W} \frac{\partial X_j}{\partial x_i} \right) \\ &= -\lambda \frac{\partial T}{\partial x_i} - \sum_{k=1}^N \rho h_k D_k \frac{W_k}{W} \frac{\partial X_k}{\partial x_i} + \rho h \left(\sum_{j=1}^N D_j \frac{W_j}{W} \frac{\partial X_j}{\partial x_i} \right) \\ &= -\lambda \frac{\partial T}{\partial x_i} - \sum_{k=1}^N \rho h_k D_k \frac{W_k}{W} \frac{\partial X_k}{\partial x_i} + \sum_{j=1}^N \rho h D_j \frac{W_j}{W} \frac{\partial X_j}{\partial x_i} \\ &= -\lambda \frac{\partial T}{\partial x_i} - \sum_{k=1}^N \rho (h_k - h) D_k \frac{W_k}{W} \frac{\partial X_k}{\partial x_i} \end{aligned} \quad (5.25)$$

We can now introduce the j -th fictive species $Y_{fic,j}$ which yields to :

$$q_i = -\lambda \frac{\partial T}{\partial x_i} - \sum_{j=1}^{N_{fic}} \left(\sum_{k=1}^N \rho (h_k - h) D_k \frac{W_k}{W} \frac{\partial X_k}{\partial Y_{fic,j}} \right) \frac{\partial Y_{fic,j}}{\partial x_i} \quad (5.26)$$

In this expression appears the enthalpy of the specie k (h_k) that needs to be tabulated. Such enthalpy are impacted by compressible effects and therefore cannot be directly tabulated. In order to take into account compressibility effects, a similar treatment as the original TTC formalism is done. Let us split the previous equation in two terms for the sake of clarity :

$$q_i = -\lambda \frac{\partial T}{\partial x_i} - \sum_{j=1}^{N_{fic}} \left(\sum_{k=1}^N \rho h_k D_k \frac{W_k}{W} \frac{\partial X_k}{\partial Y_{fic,j}} \right) \frac{\partial Y_{fic,j}}{\partial x_i} + \sum_{j=1}^{N_{fic}} \left(\sum_{k=1}^N \rho h D_k \frac{W_k}{W} \frac{\partial X_k}{\partial Y_{fic,j}} \right) \frac{\partial Y_{fic,j}}{\partial x_i} \quad (5.27)$$

The second term, related to the corrective velocity does not need to be corrected by compressible effects : indeed, the real enthalpy h can be directly retrieved from the compressible energy transported by the CFD code as : $h = e + \frac{P}{\rho}$. For h_k we use the following relation :

$$h_k - h_k^{tab} = c_{p_k}^{tab} (T - T^{tab}) \leftrightarrow h_k = h_k^{tab} + c_{p_k}^{tab} \Delta T \quad (5.28)$$

with $c_{p_k}^{tab}$ given by the database. With this expression, we can write the heat flux vector in a more compact form, highlighting the quantities that are stored in the table :

$$q_i = -\lambda \frac{\partial T}{\partial x_i} - \sum_{j=1}^{N_{fic}} \frac{\rho}{W} \left[\mathcal{A}_j^{tab} + \mathcal{M}_j^{tab} \Delta T - \mathcal{L}_j^{tab} h \right] \frac{\partial Y_{fic,j}}{\partial x_i} \quad (5.29)$$

with :

$$\mathcal{A}_j^{tab} = \sum_{k=1}^N h_k D_k W_k \frac{\partial X_k}{\partial Y_{fic,j}} \quad (5.30)$$

$$\mathcal{M}_j^{tab} = \sum_{k=1}^N C p_k D_k W_k \frac{\partial X_k}{\partial Y_{fic,j}} \quad (5.31)$$

$$\mathcal{L}_j^{tab} = \sum_{k=1}^N D_k W_k \frac{\partial X_k}{\partial Y_{fic,j}} \quad (5.32)$$

5.2.3 Validation of the extended FPV methodology in AVBP

The extended FPV approach is validated in the AVBP compressible solver by simulating a 1D counterflow diffusion flame. One of the difficulties relies in the fact that flamelets are generated in the flamelet solver with an imposed Strain-Rate as stated in Section 5.1.1. However, AVBP solver formulation prescribes a fixed velocity : a correction of the boundary conditions is therefore first needed to ensure the consistency between both solvers.

Derivation of boundary conditions for the counterflow diffusion problem

Let us consider the geometry definition in Figure 5.11 and define the velocity field \mathbf{u} such as :

$$\mathbf{u} = u(x, y)e_x + v(x, y)e_y \quad (5.33)$$

u is the transverse velocity component, and v is the axial velocity component.

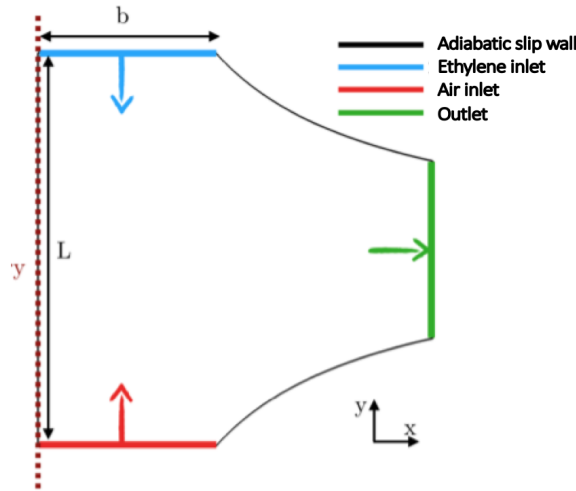


Figure 5.11: *Geometry of the counterflow problem*

In the following, we consider a planar counterflow diffusion flame. At the boundary, one can write a general mass conservation equation :

$$\frac{dv}{dy} + \frac{du}{dx} \Big|_{boundary} = 0 \quad (5.34)$$

In order to compare the results of AVBP with a 1D counterflow laminar computed with the flamelet solver REGATH, we define the **strain rate** a such as

in REGATH :

$$a = \left. \frac{du}{dx} \right|_{fuel} \quad (5.35)$$

Using the mass equation , the strain rate can also be written :

$$a = - \left. \frac{dv}{dy} \right|_{fuel} \quad (5.36)$$

In order to write the strain-rate in the oxidizer side, we can use the conservation of the quantity ρu^2 , which yields to :

$$a = - \frac{\sqrt{\rho_{fuel}}}{\sqrt{\rho_{ox}}} \left. \frac{dv}{dy} \right|_{ox} \quad (5.37)$$

and

$$a = \frac{\sqrt{\rho_{fuel}}}{\sqrt{\rho_{ox}}} \left. \frac{du}{dx} \right|_{ox} \quad (5.38)$$

Equations 5.35 to 5.38 enable to prescribe boundary conditions in AVBP for the velocities.

Boundary conditions for the non-reactive flow :

- *Fuel size :*

$$u(x, y) = ax \quad v(x, y) = -ay \quad (5.39)$$

- *Oxidizer size :*

$$u(x, y) = \sqrt{\frac{\rho_{fuel}}{\rho_{ox}}} ax \quad v(x, y) = -\sqrt{\frac{\rho_{fuel}}{\rho_{ox}}} ay \quad (5.40)$$

Numerical set-up and results :

The 2D mesh is generated by CENTAUR and is composed of 1 million triangles, and is chosen such as the reaction zone of the flame is about 1/3 of the outlet length. The strain-rate is imposed at 120 s^{-1} .

The two walls of the domain are defined by streamlines whom equations are defined in potential flow theory. Two inlets using NSCBC formalism are considered. For each of them, a temperature, velocity and fictive species values are

prescribed. The outlet of the domain is also based on NSCBC formalism, but only the pressure is imposed at 1 bar.

Figure 5.12 presents the obtained fields of mixture fraction Z , temperature T , progress variable Y_c , the difference between table temperature and calculated temperature in AVBP.

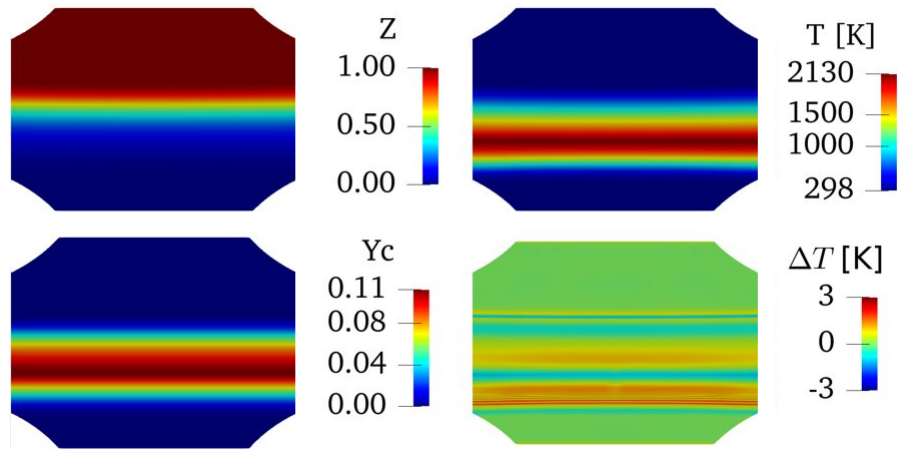


Figure 5.12: *Obtained fields on the counterflow diffusion flame computed in AVBP. The strain rate is set at $120s^{-1}$.*

It can be observed that fields are invariant along the transverse direction, and that the temperature computed by AVBP is very close to the expected temperature of the table. The fact that both temperatures are not strictly equal (characterized by a $\Delta T \neq 0$) relies on compressible effects not taken into account in REGATH.

Figure 5.13 presents direct comparisons with the REGATH code with the KM2 mechanism and detailed transport properties. The temperature, energy, enthalpy of the mixture (in AVBP this quantity is reconstructed via the energy transported) and the progress variable fields are displayed. An excellent agreement between the implementation in AVBP and the REGATH code is observed, which validates the methodology employed. Let us note that the enthalpy is not a linear function of Z since differential diffusion effects are taken into account.

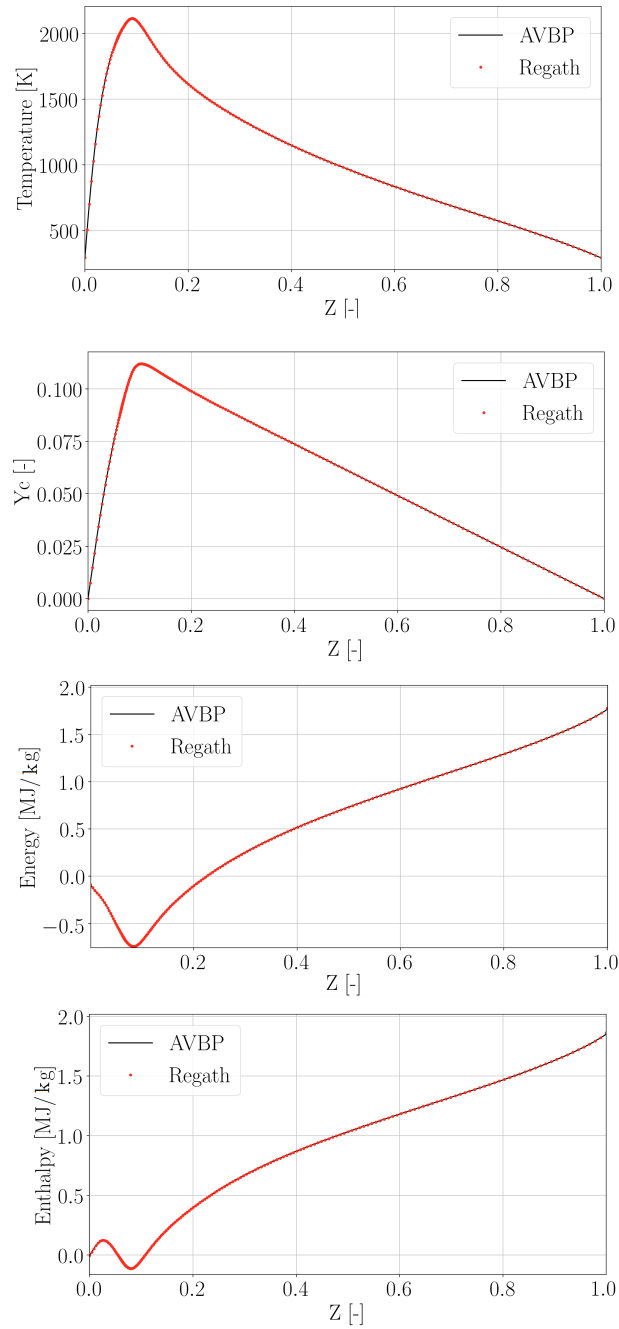


Figure 5.13: Comparison of profiles obtained in AVBP (tabulated chemistry) and in the flamelet solver REGATH with differential diffusion. The strain rate is set at 120 s^{-1} .

5.3 Treatment of PAHs for sooty flames

5.3.1 Limitation of FPV/RFPV method with PAHs

In order to compute sooty flames with the FPV method, additional information such as the source terms for the different soot formation mechanisms needs to be tabulated. Gaseous species which leads to soot formation are known as Polycyclic Aromatic Hydrocarbons (PAHs). They can be also stored in the look-up table, as these gaseous species are included in the detailed mechanism used to generate the flamelets.

However, PAH species have relatively low chemistry timescales (Bisetti et al. (2012), Attili et al. (2014)) and do not relax fast enough on the flamelet manifold. Therefore, obtain the PAHs directly from the database is not accurate. PAHs are then computed in the code with their own transport equation.

In turbulent flames (where unity Lewis numbers are assumed), one strategy is to be considered a lumped-PAH approach : a single transport equation is solved for an equivalent lumped-PAH (Mueller and Pitsch (2012)) instead of considering all the PAHs. This enables to reduce the simulation cost, as less equations are solved. This methodology has been considered to obtain the CFD and soot fields used in Chapters 3 and 4 (Rodrigues et al. (2018), Rodrigues et al. (2019)).

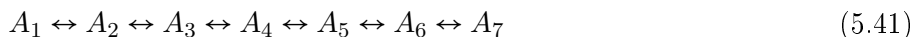
In the context of differential diffusion for the studied laminar flame, this strategy is however not suitable : indeed, the diffusion coefficient of a lumped-PAH cannot be defined since all the PAHs have their own diffusion coefficient. Therefore, we need to transport one equation per PAH.

5.3.2 Multi-PAH model and extension to differential diffusion

Original formulation for Unity-Lewis numbers :

In the study of Xuan et al. (2014), each class of PAH has its own dynamic : each PAH needs to be transported in order to retrieve their production which will impact soot formation.

For the KM2 kinetic scheme considered, the following PAHs and production are considered :



This is a schematic point of view where a PAH composed of j aromatic cycles is noted A_j .

For each PAH_j , the following transport equation, assuming Unity Lewis num-

bers, is solved :

$$\frac{\partial \rho Y_{\text{PAH}_j}}{\partial t} + \frac{\partial \rho u_i Y_{\text{PAH}_j}}{\partial x_i} = \frac{\partial}{\partial x_i} \left(\rho D_{\text{PAH}_j} \frac{\partial Y_{\text{PAH}_j}}{\partial x_i} \right) + \dot{m}_{\text{PAH}_j} \quad (5.42)$$

where D_{PAH_j} is the considered diffusion coefficient for the j-th PAH and \dot{m}_{PAH_j} is the source term taking into account gaseous production and consumption of the PAH.

Since PAH species have low chemistry timescales , their source term \dot{m}_{PAH_j} is not directly taken from the table. The source term is relaxed based on the current value of the PAH mass fraction and is written:

$$\dot{m}_{\text{PAH}} = \dot{m}_+^{\text{tab}} + \dot{m}_-^{\text{tab}} \left(\frac{Y_{\text{PAH}}}{Y_{\text{PAH}}^{\text{tab}}} \right) + \dot{m}_D^{\text{tab}} \left(\frac{Y_{\text{PAH}}}{Y_{\text{PAH}}^{\text{tab}}} \right)^2 \quad (5.43)$$

where $\dot{m}_+^{\text{tab}}, \dot{m}_-^{\text{tab}}$ and \dot{m}_D^{tab} correspond respectively to the tabulated PAH gaseous production, gaseous consumption and dimerization consumption source terms. $Y_{\text{PAH}}^{\text{tab}}$ corresponds to the tabulated value of the PAH.

Our objective here is to extended the approach to take into account differential diffusion effects.

Formulation accounting for differential diffusion :

The derivation of this model follows the same philosophy than the extension of FPV model :

- We correct the convective heat flux vector which appears in the energy equation by separating the contribution of non-PAHs species (which are stored in the table) and PAHs species, which are directly transported.
- Then we re-express the species diffusive flux vector in function of the transported variables, which will modify the set of Equations 5.42

Expression of the heat flux vector

Recalling the expression of q_i derived for the extended FPV model, we can split the contributions due to PAH transported and the gaseous species tabulated in $\mathcal{A}_j^{\text{tab}}, \mathcal{M}_j^{\text{tab}}$ and $\mathcal{L}_j^{\text{tab}}$:

$$q_i = -\lambda \frac{\partial T}{\partial x_i} - \sum_{j=1}^{N_{\text{fic}}} \frac{\rho}{W} \left[\mathcal{A}_j^{\text{tab}} + \mathcal{M}_j^{\text{tab}} \Delta T - \mathcal{L}_j^{\text{tab}} h \right] \frac{\partial Y_{\text{fic},j}}{\partial x_i} - \sum_{j=1}^{N_{\text{PAH}}} \left[\frac{\rho}{W} \left[\mathcal{A}_j^{\text{PAH}} + \mathcal{M}_j^{\text{PAH}} \Delta T - \mathcal{L}_j^{\text{PAH}} h \right] \frac{\partial X_{\text{PAH},j}}{\partial x_i} \right] \quad (5.44)$$

where the quantities superscripted *tab* refers now to non-PAH values:

$$\mathcal{A}_j^{tab} = \sum_{\substack{k=1 \\ k \neq PAH}}^N h_k D_k W_k \frac{\partial X_k}{\partial Y_{fic,j}} \quad (5.45)$$

$$\mathcal{M}_j^{tab} = \sum_{\substack{k=1 \\ k \neq PAH}}^N Cp_k D_k W_k \frac{\partial X_k}{\partial Y_{fic,j}} \quad (5.46)$$

$$\mathcal{L}_j^{tab} = \sum_{\substack{k=1 \\ k \neq PAH}}^N D_k W_k \frac{\partial X_k}{\partial Y_{fic,j}} \quad (5.47)$$

and the quantities superscripted *PAH* refers to the 7 PAHs considered and are tabulated separately with the 3 previous expressions :

$$\mathcal{A}_j^{PAH} = \sum_{k=1}^{N=PAH} h_k^{PAH} D_k^{PAH} W_k^{PAH} \quad (5.48)$$

$$\mathcal{M}_j^{PAH} = \sum_{k=1}^{N=PAH} Cp_k^{PAH} D_k^{PAH} W_k^{PAH} \quad (5.49)$$

$$\mathcal{L}_j^{PAH} = \sum_{k=1}^{N=PAH} D_k^{PAH} W_k^{PAH} \quad (5.50)$$

Expression of the transport equation of PAHs :

The general transport equation of the *j* - *th* PAH is written :

$$\frac{\partial \rho Y_{PAH_j}}{\partial t} + \frac{\partial \rho u_i Y_{PAH_j}}{\partial x_i} = -\frac{\partial}{\partial x_i} (J_{i,j}) + \dot{m}_{PAH_j} \quad (5.51)$$

with $J_{i,j}$ the diffusive species-flux vector of the *j* - *th* PAH, is :

$$J_{i,j} = -\rho D_j \frac{W_j}{W} \frac{\partial X_j}{\partial x_i} + \rho Y_j \sum_{l=1}^N D_l \frac{W_l}{W} \frac{\partial X_l}{\partial x_i} \quad (5.52)$$

The first term does not need to be modified as X_j can be computed directly from Y_j transported in the CFD solver. The second term involves all the species of

the mechanism : it needs to be split into the PAHs species (directly computed) and the others (tabulated as done for the FPV/RFPV extended approach). This leads to the following expression :

$$J_{i,j} = -\rho D_j \frac{W_j}{W} \frac{\partial X_j}{\partial x_i} + \rho Y_j \sum_{l=1}^{N=PAH} D_l \frac{W_l}{W} \frac{\partial X_l}{\partial x_i} + \rho Y_j \sum_{k=1}^{N_{fic}} \left[\sum_{\substack{l=1 \\ l \neq PAH}}^N D_l^{tab} W_l \frac{\partial X_l}{\partial Y_{fic,k}} \right] \frac{\partial Y_{fic,k}}{\partial x_i} \quad (5.53)$$

Recalling the definition of \mathcal{L}_k^{tab} (equation 5.47), we get :

$$J_{i,j} = -\rho D_j \frac{W_j}{W} \frac{\partial X_j}{\partial x_i} + \rho Y_j \sum_{l=1}^{N=PAH} D_l \frac{W_l}{W} \frac{\partial X_l}{\partial x_i} + \rho Y_j \sum_{k=1}^{N_{fic}} \mathcal{L}_k^{tab} \frac{\partial Y_{fic,k}}{\partial x_i} \quad (5.54)$$

which gives the final formulation for the transported equation for each PAH :

$$\frac{\partial \rho Y_{PAH_j}}{\partial t} + \frac{\partial \rho u_i Y_{PAH_j}}{\partial x_i} = -\frac{\partial}{\partial x_i} \left(-\rho D_j \frac{W_j}{W} \frac{\partial X_j}{\partial x_i} + \rho Y_j \sum_{l=1}^{N=PAH} D_l \frac{W_l}{W} \frac{\partial X_l}{\partial x_i} + \rho Y_j \sum_{k=1}^{N_{fic}} \mathcal{L}_k^{tab} \frac{\partial Y_{fic,k}}{\partial x_i} \right) + \dot{m}_{PAH_j} \quad (5.55)$$

Let us recall that \dot{m}_{PAH_j} is given by the relaxation model (see Equation 5.43).

5.3.3 Validation in AVBP and comparison with REGATH

The same case as the one presented in Section 5.2.3 is retained. 7 PAHs are transported in addition to two equations for Z and Y_c . The soot phase is described with the sectional method implemented in AVBP [Rodrigues et al. \(2018\)](#) with 25 sections. Figure 5.14 presents the obtained fields the PAH A_1 , the volume fraction f_V and the number density of particles N_{part} . The last two fields are given by the sectional model.

The comparison of A_1 , f_V and N_{part} with the REGATH 1D flamelet solver is shown Figure 5.15. Here again, an almost perfect agreement is obtained which validates the approach and the methodology.

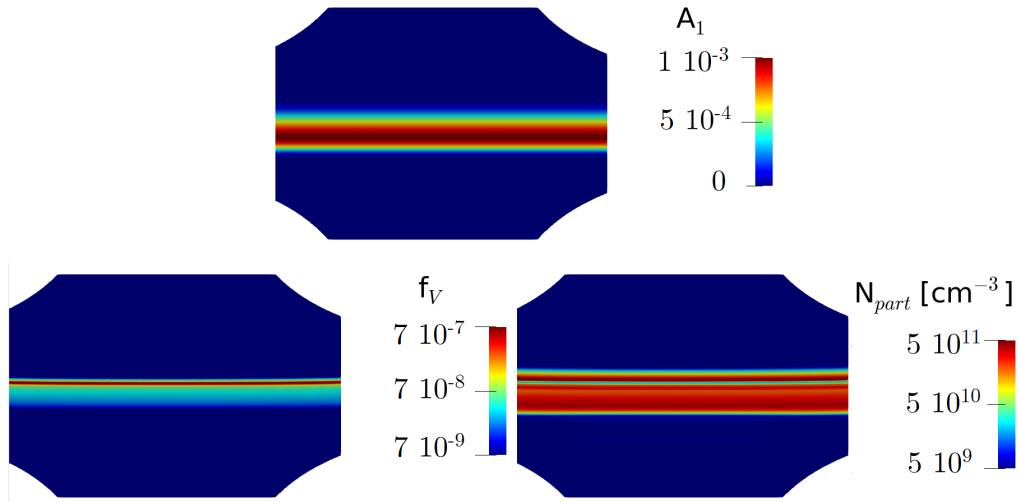


Figure 5.14: Obtained fields on the sooty counterflow diffusion flame computed in AVBP. The strain rate is set at $120s^{-1}$.

5.4 Conclusion

The chosen soot and combustion modeling are similar to the previous CFD simulations carried out by P. Rodrigues in his thesis. The corresponding results in turbulent flames have been used to quantify soot and gas radiation in chapters 3 and 4. The modeling approach consists in several parts:

- FPV/RFPV model to minimize the CPU cost and keep the information from detailed chemistry,
- A model of transported PAH as flamelet assumption is not valid for such species,
- The soot sectional model for the soot phase. It provides detailed description of soot mechanisms (formation, growth, oxidation) and also gives information on soot morphology, which is needed to compute RDGFA coefficients.

These models need to be adapted in order to take into account differential diffusion effects in the studied laminar flame:

- A new definition of FPV/RFPV parameters have been chosen,
- A transport equation is solved for each considered PAH,
- A consistent formulation of diffusive molecular transport (heat and species fluxes) is required.

These modifications have been implemented in the compressible flow solver AVBP using the TTC formalism and validated by comparison with the REGATH solver that takes into account detailed chemistry and transport.

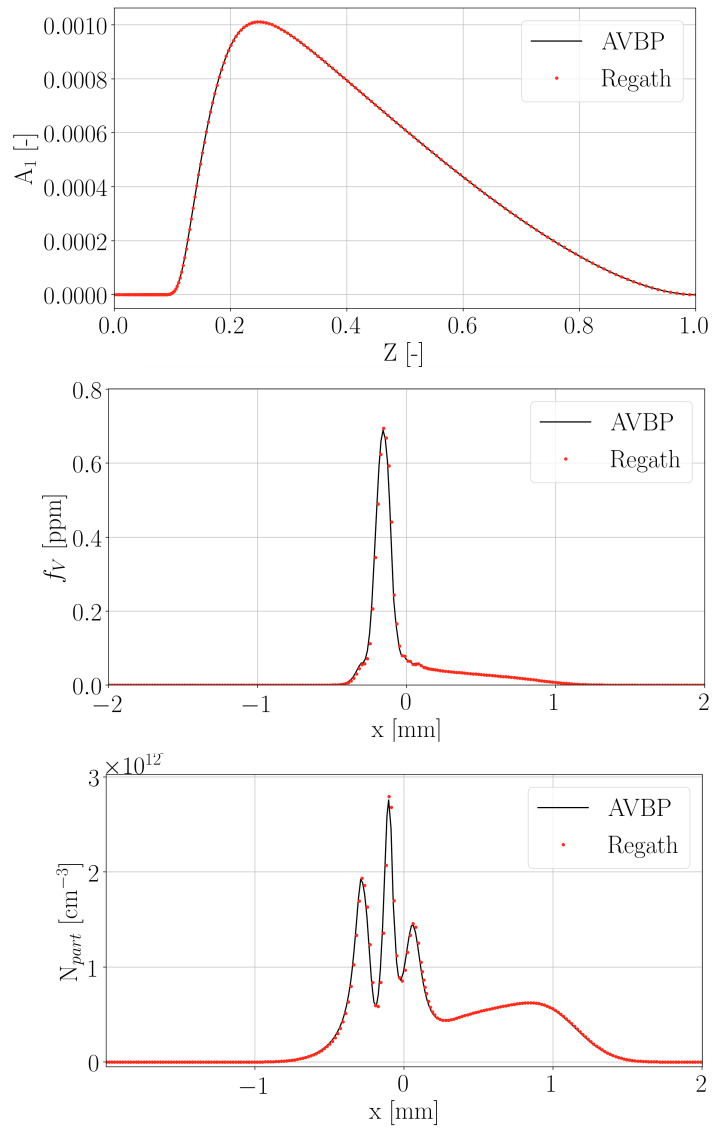


Figure 5.15: Comparison of the profiles obtained in AVBP and in the flamelet solver REGATH (sooting case). The strain rate is set at $120s^{-1}$.

Chapter 6

Coupled simulation of an axisymmetric ethylene air-flame

In Chapter 5, a model of tabulated chemistry has been derived to account for differential diffusion effect in sooty flames. This model, with the sectional method, is considered in this chapter to compute an axisymmetric laminar ethylene-air flame initially studied by Santoro and coworkers (Santoro et al. (1987)). In the literature, exhaustive experimental data is available in order to assess the accuracy of the radiative models discussed and developed until here. The objective in this chapter is to perform multi-physics simulations of Santoro's burner, by including detailed radiative properties and conjugate heat transfer at the burner walls. In a first part, the experimental and numerical set-up is presented and justified. In a second part, the 3-codes coupling framework used to perform such simulations is presented along with the modifications performed in this thesis. Finally, results and comparison with the literature data are presented and discussed.

Contents

6.1	Experimental and numerical set-up : Santoro's burner	168
6.1.1	Experimental set-up	168
6.1.2	Numerical set-up	169
6.1.3	Modifications of the coupling framework during the thesis:	178
6.2	Results and comparison with experimental data . .	179
6.2.1	Numerical fields	179
6.2.2	Comparison with experimental data	185
6.3	Analysis of fuel preheating	194
6.3.1	Wall and fuel temperature	194
6.3.2	Energy balance	198
6.3.3	Wall heat fluxes	198

6.4	Analysis of radiative heat transfer	200
6.4.1	Radiative power fields	200
6.4.2	Spectral emitted and absorbed radiative power	202
6.4.3	Transmissivity and soot/gas interaction	204
6.4.4	Accuracy of RDG-FA model and scattering impact	207
6.5	Conclusion	209

6.1 Experimental and numerical set-up : Santoro's burner

6.1.1 Experimental set-up

The burner consists of two concentric tubes, with the fuel flowing through the central tube and air through the outer passage. Inner and outer tubes have respectively a radius of 5.5mm and 50.8mm. The thickness of the tubes is 0.45mm. A uniform exit flow profile is ensured by screens and glass beads. A ceramic honeycomb section is used as the final section of the air flow passage to smooth the flow. A chimney is usually used to shield the flame from surrounding disturbance to make stable measurements.

Figure 6.1 represents a schematic of the experiment configuration. Holes in the chimney enables to probe different flame measurements.

In this study, ethylene and air are considered as fuel and oxidizer. The bulk inlet velocities are respectively of 3.98 cm/s for the ethylene and 8.90 cm/s for the air flow. The fairly simple resulting flame configuration enables to provide comprehensible measurements on soot particle structure : soot aggregate fractal dimension (Dobbins and Megaridis (1990)), primary particle diameter and number density (Megaridis and Dobbins (1988), Dobbins (1989)), soot aggregate number density (Puri et al. (1993)), and the average number of primary particles per aggregate (Iyer et al. (2007)). Additional results focusing on soot radiative properties are also available in the literature. In the study by Puri et al. (1993), extinction coefficients, scattering cross-sections and radiative intensities are obtained using Laster Extinction and Scattering technique, at 514 nm, and transmittances are given in the study by Santoro et al. (1987). Tomographic reconstructions have been used in work by Best et al. (1991) to obtain radiances and transmittances for several wavelengths. Finally, radiative intensities at 800 nm at different heights above the burner are provided in the study by Lu et al. (2009).

The numerous experiments carried out on this flame have enabled to characterize soot formation mechanisms as depicted in Figure 6.2.

Near the burner exit, PAHs are forming and lead to soot formation due to particle inception. Surface growth, which is the dominant mechanism in this

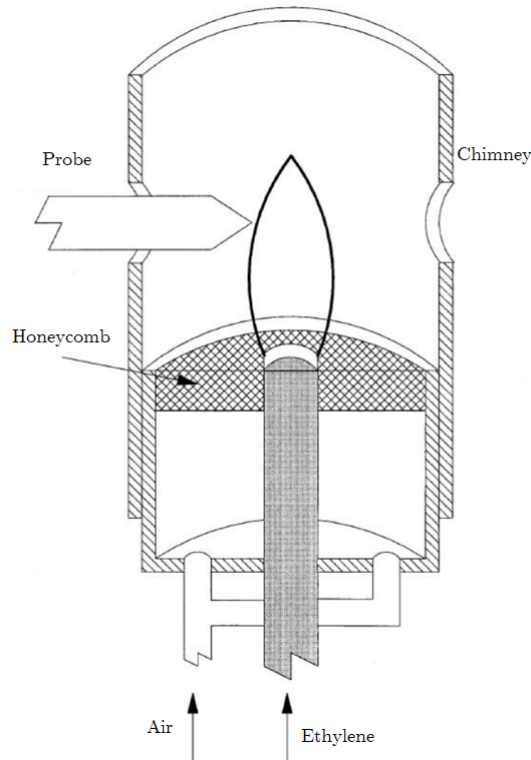


Figure 6.1: *Schematic of Santoro's burner. Extracted from Santoro et al. (1987).*

type of flame, occurs downstream the burner. This leads to an important soot volume fraction (around 8 ppm) observed near the wings of the flame (corresponding to the luminous flame envelope), before being oxidized. Such a simple configuration enables to challenge soot models, without the difficulties introduced by turbulence modeling or complex chemical fuel description.

6.1.2 Numerical set-up

6.1.2.1 Importance of codes-coupling approach in laminar flames

Most of the coupled CFD simulations on laminar diffusion flames are focusing on flow solver-radiation framework (Liu et al. (2004), Wu and Zhao (2020)) since the effect of radiative models on the flame temperature and soot volume fraction are noticeable (around 100-150 K, and almost 1 ppm of difference for soot volume fraction). In most cases, the temperature of the fuel inlet is set higher than the ambient temperature, at 400 K for the investigated Santoro's configuration, in order to reproduce the fuel preheating effect from the hot burner walls. However, there is no experimental data of radial temperature distribution at the exit of the pipe nor along the pipe to confirm such value.

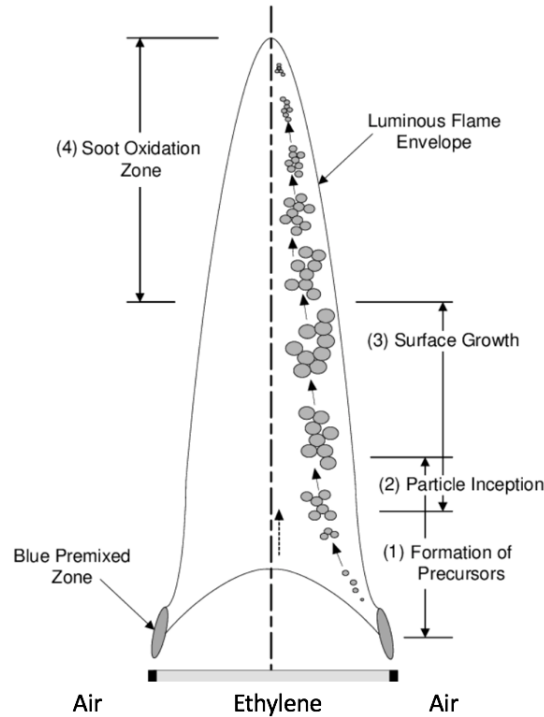


Figure 6.2: Soot formation mechanisms in a laminar diffusion coflow flame. Extracted and adapted from [Intasopa \(2011\)](#).

Fuel preheating studies has received a specific interest in laminar flames, since it has an impact on velocity and temperature profiles predicted numerically. In the work by [Guo et al. \(2002\)](#), two computations have been carried out : one imposing directly a temperature of 400K for the fuel inlet (without considering the fuel pipe), and one taking into account isothermal boundary conditions (specifying a temperature profile) on the fuel pipe to take into-account fuel heating. They found that the soot volume fraction increased when considering fuel preheating in this configuration. Let us notice that temperature radial profiles along the domain have been measured by Gulder ([Gülde et al. \(1996\)](#)), but no wall temperature have been reported.

This influence of preheating on soot mechanisms has been confirmed experimentally ([Konsur et al. \(1999\)](#)). A recent study carried out by [Qi et al. \(2020\)](#) imposed different values of the fuel temperature on the Santoro's configuration for different fuels: methane, ethylene with and without nitrogen dilution. A strong impact on soot volume fraction prediction is shown on each case. Similar conclusions were found for air-preheating in a methane/air diffusion flame ([Mandal et al. \(2006\)](#)).

Finally, it is important to notice that fuel preheating can have an impact on the stabilization of laminar flames. Methane and hydrogen coflow-diffusion flames have been numerically investigated in the work by [Gao et al. \(2017\)](#) by modifying the temperature at the burner lip. It has been found that the flame is either attached (for high lip temperatures) or detached (for low lip temperatures) for methane fuels.

The literature shows the importance of taking into account the fuel preheating. Despite the role of heat transfer in such configurations, the proper modeling of the burner and fuel temperatures with coupled simulations involving conjugate heat transfer has never been considered. The first objective of this chapter is therefore to accurately describe the fuel pre-heating *without* imposing ad-hoc temperature profiles or specific fuel temperature. Several codes must be coupled in order to take into account these effects. Three codes are considered in this study and are presented hereafter.

6.1.2.2 CFD solver : AVBP

The following simulations are carried out using the AVBP solver ([Schönfeld and Rudgyard \(1999\)](#)) along with the tabulated chemistry model developed in Chapter 5. The AVBP solver is a parallel CFD code, developed at CERFACS which solves the three-dimensional compressible Navier-Stokes equations on structured and unstructured meshes. The high-order TTGC scheme ([Colin and Rudgyard \(2000\)](#)) is considered in the following.

The lookup table used to describe gaseous phase is discretized in $100 \times 100 \times 20$ grid points, for Z , C and H variables respectively. Three transport equations for Z , Y_c and h' are considered in AVBP, and 25 sections are transported for the soot phase, to describe the particle size distribution. The PAH transport model, already introduced in Chapter 5, accounts for 7 PAHs (from A1 to A7). The database used to generate the look-up table is composed of 1D-counterflow diffusion flames, generated with the REGATH package ([Franzelli et al. \(2013\)](#)) and the detailed kinetic scheme KM2 with differential diffusion. The extended RFPV formulation accounting for differential diffusion, developed in Chapter 5 is considered.

Buoyancy effects in this laminar configuration are important and are taken into account by considering a gravity source term in the momentum and energy equations.

The computational domain (Figure 6.3) is composed of two inlets, where the temperature, the composition and the velocity are specified, and one outlet where the pressure is imposed. Inlets and outlet are based on the NSCBC

formalism (Poinso (1992)), which has been adapted to the tabulated chemistry used in the present work (Vicquelin et al. (2011)). The domain extends to 12 cm downstream the pipe, and 8 cm in the radial direction. The pipe is finely meshed with $\Delta x \approx 0.1$ mm at the beginning of the pipe down to $\Delta x \approx 0.05$ mm at the exit. The mesh is fine enough to capture the boundary layer development on the outer wall of the pipe on the coflow side. The pipe length is 15 cm, which is long enough such that the pipe reaches the ambient temperature away from the attached flame.

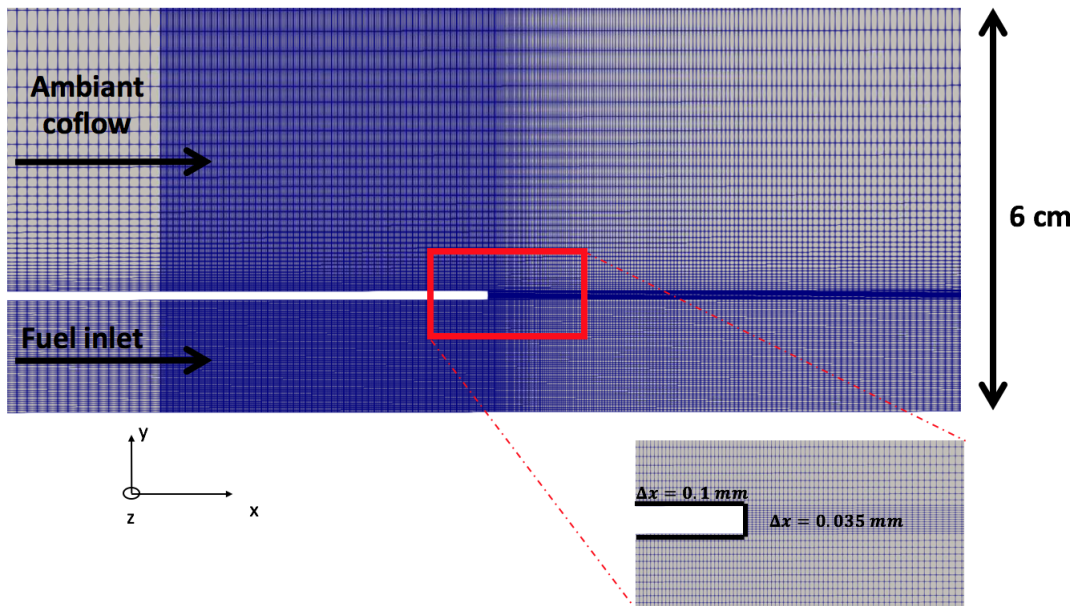


Figure 6.3: Visualisation of the computational domain and zoom on the pipe area.

In order to reduce the mesh and, hence, save CPU time, simulations are performed on an axisymmetric configuration. This is done in AVBP with one cell in the orthoradial direction, and a specific boundary treatment at the axis. The mesh is then composed of 180 000 hexahedron cells, with 300 elements along the axis of symmetry. The detail of the used boundary conditions in the AVBP solver is provided in Table 6.1.

In Table 6.1, the velocity profiles imposed at fuel and oxidizer inlets are respectively a Poiseuille flow and a flat profile. The temperature and composition target values at both inlets provide boundary conditions for the transported scalars : Z (the mixture fraction), Y_c (the progress variable), h' (the fictive enthalpy), e_t (the total energy) and $Y_{PAH,i}$ (the i PAHs species). No-slip wall conditions are considered for the pipe walls. These walls' temperature field is determined in a conjugate heat transfer (CHT) approach with a separate solid solver, which solves the conduction problem in the walls. The corresponding set-up is detailed in the next sections. This coupling avoids to specify an ad-hoc temperature at the walls. This is of primal importance since the temperature

Name of the boundary	Type of boundary condition	Parameters
Inlet Fuel	NSCBC with specified temperature, species and velocity	Poiseuille flow : $U = 3.98$ cm/s $T = 300$ K Ethylene
Inlet Air	NSCBC with specified temperature, species and velocity	Flat profile : $U = 8.9$ cm/s $T = 300$ K Air
Outlet	NSCBC with specified pressure	$P = 1$ atm
Outer Lip Wall	No-slip wall	Isothermal wall : Coupled with solid solver
Lip Wall	No-slip wall	
Inner Lip Wall	No-slip wall	
External Wall	Slip wall	Adiabatic
Axis	Axisymmetry axis	

Table 6.1: List of boundary conditions used in the AVBP solver for the simulation of Santoro's non smoking flame.

at the walls is not provided in experimental data.

6.1.2.3 Solide solver : AVTP

The AVTP code (Jaure et al. (2013)) is used to solve the unsteady heat conduction within the solid walls with a spatial second-order Galerkin diffusion scheme (Donnea and Huerta (2003)) and a first-order backward Euler scheme time integration.

The AVTP domain length and mesh size are based on a preliminary mesh convergence study. A very fine mesh is applied near the burner lip and 2 cm upstream on the inner and outer walls : the same mesh size are applied in AVBP domain, in order to have conform meshes and to capture accurately the heat-fluxes evolution. A sketch of solid part is displayed Figure 6.4.

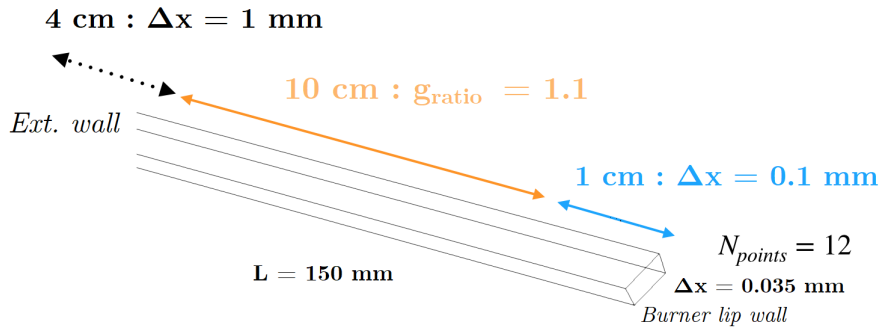


Figure 6.4: Solid part sketch with corresponding length and mesh sizes. g_{ratio} is the growth rate applied.

The mesh is slightly coarsen along the pipe with a growth ratio $g_{ratio} = 1.1$ in order to reduce the total number of cells.

The pipe is composed of 6 faces with the following boundary conditions :

- The burner lip wall where a heat-flux is prescribed from AVBP
- The burner inner/outer walls where a heat-flux is also prescribed
- The side walls where adiabatic condition is prescribed such that the axisymmetry is prescribed
- The external wall where an isothermal condition of $T_w = 300$ K is imposed

6.1.2.4 Radiative solver : Rainier

Finally, the radiative power and fluxes are computed using the Rainier Monte-Carlo solver. The Randomized Quasi-Monte-Carlo (RQMC) method (Lemieux (2009)) based on Sobol low-discrepancy sequences is used and combined with the ERM method (Tessé et al. (2004)). Simulations are performed with a relative and absolute prescribed error of 1%. This choice is driven by a trade-off between accuracy and coupled simulations CPU time.

The ck-model and the RDG-FA model are retained for the gaseous phase and the soot particles. The scattering by soot particles is also taken into account in this simulation with all the methodologies developed in Chapter 2: forced-scattering and RQMC. The primary particles parameters of an aggregate (n_p , d_p) are given by the second surface-volume relationship proposed in Chapter 3 (**sv-model2**).

Emissivities for the three coupled walls (the burner lip, the inner and outer walls) are respectively set to 0.8 (oxidized steel) for the burner lip and 0.5 for the two other walls as no experimental data are available for these values. For the other walls, an emissivity of 1 is prescribed.

6.1.2.5 Communication scheme for coupled simulations

A 3 codes coupling framework has been developed based on the OpenPalm library (Duchaine et al. (2015)) and is presented Figure 6.5.

At each coupling time step, the following communications are done :

- *Rainier* \Leftrightarrow *AVBP and AVTP* : The radiation solver sends the radiative power field P^R to AVBP and radiative fluxes ϕ_{wall}^R to AVTP. It receives information about species concentration (tabulated values of X_{H_2O} and X_{CO_2} , temperature, pressure, soot volume fraction and particle number density (to compute the scattering coefficient) from AVBP as well as the wall temperature from the solid solver for next radiative power and fluxes calculations
- *AVBP* \Leftrightarrow *AVTP and Rainier* : AVBP sends the fluid heat flux ϕ_{cc} to AVTP and the aforementioned informations to Rainier. AVBP receives the radiative heat flux calculated by Rainier and the wall temperature computed by AVTP.

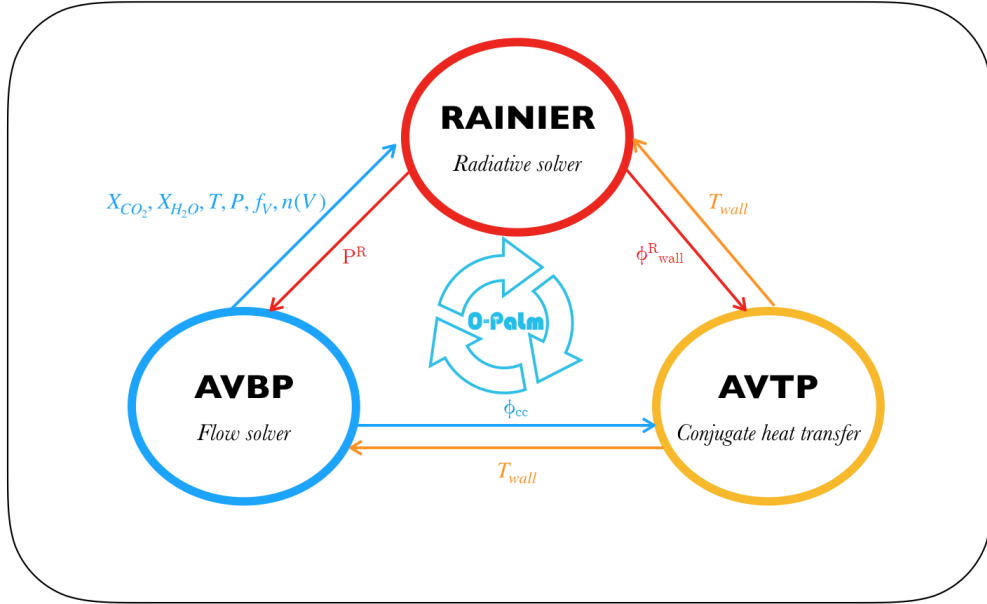


Figure 6.5: Communication scheme between the three solvers with corresponding exchanged quantities.

- $AVTP \Leftrightarrow AVBP$ and $Rainier$: AVTP sends the wall temperature to both solvers and receives fluxes from both solvers.

We note here that the coupling set-up corresponds to a classical Neumann-Dirichlet approach between AVBP and AVTP, as the temperature is prescribed for AVBP and the heat fluxes for AVTP. One drawback of this methodology is that the coupling period must be prescribed by the user before the simulation and is obviously case dependent. Several strategies to overcome this issue have been developed in the work of [Koren et al. \(2018\)](#) who proposed an adaptive coupling time step based on an hybrid Neumann-Dirichlet methodology : the HCND method. In our case, since the flow is stationary, such advanced method is not required and the classic approach is retained instead.

Table 6.2 gathers the total size of each mesh considered, and the number of CPU cores used for the simulation.

Code	Number of cells	Number of CPU cores
AVBP	180k	160
RAINIER	180k	70
AVTP	60k	10

Table 6.2: Repartition of the CPU cores between the different codes for the coupled calculation.

6.1.2.6 Coupling time-step

When a coupled simulation is performed, the coupling time-step indicates how often the codes are exchanging information. Such parameter has a strong impact on the stability of the simulation, on the accuracy of the results and the CPU cost associated. Between two coupling time-step, each code solves separately its own system of equation using the data exchanged at the previous coupling step (cf. Figure 6.5).

Ideally, the three codes should exchange data at each iteration ($N_{cpl} = 1$) : when AVBP performs 1 iteration, Rainier and AVTP solve respectively the radiative transfer equation and the equation of heat. Although efforts have been done to reduce the CPU cost of the Monte-Carlo simulation, such coupling is not affordable in practice.

This is mainly due to the simulation time required in AVBP to obtain a stationary state. Assuming that one wants to simulate 4 convective times, this corresponds to a simulation physical time of $t_{simu} \approx 6s$. Knowing that the fluid time-step, limited by the CFL condition, is around $\Delta t_{fluid} = 4 \cdot 10^{-7} s$, more than 14 millions of coupling would be required to reach t_{simu} . With the prescribed errors in the Monte-Carlo simulation, one Rainier iteration corresponds to 1 minute of real time (with 70 CPU cores), which means that around half a year is needed to perform this simulation. Hopefully, such a refined coupling with RAINIER is not needed given that the solver input fields barely change between two AVBP iterations, and that a steady state solution is sought. The coupling with thermal radiation will be safely coarsened.

In parallel, between two coupling exchanges, AVTP solves the instationary heat conduction problem, which corresponds to a simulated physical time $\Delta t_{cpl,solid}$. Two strategies can then be performed between two coupling exchanges :

- The coupling is *synchronous* : the physical time of both codes are the same. The simulated time between two coupling exchanges $\Delta t_{cpl} = \Delta t_{cpl,fluid} = \Delta t_{cpl,solid}$ is the same between the codes.
- The coupling is *desynchronous* (Duchaine et al. (2009)) : in this approach, the physical times of each code are not synchronized and the flow solver simulated a physical time of $\Delta t_{cpl,fluid}$ while the solid heat transfer solver simulated a physical time of $\alpha \Delta t_{cpl,fluid}$, much larger to accelerate the long thermal transient of the solid parts.

One can estimate a solid characteristic timescale for conduction, based on the pipe length and steel diffusivity coefficient, which gives $\tau_{solid} \approx 100s$. The strong difference with the convective fluid timescale of 1.5s prevents the use of the synchronous approach. A significant amount of computational resources

would be wasted to reach steady state. Therefore, the desynchronous approach is retained.

If the desynchronous parameter α is too important, the coupled simulation may become unstable (Duchaine et al. (2009)). Moreover, the accuracy of the result depends on N_{cpl} which must not be too large as well.

In order to select the parameter α , we have performed a transient AVTP stand-alone to assess the solid response to a flux perturbation. In this computation, the solid is initially set at 320 K, the mesh size and pipe length are the one determined before, and the heat flux from the fluid are imposed from the solution obtained in preliminary calculations where an *ad-hoc* temperature profile was specified. The solid time-step to solve the instationary problem is fixed at 1 ms. The obtained temperature profile is displayed Figure 6.6.

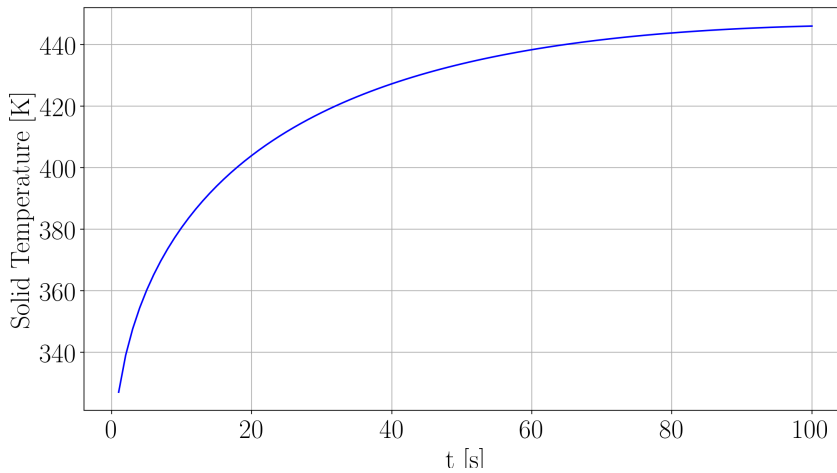


Figure 6.6: Pipe response to a heat-flux perturbation : temperature of the solid.

It can be seen that the temperature reaches a steady state around 100 s, which is consistent with our estimated characteristic timescale of the solid. However, in order to minimize the variation of temperature between two coupling iterations for AVBP, we have chosen to set $\Delta t_{cpl,solid} = 0.5$ s (which corresponds to a variation of around 10 K). Fixing this coupling period for AVTP, we have performed coupled calculations between AVBP and AVTP while changing the number of iterations N_{cpl} in AVBP between two coupling steps. It has been observed that, increasing N_{cpl} too much leads to oscillations of the temperature in the fluid domain. The choice of $N_{cpl} = 10000$ iterations enables to suppress these oscillations, without being too computationally expensive. Therefore, the corresponding desynchronisation parameter α can be calculated is equal to : $\alpha = 10000 \cdot 4 \cdot 10^{-7} / 0.5 = 2000$.

Finally, it is important to ensure that $N_{cpl} = 10000$ does not lead to an important error in our radiative solver. To do so, we consider the metric used in [Rodrigues et al. \(2019\)](#) to estimate the error associated to the coupling frequency. At iteration "0", AVBP and Rainier are exchanging their data, and Rainier is computing the radiative power P_0^R associated to its input data. The temperature sent by AVBP at this reference iteration is noted T_0 . The error is evaluated in terms of L2 error norms on the temperature and the radiative power after N_{cpl} iterations defined by :

$$\begin{aligned}\alpha_T(N_{cpl}) &= \sqrt{\int_V |T_{N_{cpl}} - T_0|^2 dV} / \sqrt{\int_V |T_0|^2 dV} \\ \alpha_{PR}(N_{cpl}) &= \sqrt{\int_V |P_{N_{cpl}}^R - P_0^R|^2 dV} / \sqrt{\int_V |P_0^R|^2 dV}\end{aligned}\tag{6.1}$$

where V is the volume of the computational domain. In [Figure 6.7](#), both L2 error norms are plotted in function of the number of iterations N_{cpl} . It can be observed that, even for an important number of iterations, both errors are small. It is therefore possible to coupled less often while keeping a small error, with an accurate transient and without stability issues. N_{cpl} is then, in this specific case, limited by the AVBP-AVTP coupling part as oscillations may occur for high values of N_{cpl} . The retained value $N_{cpl} = 10000$ enables to have an error less than 1% for the coupling with thermal radiation, which is very satisfactory and consistent with the Monte-Carlo prescribed accuracy.

6.1.3 Modifications of the coupling framework during the thesis:

In this thesis, four main modifications to the communication scheme initially derived in P. Rodrigues thesis ([Rodrigues et al. \(2018\)](#)) have been performed in order to perform the simulations presented in the next sections :

- 1. Adapting the 3 codes coupling to the classic Neumann-Dirichlet approach : originally, the framework with the RAINIER solver was adapted to HCND method only, which requires additional exchanged variables not needed in this work.
- 2. Adapting the framework to axisymmetric configurations. In the considered configuration, multi-topology meshes are encountered : the axis wedge is meshed with prisms, while the remaining computational domain is meshed with hexahedron. Originally, the coupling scheme was adapted for a single mesh topology. Therefore, modifications of the subroutines handling exchanges were needed.
- 3. Including the scattering treatment in the coupling framework as it requires the detailed number density function to be exchanged between AVBP and Rainier.

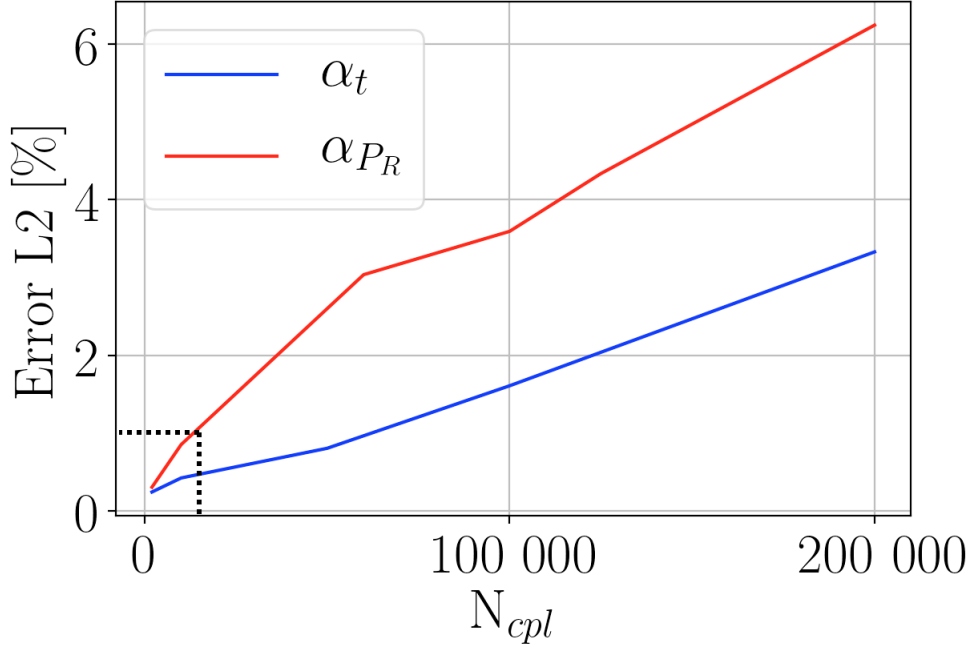


Figure 6.7: Evolution of L2 error norms of temperature T and radiative power as a function of the fluid solver iteration N_{cpl} .

- 4. Handling the connectivity between the different patches : the indexing of cells nodes, used to perform the connectivity between the codes, is different between the 3 codes and the coupling interface based on OpenPalm.

6.2 Results and comparison with experimental data

6.2.1 Numerical fields

6.2.1.1 Temperature and radiative participating species

Figure 6.8 presents the temperature, the molar fraction of CO_2 and H_2O , the soot volume fraction f_V and the progress variable Y_c after convergence of the coupled simulation.

The highest temperatures are obtained near the burner lip and along the iso-Z black line. These zones correspond to high progress variable Y_c values. The effect of the fuel pre-heating due to the coupling with the pipe is also noticeable as the temperature in the pipe increases from 300 K (upstream) to around 400 K at the exit of the pipe. Along the centerline, the temperature gradually increases, although a noticeable decrease is located where the soot volume

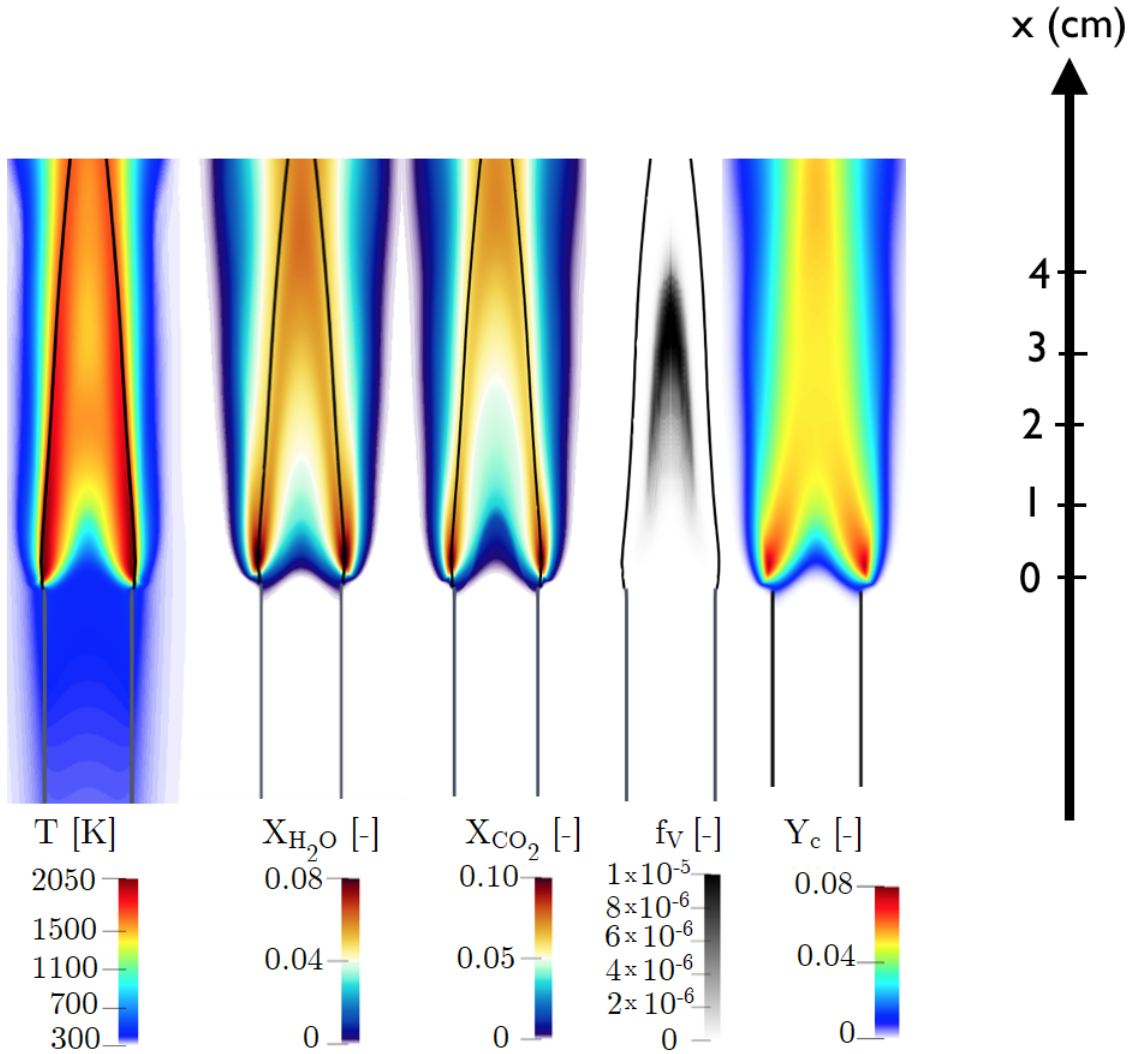


Figure 6.8: Temperature, molar fractions of H_2O and CO_2 , soot volume fraction, and progress variable results from the coupled simulation. The contour $Z = 0.064$ is also displayed in black line.

fraction is maximum (located 4 cm above the burner exit). An important maximum level of soot fraction is obtained along the centerline (around 10 ppm).

The obtained flame is attached, which disturbs the flow, especially near the burner lip. In this case, the flame dominates the flow field, and the maximum temperature is located near the burner lip, where high residence-times are observed (or low-strain rates). Recalling the S -curve presented in Chapter 5, which characterizes the counterflow diffusion flame, the progress variable Y_c is important for these strain-rates. This behaviour is confirmed in Figure 6.8

where the computed progress variable is displayed and achieve maximum values in this zone. It is worth noticing that, due to the presence of radiative species, the temperature achieved in this zone is 300K lower than the adiabatic temperature.

It is clear that, accounting for radiation in such configuration is essential in order to correctly predict the flame structure and the temperature fields. However, before analyzing the radiative power obtained in this coupled simulation, it is important to understand first how the different soot mechanisms leads to the computed soot volume fraction field in Figure 6.8.

6.2.1.2 Analysis of soot formation mechanisms

Figure 6.9 shows the obtained fields of soot volume fraction with the total particles number density N_{part} . The contour $Z = 0.064$ is also displayed with a solid black line.

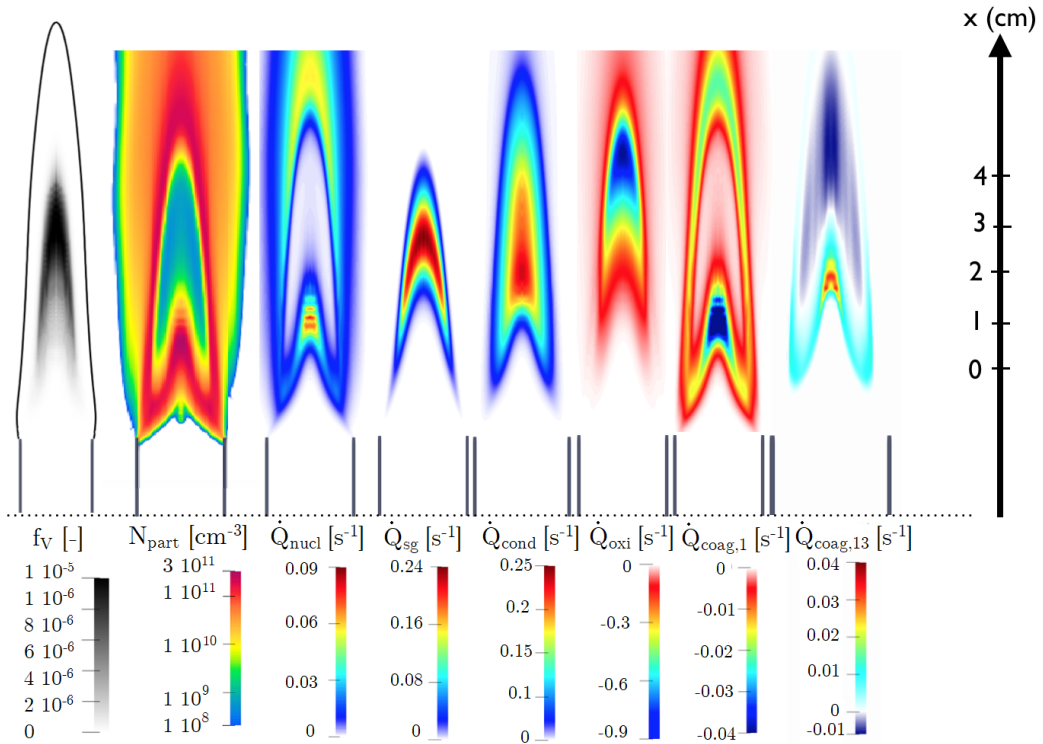


Figure 6.9: Soot volume fraction, total particles number density and soot source terms (nucleation, surface growth, coagulation, oxidation and condensation for two sections.)

One can notice that soot particles are located in the rich side of the flame (when $Z > 0.064$), while the maximum density of particle is encountered 1 cm

above the pipe exit, on the centerline, and along the flame wings. In order to understand how soot particles are organized in this flame, let us look at the different soot source terms also displayed Figure 6.9. Let us recall the different mechanisms at stake here :

- The nucleation (source term \dot{Q}_{nucl}) corresponds to the formation of the smallest soot particles through the dimerization collisional process
- The surface growth (source term \dot{Q}_{sg}) corresponds to the increase of the soot surface, governed by the HACA mechanism (Frenklach and Wang (1991))
- The coagulation, (source term \dot{Q}_{coag}) corresponds to the collision of two soot particles which form a bigger one
- The condensation (source term \dot{Q}_{cond}) corresponds to the collision between a soot particle and a PAH
- And the oxidation (source term \dot{Q}_{oxi}) corresponds to the destruction of a soot particle, due to the presence of O_2 and OH .

In Figure 6.9, nucleation, surface growth, condensation and oxidation source terms are sum over all of the 25 sections to extract the global contribution. Coagulation being an exchange between different sections with a null global contribution, the fields for section 1 and 13 are presented.

The nucleation process occurs in three main areas : at the bottom of the flame, on the centerline, and further downstream. In the study by Zhang et al. (2009), the nucleation rate along the centerline is reported for this flame, using a detailed mechanism and an advanced sectional method with a more complete PAH description. Qualitatively, the peak position is consistent with the obtained field Figure 6.9, however, the nucleation rate tends to monotonically decrease along the centerline, without re-increasing downstream. The same behaviour is observed in the work by Escudero (2019). Both studies are using detailed chemistry instead of a tabulated approach. This inconsistency is addressed later in this section.

The surface-growth mechanism occurs downstream the nucleation one : indeed, the new nuclei particles tend to increase their mass due to the presence of species such as the acetylene C_2H_2 which is the main contributor in the HACA mechanism. Such mechanism contributes to increase the soot volume fraction level. Looking at the values reached by the source term, it can be noticed that this mechanism dominates (of a factor 3) the nucleation process and is of the same order of magnitude as the condensation process. In the work by Escudero (2019), it has been reported that the condensation in this laminar diffusion flame is the mainly dominant process along the centerline, followed by the surface growth, which is consistent with the obtained fields in Figure 6.9.

The coagulation source term for the first section, along the centerline, is negative. This means that these small particles (formed with the nucleation) are "leaving" the section since their volume increases. These small particles are moved towards higher sections. In the 13th section for example, it can be observed that the term is positive upstream corresponding to a creation of particles belonging to this section and becomes negative downstream (similarly, these particles are moved towards bigger sections). Coagulation impacts the number density of particles : since the nucleation is less important than coagulation (around 3cm above the burner exit), bigger particles are formed which leads to an increase of the soot volume fraction, and a decrease of the density of particles.

Regarding the oxidation, it occurs at the top of the flame where O_2 is important (which corresponds to $Z = 0$ in our calculations). After this point (around 4 cm above the pipe exit), the soot volume fraction quickly decreases.

The inconsistency of the increasing nucleation rate after the oxidation region still needs to be explained. In order to understand this behaviour, Figure 6.10 reports three different PAH fields with increasing size : A_3 , A_4 and the biggest PAH considered, A_7 (CORONEN).

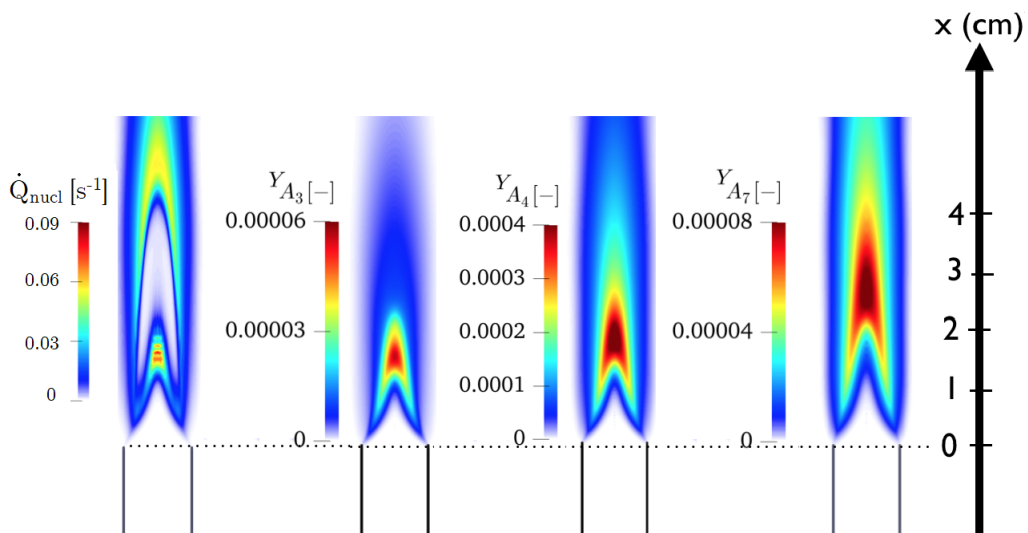


Figure 6.10: Mass fraction fields of three PAHs : A_3 , A_4 and A_7 . The nucleation source term is also displayed on the left.

The advantage of transporting the different PAHs using the multi-PAH model described in Chapter 5 enables to provide a finer analysis of the nucleation source term. The smallest PAHs are forming first, and are majoritarily located

along the centerline. This important PAH zone is responsible for the peak in the nucleation source term observed in Figure 6.10 at $x = 2$ cm. The PAH with a bigger size are formed downstream, and the biggest one, A_7 , is formed again near the centerline at around $x = 3$ cm. However, looking at Figure 6.9, the oxidation term dominates the nucleation process. Therefore, as the PAHs are forming the smallest soot particles, these particles are directly oxidized. The A_7 PAH mass fraction is still important after the oxidation zone (after 4 cm) and is directly correlated to the nucleation source term zone observed downstream.

It is important to note that the PAHs species are transported directly in the AVBP code. Their source term is not directly taken from the table, but are relaxed based on the transported PAH value (see Equation 5.43 in Chapter 5). The corresponding source term is shown Figure 6.11 for the PAH A_7 .

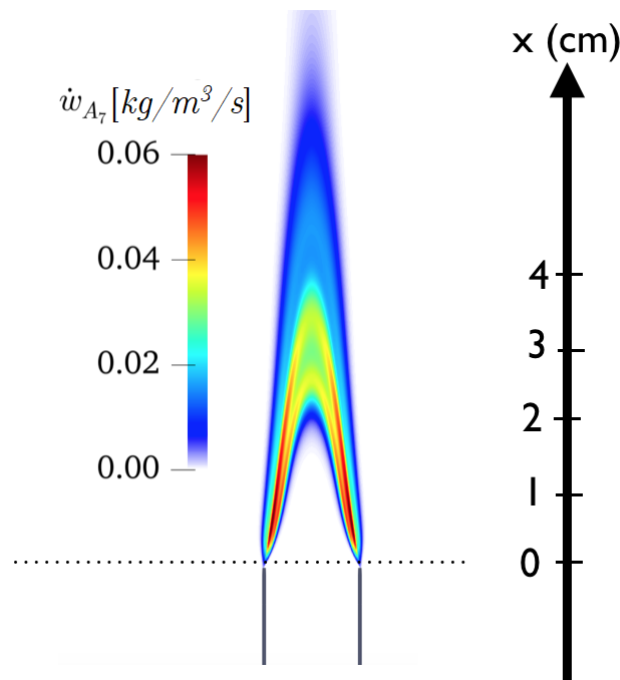


Figure 6.11: Source term of the biggest PAH considered in this study (A_7) based on the relaxation model presented in Chapter 5.

It can be observed that the source term is important near the burner lip and for $x \geq 3$ cm, which means such PAH is forming in these two regions. Consequently, the presence of PAH at 4 cm and the absence of significant oxidation or coagulation explains the nucleation observed downstream. Therefore, the inconsistency of the nucleation source term can be attributed to an inaccurate PAH description due to the tabulation employed.

To sum up, near the burner-lip, the nucleation process dominates which tend to increase the particle number density N_{part} . Downstream, the coagulation tends to decrease the particle number density as it becomes the dominant process. At a certain point, the coagulation impact decreases, and, since PAHs are still forming in this region, the nucleation tend to increase, which again increases the particle number density.

6.2.2 Comparison with experimental data

6.2.2.1 Centerline

The results of the coupled simulations are first compared against available experimental data along the centerline : temperature, axial velocity, soot volume fraction and number density of particules, in Figure 6.12.

Axial velocity and temperatures profiles are in a very good agreement with the available experimental data. The effect of fuel preheating can be highlighted on the temperature profile as the obtained value at $x = 0$ (corresponding to the exit of the pipe) is greater than 300 K. The temperature around 3 cm starts to decrease due to the increasing heat-losses from soot radiation. f_V and N_{part} are over-predicted along the centerline. Uncertainties in the chemical mechanism and in the retained sectional method can explain these results. It can be noticed, however, that the good order of magnitude is retrieved for the f_V with the same trend than the experimental data. The peak location along the centerline is also well retrieved. Finally, the tabulated approach with the sectional method fails to predict the particle number density evolution after 4cm as this number increases instead of remaining constant. This issue has been discussed in Section 6.2.1.2.

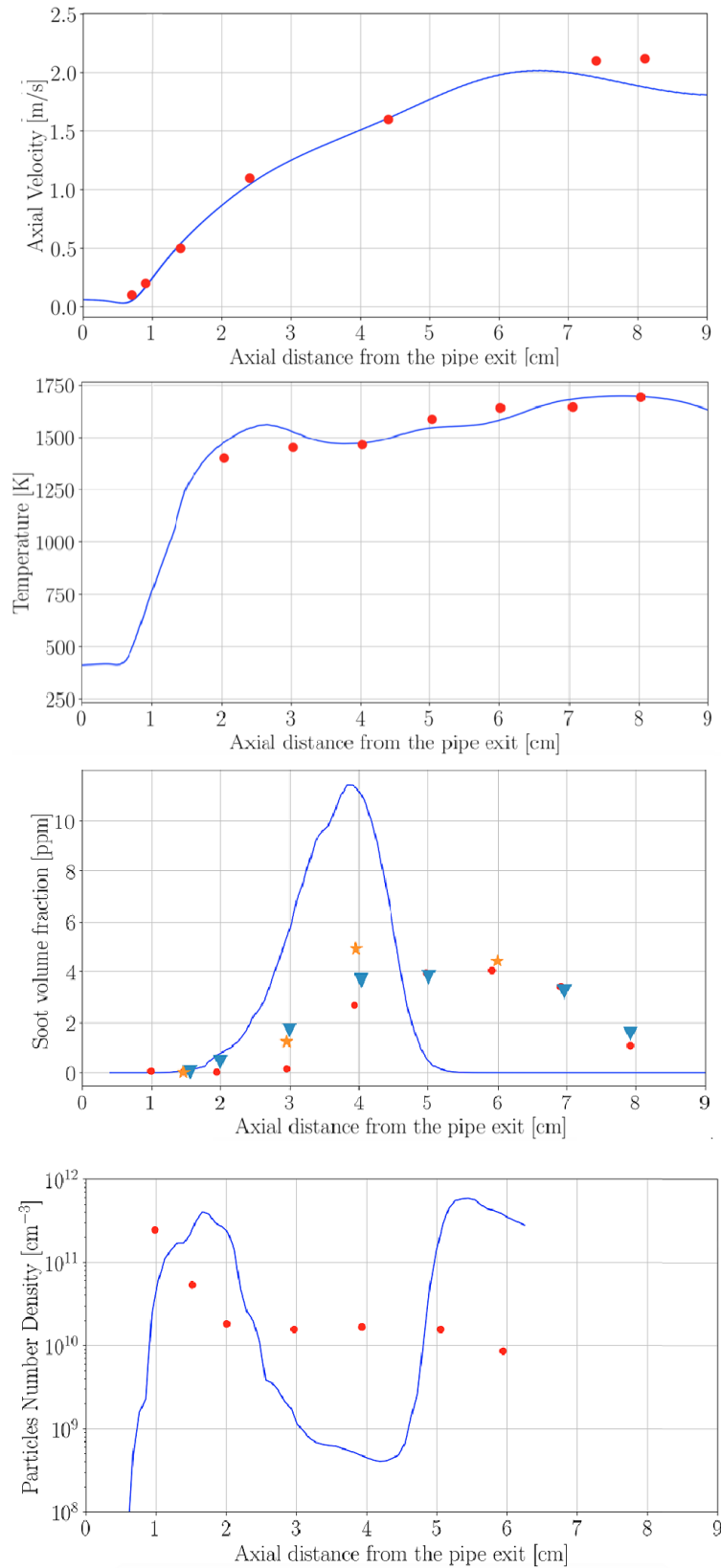


Figure 6.12: Centerline profiles of temperature, axial velocity, soot volume fraction and N_{part} with comparison to experimental data : Santoro et al. (1983) (\bullet), Köylü et al. (1997) (\blacktriangledown), McEnally et al. (1997) (\star).

Figure 6.13 compares the calculated axial distribution of the integrated soot volume fraction $f_{V,int}$ with the measurements of Santoro et al. (1987). Such quantity is defined as $\int_0^\infty f_v 2\pi r dr$ and is related to the total amount of soot formed at a given axial height. Due to the high oxidation observed in Section 6.2.1.2, the evolution of the integrated soot volume fraction is not captured downstream the flame. However, the levels achieved with the experimental data are in a good agreement up to $x = 3$ cm.

Soot oxidation is due in the retained model to the O_2 and OH presence and are obtained in the look-up table knowing the values of Z , Y_c and h' . In Liu et al. (2006), comparisons between a 2D simulation with detailed chemistry and with a flamelet approach are carried out on an axisymmetric coflow ethylene-air flame, without soot formation nor heat transfer. The distribution of mass fraction OH is overpredicted along the centerline using the flamelet model and can explain, in our case, the high oxidation rate observed.

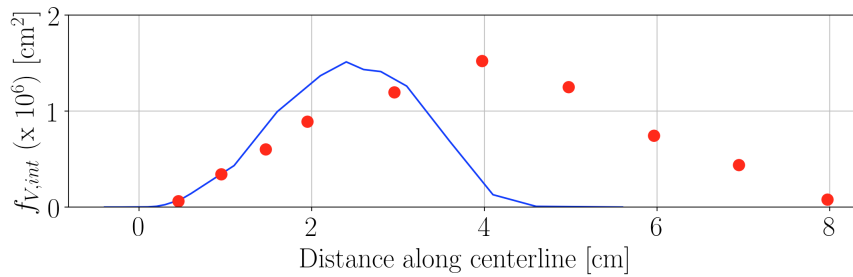


Figure 6.13: *Integrated soot volume fraction distribution along the axis height above the burner : experimental data from Santoro et al. (1983) (●)*

Finally, the impact of the optically thin assumption on the centerline soot volume fraction profile is assessed in Figure 6.14. In this additional calculation (OTA in Figure 6.14), the wall temperature profile is imposed identical to the one obtained in the reference coupled calculation (MC in Figure 6.14)). Considering the optically thin assumption lowers the temperature along the centerline, which impacts soot formation since the soot volume fraction decreased. However, the OTA strongly under-estimates the temperature comparing to experimental data. The moderate impact on f_V shows that achieving significantly better soot predictions is then not related here to radiation modeling, but is rather impacted by the tabulated chemistry approach considered and large uncertainties that remain in the soot modeling. The soot sectional approach is the same as the one developed in Rodrigues et al. (2018) and can be further improved.

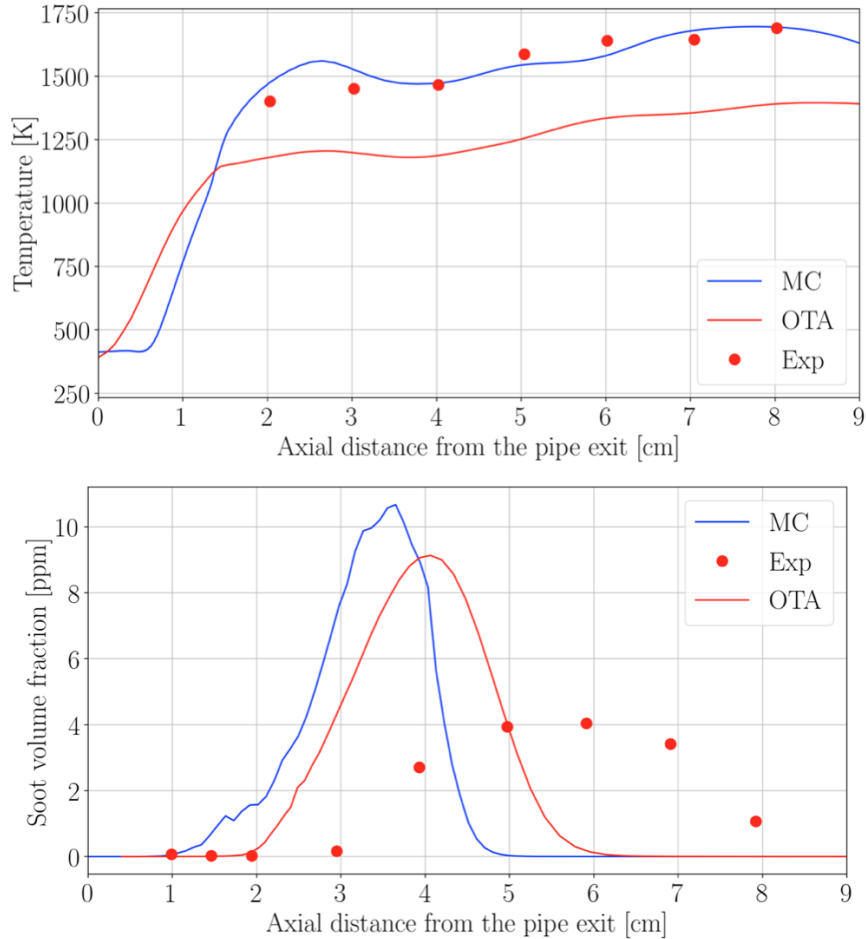


Figure 6.14: Comparison Coupled Calculation / optically thin assumption on the predicted soot volume fraction along the centerline and temperature. Experimental data ((●)) from Santoro et al. (1983).

6.2.2.2 Radial profiles

Figure 6.15 presents the temperature radial profiles at three axial heights (0.7, 2 and 7 cm) compared with experimental data (Santoro et al. (1983)).

A good agreement with experimental data is observed for the three considered heights. However, the temperature peak is obtained slightly closer to the axis for the cases at 0.7 cm and 2 cm. Further downstream, the temperature is constantly underpredicted.

Figure 6.16 presents the obtained axial velocity radial profiles. At the bottom of the flame (smallest heights above the burner), a very good agreement is obtained with experimental data. On the top, due to the low predicted temperatures, the velocity is also under-predicted compared to experimental data.

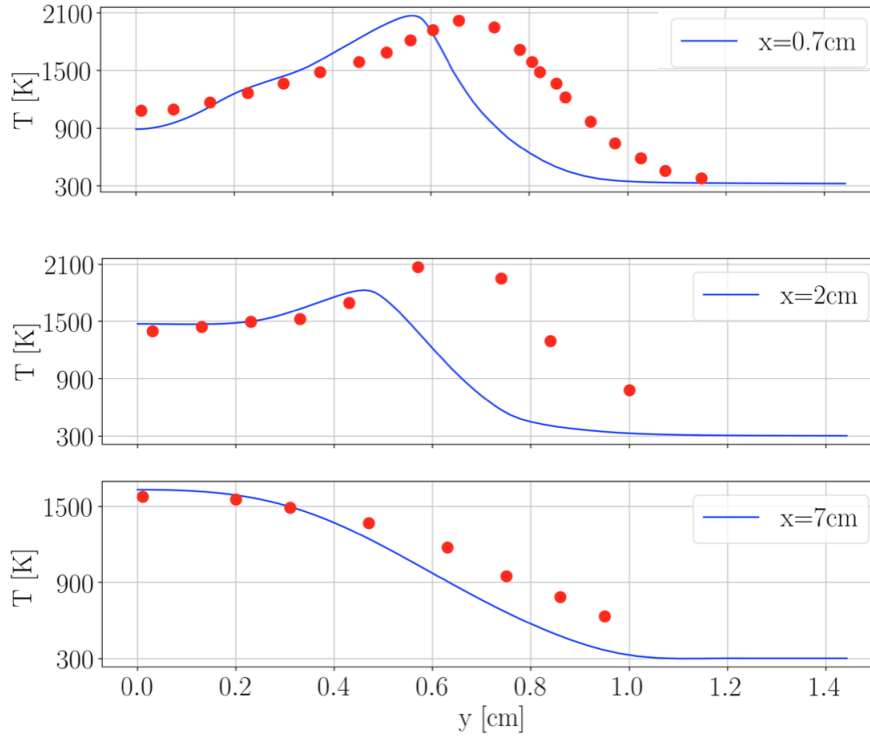


Figure 6.15: Comparison of radial temperature profiles obtained for three different axial heights above the burner with experimental data from Santoro et al. (1983) (●)

The same behaviour is observed for radial velocity profiles displayed in Figure 6.17.

Surface growth and oxidation of soot particles are strongly correlated to the presence of acetylene (C_2H_2) and OH respectively. The tabulated chemistry enables to retrieve the values of such species knowing Z , Y_c and h' in the domain. Such reconstructed values are plotted and compared against available experimental values in Figure 6.18.

Looking at the values reached for both species at $x = 0.7$ cm, reasonable agreement with experimental data is obtained as the trend and the values are correctly reproduced. However, for $x = 2$ cm, although the global evolution of the species are well retrieved, significant under-prediction of C_2H_2 and an over-prediction of OH are observed. At $x = 1.5$ cm, the soot volume fraction profile f_V is reasonably well predicted, but in our simulation, oxidation occurs for lower y values than the experimental data.

In order to understand the relation between C_2H_2 and OH predictions and f_V , the soot volume fraction f_V at $x = 2$ cm is also reported Figure 6.18. At this

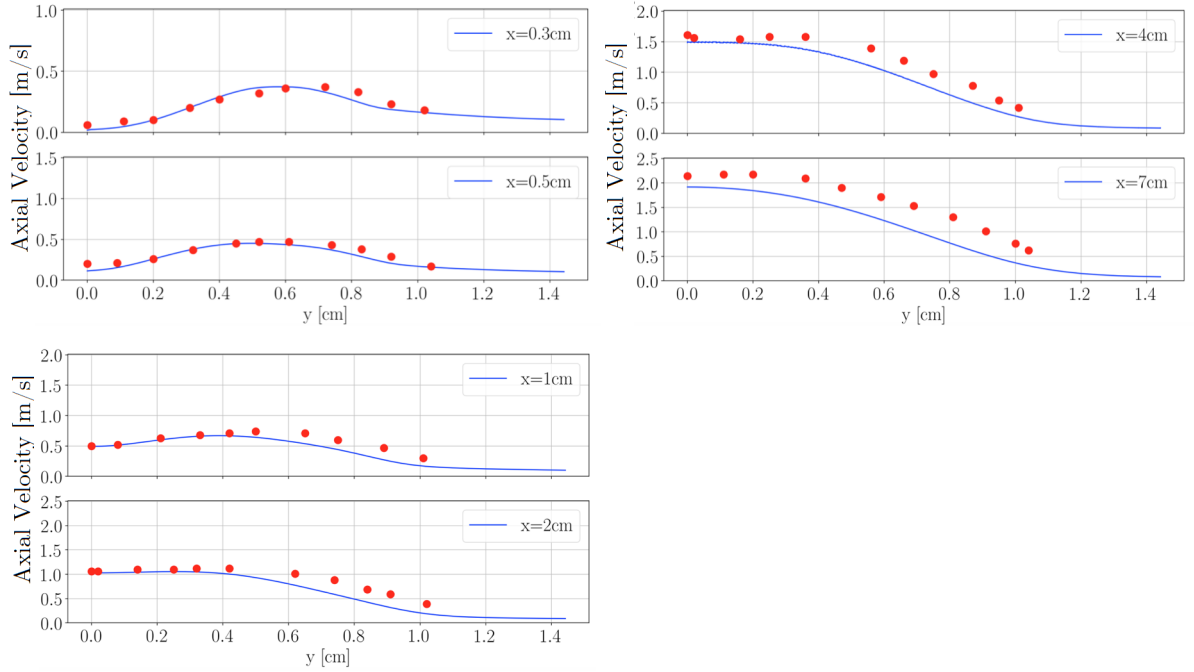


Figure 6.16: Comparison of axial velocity profiles for six axial heights above the burner with experimental data from *Santoro et al. (1983)* (●).

height, the presence of C_2H_2 activates the surface growth mechanism, which leads to the increase in soot volume fraction for $y < 0.5$ cm. On the contrary, the oxidation mechanism is very important for $y > 0.5$ cm. Such mechanism leads to the soot destruction, which explains the absence of f_V at this location and hence the under-prediction of f_V for higher y .

The prediction of these species are therefore important to accurately predict f_V . The flamelet model needs to be accurate in such configuration so these species can be reconstructed via an interpolation within the flamelet database. This is discussed later on in Section 6.2.2.4.

6.2.2.3 Flame wings

Soot-related quantities along the pathline maximum soot volume fraction at the outer edge of the flame (near stoichiometry), usually referred as "flame wings", are plotted Figure 6.19 : the soot volume fraction, the mean number of primary particles \bar{n}_p and diameter \bar{d}_p . As explained in Chapter 4, these last two quantities are computed from an assumed surface-volume relationship.

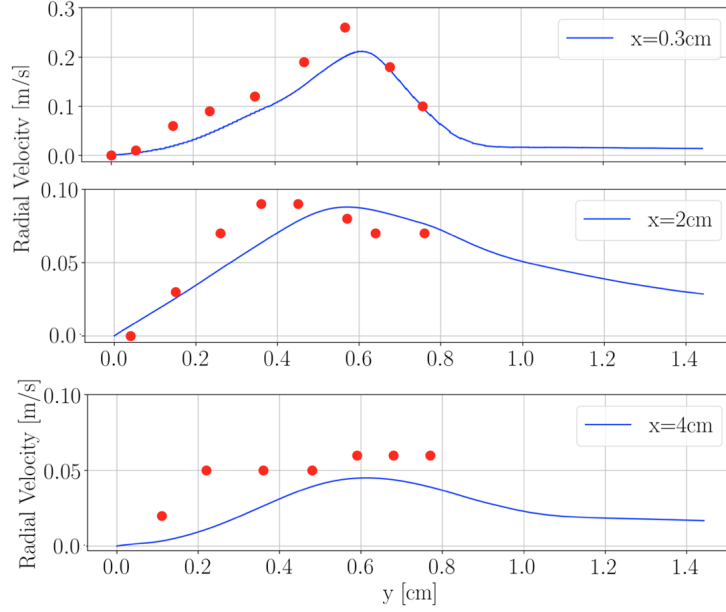


Figure 6.17: Comparison of radial velocity profiles for six axial heights above the burner with experimental data from *Santoro et al. (1983)* (●).

\bar{n}_p and \bar{d}_p are defined similarly to the study of *Zhang et al. (2009)* :

$$\bar{n}_p = \frac{\int_0^{+\infty} n(V)n_p(V)dV}{\int_0^{+\infty} n(V)dV} \quad (6.2)$$

$$\bar{d}_p = \frac{\int_0^{+\infty} n(V)d_p(V)dV}{\int_0^{+\infty} n(V)dV} \quad (6.3)$$

where n_p and d_p are the number and diameter of primary particles of an aggregate with a volume V , given by the surface-volume relationship.

The evolution of \bar{n}_p and \bar{d}_p are in a fair agreement with experimental data with a correct order of magnitude. \bar{d}_p is slightly underpredicted and \bar{n}_p is over-predicted of a factor 3. Let us recall that the surface-volume relationship proposed is an ad-hoc formulation, and more effort needs to be done in the soot morphology modelling. The soot volume fraction levels reached are consistent with experimental data, however, the peak is once again predicted closer to the burner exit.

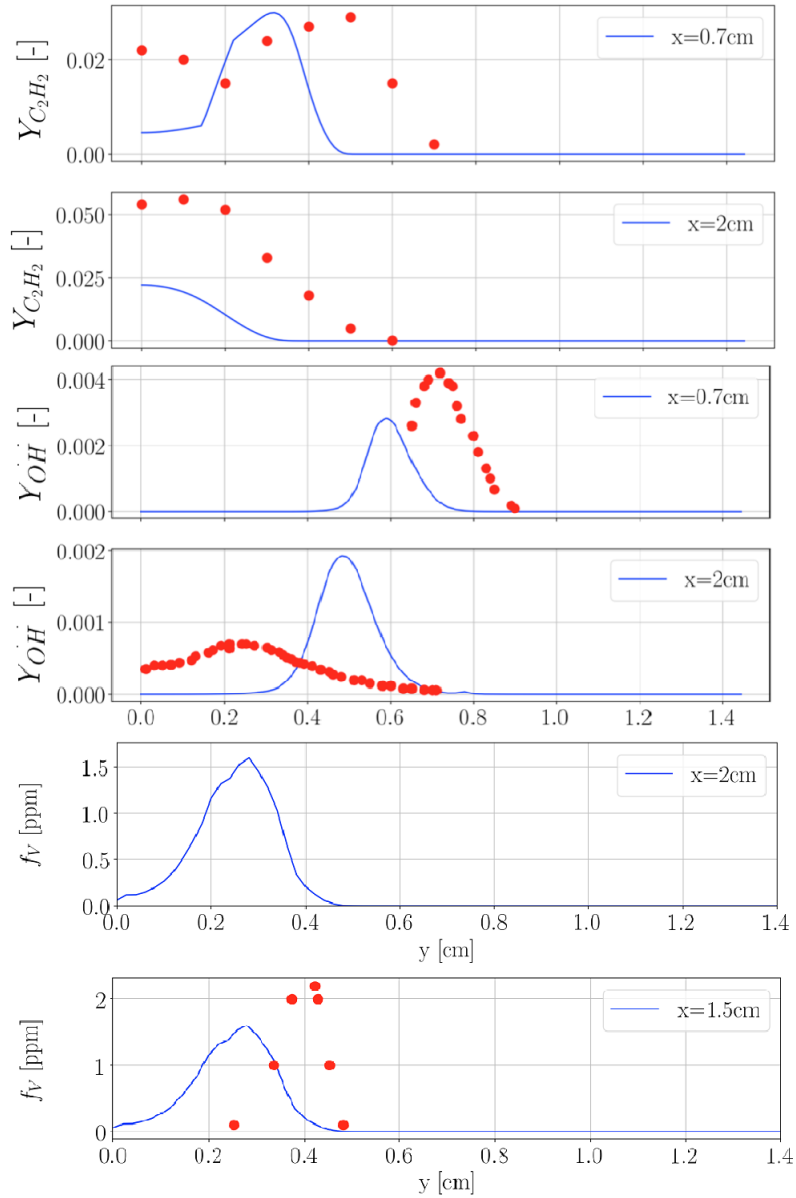


Figure 6.18: Comparison of radial profiles mass fraction of C_2H_2 , OH and soot volume fraction with experimental data from *Santoro et al. (1983)* (●) at a fixed height above the burner exit.

6.2.2.4 Discussion of uncertainties

The soot volume fraction is around 11 ppm along the centerline, while the experimental values are around 6 ppm. Such overprediction could be attributed to the use of KM2 mechanism, as recent mechanisms (*Zhang et al. (2009)*, *Dworkin*

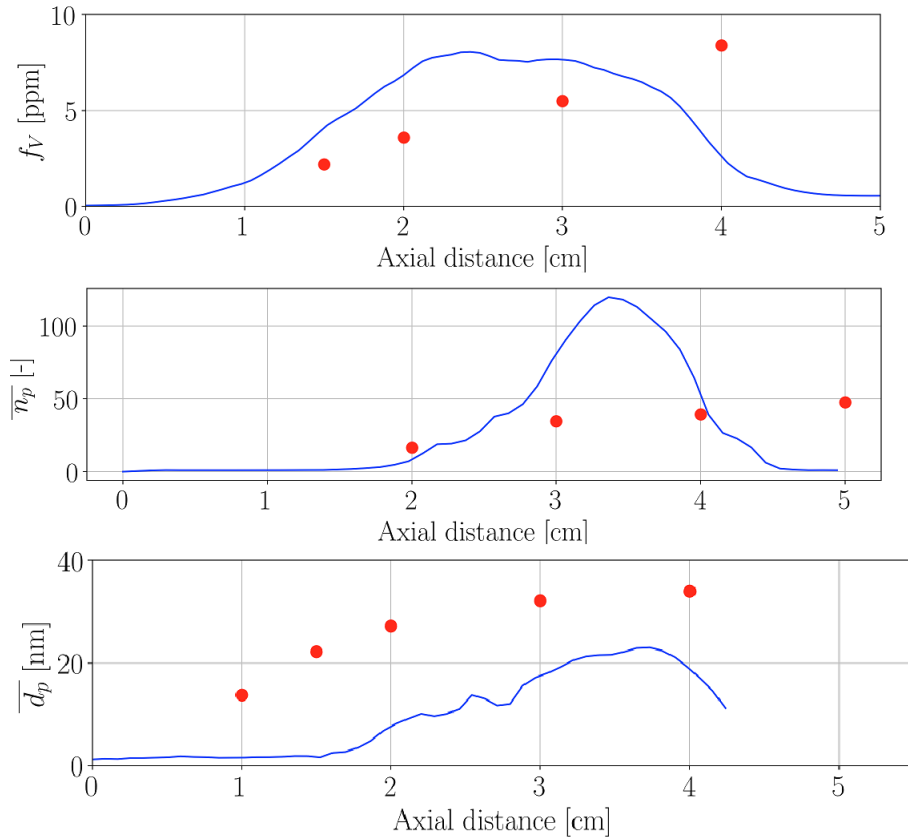


Figure 6.19: Evolution of soot volume fraction, primary particle number and diameter along the flame wings, with comparison with experimental data from Santoro *et al.* (1983) (●).

et al. (2011), Escudero (2019)) improves the prediction of PAHs growth along the centerline for this configuration. Moreover, these works are focusing on the modification of the HACA parameters (which controls the surface-growth mechanism) in order to retrieve soot target quantities. However, even with such mechanisms, the soot volume fraction along the centerline is under-predicted. More generally, a lot of uncertainties remains on the HACA mechanism, and very recent work Tardelli *et al.* (2019) aims at having a better understanding of this mechanism and latests improvements on more complex configurations.

Another source of uncertainty is related to the flamelet approach retained for the laminar flame, since we wanted to retain a similar set-up than the calculations carried out in Chapters 3 and 4 on turbulent flames. It is important to notice that the flamelet model predicts the location of the maximum H_2O and CO_2 at the same place (see Figure 6.8). Indeed, in the counterflow flames, such concentrations are predicted close to equilibrium at low strain-rates, such as

noted in Liu et al. (2006) for another ethylene-air coflow configuration. In the same work, calculations have been performed with detailed mechanism, and the authors have found that both species are not located at the same place. This can introduce error in the predicted location of these two species and therefore, on the computed radiative power.

Unfortunately, soot formation was not taken into account in the calculations by Liu et al. (2006), and, to our best knowledge, such work is the only one assessing the impact of a flamelet model in a laminar diffusion flame. Additional calculations, based on the unity Lewis-number assumption (corresponding to the original RFPV approach) have been carried out. The soot volume fraction obtained in such calculations is around two order of magnitude lower than the experimental measurements. Despite the whole uncertainties associated with the RFPV approach, it is clear that the model developed in Chapter 5 enables to significantly improve the results.

6.3 Analysis of fuel preheating

6.3.1 Wall and fuel temperature

The coupled simulation accounts for conjugate-heat transfer which enables to quantify the fuel pre-heating impact. It is important to recall that no experimental measurements along the pipe walls are reported. Many simulations of the Santoro's burner accounts for fuel pre-heating by assuming a uniform temperature of 400 K at the inlet of the domain with a parabolic Poiseuille shape for velocity. The objective of this section is to verify whether these assumptions are valid or not. The results of the simulation accounting for conjugate heat transfer are compared with other calculations performed with adiabatic walls.

The obtained wall temperature profiles at the inner and outer walls are displayed Figure 6.20.

Before reaching the flame zone (attached at $x = 0$ cm), it can be observed that the evolution of both profiles along the inner and outer walls are very similar. This can be explained by the fin thermal approximation, since the solid characteristic time of conduction is much lower than the characteristic time of conducto-convection. The temperature reached is the same for both faces of the fin. The only difference is obtained at $x = 0$ cm, which corresponds here to the exit of the pipe, and is attributed to a flame effect.

Along the pipe, the fuel receives energy from the inner wall and is heated. Figure 6.21 presents different radial temperature profiles obtained along the pipe. The indicated positions are relative to the exit of the pipe. At 10 cm of the exit of the pipe, the temperature is uniform and equal to the ambient temperature.

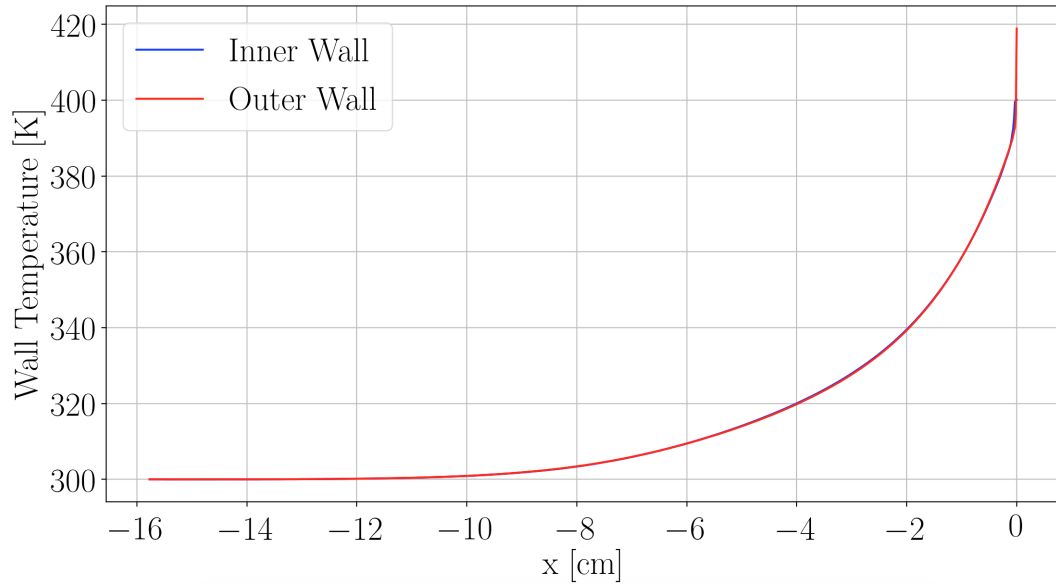


Figure 6.20: Obtained wall temperature profiles for the inner, outer and lip walls, accounting for conjugate heat transfer.

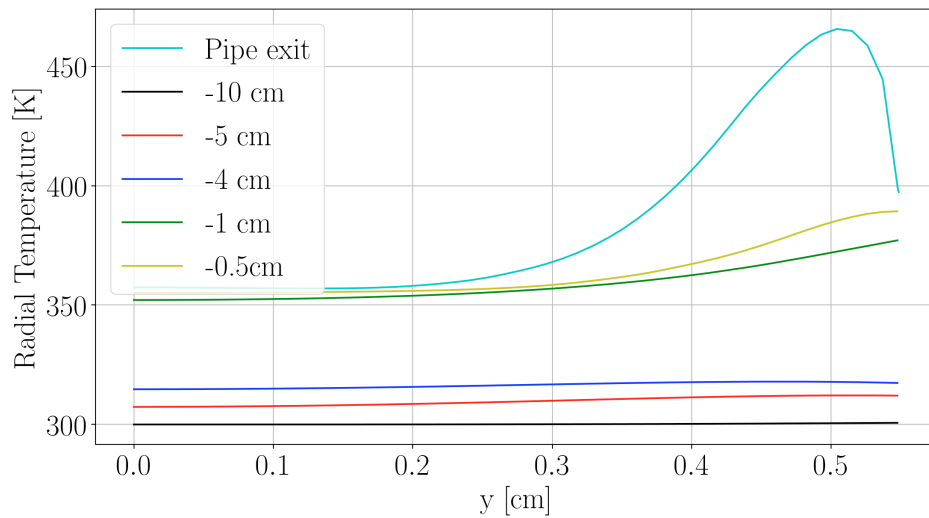


Figure 6.21: Radial temperature profiles obtained at various locations along the pipe when accounting for fuel preheating (CHT). The referred positions are relative to the exit of the pipe.

As long as the fuel moves forward in the pipe, its temperature increases. Up to 0.5 cm before the exit of the pipe, the wall is hotter than the fuel temperature. The fuel is therefore simply heated up by the hot walls. A strong modification of the temperature profile is however observed at the exit of the pipe, which is

attributed to the flame which directly transfers its energy to the fuel. It can be noticed that the preheated region extends up to the central axis for all profiles : beyond 4 cm from the pipe exit, the fluid conductive time is short enough to homogenize the temperature field ; closer to the exit, the same time scale cannot compete enough with the sharp raise in wall temperature, and the fuel stream temperature becomes inhomogeneous.

In order to validate the literature assumption of considering a fuel at 400 K at the inlet, a bulk temperature T_b at the exit of the pipe is computed as

$$T_b = \frac{\int_A \rho u c_p T dA}{\int_A \rho u c_p dA} = 376 \text{ K} \quad (6.4)$$

where A is the section of the exit, ρ the density of the mixture, T the computed temperature and c_p the heat capacity, which is obtained via the look-up table. The obtained value is below the classically prescribed temperature for this computation, which shows the need for taking into account CHT to provide accurate boundary conditions.

The complex temperature distribution at the exit of the pipe has a direct impact on the velocity. The axial velocity profiles are extracted from the same locations than Figure 6.21 and presented Figure 6.22. At -10 cm, the axial velocity exhibits a Poiseuille profile. Along the pipe, due to the increase of temperature, the mass flow rate conservation yields to a decrease of the velocity near the axis. Moreover, the velocity profile has no longer a Poiseuille shape at the exit of the pipe.

The axial velocity profile at the exit of the pipe is compared with the one obtained without fuel preheating in Figure 6.23. In the pipe, both profiles have very different shapes. Without accounting for CHT with adiabatic walls, the obtained profile is a classic parabolic Poiseuille flow. On the contrary, when considering CHT, the velocity profile is not monotonically decreasing along the axis. In the pipe, since the temperature increases close to the wall (radial distance around 0.4 cm), the velocity increases as well. On the contrary, as already stated, the mass conservation yields to a decrease of the velocity near the axis.

This result shows that imposing a Poiseuille velocity profile at the fuel inlet is inaccurate and does not reproduce the fuel preheating and emphasize the need for taking into account CHT to provide accurate boundary conditions.

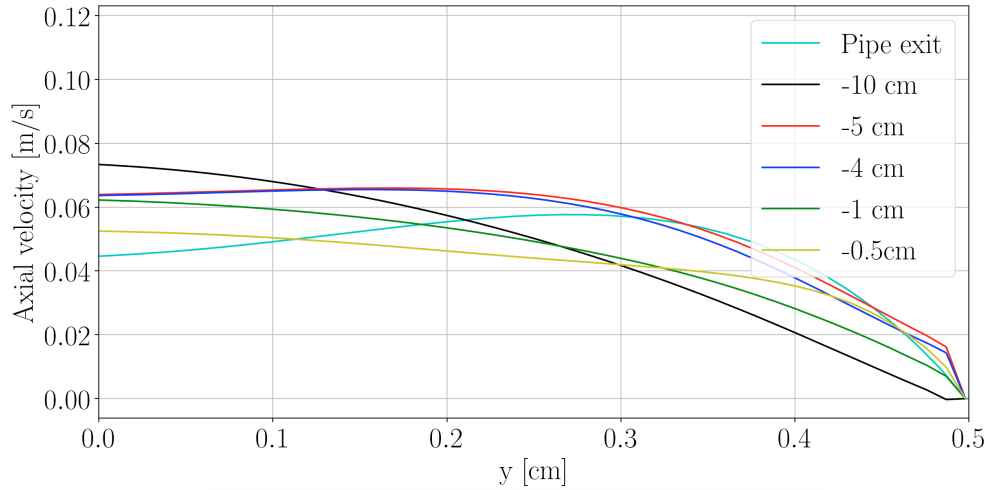


Figure 6.22: Radial axial velocity profiles obtained at various locations along the pipe when accounting for fuel preheating (CHT). The referred positions are relative to the exit of the pipe.

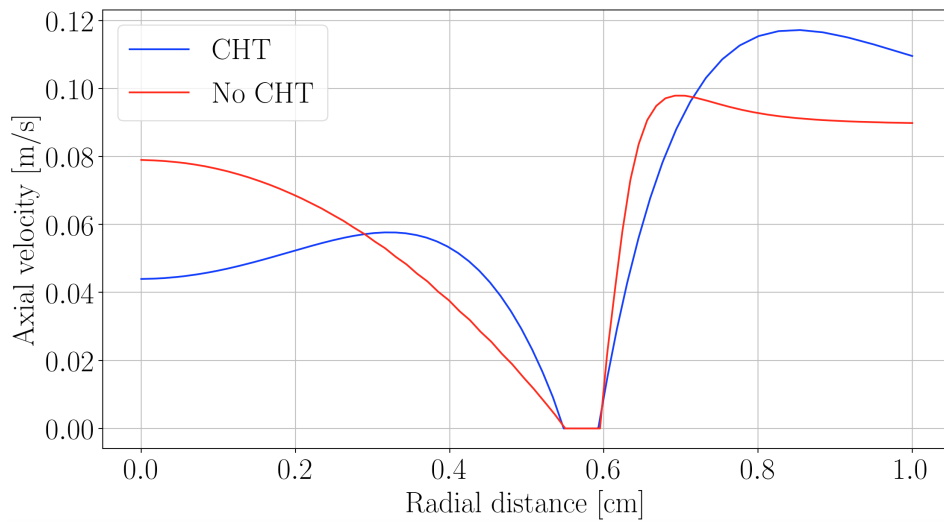


Figure 6.23: Comparison between axial velocity profiles at the exit of the pipe, accounting for fuel preheating (CHT) or not. The pipe extends radially between 0 and 0.55 cm, while the coflow extends above 0.59 cm.

6.3.2 Energy balance

A balance equation of sensible enthalpy can be written inside the computational domain:

$$\underbrace{\int_{\text{outlet-inlet}} \rho h_s \mathbf{u} \cdot d\mathbf{S}}_{\text{(I)}} + \underbrace{\int_{\text{pipe}} \phi_{\text{pipe walls}} \cdot d\mathbf{S}}_{\text{(II)}} + \underbrace{\int_V -P^R dV}_{\text{(III)}} = \underbrace{\dot{\Omega}}_{\text{(IV)}} \quad (6.5)$$

This equation shows the different contributions to the integrated heat release rate (term (IV)). The first term (I) represents the outlet and inlet convective fluxes. The second term (II) corresponds to the integrated conductive flux on the pipe walls, and the third term (III) is the source term due to radiation.

The different contributions for two cases are reported in Table 6.3 : the adiabatic case (no radiation and no wall heat fluxes) and the coupled case with radiation and conjugate heat transfer.

Case	Conv. flux (Out-In)	Cond. flux	Rad. source term	HR rate
Adiabatic	30.24	0	0	30.24
Coupled	21.6	0	8.64	30.24

Table 6.3: Contributions of the terms I, II, III in the integrated heat release (HR) rate in W.

In the coupled calculation, the conductive flux has a null contribution, since the flux received by the burner lip is distributed along the inner and outer walls. The radiative power contribution is around 20 %, which shows the importance of radiation in this configuration. The radiative power term corresponds to a heat loss of 8.64 W. The convective flux is decreasing between the adiabatic case and the coupled simulation : this is explained by the lower temperature reached by burnt gases at the outlet of the domain when introducing heat losses.

6.3.3 Wall heat fluxes

The contribution of the term (II) can be split between the burner lip, the inner and outer walls (cf. Figure 6.4). The energy balance on the pipe walls writes :

$$\Phi_{lip}^{conv} + \Phi_{lip}^{rad} + \Phi_{outer}^{conv} + \Phi_{outer}^{rad} + \Phi_{inner}^{conv} + \Phi_{inner}^{rad} = 0 \quad (6.6)$$

where Φ denotes the surface-integrated values of convective/radiative fluxes on the walls. Algebraic values are considered with a positive sign when the solid part is heated.

Wall convention	Convective	Radiative	Total
Burner lip	1.1	0.34	1.492
Inner Wall	-0.12	0.002	-0.122
Outer Wall	-1.494	0.10	1.394

Table 6.4: *Detailed analysis of convective/radiative fluxes (in W) on the pipe walls.*

Table 6.4 gathers the different wall heat-flux contributions.

For the burner's lip, the radiative contribution is around 20 % of the total wall heat fluxes. This contribution is much smaller for the inner and outer walls. The high emissivity of the steel for the burner lip (0.8), the temperatures and the presence of participating species above the burner can explain these differences. This shows that considering radiative heat transfer at the burner's lip is needed.

The energy (radiation + convection) from the burner lip is redistributed along the outer and inner walls. The inner wall releases energy (negative convective flux) to the fluid (the fuel), which corresponds to the fuel pre-heating effect. Along the outer wall, the co-flow is also heated-up. Due to the higher velocities encountered, the convective flux along the outer wall is more important (in magnitude) than the inner wall. The flame is attached to the outer wall, which results in a positive radiative flux.

The radiative and convective fluxes profiles along the inner and outer walls are plotted Figure 6.24, with a zoom view near the burner lip. The convective flux sign convention is kept from the solide side : a positive flux means that the solid is heated-up.

The values reached by the convective fluxes are one order of magnitude higher than the radiative fluxes. The inner wall is first heating the fluid, which corresponds to a negative convective flux. Then, the fluid, due to the flame effect, is heating up the wall, which corresponds to a positive convective flux. A similar behaviour is observed with the outer wall. However, the wall flux peak observed at $x = 0$ cm, corresponding to the attached flame for the outer wall is more important to the higher temperature involved.

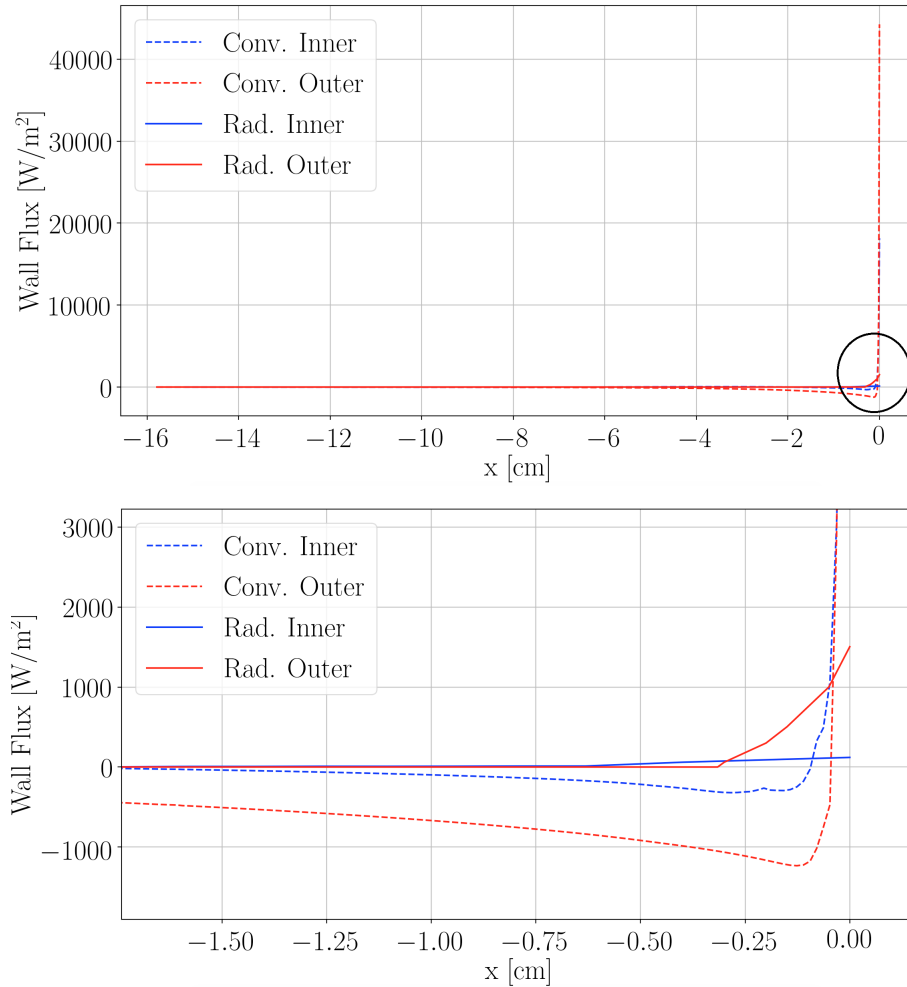


Figure 6.24: Convective and radiative wall fluxes profiles along the inner and outer pipe wall.

6.4 Analysis of radiative heat transfer

6.4.1 Radiative power fields

Figure 6.25 presents the soot and gas contributions to the radiative power and the total radiative power. These two contributions corresponds to results from SESA/GECA calculations (see Section 6.4.2 for more details). Let us recall that the net radiative power corresponds to the difference between the absorbed power and the emitted power.

The radiative power due to the participating gases is spreading all along the flame, while the radiative power due to soot particles is more localized. The emission due to gases is maximum where the concentration of H_2O and CO_2 is

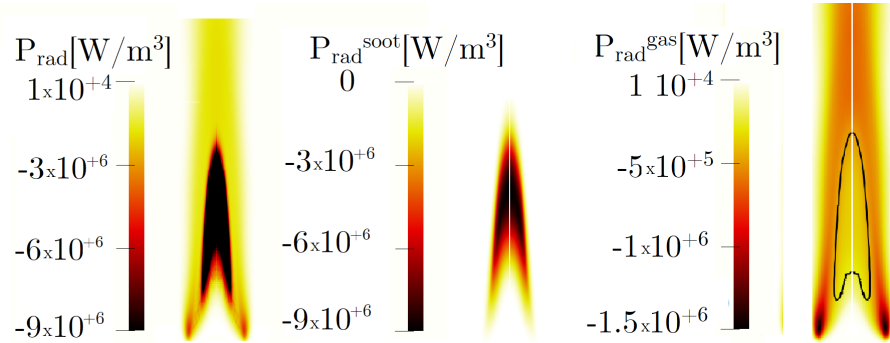


Figure 6.25: *Participating gases and soot particles contributions to the total radiative power. An iso-contour of $f_V = 1\text{ppm}$ is also displayed on the gaseous phase contribution.*

maximum, and in regions with high temperatures (see Figure 6.8). Along the centerline, the contribution due to gases increases as the temperature and the concentration of such species also increases. Finally, radiative power is positive in lean and rich regions, corresponding to areas with low temperature (below 1000 K) where absorbed power from CO_2 and H_2O is higher than emitted power.

In parallel, the contribution of soot particles is located where the soot volume fraction is the most important. This is expected as the absorption coefficient is directly proportional to f_V in the RDG-FA theory. Looking at the levels reached by the radiative power, it is clear that soot radiation is a key contributor to the total heat losses in the flame as the radiative power is around 6 times more important than the one due to gases.

Few studies have assessed the impact of soot radiation in laminar flame compared to the gaseous phase, especially for this configuration. Similar conclusions have been found in the study by Liu et al. (2002) who reported, in a similar flame but with different boundary conditions, that soot radiation has a greater impact on the temperature decrease than the gaseous phase. It can be seen that, due to the location of their corresponding radiative power, the gaseous phase tends to decrease the temperature near the burner lip and along the flame wings, in the lower part of the flame, while soot particles tend to decrease the temperature in the upper portion of the flame, as reported in the study of Liu et al. (2002). Further downstream ($x > 4\text{ cm}$), hot burnt gases are still present in a large zone, which also increases heat losses here.

These results have been obtained taking into account emission and absorption by soot and gaseous phases. Figure 6.26 presents the emitted and absorbed radiative power in this flame. The ratio between both quantities is also pro-

vided. It can be observed that, in lean regions (on the oxidizer side), due to the low temperatures and the presence of gaseous contributors, the absorption dominates the emission (the ratio is greater than 100 % as the gaseous phase absorbs more power than it emits), this corresponds to a positive radiative power as discussed Figure 6.25. Inside the flame, absorption accounts for 10 to 20 % of the total radiative power. Moreover, integrating the values of absorbed and emitted power over the whole domain, one finds respectively 1.5 W and 9.72 W respectively, which means that 15% of the radiative power is absorbed. The absorption might appear small but, as outlined in Chapter 3, the spectral dependency of thermal radiation reveals that the contributing bands are characterized by moderate to large optical thickness, especially for the gas phase contribution. The global and local (right of Figure 6.26) impact of radiation show the need to solve the Radiative Transfer Equation in such configuration and outlining the inadequacy of the optically thin radiation model which neglects the reabsorption phenomenon.

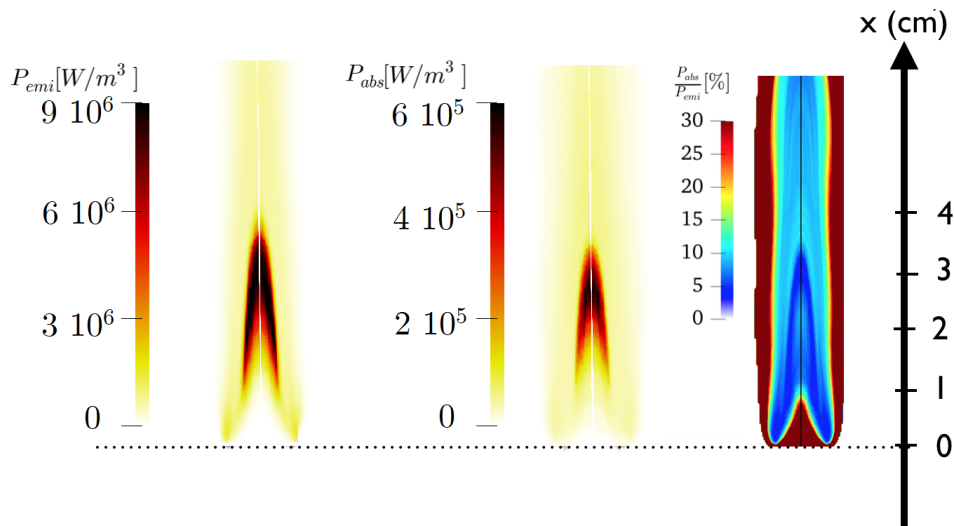


Figure 6.26: *Emitted and absorbed radiative power due to soot and gaseous phase. The ratio between the absorbed and emitted power is also displayed on the right.*

6.4.2 Spectral emitted and absorbed radiative power

In Section 6.4.1, a global analysis has been carried out on total integrated radiative power fields obtained via the coupled simulation. Let us recall that the radiative properties of gaseous species (the ck-model) and soot particles (RDG-FA) rely on spectral formulations. A deeper analysis can then be performed by looking at band-integrated spectral values of the radiative power in order to understand the role of gaseous participating species and soot particles in the total radiative power analyzed in Section 6.4.1.

Five additional *spectral* Monte-Carlo computations have been carried out based on the solution obtained via the coupled calculation. One based on both soot and gaseous phases contribution (computation **Ref.**), one considering only gas emission and gas absorption (computation **GEGA**), one considering only gas emission and soot absorption (computation **GESA**), one considering only soot emission and gas absorption (computation **SEGA**) and one considering only soot emission and soot absorption (computation **SESA**).

Figure 6.27 presents the obtained the spectrum of emitted and absorbed power for each case.

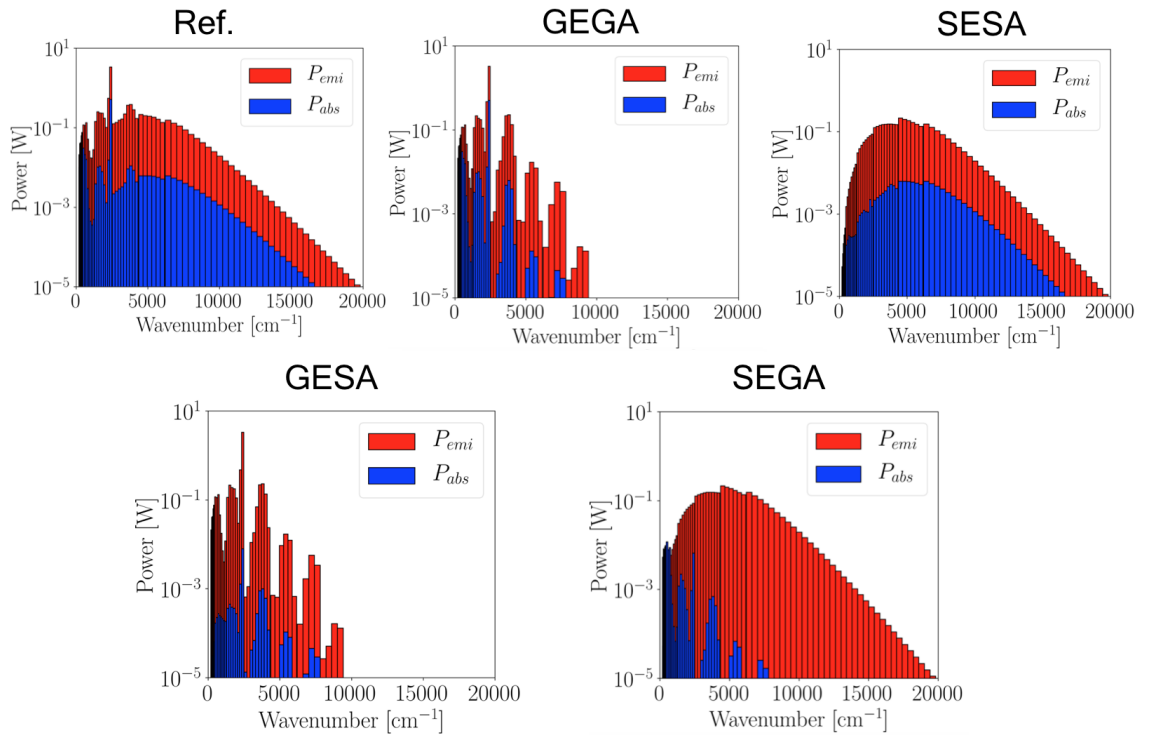


Figure 6.27: *Spectral emitted and absorbed volume-integrated powers for the instantaneous representative solution. Results correspond to the reference case taking into account gas and soot particles emission and absorption and the four other studied cases: GEGA, GESA, SEGA and SESA.*

The computed spectrum on the **Ref.** case exhibits two distinct structures : for low wavenumbers, it is highly dynamic while for the high wavenumbers, it is smooth. Looking at the **GEGA** case, the highly dynamic bands are explained by the gaseous phase contribution. It should be noted that two ck-bands (between 2000 and 2500 cm^{-1}) are the major contributors to the radiative power corresponding to CO_2 radiation. For this band an important reabsorption is noticed. Considering the **SESA** case, it can be noticed that the obtained spectrum is continuous, which shows that the high-wavenumber contribution

observed in **Ref.** is due to the soot contribution. Globally, the reabsorption by soot particles is very low since the absorbed power is about two order of magnitudes lower than the emission. It is interesting to note that the levels achieved by soot particles emission are in the same order of magnitude that the gaseous contribution, showing the importance of taking into account soot emission in this flame. The cases **GESA** and **SEGA** quantify the interaction between soot and gaseous phases. Very small interactions are observed between soot particles and gaseous species in terms of radiative transfer as soot reabsorb a small part of the gaseous emissions, and reciprocally.

The spectral integrated of the emitted and absorbed radiative power presented Figure 6.27 are gathered in Table 6.5.

Case	P_e [W]	P_{abs} [W]	P^R [W]
REF	11.54	2.9	-8.64
GEGA	7.72	2.12	-5.6
SESA	3.82	0.54	-3.28
GESA	7.72	0.13	-7.59
SEGA	3.82	0.11	-3.71

Table 6.5: Spectral integrated values of emitted and absorbed power for each case presented Figure 6.27.

Due to the high soot volume fraction, soot radiation has a strong contribution to the radiative power (around 30 % of the total emission and almost half of the radiative power). In our calculation, the soot volume fraction is however slightly over-predicted compared to experimental data, which means these values are slightly over-estimated. It still shows the need for accurately taking into account soot radiation in such configuration. Interactions with the gaseous phase (GESA and SEGA) are small. Only 10 % of the power emitted by soot particles is reabsorbed by soot phase (SESA).

6.4.3 Transmissivity and soot/gas interaction

It is important to note that the previous analysis is performed by integrating spectral values all over the computational domain, therefore, local effects cannot be noticed here. In order to emphasize the impact of soot and gaseous phase in the radiative transfer, it is possible to compute a local transmissivity spectrum at a given height of the burner. Such transmissivity is calculated by :

$$\tau_\nu(x) = \exp\left(-\int_{y=-\infty}^{+\infty} (\sigma_\nu + \kappa_\nu)(y, z = 0) dy\right) \quad (6.7)$$

In the experimental work by [Best et al. \(1991\)](#), a transmissivity spectrum has been calculated using tomographic reconstruction in the infrared, at a height

$x = 4$ cm and at a radial position of 2 mm. The comparison with the coupled calculation is displayed Figure 6.28.

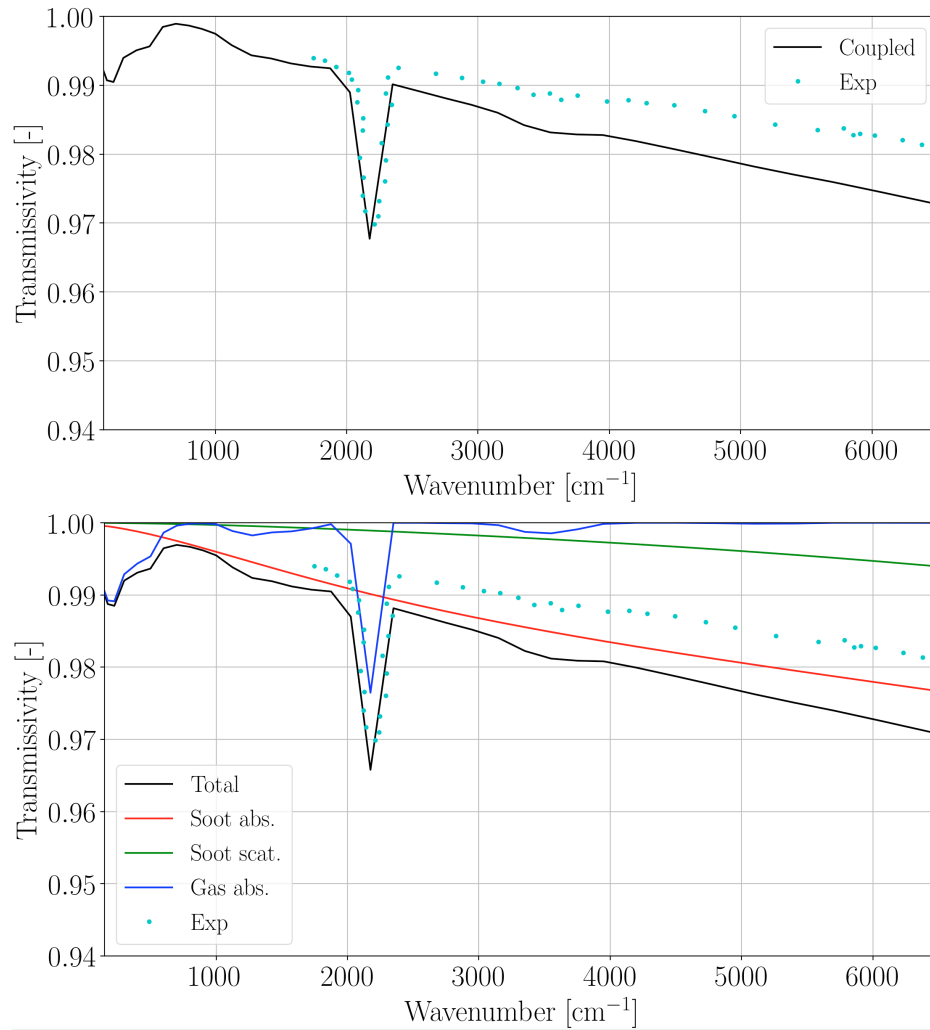


Figure 6.28: Spectral transmissivity computed at $x = 4$ cm above the burner and comparison with experimental data (top), and detailed contribution of gas and soot particles (bottom).

A very good agreement with the experimental data is obtained : the peak around 2300 cm^{-1} is correctly reproduced, while the levels of transmissivity achieved for higher wavenumbers are very close to the experimental data.

In order to understand the contribution from gases and soot particles in this transmissivity, Figure 6.28 (bottom) presents the contribution of both phases. It can be observed that the peak at 2300 cm^{-1} is not only due to the gases

contribution (blue curve) but also to soot radiation (red curve). Therefore, taking into account soot radiation is essential to retrieve the experimental levels of transmissivity. The transmissivity obtained for wavenumbers greater than 3000 cm^{-1} is mostly due to the soot particles. It can be observed that for low wavenumbers, the scattering contribution (green curve) is negligible, but increases with ν .

Both RDG-FA and the ck-model are then able to reproduce spectral evolutions on this flame. However, the soot volume fraction level is over-predicted at this height comparing to experimental data. The absorption coefficient in the RDGFA model is directly related to the soot volume fraction f_V : $\kappa_\nu = C_0 f_V \nu$ with ν the wavenumber. For high values of ν , only soot contributes to the transmissivity obtained. The slope of the transmissivity for high values of ν is therefore controlled by the value of the absorption coefficient, hence f_V .

These results have been obtained for a variable optical index m (the spectral formulation introduced in Chapter 1). Figure 6.29 shows the impact of the soot optical index modeling (constant or spectral formulation) on the obtained transmissivity. It can be seen that, as already observed in Chapter 4, the spectral formulation differs for the lowest wavenumbers (or the highest wavelength) leading only to small differences.

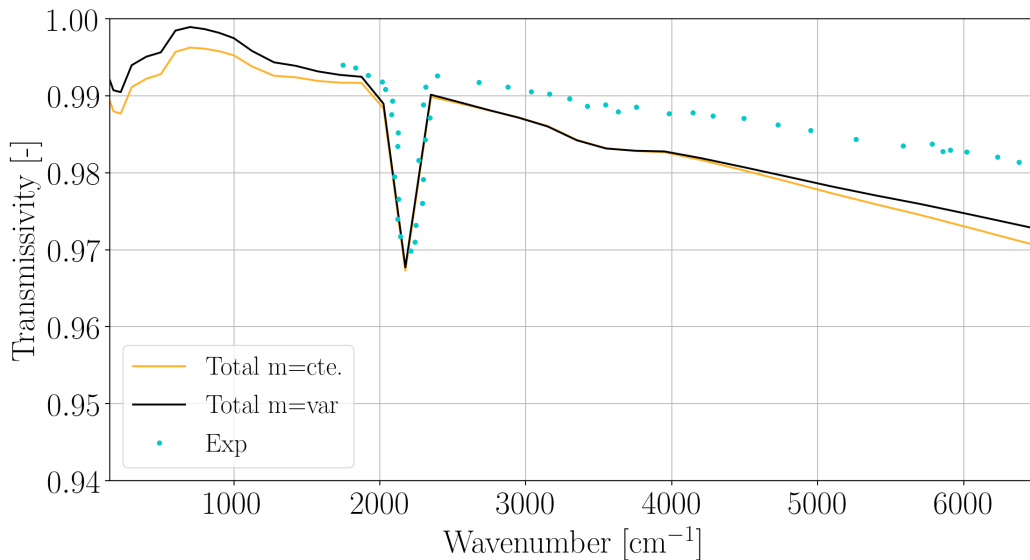


Figure 6.29: Impact of soot optical index formulation on the computed transmissivities and comparison with experimental data.

6.4.4 Accuracy of RDG-FA model and scattering impact

The previous analysis carried out on transmissivities has shown the need for taking into account spectral radiative properties for gas and soot particles to reproduce experimental data. However, it has also been noticed that the scattering impact on the transmissivity was small in the considered spectral range. Hence, no definitive conclusions can be drawn on the scattering accuracy description provided by the RDG-FA model.

In the study by Puri et al. (1993), laser scattering measurements have been performed at several axial heights on the studied configuration and scattering related coefficients have been provided. These measurements enable to assess the validity of RDGFA scattering formulation for the present CFD results. The vertical-vertical scattering coefficient is defined in the experimental study by :

$$Q_{vv}(\theta_i) = n_p^2 x_p^6 F(m) N_{part} f(\theta_i) k^2 \quad (6.8)$$

where θ_i is the scattering angle measured from the direction of the incident polarized light, n_p the mean number of primary particles in an aggregate, x_p the size parameter, $F(m)$ a function of the optical index, introduced in chapter 1, N_{part} the number of particles density, f the form factor, and $k = \frac{2\pi}{\lambda}$ with λ the wavelength. The measurements have been reported for an angle $\theta_i = 90^\circ$ and a wavelength $\lambda = 513nm$. The obtained results in the coupled simulation are compared with the experimental data in Figure 6.30. The mean number of primary particle and diameter \bar{n}_p and \bar{d}_p are considered in order to be consistent with the proposed experimental formulation.

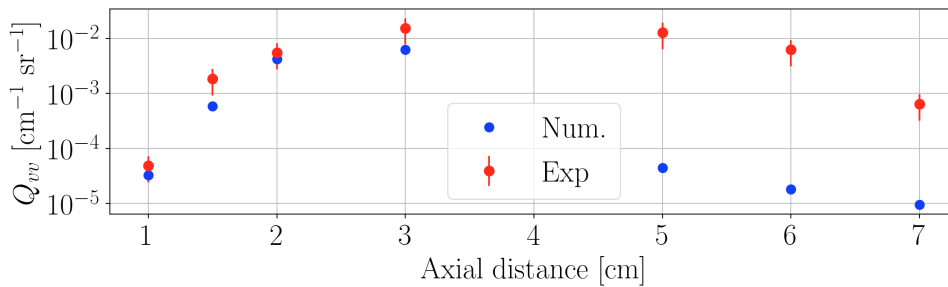


Figure 6.30: Axial evolution of the vertical-vertical scattering coefficient (for an angle of $\theta_i = 90^\circ$ and a wavelength $\lambda = 513nm$). Experimental values with associated errors are also reported.

Let us recall first that the computation of Q_{vv} depends on the particle number density N_{part} and the soot morphological description via n_p and d_p (included in the size parameter). At the bottom of the flame, it can be observed that the

RDG-FA model is in an excellent agreement with the experimental values. As mentioned in Figure 6.19, the values obtained for \bar{n}_p and \bar{d}_p are in a fair agreement with experimental data. Therefore, a reasonable comparison between the RDGFA model and the experimental values can be done in log-scale for $x < 3$ cm. The model is able to reproduce both levels of magnitude and trend of the scattering coefficient obtained experimentally.

Downstream the flame, it can be observed that the scattering vertical-vertical coefficient is underpredicted. This is explained by the low d_p and n_p values reconstructed from the surface-volume relationship at these heights (see figures 6.19).

Finally, the extinction coefficient β_{nu} , defined as the sum of κ_ν and σ_ν is also computed at the same wavelength and compared with experimental values in Figure 6.31.

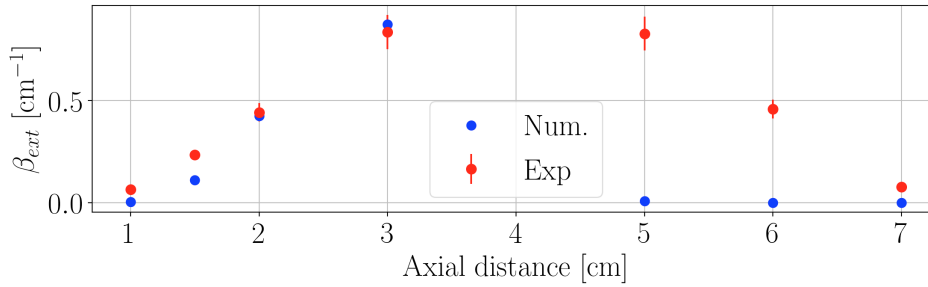


Figure 6.31: Axial evolution of the extinction coefficient at wavelength $\lambda = 513\text{nm}$. Experimental values with associated errors are also reported.

The same conclusions as for the vertical-vertical scattering coefficient can be drawn. Providing an accurate description of soot morphology and soot volume fraction (which is the case in our computation at the bottom of the flame) enables to correctly retrieve the extinction coefficients along the centerline. Further downstream, due to the strong oxidation encountered, the computed soot volume fraction at 5cm is almost null. Since the obtained extinction coefficient is also almost null, both absorption and scattering coefficient in this zone, for the considered wavelength are small.

Recalling the experimental soot volume fraction obtained along the centerline 6.12, it can be noticed that the extinction coefficient evolution is also strongly correlated to the soot volume fraction evolution, and hence, the soot absorption coefficient (since this coefficient is proportional to f_V).

Finally, the spectral albedo ω_λ for an aggregate distribution at a given wavelength (Equation 3.2.4) can be compared with the results of Iyer et al. (2007) who reported the albedo for different heights above the burner. The comparison

is provided Figure 6.32. Again, a very good agreement with experimental data is obtained for the lower portion of the flame : this shows the good capability of RDGFA to reproduce experimental measurements with a good accuracy.

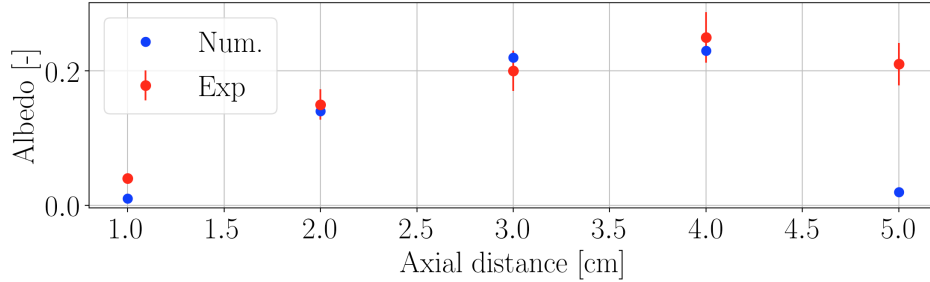


Figure 6.32: Reconstructed albedo of aggregates at various heights above the burner with experimental data comparison at 513nm. Errors bars are taken from Iyer et al. (2007).

In order to assess the global impact of scattering (*i.e.* considering all the spectrum), Figure 6.33 (left) presents the difference on the radiative power between the case with and without scattering. It can be observed that the maximum difference is located near the centerline, where numerous and big soot particles are encountered. This difference corresponds to around 1.5 % of the local radiative power. Since the Monte-Carlo computation accuracy is prescribed to 0.1% of the local radiative power, the convergence criteria ensures that the obtained difference is statistically meaningful.

On the other hand, the effective albedo importance $\bar{\omega}^{eff}$ and mean asymmetry factor \bar{G} metric derived in Chapter 3 are also reported on the middle and right parts of Figure 6.33. The effective albedo $\bar{\omega}^{eff}$ takes relatively small values (around 0.1) along the centerline and along the wings, where it can be noticed that the scattering impact on the radiative power is fairly small. Finally, \bar{G} indicates how the scattering occurs. Small and positive values are obtained throughout all the domain. In this case, the scattering is moderately forward : the photons are allowed to scatter for a relatively wide range of angles, which results to a marginal attenuation of the scattering impact. Therefore, the computation of $\bar{\omega}^{eff}$ and \bar{G} enables once again to estimate the importance of scattering prior any Monte-Carlo simulation.

6.5 Conclusion

In this chapter, a multi-physics simulation has been performed on a laminar configuration, accounting for sooting flame, detailed radiation and conjugate heat transfer at the walls. The good prediction of soot related quantities (soot volume fraction ...) is still a numerical challenge in the literature, even in this

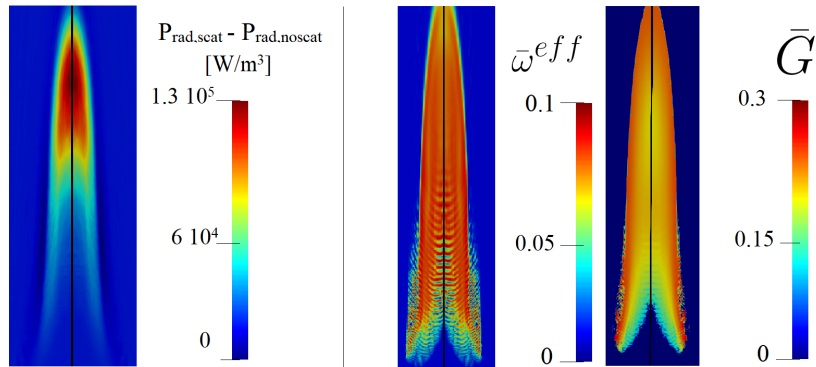


Figure 6.33: *Difference of radiative power due to scattering, effective albedo importance and mean asymmetry factor fields for the studied configuration.*

simple configuration.

The obtained soot volume fraction is overpredicted along the centerline, which is attributed either to the retained chemical model, or the PAH description in the KM2 mechanism which is not accurate enough for the given configuration or the modelling of soot formation mechanisms in the sectional approach (the oxidation takes place too soon for example). Soot related quantities (aggregates description, number of particles) are still in good agreement in the lower part of the flame, near the burner exit.

In this flame, thermal radiation represents 30% of the total heat release. On the other hand, soot radiation has been quantified and represents around 30% of the total emitted power but the local effects are much greater where soot particles are present. Accounting for soot radiation with accuracy is therefore crucial in this configuration. The use of the state-of-the-art RDGFA has also enabled to quantify the scattering impact, which is small. This observation is also confirmed by the a-priori metrics developed in Chapter 3.

The wall temperature profiles have been determined by accounting for conjugate heat transfer. This result is of primal importance since no experimental wall temperature profile is reported in the literature in this configuration. The fuel pre-heating effect is usually simplified by imposing a temperature at the inlet of 400 K with a Poiseuille flow. Our study simulate this pre-heating effect and predicts a bulk temperature of 370 K. It also shows that the exiting temperature profile is not uniform that a Poiseuille flow profile is incorrect. Inhomogeneous profiles should then be imposed instead, if not predicted. Also, the heating of the burner lip must surely account for the flame incoming radiation (20% of the total flux in our case). The result is however sensitive to the material property.

Finally, for the first time in this type of configuration, an experimental transmissivity is compared with detailed radiative properties from CFD. A very good agreement is obtained: both gaseous and soot radiative models are accurate enough to retrieve experimental features. The accuracy of the RDGFA model is further investigated by comparing the coefficients from the model to experimental albedo, extinction coefficient and scattering cross-section. In the lower part of the flame, a very good agreement is again obtained for the heights where the soot formation predictions are correct. Remaining modeling errors certainly affect the quality of the results. Nonetheless, experimental and numerical data fields on soot particles, spectral transmissivities and albedo allow for an exhaustive investigation of the soot morphology and formation mechanism.

Chapter 7

Numerical synthesis of scattered Laser signals by soot particles

Experimental diagnostics, such as Laser scattering, rely on a Laser beam crossing the flame, whose intensity is collected by an optical apparatus at various angles from the beam emission. The obtained signal is determined by scattering from soot particles. It enables access to particle information such as aggregate primary particle size or fractal parameters. A difficulty in such experiments is anticipating where the sensor must be placed, which sensitivity is required, which source wavelength is appropriate. The perception of these features is crucial to maximizing the measured scattered signal. This chapter aims to numerically synthesize such signals using the fields obtained from coupled simulations carried out on the Santoro laminar flame in Chapter 6 and assess the impact of the sensor position. The experimental setup constraints (such as the Laser wavelength, positions, geometry) are reproduced in the Monte Carlo solver to provide a qualitative comparison between the synthesized and measured signals. A numerical strategy based on the peel-off technique implemented in Rainier is proposed and validated in the first part. In the second part, the technique is applied to the coupled numerical fields obtained in Chapter 6. The impact of the sensor position and wavelength is studied. Finally, in the last part, the same analysis is carried out on fields taken from detailed chemistry calculations to study the impact of the chemistry modeling.

Contents

7.1	Description of the problem and numerical strategy	214
7.1.1	Parametrization and limitation of standard Monte-Carlo methods	214
7.1.2	Introduction to the peel-off Monte-Carlo technique .	216
7.1.3	Computation of the direct contribution Source-Observer	217

7.1.4 Computation of the peeled contribution Source-Observer 219

7.1.5 Validation : isotropic medium 221

7.1.6 Validation : anisotropic medium 224

7.2 Application of peel-off technique to CFD fields from coupled calculations 226

7.2.1 Numerical setup 226

7.2.2 Impact of observer angle 228

7.2.3 Impact of the source wavelength 233

7.3 Application of peel-off technique to CFD fields from detailed chemistry calculations 236

7.3.1 Numerical setup 237

7.3.2 Results and comparison with coupled calculations 238

7.4 Conclusion 242

7.1 Description of the problem and numerical strategy

7.1.1 Parametrization and limitation of standard Monte-Carlo methods

Let us consider the problem depicted in Figure 7.1. A Laser generates a beam, which goes into an optical apparatus composed of several lenses, not shown here. In Figure 7.1, only the beam that leaves the optical apparatus (called **source** in the following) is considered. The source is placed at a fixed position from the flame, and is characterized by a wavelength λ , a power ϕ and a diameter of the exit lens, d_{source} , and a solid angle Ω_{source} .

Table 7.1 gathers the information of the source that is used in the experimental configuration of the Santoro’s ethylene flame carried out by G. Legros, J. Bonnetty and co-workers at the Institut Jean-Le-Rond-d’Alembert. It can be seen that the solid angle is negligible. In the following, we consider collimated irradiation ($\Omega_{source} = 0$) to simplify the treatment of the beam.

Laser Excelsior			
Wavelengths	405 nm	635 nm	785 nm
Lens diameter	10 cm	10 cm	10 cm
Power	1 mW	4 mW	1 mW
Distance to flame	50 cm		
Solid angle	$2.18 \cdot 10^{-6}$ sr		

Table 7.1: *Experimental data of the Laser considered in this study.*

The beam then enters into the flame, and is scattered due to the presence of soot particles. The scattered beam leaves the flame and is captured by an optical apparatus of collection. Only the lens of collection is considered in this study and is called **observer**. The observer is characterized by a diameter of the lens d_{obs} , a solid angle Ω_{obs} , and a distance from the flame that is fixed as well. Table 7.2 gathers the information of the collection lens used in this study. Due to the low values of Ω_{obs} , we consider here again that $\Omega_{obs} \approx 0$. In Appendix ??, the treatment of $\Omega_{obs} \neq 0$ is considered. Since we are interested in the angular position of the observer, we introduce the angle ξ_{obs} defined by the two unitary normal vectors of the observer and the source :

$$\cos(\xi_{obs}) = \vec{n}_{obs} \cdot \vec{n}_{source} \quad (7.1)$$

Observer			
Lens diameter	10 cm	10 cm	10 cm
Distance to flame	80 cm		
Solid angle	$3.14 \cdot 10^{-6}$ sr		

Table 7.2: Experimental data of the observer considered in this study.

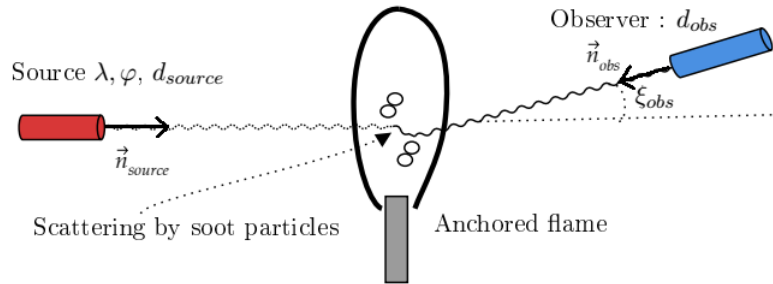


Figure 7.1: Schematic of the studied problem: a Laser beam scattered and collected by an observer (2D view). The source and observer are actually much wider.

The lenses diameter allows for capturing the full height of the flame. The objective of the study is to compute the spectral and directional intensity captured by the observer from the source. In this case, conventional Monte-Carlo techniques such as forward and backward methods are in fact inefficient.

In order to understand the limitation of the conventional techniques, let us consider Figure 7.2 where a source element (point S) and an observer element (point O) are represented. In the forward Monte-Carlo method, photons are computed throughout the whole domain, and only a few of them will reach the

observer within the collection angle. A very high number of photons must be generated, to achieve statistically meaningful results. In the case of the backward Monte-Carlo, photons are traced from the desired location (the observer), but reciprocally only a few of them will reach the source with the correct angle corresponding to the collimated Laser.

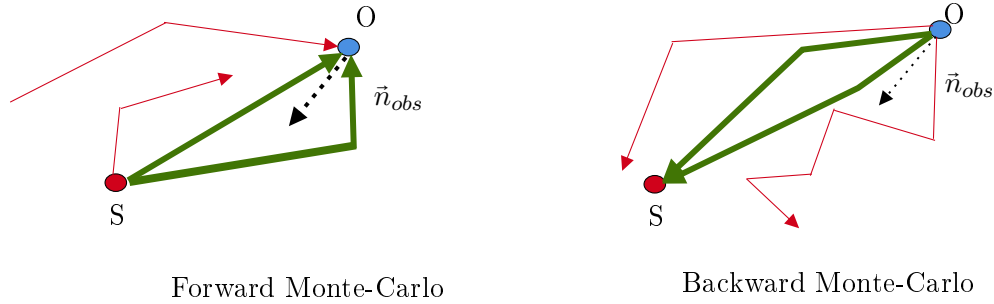


Figure 7.2: Traditional forward (left) and backward (right) Monte Carlo methods. In both cases, only the rays exchanged between O-S are needed. For the targeted application, both methods are inefficient in computing the radiative fluxes impinging the observer (O point) from the Laser (S point).

7.1.2 Introduction to the peel-off Monte-Carlo technique

The peel-off technique (Yusef-Zadeh et al. (1984); Wood and Reynolds (1999); Steinacker et al. (2013); Lee, G. K. H. et al. (2017)) overcomes the difficulties arisen in Section 7.1.1. This method, also called *next event estimate*, has been originally developed in the context of astrophysics where scattered light by stars and nebulae (equivalent to the source) needed to be collected by telescopes (equivalent to the observer). The method is based on the following property:

At each interaction (emission and scattering) , the probability of being scattered towards a given direction is calculated. A photon is then forced towards the observer but with its contribution weighted by this probability.

Since we are using the Emission Reciprocity Method, which is a backward Monte-Carlo-based approach, the photons are traced from the desired location (the observer) throughout the whole computational domain. Hence, since the position of the source is known, it is possible to compute the probability that the bundle would have scattered from the source, as shown in Figure 7.3. Each peeled-ray contributes to the radiative flux obtained on the observer, which can be written as the sum of to contributions :

$$\phi_{obs} = \phi_{direct} + \phi_{peeled} \tag{7.2}$$

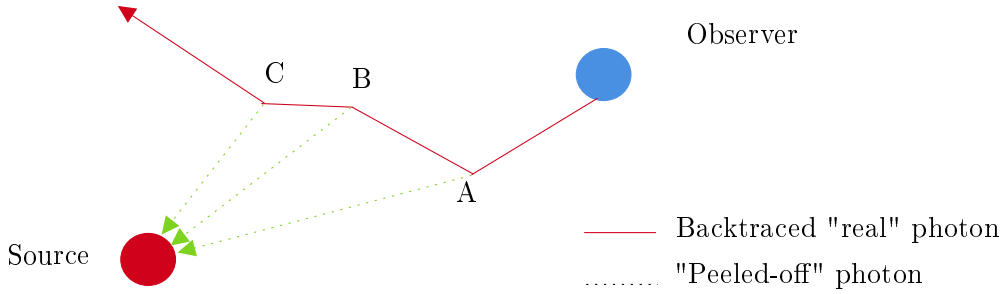


Figure 7.3: Principle of peel-off illustrated with a photon scattered three times (points A, B, C). At each scattered location, an additional ray is generated and is traced towards the source.

where ϕ_{direct} is relative to the direct contribution of the source to the observer (without scattering) when their respective solid angles see each other, and ϕ_{peeled} , which is our quantity of interest, the radiative flux obtained from the photons peeled at the scattering locations.

It is important to notice that the "real" photons do not see the source in RAINIER : the ray cannot impinge on the source object with its emission property. Only the peeled photons are aware of the source: this ensures that the radiative flux is not counted twice in the calculation. The following paragraphs focus on the implementation and the formulations of the radiative exchanges for the direct and the peeled contributions. Equation 7.2 accounts for the source-observer exchanges only. It can be compared to experimental data after subtracting the background signal of the natural flame emission from the measured signal.

7.1.3 Computation of the direct contribution Source-Observer

To save computational time, the direct contribution Source-Observer calculation is only performed once before any photon is traced from the observer point. To simplify, the direct contribution does not involve the scattering stochastic treatment presented in Chapter 2. Instead, the attenuation due to scattering is explicitly taken into account for this specific calculation. Figure 7.4 presents the parametrization used to compute the direct contribution source-observer. In Figure 7.4, the finite-size source is characterized by a center C_{source} and a radius R_{source} . As the source is considered collimated, the area span by the source is a cylinder. Hence, if an observer point P_{obs} lies in this cylinder, the direct contribution between the source and the observer can be calculated. This criterion is verified if and only if :

$$P_{obs} \in \mathcal{C}_{source} \iff d_{P_{obs}, \bar{n}_{source}} \leq R_{source} \quad (7.3)$$

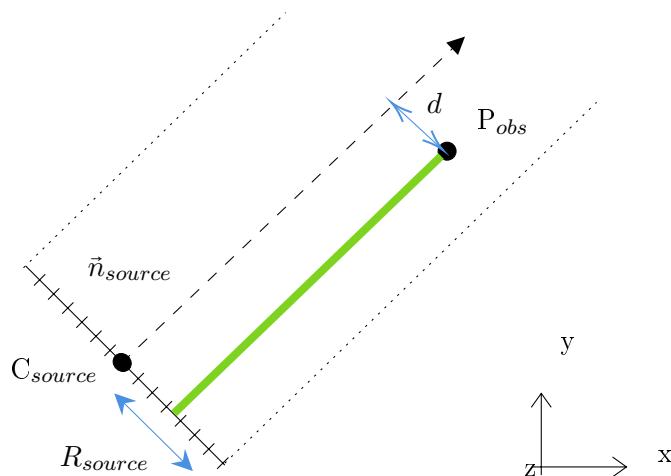


Figure 7.4: Parametrization used to compute the direct contribution Source-Observer (green line). The source is characterized by its center C_{source} , its radius R_{source} , a direction characterized by a normal vector \vec{n}_{source} , its power and the emission wavelength.

where $d_{P_{obs}, \vec{n}_{source}}$ is the distance between the observer point P_{obs} and its orthogonal projection onto the axis directed by the normal at the source surface. In 3D, the distance is expressed by

$$d_{P_{obs}, \vec{n}_{source}} = \frac{\|\vec{CP}_{source} \times \vec{n}_{source}\|}{\|\vec{n}_{source}\|}, \quad (7.4)$$

with the sign \times denoting the curl product. Moreover, because of the collimated hypotheses, the following relation on the normals of the source and the observer must be verified:

$$\vec{n}_{source} = -\vec{n}_{obs} \quad (7.5)$$

If these criteria are not verified, the Rainier solver starts without computing the direct contribution. In the other case, the direct contribution is calculated in two steps.

The first step consists of calculating the radiative exchanges between the photon traced from the observer and the points of the computational domain until the photon reaches the source.

The photon is emitted from the observer and follows the classic ERM approach described in Chapter 2 in Section 2.1.2. The initial direction is imposed, parallel to \vec{n}_{obs} , since collimated observer and source are assumed. The wavenumber is imposed by the source. As stated earlier, the stochastic scattering treatment is not considered for the direct contribution. The major difference relies

on the spectral absorptivity $\alpha_{j,m,\nu}$ (see Equation 2.10 for the definition and notations), which is replaced by $1 - \exp\left[(-\kappa_\nu + \sigma_\nu)(T_j)l_{jm}\right]$ to take into account the attenuation due to scattering.

In a second step, once the photon traced from the observer has reached the source, the radiative exchanged flux between the surface (the source S) and the adjacent cell is computed, using Equation 2.13.

This is repeated for every point P of the observer, enabling reconstruction of a complete image of the signal.

7.1.4 Computation of the peeled contribution Source-Observer

Figure 7.5 presents the parametrization used to compute source-observer contributions in the case of a scattering event, occurring at the point P_{scat} . The situation is very similar to the case of direct contribution computation: first, we assess whether or not P_{scat} belongs to the cylinder generated by \mathcal{C}_{source} with a radius R_{source} :

$$P_{scat} \in \mathcal{C}_{source} \iff d_{P_{scat}, \vec{n}_{source}} \leq R_{source} \quad (7.6)$$

If the condition is verified, another ray that carries the same energy as the original ray from A is generated from P_{scat} . The original one is scattered towards a point B in Figure 7.5, following the default scattering procedure, while the other ray is forced to scatter towards the source.

Contrary to the direct contribution, the probability p_{peeled} that the photon would have scattered towards the source must be computed :

- In the case of **isotropic scattering**, all the scattering events are occurring with the same probability : hence, $p_{peeled} = \frac{1}{4\pi}$
- In the case of **anisotropic scattering**, p_{peeled} is given by the phase function evaluated at the peeled-off scattering angle θ_{po} : $p_{peeled} = \Phi_\nu(\theta_{po})$.

The peeled-off scattering angle, using the notations of Figure 7.5 is given by :

$$\cos(\theta_{po}) = \frac{|\vec{AP}_{scat} \cdot \vec{n}_{source}|}{\|\vec{AP}_{scat}\| \|\vec{n}_{source}\|} \quad (7.7)$$

In practice, before any scattering event, a standard ERM calculation is performed. The initial direction of the photon is imposed parallel to the observer normal (collimated irradiation). The wavenumber is imposed by the source and only the scattering optical thickness τ_s is randomly generated. Since the stochastic approach is retained for scattering, the attenuation of the photon

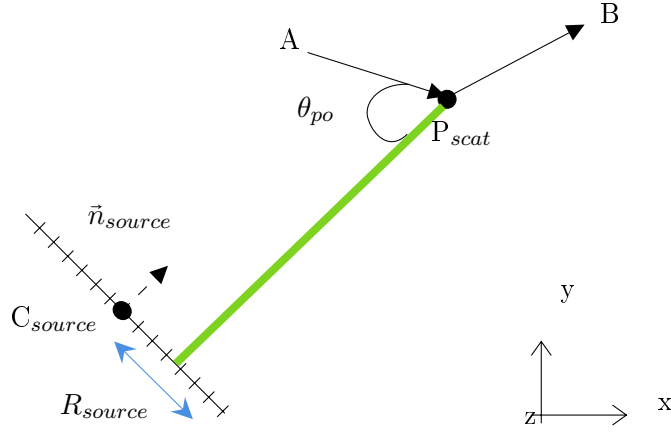


Figure 7.5: Parametrization used to compute the scattering contribution Source-Observer (green line). The real photon computed by Rainier is scattered at P_{scat} and goes to B . θ_{po} represents the angle between the initial direction and the direction pointing towards the source.

along the path is only calculated with the absorption coefficient κ_ν (the attenuation due to scattering is characterized by τ_s). Along the path, the total optical thickness due to absorption and scattering is still stored.

Once the scattering event occurs, the ray is split in two :

- The standard ray, scattered in a random direction, which depends the phase function, (ERM treatment)
- The peeled-off ray, which is forced to scatter towards the source. The direction is imposed by the angle θ_{po} . Similarly to the direct contribution, the peeled-off ray does not use the stochastic scattering treatment. Hence, the attenuation of scattering is taken into account using the total optical thickness previously stored and incremented along the path towards the source.

Finally, once the peeled-off photon reaches the source, the exchanged flux between the source and the adjacent cell is calculated.

This procedure is repeated for each point P of the discretized observer.

Note that it is possible to combine the peel-off technique with importance sampling such as the fast-forced-scattering technique presented in Chapter 2. In this case, the radiative power $P_{exch,scat,ij}$ is weighted by the appropriate factor.

7.1.5 Validation : isotropic medium

Let us then consider the 3D case presented Figure 7.6. The source (with a wavelength equals to 140 cm^{-1}) is set to be at the same position as the left wall of the cube, and is set big enough to englobe the wall surface. The front, back, top, and bottom faces are set with periodic boundaries. One hundred points are set on the x and y direction, and 10 points are considered for the z direction. Each side of the cube has a length $L = 0.1 \text{ m}$.

The domain and the walls are set at an identical temperature $T = 300 \text{ K}$. This ensures that the rays only interact with the source. A gray gas, with a constant absorption coefficient $\kappa = 0.1 \text{ m}^{-1}$ is considered, and the medium is supposed to scatter isotropically and is characterized by an albedo ω .

Since the domain and wall temperature are constant, only exchanges between the observer and the source occur. Thus, both observer and source are collimated.

The chosen set-up enables to compare the observer radiative flux computed from:

- the classic Rainier solver (*ERM case*), which is expected to be inefficient as discussed in Section 7.1.1.
- the peel-off method (*Peel-off case*)

The important point is that the condition to precisely align the randomly scattered ray direction with \vec{n}_{source} is never fulfilled in practice for standard ERM computations. Therefore, a tolerance threshold or 1% is accepted to have still a contribution of the scattered rays for the ERM. This limitation is not problematic for peel-off computations as the peeled ray is forced to be correctly aligned, which shows the benefits of this method compared to the standard ERM.

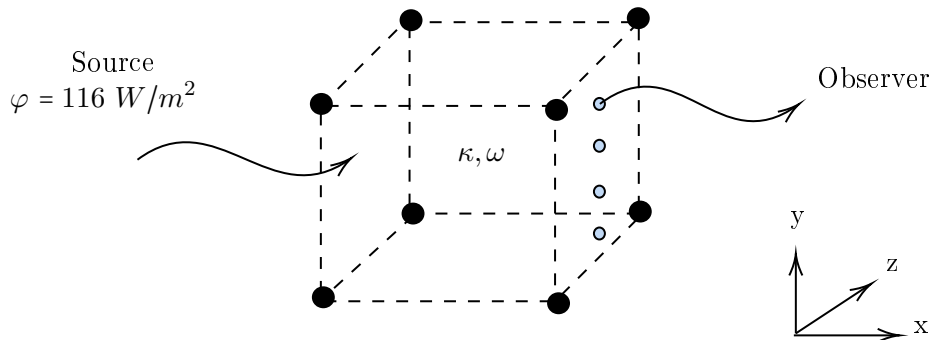


Figure 7.6: *Peel-off validation case: uniform slab with absorption coefficient κ and albedo ω ; the source is defined on the left of the cube with an imposed surface flux; the observer elements are placed along the right face of the cube.*

In both computations, the convergence is done at a fixed number of ray ($M = 20$ trials and $P = 100000$ rays per trial). The albedo is increased from 0 (no scattering) to 0.9. To improve the scattering treatment, the *full-RQMC* with fast-forced scattering developed in Chapter 2 is used in these computations. The corresponding characteristic length is chosen equal to 0.01 m.

All fields are homogeneous in transverse directions. The results of the obtained radiative fluxes for one observer are presented in Figure 7.7. The radiative flux impinging the observer due to the source is decreasing as the albedo increases. This is explained by the increasing optical thickness of the domain as σ increases with the albedo. An excellent agreement of both methods is obtained. Let us recall that a tolerance factor needs to be applied for the ERM to have consistent results with the peel-off technique.

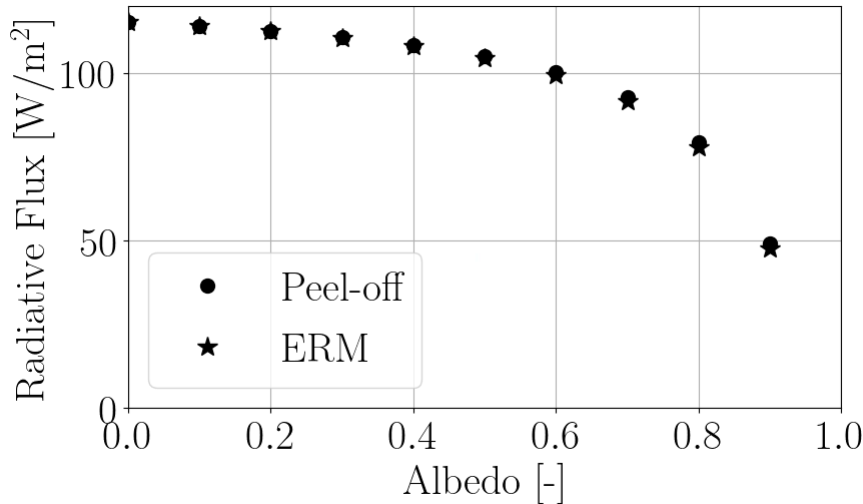


Figure 7.7: Radiative flux at the observer as function of the albedo for the ERM (\bullet) and peel-off (\star) methods in the case of an homogeneous and isotropic medium ($\kappa L = 0.01$).

Moreover, the peel-off method enables to isolate the direct contribution from the one due to scattering. These two contributions are shown in Figure 7.8. It can be noticed that the direct contribution is much more important than the scattered contribution given the facing of observer and source in the present situation. As the albedo increases, the contribution due to scattering also increases while the direct contribution decreases as expected.

The techniques developed in Chapter 2 for the ERM enable to improve the convergence of scattering computations by lowering the obtained error. A similar analysis as the one performed in Chapter 3 is then carried out for the case of $\omega = 0.9$ by comparing the ERM and the Peel-off relative standard deviations

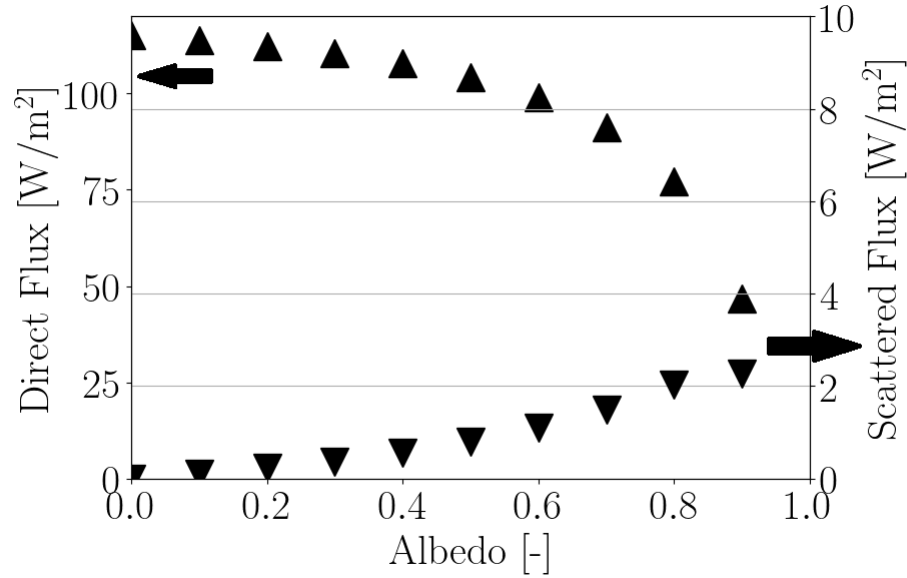


Figure 7.8: Radiative flux direct (▲) and scattered (▼) contributions computed with the peel-off methods in the case of an homogeneous and isotropic medium ($\kappa L = 0.01$).

as a function of the total number of rays N . The convergence plot is presented in Figure 7.9. The *full-RQMC* with fast-forced scattering approach is used for both computations.

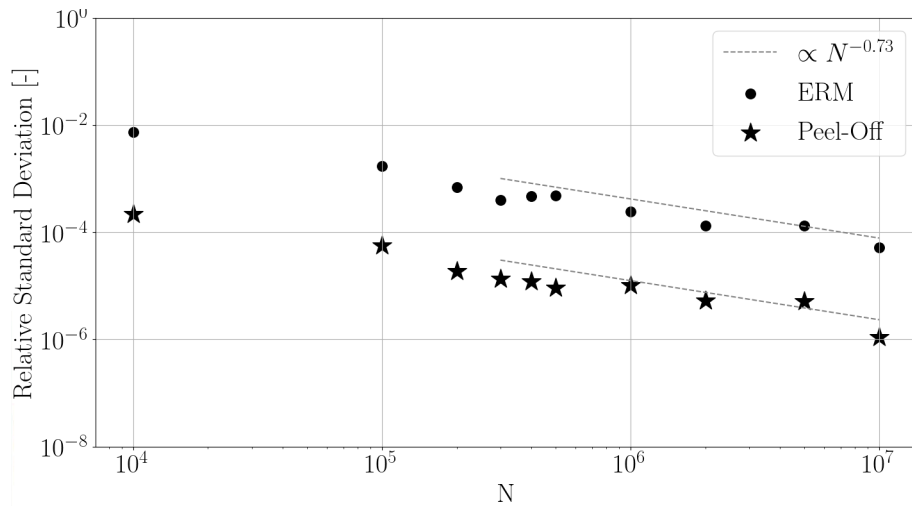


Figure 7.9: Relative standard deviation of the computed scattered flux as a function of the total number of rays N for the ERM (●) and the peel-off (★) methods. The fitted convergence rate is depicted by dashed lines.

In Figure 7.9, the convergence rate of both methods is similar: this is expected as both computations are done using RQMC technique which drives the value of the convergence rate. However, a significant improvement in the error is obtained using the peel-off technique compared to the ERM: To achieve a relative error of 10^{-4} , around 100 times more rays are required using the ERM than the Peel-off method.

The consistency between the ERM and Peel-off methods allows validating the current implementation of the peel-off technique while making sure that it is much more efficient. The validation is pursued with an anisotropic phase function such as the one provided by the RDGFA model.

7.1.6 Validation : anisotropic medium

In this validation case, the same 3D geometry is considered (Figure 7.6). The source is set to be at the same position as the left wall of the cube. The front, back, top, and bottom faces are set with periodic boundaries. Again, 100 points are set on the x and y direction, and 10 points are considered for the z direction. Each side of the cube has a length $L = 0.1\text{m}$. The domain and the walls are set at $T = 300\text{ K}$.

The RDGFA model with the fractal parameters $D_f = 1.8$ and $k_f = 1.2$ is considered for fractal aggregates parameters. A uniform distribution of soot aggregates is considered, with :

- $f_V = 10^{-6}$,
- $n_p = 500$ primary particles per aggregates
- $d_p = 50\text{ nm}$ for each primary particle diameter

These values enable boosting scattering contribution in the validation case. The spectral formulation of the soot optical index m from [Chang and Charalampopoulos \(1990\)](#) is considered.

Several wavelengths for the source are considered in this validation case, from $0.4\ \mu\text{m}$ to $2\ \mu\text{m}$. This range corresponds to values where soot particle radiation is important (near-infrared and visible regions). For each wavelength, Table 7.3 presents the values of the absorption and scattering coefficient of soot particles and the corresponding albedo.

In both ERM and Peel-off computations, the number of ray is fixed ($M = 20$ trials and $P = 100000$ rays per trial). The *full-QMC* method along with the *Fast-forced-scattering* (with a reference length equal to $0.1m$) is used.

Figure 7.10 compares the radiative fluxes on the observer obtained with standard ERM calculation and the peel-off calculation for different wavelengths. Both methods are in very good agreement, which validates the implementation

Wavelength [μm]	Absorption optical thickness κL	Scattering optical thickness σL	Albedo
0.4	1.223	0.346	0.22
0.5	0.978	0.211	0.18
0.6	0.815	0.140	0.15
0.7	0.699	0.099	0.12
1	0.489	0.043	0.08
1.5	0.326	0.017	0.05
2	0.244	0.008	0.03

Table 7.3: Radiation characteristics as a function of the source wavelength

of the peel-off methodology along with RDGFA and anisotropic scattering.

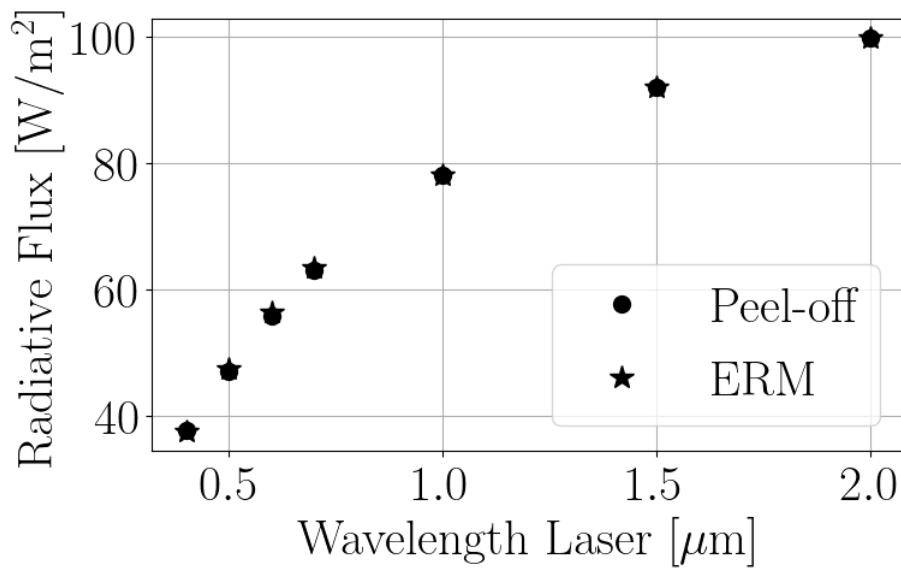


Figure 7.10: Radiative flux at the observer as a function of the source wavelength for the ERM and peel-off methods in the case of anisotropic scattering due to soot particles.

As the wavelength of the source/Laser increases, the radiative flux reaching the observer increases as well: this is due to the lower optical thickness of the domain as observed in Table 7.3. On the contrary, a high optical thickness for low wavelengths explains the observer's low radiative flux.

Looking at the albedo values in Table 7.3, it is clear that the scattered contribution on the radiative flux is the highest for these low wavelengths. This

is confirmed in Figure 7.11 where the direct and scattered contributions are plotted using the peel-off technique. In the range 400 – 1000 nm, the direct contribution dominates the scattered one by a factor between 2 to 20. The scattered contribution is small and the peel-off method benefits from the *full-QMC* and *Fast-forced-scattering* techniques developed in Chapter 2 to yield an efficient computation.

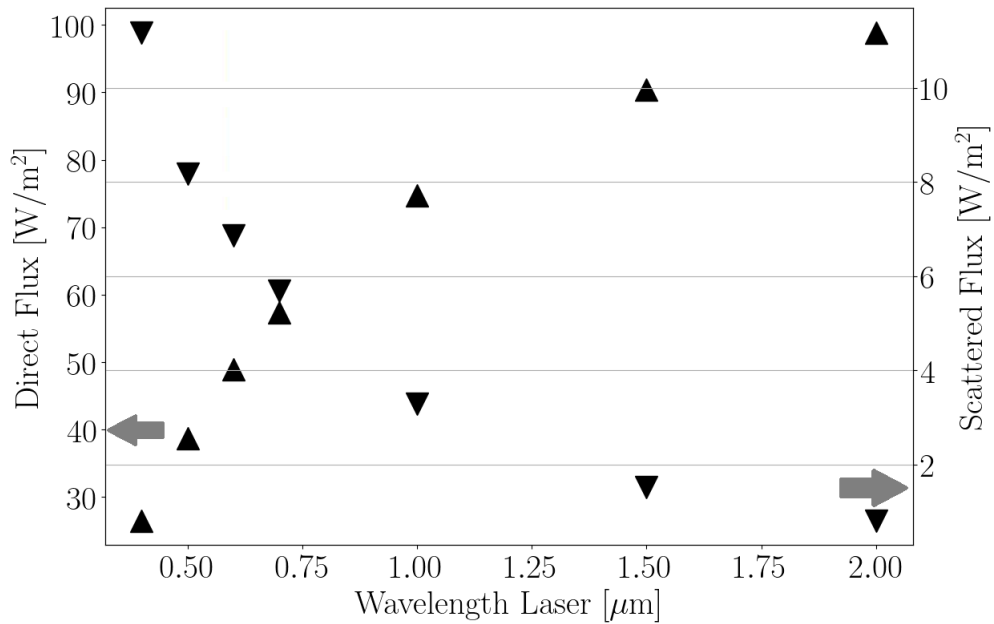


Figure 7.11: Radiative flux direct (▲) and scattered (▼) contributions at the observer as a function of the source wavelength for the ERM and Peel-off methods in the case of anisotropic scattering due to soot particles.

7.2 Application of peel-off technique to CFD fields from coupled calculations

In this section, the peel-off technique is applied on the coupled simulation fields obtained in Chapter 6.

7.2.1 Numerical setup

As explained in Section 7.1, the experimental setup at the Institut Jean Rond d'Alembert presents several constraints that need to be taken into account to compare the synthesized and experimental signals qualitatively.

Retained experimental constraints:

- The source-flame distance d_{sf} is fixed to 50 cm,
- The observer-flame distance d_{of} is fixed to 80 cm,
- The radius of the source and observer are equal to 10 cm,
- Three wavelengths are considered : 405, 605 and 785 nm,
- The Laser power is equal to 1 mW for $\lambda = 405$ nm and $\lambda = 785$ nm, and 4 mW for $\lambda = 605$ nm

Simplifications of the experimental set-up:

- The considered source and observer are respectively placed after and before the optical apparatus leading to the Laser and imaging camera,
- Accordingly with the experimental optical setup, both source, and observer are considered perfectly collimated,
- The Laser beam has no spectral width,
- The apparatuses behind the lenses of emission/collection are not modelled,
- The Laser intensity is homogeneously distributed

General parametrization:

The observer position is a rectangular plane whose center is positioned at an angle α_o as shown in Figure 7.12. Since the distance flame-observer is fixed, the observer planes are placed along a circle of a radius equal to d_{of} . The observer itself is discretized with 100 points in the vertical direction and 20 in the horizontal direction.

For each point, the solver Rainier computes the local radiative flux with the implemented peel-off method. The full-RQMC approach developed in Chapter 2 is used. The RDGFA model with the same parameters (form factor, fractal parameters, surface-volume relationship sv-model 2) as those of Chapter 6 is considered to compute soot radiative properties. The relative and absolute error of the Monte-Carlo solver are set to 0.1%. Such small error can be prescribed at a reasonable CPU cost since rays are only emitted from the desired location (the observer) which greatly limits the number of photons.

The direction \vec{n}_{obs} is readily calculated with the angle α_o in the absolute frame x, y, z :

$$\vec{n}_{obs} = -\sin(\alpha_o)\vec{y} + \cos(\alpha_o)\vec{z} \quad (7.8)$$

The position of an observer point M is then given by the expression

$$O\vec{M} = h_v\vec{x} + (d_{of}\sin(\alpha_o) + h_h\cos(\alpha_o))\vec{y} + (-d_{of}\cos(\alpha_o) + h_h\sin(\alpha_o))\vec{z} \quad (7.9)$$

where h_v and h_h are the coordinates of M in the local frame of the observer plane.

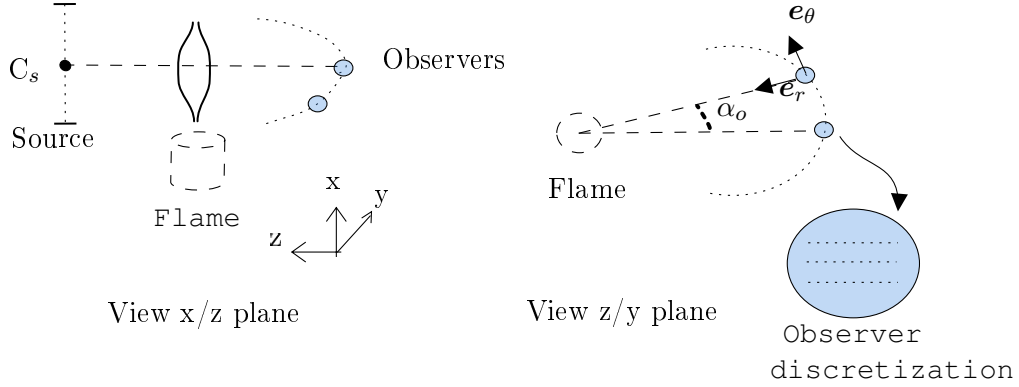


Figure 7.12: Parametrization used to generate signals from the Santoro laminar diffusion flame. Left : side view, right : top view.

Calculations are carried out using the RDG-FA model with the spectral formulation of Chang and Charalampopoulos (1990) for the optical index, and fractal parameters are set to $D_f = 1.8$ and $k_f = 1.2$. To stay consistent with the coupled calculations, the form factor expression is given by Yang et al. (2005).

7.2.2 Impact of observer angle

For all the calculations in this section, the Laser wavelength is set to 405 nm and α_{of} varies from 0 to 90 degrees (clockwise and anticlockwise).

First of all, let us consider the case where the Laser, the flame, and the observer are aligned, which corresponds to $\alpha_o = 0$. In Figure 7.13, the *total* signal collected by the observer is presented. This signal is the sum of the direct contribution due to the Laser, and the scattered signal. The signal is dominated by the direct Laser contribution, and the angle $\alpha_o = 0$ cannot be used in practice to study soot scattering. The attenuation of the direct signal by scattering can be observed and is located where soot particles are present in the flame.

Let us analyse the scattering contribution obtained in order to extract more specific information. The scattered signal collected by the observer, in this case, is displayed in Figure 7.14. The corresponding contribution is approximately two orders of magnitude lower than the Laser direct contribution. It is important to mention that, since we are considering the solid angle $\Omega = 0$, the collected signal due to scattering is slightly underestimated. In this signal, high values are obtained near the axis, for locations $x = 3$ cm. At this height, a high number of particles is present, which enhances the scattering. The surface growth mechanism is also important in this zone, which increases the size of

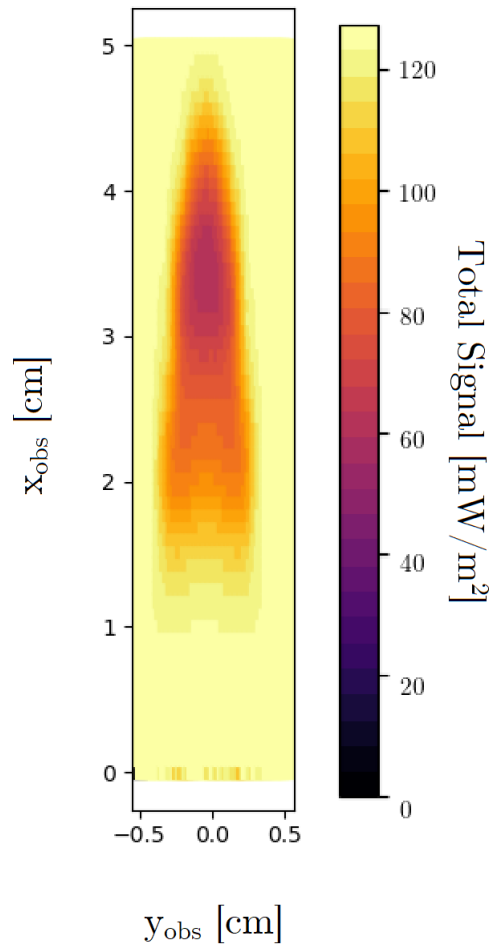


Figure 7.13: *Synthesized image of total signal obtained on the observer. Wavelength: 405 nm. Angle: $\alpha_o = 0^\circ$.*

the particles, and therefore, the scattering impact.

As explained in Chapter 6, the high concentration of particles near the axis instead of the flame wings is attributed to the uncertainties in the sectional model and the chemical description of the soot precursors (using the KM2 mechanism and the extended RFPV model). Although this is inconsistent with experimental observations, the peel-off technique replicates consistent results with the CFD fields and the expected associated behaviour of scattering.

A smaller but still significant proportion of the collected signal corresponds to the scattering due to particles located along the wings of the flame, where the particle number is still important. In the remaining zones, where small par-

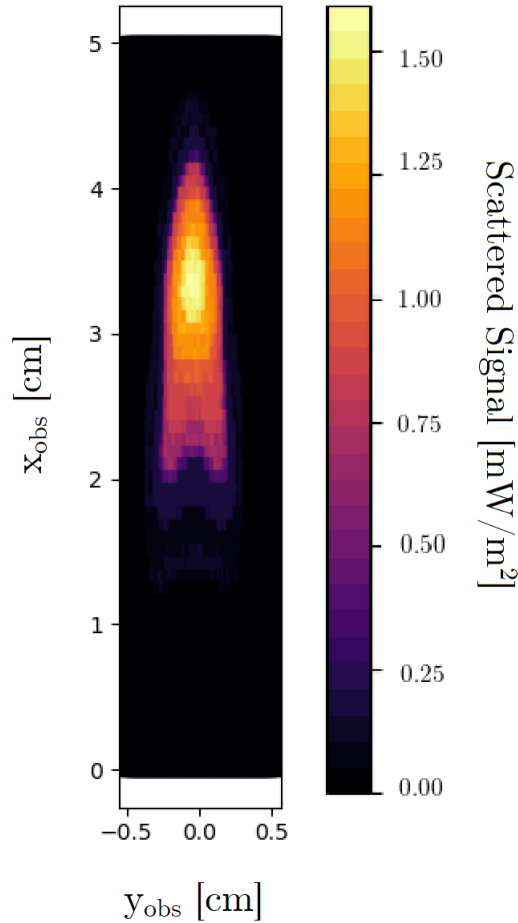


Figure 7.14: *Synthesized image of scattered signal obtained on the observer. Wavelength: 405 nm. Angle: $\alpha_o = 0^\circ$.*

ticles exist (near the burner lip) or not (downstream where the particles are oxidized), no scattered signal is captured.

To avoid the important direct contribution, different angles are examined. An example of the images obtained at $\alpha = 40^\circ$ and $\alpha = -40^\circ$ are presented in Figure 7.15. The signal is very similar to the scattered one obtained at $\alpha_o = 0^\circ$: a maximum signal is located in the zone where the number of soot particles is important and with an important size.

The intensity values obtained are, however, strongly lower than in the case $\alpha_o = 0^\circ$. This result is related to the phase function that gives information on the probability of being scattered from a given angle. It has been shown in Chapter 3 that the scattering phase function for the RDG-FA approach predicts, for the biggest particles, a strong forward scattering which means small

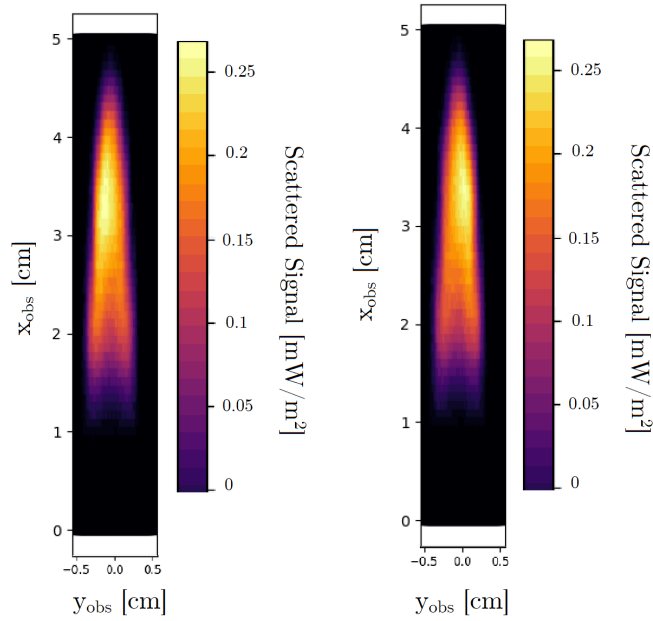


Figure 7.15: *Synthesized image of scattered signal obtained on the observer. Wavelength: 405 nm. Angle: $\alpha_o = -40^\circ$ (left), $\alpha_o = 40^\circ$ (right).*

angles of scattering are expected. In Figure 7.16, the scattering phase function for a distribution of aggregates located at the maximum signal is reconstructed at the considered wavelength. The scattering phase function presents indeed a peak shape located towards small angles (close to 0°). Hence, the scattered direction most probably corresponds to small angles. Therefore, for the considered angle of 40° , a small amount of signal is collected.

Each figure in Fig. 7.15 presents a signal asymmetry which is mirrored between 40° and -40° . The most noticeable changes occur in the zone of maximum signal. At $\alpha_o = -40^\circ$, only the left part of the centered zone captures the maximum signal, while it is the right part for $\alpha_o = 40^\circ$. The asymmetry is attributed to the fact that some rays need to travel a longer portion of the flame to reach the observer. The optical thickness along the path therefore increases, and less signal reaches the observer.

The impact of the observer angle is now analyzed in Figure 7.17 in terms of integrated scattered contribution to the radiative flux on the observer plane. The signal is symmetric. This behaviour is expected since the flame is axisymmetric and the phase function is symmetric. Around relatively small angles (lower than 10°), the scattered contribution decreases strongly. This is again explained by looking at the phase function behaviour for these small angles, and at the considering wavelength (Figure 7.16). The phase function values

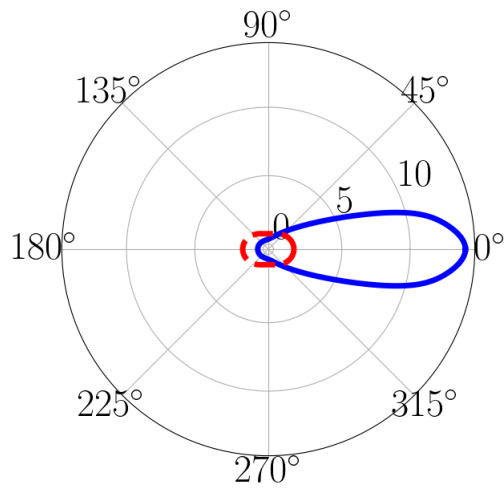


Figure 7.16: Phase function given by the RDGFA model for an aggregate distribution localized at the maximum signal location in Figure 7.15. The phase function given by Rayleigh theory is indicated by the red dashed line.

decrease very quickly for scattered angles larger than 10° , which indicates that the probability of being scattered for important angles is small. Hence, the collected signal by the observer due to scattering is decreasing for larger angles.

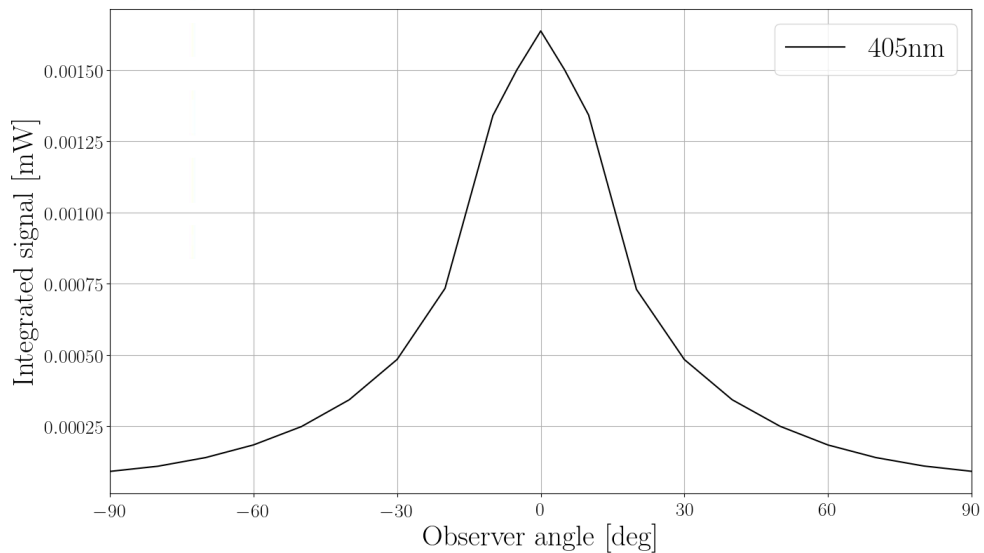


Figure 7.17: Angular evolution of the integrated radiative flux on the observer. Wavelength : 405 nm.

7.2.3 Impact of the source wavelength

In this section, an additional calculation is performed at 785 nm. The results are compared with the previous ones obtained at 405 nm in Figure 7.18.

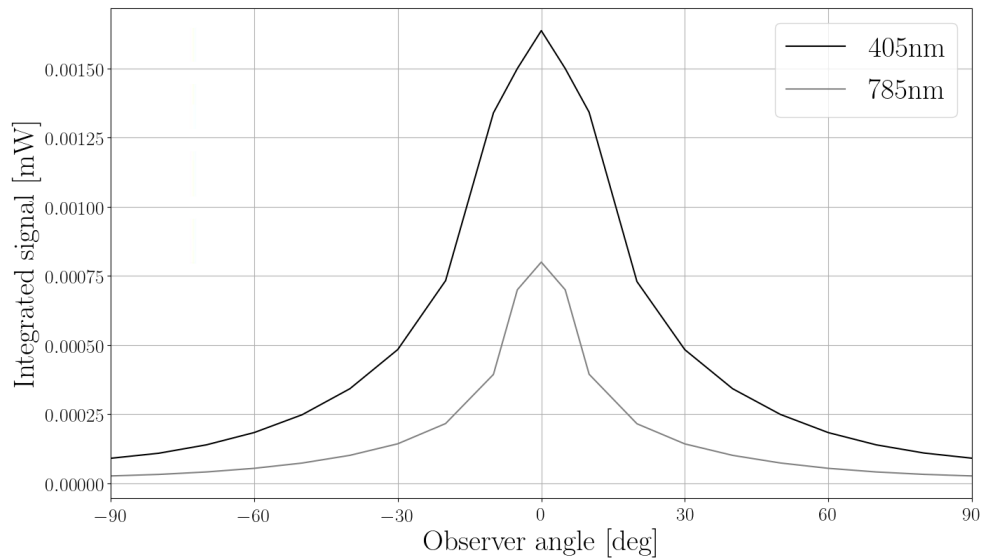


Figure 7.18: Angular evolution of the integrated radiative flux on the observer for two wavelengths : 405 nm (black line) and 785 nm (gray line).

The same angular behaviour is observed for both cases: the maximum signal is obtained for an observer angle equal to 0° and decreases as the angle goes to 90° or -90° . The scattered radiative flux obtained for the longer wavelength is lower, consistent with the corresponding decreasing impact of scattering.

The decay rate of the signal tails for large angles appears more moderate when considering a higher wavelength. In other words, although the signal collected is slight, variations with the angle are less sensitive to the signal attenuation. The phase function for the same aggregate distribution as the one considered in Figure 7.16 (at 405 nm) is shown in Figure 7.19 for the considered wavelength of 785 nm. The probability to be scattered at larger angles is indeed increased at this wavelength. Therefore, the collected signal is relatively still important for moderate observer angles, which is depicted by a smoother decrease of the signal profile in Figure 7.18.

The impact of the wavelength on a single point of the observer, at a fixed angle (here, at $\alpha_o = 0^\circ$) is further examined to understand the different behavior of soot scattering properties. Figure 7.20 presents the spectral variation of the heat flux reaching the center of the observer.

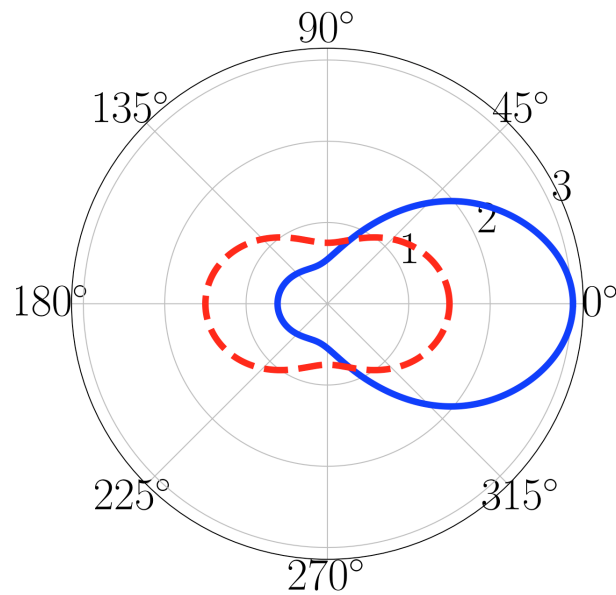


Figure 7.19: Phase function given by the RDGFA model for an aggregate distribution localized at the maximum signal location at 785 nm. The phase function given by Rayleigh theory is indicated by the red dashed line.

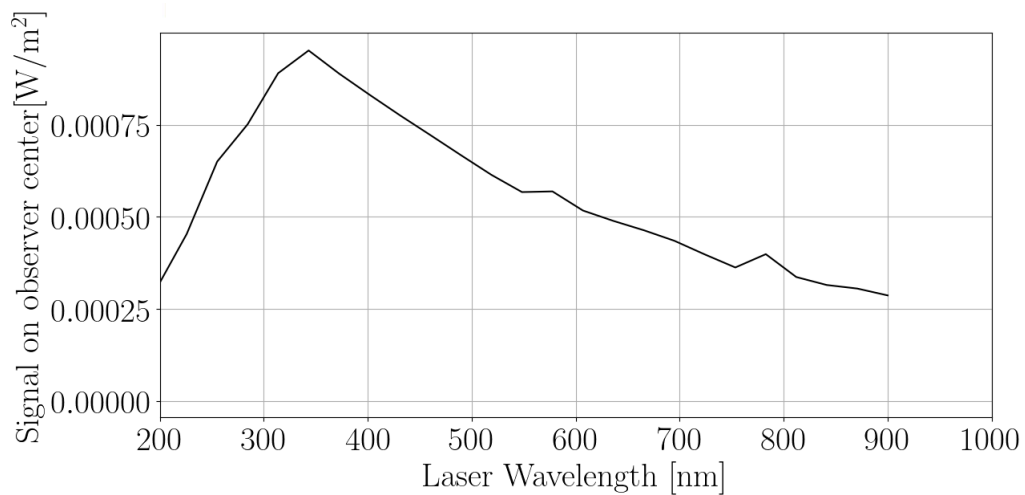


Figure 7.20: Spectral evolution of the scattered radiative flux on the center of the observer, for an angle $\alpha_o = 0^\circ$.

The figure exhibits a maximum of around 350 nm. This shows the interest in operating at low wavelengths as considered in the experimental study. From this maximum, increasing the wavelength lowers the obtained signal due to scat-

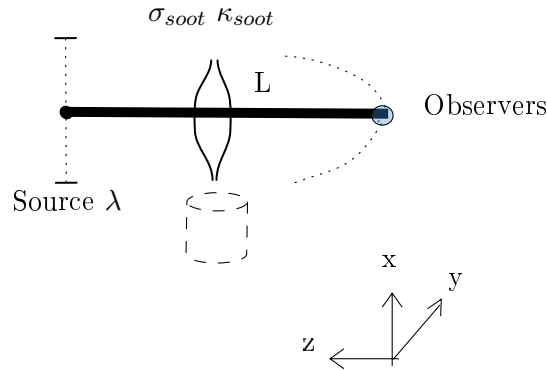


Figure 7.21: Considered ray for the study of the spectral optical thickness evolution.

tering, as already noticed previously. However, below 350 nm, the scattered signal contribution is reduced, even though the scattering coefficient σ_{soot} is increasing (in the classic Rayleigh theory, it is proportional to $\frac{1}{\lambda^4}$).

The peel-off contribution depends on the phase function and the attenuation of the photon from the scattering point towards the observer. The scattering phase-function patterns are very similar for low wavelengths (we are far from the Rayleigh pattern, and forward scattering is favored). A possible explanation is then the optical thickness of the medium that has increased. Indeed, not only σ_{soot} increases with a lower wavelength, but also the absorption coefficient κ_{soot} : it is proportional to $\frac{1}{\lambda}$.

In order to assess the optical thickness of the medium and its impact on the results for $\alpha_o = 0^\circ$, let us consider a photon going from the source to the center of the observer, at $y = 0$ as shown in Figure 7.21. Figure 7.22 represents the evolution of the average κ_{soot} and σ_{soot} along the optical path with the wavelength λ , and the corresponding albedo ω . As expected for soot particles in the visible range, the absorption coefficient dominates the scattering coefficient, resulting in a relatively low albedo. However, near the UV, the albedo is much stronger because of the σ_{soot} sharp increase.

Hence, as λ decreases, σ_{soot} increases, and more signal from scattering is expected. On the other hand, κ_{soot} increases as well, which traps some part of this signal. With scattering becoming more and more present, the signal is also attenuated by deviation. Both opposite terms are combined in the product $\sigma_{soot}e^{-\beta L}$ (with $\beta = \sigma_{soot} + \kappa_{soot}$). The evolution of this quantity is plotted in Figure 7.23 and is strongly linked to the spectral signal evolution obtained in Figure 7.20. Indeed, both maximums are obtained for similar wavelengths (the order of magnitude is around 350nm). The effect of scattering on the observer signal is the highest in this spectral range, which combines favorable scattering

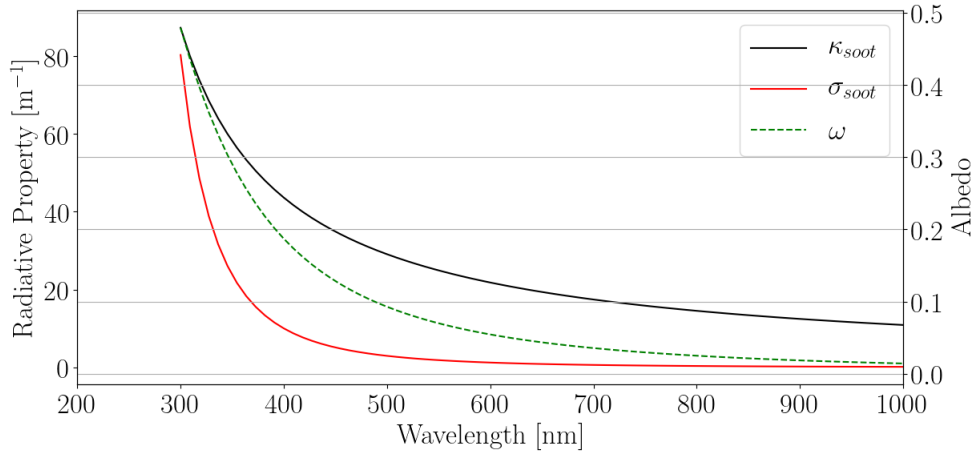


Figure 7.22: Spectral evolution of soot radiative properties averaged on a characteristic optical path along the flame.

and moderate optical thickness.

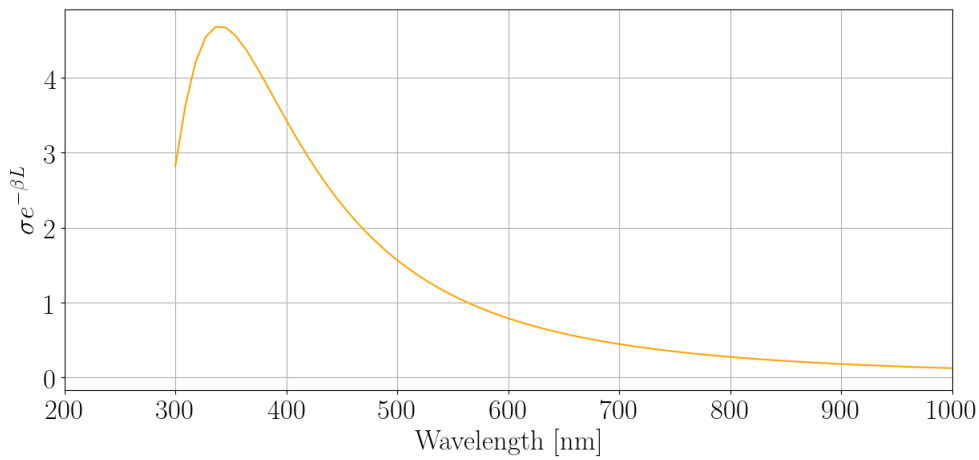


Figure 7.23: Spectral evolution of the factor $\sigma_{soot}e^{-\beta L}$ along the observer line-of-sight for $\alpha_o = 0^\circ$.

7.3 Application of peel-off technique to CFD fields from detailed chemistry calculations

In this section, numerical fields obtained using detailed chemistry calculations provided by J.L Consalvi (Escudero (2019)) are considered to assess the impact of the chemistry and soot modeling on the peel-off results for the same laminar

flame.

7.3.1 Numerical setup

Details on the chemistry and soot modeling can be found in the thesis by Escudero (2019). Here, only a summary is recalled to emphasize the differences with the simulations carried out in Chapter 6.

Gaseous phase description

The chemical mechanism considered in this simulation is the detailed one from Dworkin et al. (2011), which consists of 94 species and 723 reactions. This mechanism has been able to improve the prediction of soot volume fraction along the centerline region compared to mechanisms using other PAHs pathways. The dimerization process only involves 3 PAHs which are formed by 5 aromatic rings.

Soot phase description

A sectional method is considered to solve the population balance equation (PBE) in order to retrieve the number density function $n(V)$ of soot particles. These particles are assumed to be aggregates, with a fractal dimension $D_f = 1.8$. The primary particles are supposed spherical.

Radiative properties

The CFD results were coupled to thermal radiation with a Discrete Ordinate Method (with a T_3 quadrature). Gaseous radiative properties are described by the SNBCK model, and a Rayleigh regime for non-scattering soot particles was assumed, with the following expression: $\kappa_{\lambda,soot} = 5.5f_V/\lambda$.

Figure 7.24 presents the corresponding soot volume fraction and the density number of particle fields obtained with the presented numerical setup. The maximum level of soot volume fraction is around 8 ppm and is located along the wings of the flame, which is consistent with experimental results. Unlike the fields presented in Chapter 6, the soot volume fraction is not overestimated along the centerline, which is attributed to the chemical mechanism retained in the detailed calculation of the flame. An important number of particles is located at the bottom of the flame, which is due to the strong localization of PAHs in this zone. A second zone of high-density particles is also observed downstream the flame, near the centerline.

The peel-off methodology is applied to these detailed fields. The different soot topology fields are expected to modify the images collected by the observer compared to those obtained in Section 7.2.

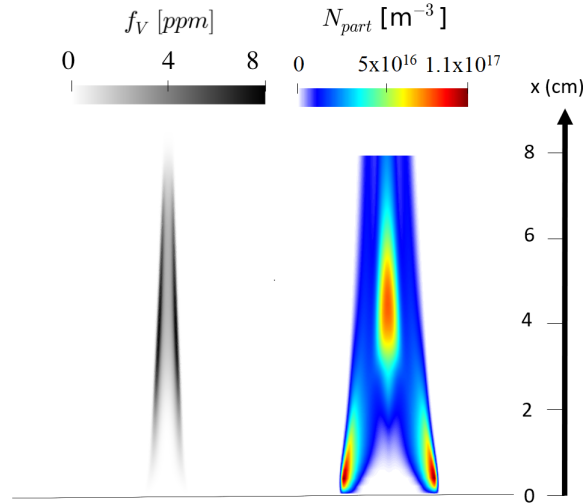


Figure 7.24: *Fields of soot volume fraction and density of the number of particles from detailed chemistry calculations.*

7.3.2 Results and comparison with coupled calculations

Figure 7.25 presents the scattered signal received by the observer at 405 nm, for an angle $\alpha_o = 0^\circ$ with the fields taken from detailed chemistry simulations (left) compared with the one obtained with coupled simulations in this thesis (right). Looking at the soot related fields obtained in both computations, it is expected that the signal captured by the observer extends on a higher height, which can be observed in Figure 7.25. The signal is collected up to 10 cm against 4 cm for the coupled calculation.

Then, a strong signal is obtained at the bottom of the flame. This strong signal is correlated with the high density of particles near the wings seen in Figure 7.24, where nucleation is dominant. The signal then decreases as one moves downstream the flame. The maximum value of the scattered signal is 6 mW/m^2 , which is three times higher than the value obtained in Section 7.2.

The achieved level of soot volume fraction between both computations is similar (around 10 ppm), which implies that the absorption coefficient values are close (since κ is proportional to the soot volume fraction). Therefore, the difference in the signal magnitude cannot be attributed to a difference in absorption attenuation. Regarding scattering, since both computations are based on RDGFA models with fixed fractal parameters and form factor, only 3 parameters are allowed to vary : the total number density of particles N_{part} , the number of primary particles of an aggregate n_P and the diameter of these primary particles d_P .

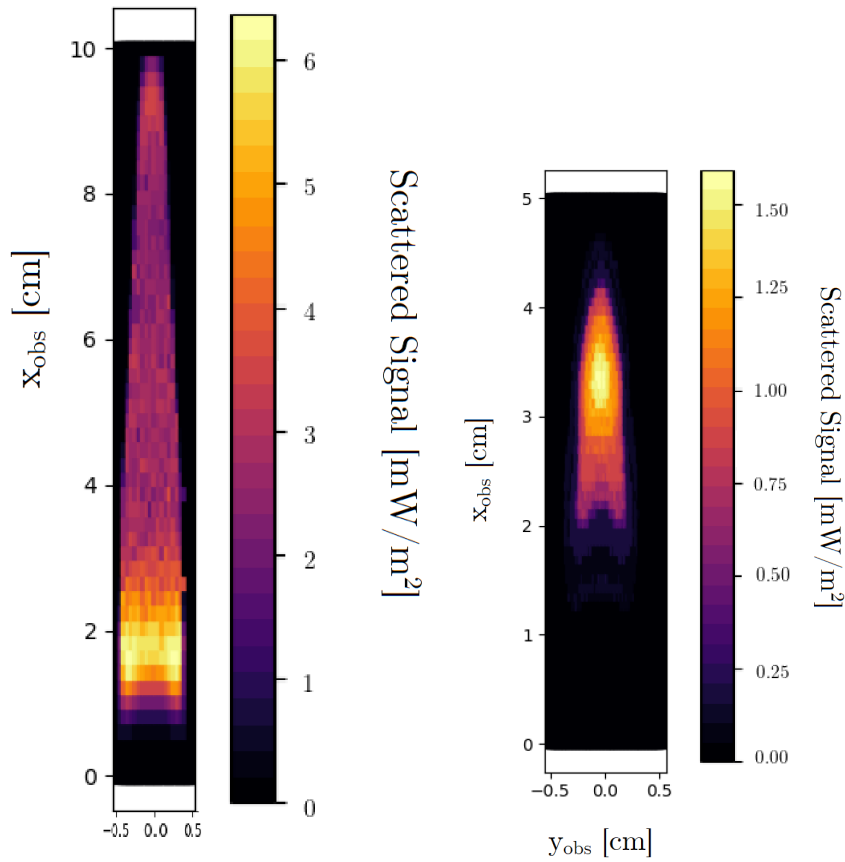


Figure 7.25: *Synthesized image obtained on the observer : scattering of particles at 405 nm, $\alpha_o = 0^\circ$. Top : detailed chemistry, bottom : tabulated chemistry.*

The comparison of the total number density of soot particles between both computations is presented in Figure 7.26. The fields present strong differences in topology. In the coupled calculation carried out in the thesis, even though an important number density of particles is located along the wings, the maximum values are encountered near the centerline. On the opposite, the detailed chemistry calculation presents a maximum at the bottom of the flame. These differences in topology are directly correlated with the maximum signal captured by the observer. Therefore, an accurate numerical prediction of the number density is crucial to synthesize the observer signal.

The signal intensity also depends on the size of the particles. Figure 7.27 presents the fields of mean diameter of primary particles, noted \bar{d}_P , for both simulations. As already mentioned in Chapter 4, the choice surface-volume relationship can have a strong influence on the scattering coefficient, and therefore, on the obtained signals. Globally, the mean particle diameter given by

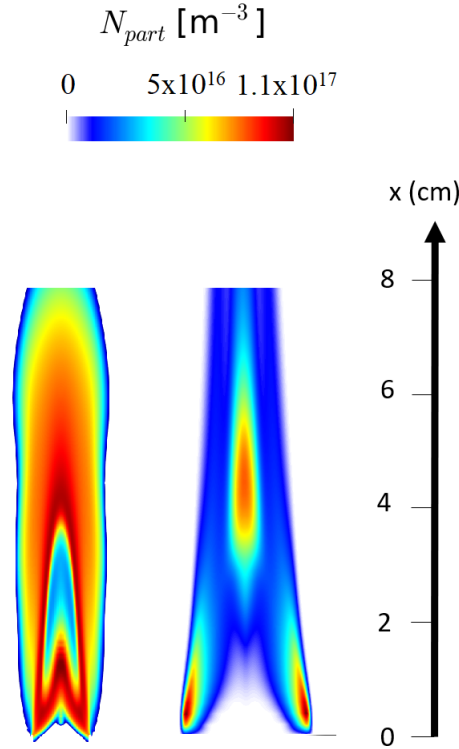


Figure 7.26: Comparison of the total density number of particles N_{part} between the coupled calculation performed in this thesis (left) and the detailed chemistry simulation (right).

the coupled calculation (left) is smaller than the one obtained by the detailed chemistry computation (right). Hence, the scattering coefficient and its impact are higher in the latter case.

Both information given in Figures 7.26 and 7.27 are needed to understand the collected scattered signals. In the thesis coupled calculation field, although the number of particles is important for $x \leq 2$ cm, the diameter of primary particles is too small to scatter photons efficiently. Near the centerline, for $x \approx 3$ cm, there is a relatively important number of particles with a bigger size, resulting in a stronger signal observed in Figure 7.25. For the field obtained with detailed chemistry, the same behavior is observed at the bottom of the flame : the overlap of important primary particle diameter and N_{part} explains that a strong scattered signal is observed near the burner exit. Downstream (for $x \geq 3$ cm), particles are bigger (which contributes to the scattered signal), but the particle number density is smaller. Hence, a lower signal is collected downstream.

The total signal collected by the observer for different angles is compared be-

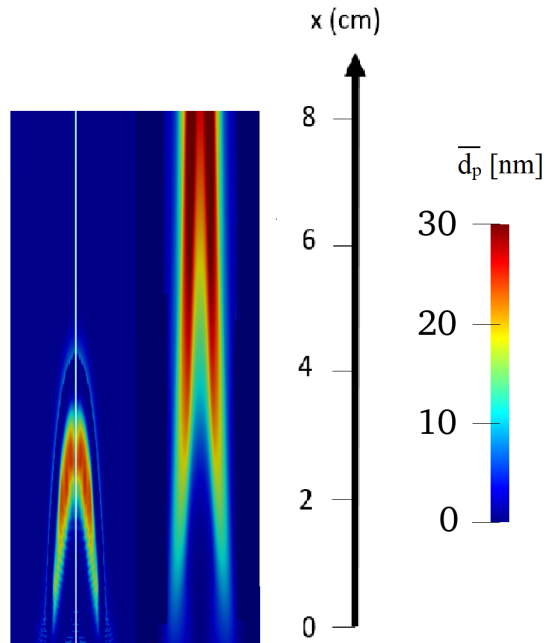


Figure 7.27: Comparison of mean primary particles diameter between the thesis computation (left) and detailed chemistry simulation (right).

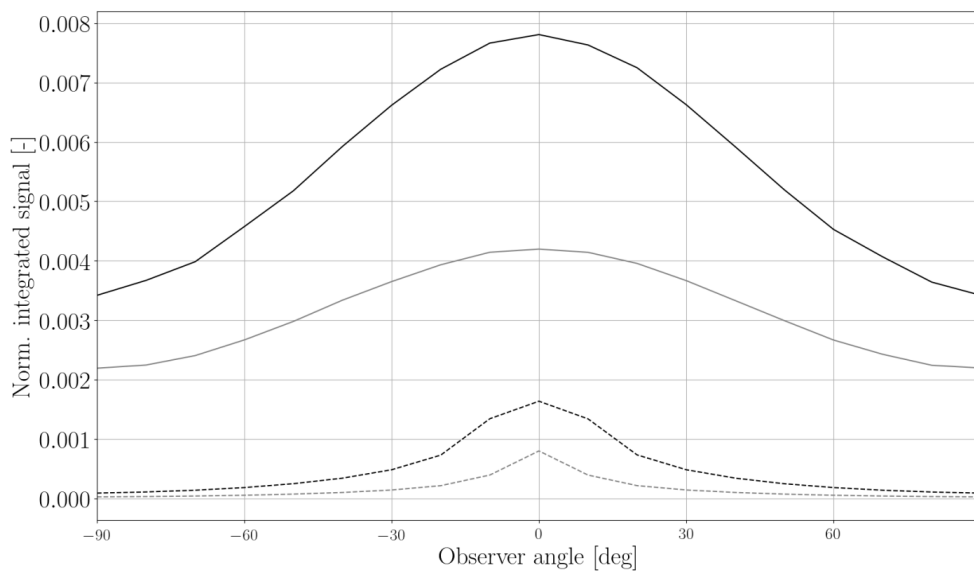


Figure 7.28: Comparison of integrated signals collected by the observer for both computations: thesis work (dashed lines), detailed chemistry (solid lines) at two different wavelengths (405 nm: black, 785 nm: gray).

tween both computations in Figure 7.28. The wavelengths 405 nm and 785 nm with the same Laser power (1 mW) are considered. The impact of the wavelength, already discussed in Section 7.2.3, is retrieved. As mentioned in the previous analysis, more signal is collected by the observer in the detailed chemistry computation.

Experimental data are often given in terms of normalized signals. In order, for further work, to compare our results with experimental measurements, scaled profiles for both computations are presented Figure 7.29. Each profile is scaled by its maximum value obtained in the corresponding computation.

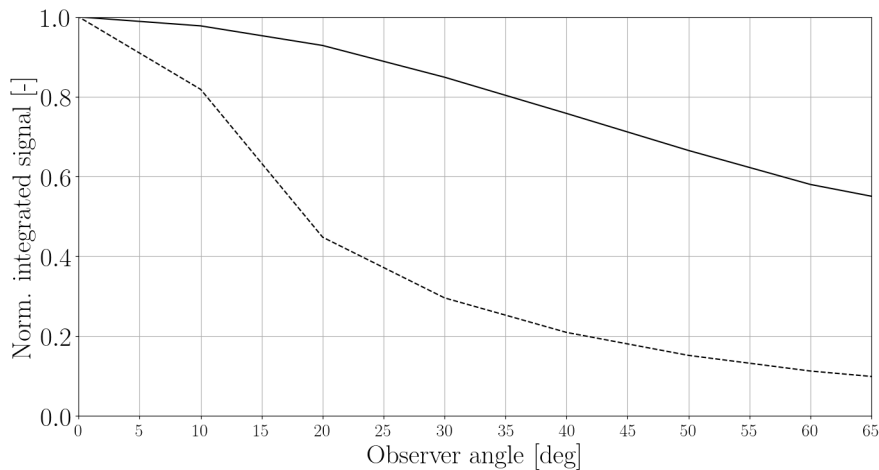


Figure 7.29: Angular variation of normalized integrated signal. Computations: detailed chemistry (solid line); thesis work (dashed line)

It can be observed that the decrease of the signal using the fields from this thesis work is steeper than the detailed chemistry. In order to understand such behaviour, let us compute the phase function at 405 nm for both cases shown in Figure 7.30. We consider the maximum values of \bar{n}_P and \bar{d}_P to compute aggregate properties and the corresponding phase function given by the RDG-FA theory. The computed phase function is narrower for low angles for the thesis simulation results. Therefore, the probability of being scattered for higher angles is smaller for this case, resulting in a faster angular decrease of the scattered signal.

7.4 Conclusion

The objective of this chapter was to generate Laser scattering signals using our Monte-Carlo solver Rainier with the fields obtained in Chapter 6. Rainier is based on the ERM approach, a Backward Monte-Carlo method, and is not

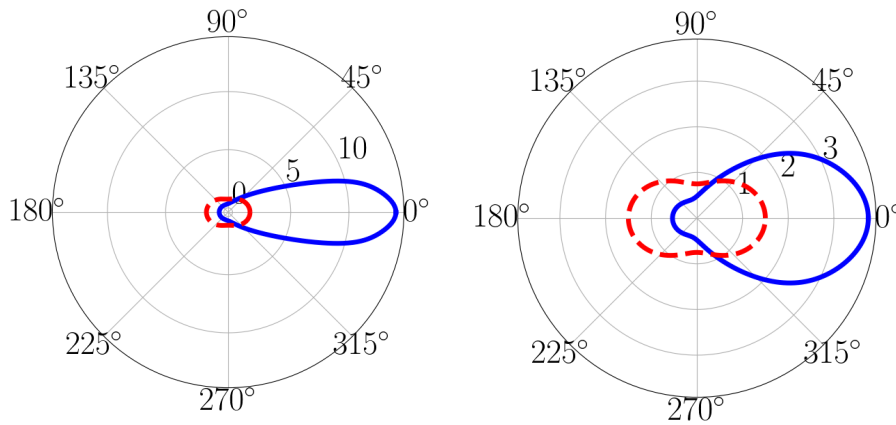


Figure 7.30: Computation of phase functions for the thesis computation (left) and detailed chemistry simulation (right) in a polar diagram. The phase function predicted by Rayleigh theory is indicated by a red dashed line.

suitable for this type of computation. Therefore, a technique known as the peel-off method has been implemented and validated in Rainier for isotropic and anisotropic scattering cases. It is then applied along with the QMC method and importance sampling for scattering developed in Chapter 2 to improve the convergence of our simulations.

Laser scattering signals have been successfully generated with two fields: the one obtained from our coupled simulations and one obtained with a detailed chemistry approach provided by J.L Consalvi. For both fields, the impact of the observer's position, which collects the signal, is assessed. The maximum signal is obtained when the Laser, the flame, and the observer are aligned. However, in this position, the signal is also polluted by the direct contribution of the Laser. The signal then decreases with the angular position. The integrated signal is higher for the detailed chemistry approach, which is due to :

- The bigger size of particles encountered in the detailed simulation associated with a larger number density of particles,
- A longer luminous flame

For both computations, the impact of the angular position and wavelength are similar. At higher wavelengths, the collected signal is reduced. The decrease of the signal with the observer position is less pronounced. This is interpreted thanks to the phase function: at higher wavelengths, more isotropic scattering occurs, which means that the probability of being scattered towards larger angles is higher. Therefore, the signal is still collected even for large observer angles. In any case, a slightly dissymmetric signal is observed when modifying the observer angle position for both computations, which has been interpreted as a difference of optical path length crossed by the photons.

We are now able to compare such signals with experimental data, which will be done in further work.

Conclusion

The global objective of this thesis was to provide a better understanding of soot radiation by assessing its impact on accurate CFD simulations.

From an industrial and practical perspective, simplified radiative models are sometimes considered in combustion chamber simulations. The Optically Thin Assumption enables to directly obtain the radiative power without any additional solver, for example. This model enables to save CPU time and is ready-to-use in a CFD solver. However, it strongly underestimates the temperature, which impacts the prediction of pollutants such as soot particles.

A more general goal of this thesis is to prove that high-fidelity and efficient simulations with detailed radiative properties can be performed in complex configurations. To do so, four main axes have been investigated: (i) the development of accurate radiative methods that can be used in any complex configuration; (ii) the evaluation of key factors which impacts the radiative power at close industrial operating points; (iii) the capability of such models to reproduce experimental data using a high-fidelity coupled calculation framework; and (iv) the synthesis of signals due to scattering which can be compared with experimental data.

In the following paragraphs, the main achievements and limits of the different works on these four axes are analyzed, and different perspectives and improvements are discussed.

Development of accurate and efficient soot radiative models

In this thesis, the radiative power and fluxes are computed by solving the Radiative Transfer Equation (RTE) with a Monte-Carlo solver. In the original solver called Rainier, the radiative soot model was limited to the standard Rayleigh model for spherical particles without scattering.

However, it is known that soot particles have an aggregate shape, and state-of-the-art models have been developed in the literature to account for this complex shape. The Rayleigh-Debye-Gans for Fractal Aggregates has been retained in this thesis because of its accuracy and simplicity. Recent studies (as developed

in Chapter 1) have shown that the RDGFA model can accurately reproduce results obtained by more sophisticated (and expensive) methods.

The assessment of RDGFA properties on the radiative power in a turbulent sooted flame has never been studied before this thesis. To do so, in Chapter 2, the treatment of scattering in our radiative Monte-Carlo solver has been detailed since the original solver was not accounting for it. One significant achievement of this thesis has been to combine this classical treatment with the Quasi-Monte-Carlo method (QMC). The QMC method enables to improve the Monte-Carlo convergence rate significantly. In other words, the same error on the radiative power/fluxes can be achieved with a much lower number of realizations. In Chapter 2, this method was applied on a simple 3D homogeneous domain with various operating conditions. The method appears to be robust, and a significant improvement (up to a factor of 20 when a small error is desired) has been noticed for most investigated cases. The error is further reduced by combining the QMC approach with importance sampling techniques, such as the forced-scattering method detailed in Chapter 2. This method is particularly interesting in regions where scattering events rarely occur.

In Chapter 3, the scattering impact on a turbulent sooted jet-flame is investigated using the RDGFA model, the scattering treatment with the QMC approach combined to importance sampling. The RTE is solved using instantaneous fields taken from previous LES coupled calculations. The sectional method, used to describe soot dynamics, provides the soot-related quantities required for the RDGFA model: the soot volume fraction f_V , and the number density function $n(V)$. Overall, at a fixed prescribed error, a speed-up factor of 3 is obtained with respect to the standard Monte Carlo approach. The efficiency of the improved method is also quantified using a local error metric. This metric emphasizes the areas where our approach brings significant enhancements. The scattering has been accurately quantified, and eventually appears small.

Three global metrics that can be computed before any Monte-Carlo simulation have been emphasized. The objective is to be able to a priori quantify the importance of scattering in any CFD simulation. The albedo importance, the mean asymmetry factor, and the mean transmissivity expressions have been reported in Chapter 3. The first metric gives the relative importance of the scattering coefficient with respect to the total extinction coefficient, both weighted on the electromagnetic spectrum. The second metric enables to underline whether forward or backward scattering prevails on the simulation. The mean transmissivity enables the assessment of the optical thickness in the domain. These metrics have been applied in all the investigated simulations in this thesis. In Chapter 3, both albedo importance and asymmetry factor values are consistent with the low impact of scattering observed in the turbulent jet

flame. Their information is eventually combined into a single metric denoted as an effective albedo importance based on the effective transport absorption and extinction coefficients.

Recent improvements on the RDGFA models have been published in the literature, as discussed in Chapter 1, to consider complex features (overlapping, polydispersity of aggregates, necking). Implementing and testing these new formulations in Rainier can be an interesting perspective.

The scattering coefficient expression depends on fractal parameters k_f and D_f whose values are uncertain. In the thesis, these parameters are fixed. Computing the radiative power/fluxes using Uncertainty Quantification tools (UQ) would be very useful to understand the impact of these factors on the results.

As encountered in various configurations in the thesis, the impact of soot scattering on heat transfer depends on the particle morphology but is usually small. Analytical models such as RDGFA provides a detailed formula for the scattering coefficient, but the absorption coefficient expression remains identical to the Rayleigh regime formula. Hence, the thesis mainly focused on scattering effects. Detailed analysis of the soot absorption coefficient reveals a 20-30% error of the standard expression [Liu et al. \(2020\)](#). The impact on heat transfer of soot emission and absorption is undoubtedly more significant than scattering. Advanced analytical formulas for the soot absorption coefficient are then very much desired. They would surely involve the knowledge of the soot aggregate morphology, which again outlines the need for (i) characterizing it experimentally and (ii) numerical modelling of the different complex shapes.

Evaluation of key factors impacting the radiative power

Solid and robust radiative models have been developed in Chapter 2 and 3 and have then been applied to various operating points in Chapter 4. In the turbulent jet flame, the size of soot particles has been artificially increased (from a few nm to 50 nm). To do so, the sectional method, which is used to describe soot dynamics, is modified. The soot volume fraction f_V , is, however, kept constant. Hence, only the scattering coefficient is impacted by this size increase. This study shows that an accurate description of aggregates is essential to assess the impact of scattering in this case. Indeed, an ad-hoc surface-volume relationship, which enables to compute the number of primary particles n_p and diameter d_p of a soot aggregate, has been initially retained. The original formulation of the sectional method yielded inaccurate results: a new empirical law fitted from experimental data has been used while outlining the need for modelling efforts on soot morphology description. The application of the metrics derived in Chapter 3 to the increased-soot-size configuration shows a substantial increase in the albedo and the mean asymmetry factor compared to

the original case with a more significant impact of scattering on the radiative power field.

The soot optical index has also been investigated in the Sandia turbulent jet flame using a constant formulation and a complex spectral expression. Both formulations yield similar results in terms of radiative power. However, accounting for a spectral expression can be done without increasing the CPU cost of the simulation.

The impact of soot volume fraction and pressure has been investigated in another turbulent configuration: the DLR FIRST test rig. This swirled non-premixed ethylene-air flame operates at 3 bars and exhibits several features encountered in industrial combustion chambers (such as secondary air injection). Scattering remains negligible in all investigated cases since the size and number of particles in this combustion chamber are small. At 3 bars, for a maximum soot volume fraction level of 100 ppm, emission of soot and gas phases have the same order of magnitude. However, due to the reabsorption by hot gases, the net impact on the radiative power is mainly due to soot particles. With increasing pressure for fixed soot levels, gases dominate radiative exchanges. As a result, the interaction between gas and soot phases has also increased. This result is essential since simplified radiative models for soot and gas phases are encountered in the literature. However, these global models usually assume a small interaction between both phases, which is not the case in the investigated configuration at 30 bars. Experimental data in industrial operating points at high pressure with realistic soot levels are required in order to draw definitive conclusions.

Coupled simulation of a co-flow laminar diffusion flame and accuracy of radiative models

Due to the large uncertainties associated with turbulent configurations (turbulence modelling, interactions with radiation), the thesis has also focused on a simple laminar configuration widely studied in the literature. In the turbulent large-eddy simulations performed before this thesis, a tabulated chemistry approach was retained to describe the gaseous phase kinetics. Hence, to be consistent with such computations, a similar approach was considered for the laminar flame. This approach was derived and detailed in Chapter 5 for laminar flames. One of the main limitations of this method is that the differential diffusion is only partially taken into account. Indeed, the tabulated chemistry relies on 1D counterflow diffusion flames, which does not enable computing multidimensional effects in the database. Moreover, the flamelet approach, as discussed in Chapter 6, is not well suited for coflow laminar flames such as the one investigated in Chapter 6. In future work, it would be interesting to perform all the simulations and analyses carried out in Chapter 6 using a detailed

chemistry approach instead.

The calculations presented in Chapter 6 have been obtained by coupling three codes: AVBP (for the fluid part), AVTP (accounting for conjugate heat transfer at the walls), and Rainier (accounting for radiative heat transfer). Modifications on the coupling framework (multi-topology mesh connectivity, exchanges between the codes) have been done to handle such computations. It has been shown that accounting for accurate radiative properties is essential to retrieve the correct temperature profile. Besides, computations without radiation have been carried out. The obtained flame is not stable and is flickering as seen in Figure 7.31. The frequency of this fluctuation has been quantified by looking at the evolution of the heat-release rate (Figure 7.32) and is around 12 Hz , which is around the values experimentally reported in buoyancy-induced laminar flames. Therefore, one effect of radiation is to stabilize the flame in this configuration, consistently with the experimental observation.

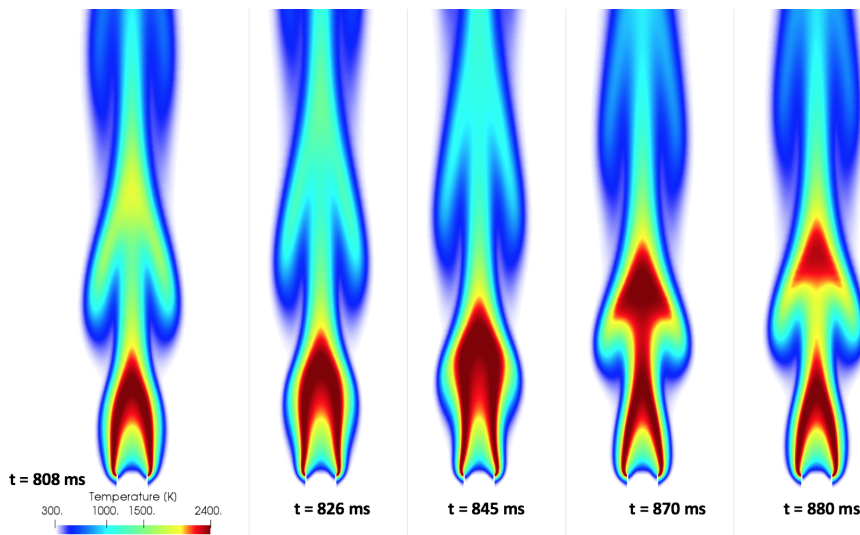


Figure 7.31: *Flickering behaviour of the laminar flame investigated in Chapter 6 without including radiation.*

Due to the limitation of the flamelet approach, the uncertainties in the chemical mechanism used to generate the flamelet database and in the soot formation model, the soot volume fraction f_V and the number of particles N_{part} are not correctly retrieving experimental measurements throughout the flame. Only the lower part gives satisfactory results.

The inclusion of conjugate heat transfer has enabled us to compute wall temperature profiles that are not given experimentally. A complete radial profile (temperature, velocity) at the pipe's exit has also been presented and can be

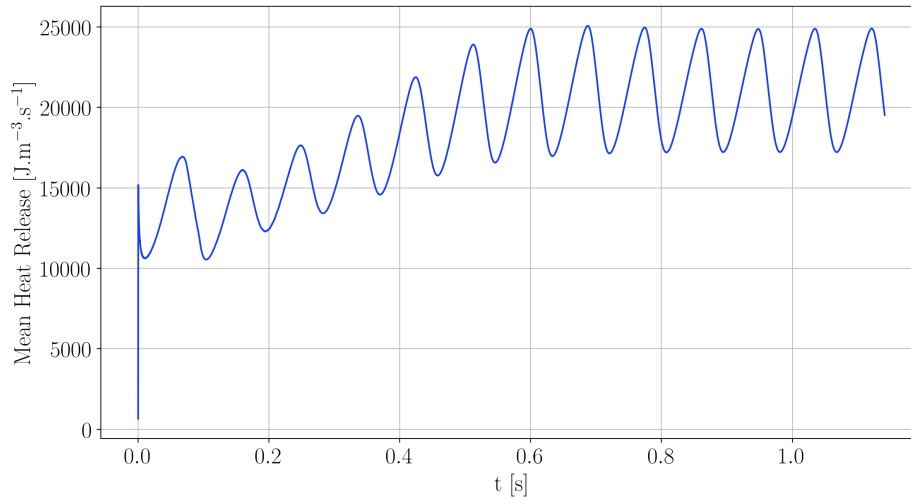


Figure 7.32: Evolution of the heat-release rate in the case of the flickering flame.

used as new input for simulations without accounting for the pipe. Indeed, it has been shown that the standard inputs considered in the literature (imposing a Poiseuille profile with a bulk temperature of 400 K) are not accurate in this simulation.

The radiative impact of soot particles has been assessed in this computation. It represents around 20% of the total radiative power and needs to be accurately taken into account. Scattering has a small impact on the radiative power and is around 4 % of the local radiative power. Again, the derived global metrics are consistent with this moderate impact.

For the first time, a comparison of the transmissivity obtained experimentally with the one computed using detailed radiative properties, has been made. The contribution of soot and gas radiative properties has been discussed: an accurate description of both phases radiative properties is required to reproduce the experimental transmissivity (peak, overall evolution).

Finally, the absorption and scattering coefficient expressions given by the RDGFA model are compared with experimental data in terms of albedo, extinction coefficient, and scattering cross-section coefficients. Here again, in the lower part of the flame, a good agreement is found, which shows the accuracy of the RDGFA approach.

Numerical synthesis of Laser scattering signals

This preliminary work has aimed at showing the capability of the Monte-Carlo solver Rainier to generate radiative intensity signals collected by a sensor. These

signals are due to a Laser which is scattered by soot particles. This configuration corresponds to an experimental setup currently carried out at the Institut Jean-Le-Rond-d'Alembert. To do so, the Monte-Carlo solver Rainier based on a Backward Monte-Carlo approach has been modified. A technique known as the peel-off method has been implemented and validated. Numerical signals have then been successfully generated for two configurations. The first is obtained in this thesis, in Chapter 6, based on the tabulated chemistry model. The second one has been provided by J.L Consalvi and uses a detailed chemistry approach. The impact of the wavelength and the sensor position has been investigated for both calculations. The results' similarities and differences between both cases have been analyzed and explained.

The experimental campaign is still in progress, and several meetings have taken place between EM2C and the Institut Jean-Le-Rond-d'Alembert. Comparison of measurements with the numerically synthesized ones is planned.

Synthesis: global metrics and simulations carried out in this thesis

The albedo importance $\bar{\omega}$, the effective albedo importance $\bar{\omega}^{eff}$ and the mean asymmetry factor \bar{G} are, by definition, not sensitive to the local number of soot particles but are determined by the particle morphology. Figure 7.33 presents the iso-contours of three metrics computed with the RDGFA model in a d_{agg} - n_p diagram: n_p is the number of primary particles of an aggregate, and d_{agg} the equivalent aggregate diameter. In the same figure are placed four simulations considered in this work: the reference Sandia jet flame case (**Ref-S**), the Sandia jet flame with the increase in particle size (**Inc-S**), the DLR FIRST test rig (**DLR**) and the laminar diffusion flame (**Santoro**).

These different points enable understanding in which case soot scattering is significant (grey to black zone) or not (light gray zone). As expected, the case **Inc-S** corresponds to the configuration with the most marked impact. Providing experimental information on d_{agg} and n_p enables us to anticipate the impact of soot scattering prior to any computation thanks to these contour plots.

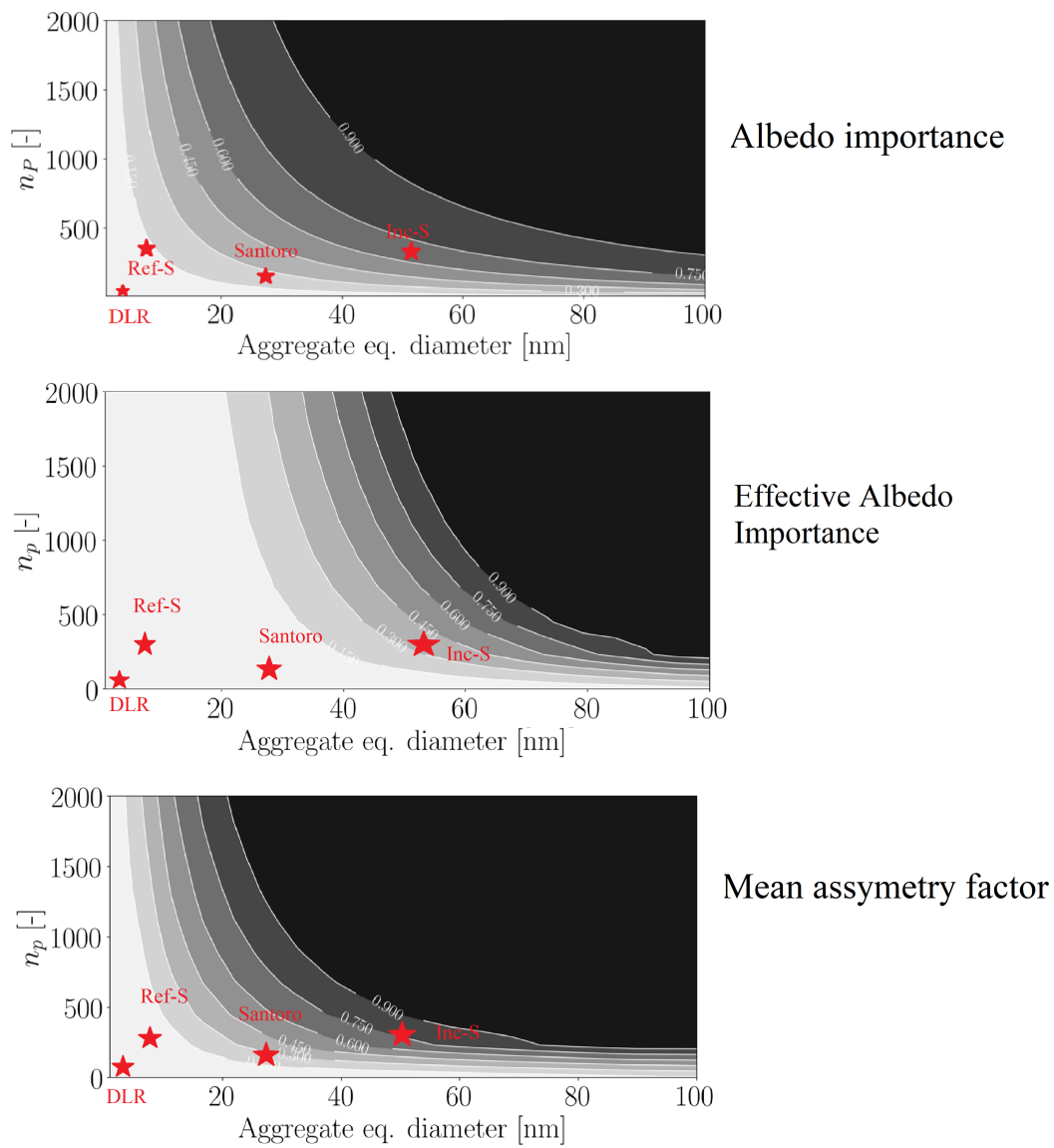


Figure 7.33: Evolution of $\bar{\omega}$ (top), $\bar{\omega}^{eff}$ (middle) and \bar{G} (bottom) for various aggregate morphology. The four studied cases in this thesis are indicated with red stars.

Appendix A

Generalization of the peel-off method for non-collimated radiation

In this section, the generalization of the peel-off technique for non-collimated radiation is proposed. The consistency with the derived model presented in Chapter 7 is also discussed.

A.1 Parametrization of the problem

Let us denote Ω_s and Ω_o the solid angle respectively of the source and the observer. As in the Chapter 7, the source is characterized by a radius R_s , and a center C_s . Let be Θ_s and Θ_o the maximum deflexion angles of the source and the observer, respectively.

Figure A.1 presents the parametrization of the problem with non-collimated radiation. Each point of the source is spanning a small solid angle Ω_s . Summing all the contributions of the points results to an equivalent source spanning a truncated cone area.

We can now consider the observer represented Figure A.2, along with the equivalent source. In Figure A.2, the source and observer planes are not parallel. Indeed, the observer is inclined with an angle α_{inc}^o with respect to the vertical axis. In order to simplify the derivation, the source is parallel to the vertical axis. However, by changing the frame of reference, cases where the source is inclined can be derived. We will therefore give the expressions for the non-inclined source and the inclined source as well. The objective is now to assess under which conditions the observer point O_1 sees the source.

In Chapter 7, two conditions have been drawn to compute the direct contribution of the source towards the observer for *collimated radiation* :

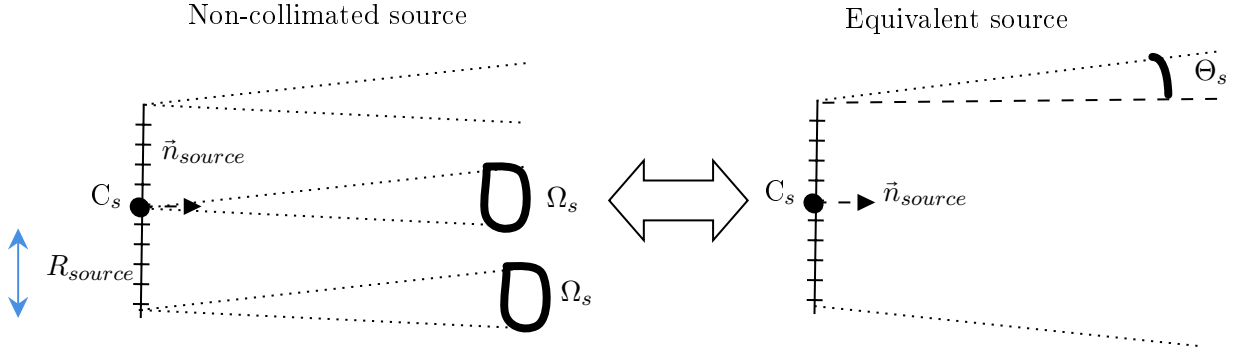


Figure A.1: Parametrization of the source for non-collimated radiation : the source is characterized by a deflexion angle Θ_s .

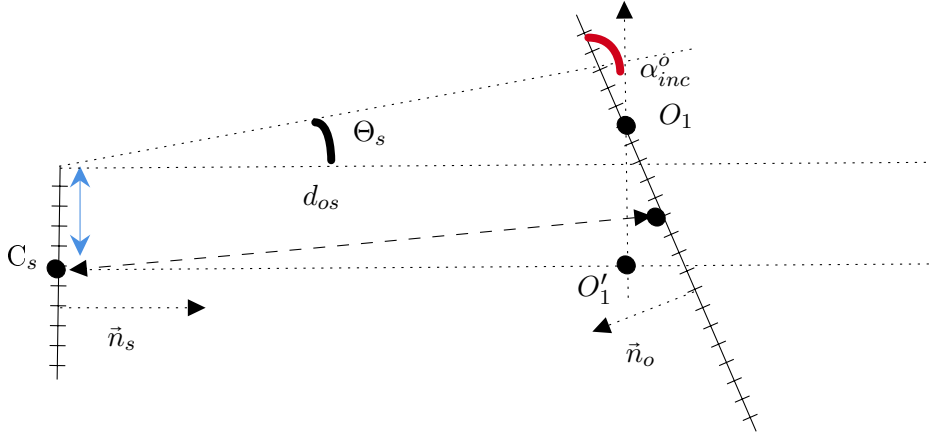


Figure A.2: Parametrization of the source-observer for non-collimated radiation. The observer is represented by the point O_1 .

- The point O_1 must rely within the cylinder spanned by the source : the distance between O_1 and the principal axis must be lower than R_{source}
- The normal of the source and the observer must be opposed.

The objectives of the next two sections is to generalize these conditions to non-collimated sources and observers.

A.2 Derivation of the first condition of detection Source-Observer generalized

Let be O'_1 the orthogonal projection of O_1 along the normal source vector \vec{n}_s . Without loss of generality, the distance $O_1O'_1$ can be written :

$$O_1O'_1 = \frac{\|\overrightarrow{C_s O_1} \wedge \vec{n}_{source}\|}{\|\vec{n}_{source}\|} \quad (\text{A.1})$$

It is clear that, the point O_1 relies in the truncated cone generated by the source if $O_1 O'_1 \leq R_{cone, O_1}$ where R_{cone, O_1} is the radius of the truncated cone at the height where O_1 is located. This distance can be split in two parts according to Figure A.2, and is equal to :

$$R_{cone, O_1} = R_{source} + \tan(\Theta_S) C O'_1 \quad (A.2)$$

Since the position of O_1 is known, it is more convenient to rewrite the previous expression using O_1 instead :

$$R_{cone, O_1} = R_{source} + \tan(\Theta_S) (-C_s O_1 \vec{n}_s \cdot \vec{n}_o) \quad (A.3)$$

We finally get, as the normal source is horizontal :

$$R_{cone, O_1} = R_{source} + \tan(\Theta_S) C_s O_1 \cos(\alpha_{inc}^o) \quad (A.4)$$

In the case where the source is inclined with an angle α_{inc}^s , the previous derivation is valid, only the final dot product between the two normal vectors is modified. We can write, then, the first general condition of source-observer detection :

Condition 1: First condition of direct computation Source-Observer

Let S be a non-collimated source, characterized by a center C_s , a radius R_{source} , a solid angle Ω_s and an inclination to the vertical α_{inc}^s and a normal \vec{n}_s

Let O_1 be a non-collimated observer, belonging to a plane with a vertical inclination α_{inc}^o .

The first condition of detection states that the point O_1 must rely within the truncated cone generated by the source \mathcal{C} :

$$O_1 \in \mathcal{C} \iff \frac{\|\vec{C}_s O_1 \wedge \vec{n}_{source}\|}{\|\vec{n}_{source}\|} \leq R_{source} + \tan(\Theta_S) C_s O_1 \cos(\alpha_{inc}^o) \cos(\alpha_{inc}^s) \quad (A.5)$$

with $\Theta_S = \cos^{-1} \left(1 - \frac{\Omega_s}{2\pi} \right)$.

Case of collimated source:

In this case, $\Omega_s = 0$ then $\Theta_S = 0$. The condition then becomes : $O_1 \in \mathcal{C}_{source} \iff O_1 O'_1 \leq R_{source}$: the distance between the observer and the axis must be lower than R_{source} which is indeed the condition used in Chapter 7.

A.3 Derivation of the second condition of detection Source-Observer generalized

So far, we have not used the fact that the observer is also characterized by the solid angle Ω_o . The initial direction of the photon emitted from the observer is constrained by the solid angle. In Figure A.3, such photon is displayed in green thick line. The photon is characterized by an angle Θ , which is smaller than the maximum polar angle Θ_{max}^o .

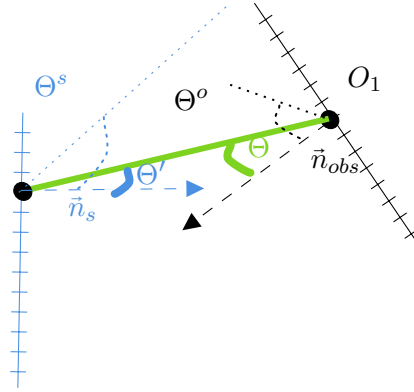


Figure A.3: Determination of the second condition for the computation of the direct contribution observer-source in a case of non-collimated radiation.

This green ray is seen by the source with an angle Θ' which also must be lower than the maximum polar angle Θ_s . Θ' is linked to the normal source and the incoming ray direction by :

$$\cos(\Theta') = -\vec{d}_{ray} \cdot \vec{n}_s \quad (\text{A.6})$$

The second condition, can therefore be written :

Condition 2: Second condition of direct computation Source-Observer

Let S be a non-collimated source, characterized by a center C_s , a radius R_{source} , a solid angle Ω_s and an inclination to the vertical α_{inc}^s and a normal \vec{n}_s

Let O_1 be a non-collimated observer, belonging to a plane with a vertical inclination α_{inc}^o .

The second condition of detection states that the ray coming from the observer must have a polar angle lower than the maximum angle due to the solid angle of the source :

$$\arccos(-\vec{d}_{ray} \cdot \vec{n}_s) \leq \Theta_s = \arccos\left(1 - \frac{\Omega_s}{2\pi}\right) \quad (A.7)$$

In the previous result, the polar angle of the observer Ω_o is actually hidden in the ray direction, since the initial polar angle of the ray is constrained by :

$$\theta = \arccos\sqrt{1 + R_\theta \left[(1 - \Omega_o / (2\pi))^2 - 1 \right]} \quad (A.8)$$

where R_θ is a random number between 0 and 1.

Case of collimated source and observer :

In this case, since $\Omega_s = 0$, $\arccos(-\vec{d}_{ray} \cdot \vec{n}_s) = 0$ since θ is greater than 0, as a polar angle. Therefore, we must have the relation :

$$-\vec{d}_{ray} = \vec{n}_s \quad (A.9)$$

It means that the direction of the ray must be opposed to the normal vector of the surface. Since the observer is collimated, $\vec{d}_{ray} = \vec{n}_o$, then $-\vec{n}_o = \vec{n}_s$ which is the second condition stated in Chapter 7.

Appendix B

Synthèse de la thèse

B.1 Introduction et problématiques :

Les particules de suies, au centre de ce travail de thèse, sont connues pour être nocives pour l'Homme et l'environnement. Dans le secteur aéronautique, les moteurs sont soumis à des campagnes de certification afin qu'ils puissent être commercialisés. Ces campagnes permettent de s'assurer que les technologies répondent aux normes mises en place, entre autres sur l'émission des particules de suies. Cependant, ces campagnes sont longues et coûteuses, contrairement aux simulations numériques. Ces simulations permettent de plus d'étudier facilement des effets de changement de technologie (injection, géométrie, ...) et leur impact sur la formation des polluants, ce qui explique leur intérêt grandissant dans l'industrie.

La prédiction des polluants par l'outil numérique est toutefois un défi de taille. En effet, les modèles physico-chimiques impliqués dans la production des suies sont encore mal connus et font défaut. Par ailleurs, dans les chambres de combustion des technologies industrielles, de multiples phénomènes pouvant impacter les suies existent, tels que la turbulence de l'écoulement ou les transferts thermiques. La thèse s'intéresse ici principalement aux transferts thermiques liés au rayonnement des suies et leur impact sur la prédiction des polluants dans des flammes laminaires et turbulentes. De nombreuses études dans la littérature emploient des modèles de rayonnement de suies. Cependant, ces modèles sont basés sur une hypothèse de particule de suie sphérique. Or, de nombreuses constatations expérimentales font état d'une structure des suies bien plus complexe se présentant sous la forme d'aggrégats. Des modèles, plus récents, considèrent cette morphologie complexe, mais n'ont jusqu'à présent pas été employés dans l'étude du rayonnement de flammes turbulentes suivies dans la littérature.

B.2 Objectifs de la thèse :

Les objectifs de la thèse sont les suivants :

- Développer des méthodes précises et efficaces permettant de prendre en compte les propriétés radiatives des suies
- Appliquer ces modèles dans deux configurations turbulentes afin de mettre en évidence les paramètres clés qui impactent le rayonnement de suies
- Evaluer la capacité des modèles à retrouver des données expérimentales détaillées dans une flamme laminaire suitée
- Reconstruire des signaux expérimentaux utiles dans le cas de diagnostics optiques

B.3 Plan du manuscrit :

- **La partie I** du manuscrit est focalisée sur les propriétés radiatives des suies. Dans le Chapitre 1, l'équation fondamentale du transfert radiatif (ETR) est présentée. Les différents mécanismes du rayonnement (émission, absorption et diffusion) sont présentés, et des stratégies numériques permettant de résoudre l'ETR sont proposées. Une revue des modèles radiatifs pour les gaz et suies est détaillée, et ceux retenus (modèle ck pour les gaz, et RDGFA pour les suies) sont justifiés. Dans le Chapitre 2, le solveur Monte-Carlo de l'ETR est présenté. A l'origine, le code ne prenait en compte que les phénomènes d'émission et d'absorption, mais pas de diffusion. Ainsi, dans ce Chapitre, l'implémentation de la diffusion dans un code Monte-Carlo est d'abord détaillée. Ensuite, une stratégie visant à accélérer les calculs Monte-Carlo, basée sur l'approche Quasi-Monte-Carlo, est introduite et appliquée à la diffusion.
- **La partie II** du manuscrit est focalisée sur l'évaluation de l'impact des modèles de rayonnement dans deux flammes turbulentes suitées. Dans le Chapitre 3, une flamme jet turbulente d'éthylène à 1 bar est étudiée. Cette flamme a été largement étudiée dans la littérature, et la diffusion du rayonnement par les suies a toujours été négligée. Dans ce chapitre, des arguments permettant d'estimer a-priori l'impact de cette diffusion du rayonnement sont avancés, et des métriques sont proposées, basées sur le modèle de rayonnement avancé RDGFA (Rayleigh Debye Gans for Fractal Aggregates) considéré. Dans le Chapitre 4, plusieurs paramètres et leur influence sur les transferts thermiques, tels que l'indice optique des suies, la fraction volumique, la pression, et la taille des particules sont considérés sur la flamme turbulente jet, ainsi que sur une flamme turbulente non-prémélangée swirlée d'éthylène-air.
- **La partie III** se focalise sur l'étude d'une flamme laminaire à co-courant d'éthylène-air. L'avantage de cette configuration est qu'elle permet d'avoir accès à de nombreuses données expérimentales permettant ainsi de valider avec plus de précision les modèles de rayonnement considérés dans la

deuxième partie. Dans le Chapitre 5, un modèle de chimie tabulé est proposée afin de prendre partiellement en compte les effets de diffusion différentielle. Ce modèle, ainsi que les modèles de rayonnement et les stratégies déployées dans la partie précédente sont appliqués sur la flamme laminaire au chapitre 6. La prise en compte de transferts de chaleur à la paroi du brûleur, responsable d'un pré-échauffement de l'éthylène avant son arrivée dans la zone de mélange est également étudiée. L'interaction entre ces différents phénomènes est prise en compte dans trois codes qui sont couplés. Les paramètres de couplage (entre autre la fréquence d'échange des informations entre ces codes) sont choisis et justifiés. Dans le chapitre 7, une ouverture sur les procédés expérimentaux est proposée, en comparant des signaux obtenus par "Laser Scattering" avec des signaux issus de la simulation réalisée au Chapitre 6.

References

- Abraham, J. and V. Magi (1997). Application of the discrete ordinates method to compute radiant heat loss in a diesel engine. *Numerical Heat Transfer; Part A: Applications* 31(6), 597–610. (p. 57, 116)
- Amin, H. M., A. Bennett, and W. L. Roberts (2019). Determining fractal properties of soot aggregates and primary particle size distribution in counterflow flames up to 10 atm. *Proceedings of the Combustion Institute*. (p. 127)
- Amin, H. M. and W. L. Roberts (2017). Soot measurements by two angle scattering and extinction in an N₂-diluted ethylene/air counterflow diffusion flame from 2 to 5 atm. *Proceedings of the Combustion Institute* 36(1), 861–869. (p. 128)
- Armengol, J. M., R. Vicquelin, A. Coussement, R. G. Santos, and O. Gicquel (2019). Scaling of heated plane jets with moderate radiative heat transfer in coupled DNS. *International Journal of Heat and Mass Transfer*. (p. 70)
- Armengol, J. M., R. Vicquelin, A. Coussement, R. G. Santos, and O. Gicquel (2020). Study of turbulence-radiation interactions in a heated jet using direct numerical simulation coupled to a non-gray Monte-Carlo solver. *International Journal of Heat and Mass Transfer*. (p. 67)
- Asano, S. and G. Yamamoto (1975). Light Scattering by a Spheroidal Particle. *Applied Optics* 14(1), 29. (p. 50)
- Attili, A., F. Bisetti, M. E. Mueller, and H. Pitsch (2014). Formation, growth, and transport of soot in a three-dimensional turbulent non-premixed jet flame. *Combustion and Flame*. (p. 161)
- Baillis, D. and J.-F. Sacadura (2000). Thermal radiation properties of dispersed media: theoretical prediction and experimental characterization. *Journal of Quantitative Spectroscopy and Radiative Transfer* 67, 327–363. (p. 31)
- Bescond, A., Jérôme Yon, T. Girasole, C. Jouen, C. Rozé, and A. Coppalle (2013). Numerical investigation of the possibility to determine the primary particle size of fractal aggregates by measuring light depolarization. *Journal of Quantitative Spectroscopy and Radiative Transfer* 126, 130–139. (p. 54)
- Bescond, A., J. Yon, F. X. Ouf, D. Ferry, D. Delhaye, D. Gaffié, A. Coppalle,

- and C. Rozé (2014). Automated determination of aggregate primary particle size distribution by tem image analysis: Application to soot. *Aerosol Science and Technology*. (p. 55)
- Best, P. E., P. L. Chien, R. M. Carangelo, P. R. Solomon, M. Danchak, and I. Ilovici (1991). Tomographic reconstruction of FT-IR emission and transmission spectra in a sooting laminar diffusion flame: Species concentrations and temperatures. *Combustion and Flame* 85(3-4), 309–318. (p. 168, 204)
- Bisetti, F., G. Blanquart, M. E. Mueller, and H. Pitsch (2012). On the formation and early evolution of soot in turbulent nonpremixed flames. *Combustion and Flame*. (p. 161)
- Blokh, A. (1988). *Heat Transfer in Steam Boiler Furnaces*. (p. 28)
- Bohren, C. F. and D. R. Huffman (1983). Absorption and scattering of light by small particles. (p. 33, 37)
- Bohren, C. F. and D. R. Huffman (1998). *Absorption and Scattering of Light by Small Particles*. (p. 39)
- Bond, T. C. and R. W. Bergstrom (2006). Light absorption by carbonaceous particles: An investigative review. *Aerosol Science and Technology* 40(1), 27–67. (p. 26)
- Bordbar, M. H., G. Wezel, and T. Hyppänen (2014). A line by line based weighted sum of gray gases model for inhomogeneous CO₂-H₂O mixture in oxy-fired combustion. *Combustion and Flame*. (p. 25)
- Borman, G. and K. Nishiwaki (1987). INTERNAL-COMBUSTION ENGINE HEAT TRANSFER. 4. (p. 57, 116)
- Brasil, A. M., T. L. Farias, and M. G. Carvalho (1999). A recipe for image characterization of fractal-like aggregates. *Journal of Aerosol Science* 30(10), 1379–1389. (p. 53)
- Buckius, R. O. and C. L. Tien (1977). Infrared flame radiation. *International Journal of Heat and Mass Transfer* 20(2), 93–106. (p. 36)
- Buras, R. and B. Mayer (2011). Efficient unbiased variance reduction techniques for Monte Carlo simulations of radiative transfer in cloudy atmospheres: The solution. *Journal of Quantitative Spectroscopy and Radiative Transfer*. (p. 69)
- Caldas, M. and V. Semião (2001). Radiative properties of small particles: extension of the Penndorf model. *Journal of the Optical Society of America A*. (p. 38)
- Carbonell, D., C. Perez-Segarra, P. Coelho, and A. Oliva (2009). Flamelet mathematical models for non-premixed laminar combustion. *Combustion and Flame* 156(2), 334 – 347. (p. 150)
- Cashwell, E. D. and C. J. Everett (1960). A Practical Manual on the Monte Carlo Method for Random Walk Problems. *Mathematics of Computation*. (p. 69, 72)
- Cassol, F., R. Brittes, F. H. FranÃ§sa, and O. A. Ezekoye (2014). Application of the weighted-sum-of-gray-gases model for media composed of arbitrary

- concentrations of h₂o, co₂ and soot. *International Journal of Heat and Mass Transfer* 79, 796 – 806. (p. 116)
- Centeno, F. R., R. Brittes, F. H. França, and C. V. Da Silva (2016). Application of the WSGG model for the calculation of gas-soot radiation in a turbulent non-premixed methane-air flame inside a cylindrical combustion chamber. *International Journal of Heat and Mass Transfer*. (p. 25)
- Centeno, F. R., R. Brittes, L. G. Rodrigues, F. R. Coelho, and F. H. França (2018). Evaluation of the WSGG model against line-by-line calculation of thermal radiation in a non-gray sooting medium representing an axisymmetric laminar jet flame. *International Journal of Heat and Mass Transfer*. (p. 25)
- Chai, J. C., H. O. S. Lee, and S. V. Patankar (1994). Finite volume method for radiation heat transfer. In *Journal of Thermophysics and Heat Transfer*. (p. 17)
- Chandrasekhar, S. (1960). *The Equation of Transfer*. (p. 16)
- Chang, H. and T. T. Charalampopoulos (1990). Determination of the Wavelength Dependence of Refractive Indices of Flame Soot. *Proceedings of the Royal Society A: Mathematical, Physical and Engineering Sciences* 430(1880), 577–591. (p. xiii, 28, 29, 88, 126, 224, 228)
- Cherkaoui, M., J. L. Dufresne, R. Fournier, J. Y. Grandpeix, and A. Lahellec (1996). Monte carlo simulation of radiation in gases with a narrow-band model and a net-exchange formulation. *Journal of Heat Transfer*. (p. 63)
- Chong, S. T., M. Hassanaly, H. Koo, M. E. Mueller, V. Raman, and K. P. Geigle (2018). Large eddy simulation of pressure and dilution-jet effects on soot formation in a model aircraft swirl combustor. *Combustion and Flame*. (p. 140)
- Chu, C.-M. and S. W. Churchill (1955). Representation of the Angular Distribution of Radiation Scattered by a Spherical Particle*. *Journal of the Optical Society of America* 45(11), 958. (p. 33)
- Coccioli, R., T. Itoh, G. Pelosi, and P. P. Silvester (1996). Finite-element methods in microwaves: A selected bibliography. *IEEE Antennas and Propagation Magazine* 38(6), 34–47. (p. 50)
- Coelho, P. J. (2008). A comparison of spatial discretization schemes for differential solution methods of the radiative transfer equation. *Journal of Quantitative Spectroscopy and Radiative Transfer*. (p. 16)
- Coelho, P. J., J. M. Gonçalves, M. G. Carvalho, and D. N. Trivic (1998). Modelling of radiative heat transfer in enclosures with obstacles. *International Journal of Heat and Mass Transfer*. (p. 17)
- Coelho, P. J., P. Perez, and M. El Hafi (2003). Benchmark simulation for radiative heat transfer in two-dimensional axisymmetric enclosures with non-gray sooting media. *Numerical Heat Transfer, part B*. (p. 19)
- Colin, O. and M. Rudgyard (2000). Development of High-Order Taylor-Galerkin Schemes for LES. *Journal of Computational Physics*. (p. 171)
- Comberg, U. and T. Wriedt (1999). Comparison of scattering calculations for

- aggregated particles based on different models. *Journal of Quantitative Spectroscopy and Radiative Transfer* 63(2-6), 149–162. (p. [xiv](#), [50](#), [51](#), [52](#))
- Cuoci, A., A. Frassoldati, T. Faravelli, and E. Ranzi (2013). Numerical modeling of laminar flames with detailed kinetics based on the operator-splitting method. *Energy and Fuels*. (p. [140](#))
- Dalzell, W. H. and a. F. Sarofim (1969). Optical Constants of Soot and Their Application to Heat-Flux Calculations. *Journal of Heat Transfer* 91(1), 100. (p. [xiii](#), [27](#), [28](#), [93](#))
- De Lataillade, A., J. L. Dufresne, M. El Hafi, V. Eymet, and R. Fournier (2002). A net-exchange Monte Carlo approach to radiation in optically thick systems. *Journal of Quantitative Spectroscopy and Radiative Transfer*. (p. [69](#))
- Deirmendjian, D., R. Clasen, and W. Viezee (1961). Mie Scattering with Complex Index of Refraction. *Journal of the Optical Society of America* 51(6), 620. (p. [33](#))
- Demarco, R., F. Nmira, and J. L. Consalvi (2013). Influence of thermal radiation on soot production in Laminar axisymmetric diffusion flames. *Journal of Quantitative Spectroscopy and Radiative Transfer* 120, 52–69. (p. [36](#), [56](#))
- Dobbins, R. A. (1989). Comparison of soot growth and oxidation in smoking and non-smoking ethylene diffusion flames. *Combustion Science and Technology*. (p. [168](#))
- Dobbins, R. A. and C. M. Megaridis (1990). Morphological Description of Flame-Generated Materials. *Combustion Science and Technology* 71(1-3), 95–109. (p. [45](#), [168](#))
- Dobbins, R. a. and C. M. Megaridis (1991). Absorption and scattering of light by polydisperse aggregates. *Applied optics* 30(33), 4747–4754. (p. [45](#), [48](#), [89](#), [90](#))
- Dombrovsky, L. A. and D. Baillis (2010). Thermal radiation in disperse systems: an engineering approach. *Begell House Redding, CT*. (p. [27](#), [38](#), [111](#))
- Domingo, P., L. Vervisch, S. Payet, and R. Hauguel (2005). Dns of a premixed turbulent v flame and les of a ducted flame using a fsd-pdf subgrid scale closure with fpi-tabulated chemistry. *Combustion and Flame* 143(4), 566 – 586. (p. [140](#))
- Doner, N. and F. Liu (2017). Impact of morphology on the radiative properties of fractal soot aggregates. *Journal of Quantitative Spectroscopy and Radiative Transfer* 187, 10–19. (p. [44](#), [53](#), [54](#))
- Donnea, J. and A. Huerta (2003). *Front Matter*. John Wiley and Sons, Ltd. (p. [173](#))
- Dorey, L. H., N. Bertier, L. Tessé, and F. Dupoirieux (2011). Soot and radiation modeling in laminar ethylene flames with tabulated detailed chemistry. *Comptes Rendus - Mecanique* 339(12), 756–769. (p. [56](#))

- Dorigon, L. J., G. Duciak, R. Brittes, F. Cassol, M. Galarça, and F. H. França (2013). WSGG correlations based on HITEMP2010 for computation of thermal radiation in non-isothermal, non-homogeneous H₂O/CO₂ mixtures. *International Journal of Heat and Mass Transfer*. (p. 25)
- Draine, B. T. (1988). The discrete-dipole approximation and its application to interstellar graphite grains. *The Astrophysical Journal* 333, 848. (p. 51)
- Duchaine, F., S. Jauré, D. Poitou, E. Quémerais, G. Staffelbach, T. Morel, and L. Gicquel (2015). Analysis of high performance conjugate heat transfer with the OpenPALM coupler. *Computational Science and Discovery*. (p. 174)
- Duchaine, F., S. Mendez, F. Nicoud, A. Corpron, V. Moureau, and T. Poinsot (2009). Conjugate heat transfer with Large Eddy Simulation for gas turbine components. (p. 176, 177)
- Dworkin, S. B., Q. Zhang, M. J. Thomson, N. A. Slavinskaya, and U. Riedel (2011). Application of an enhanced PAH growth model to soot formation in a laminar coflow ethylene/air diffusion flame. *Combustion and Flame* 158(9), 1682–1695. (p. 140, 193, 237)
- Enguehard, F. (2009). Mie Theory and the Discrete Dipole Approximation. Calculating Radiative Properties of Particulate Media, with Application to Nanostructured Materials. *Topics in Applied Physics* 118, 151–212. (p. 51)
- Escudero, F. A. (2019). *Experimental and numerical contributions to soot production in laminar axisymmetric diffusion flames*. Ph. D. thesis. These de doctorat dirigée par Consalvi, Jean-Louis Sciences pour l'ingénieur. Energetique Aix-Marseille 2019. (p. 140, 182, 193, 236, 237)
- Eymet, V., A. M. Brasil, M. El Hafi, T. L. Farias, and P. J. Coelho (2002). Numerical investigation of the effect of soot aggregation on the radiative properties in the infrared region and radiative heat transfer. *Journal of Quantitative Spectroscopy and Radiative Transfer* 74(6), 697–718. (p. xv, 93, 94)
- Farias, T. L., M. G. Carvalho, Ö. Köylü, and G. M. Faeth (1995). Computational Evaluation of Approximate Rayleigh–Debye–Gans/Fractal-Aggregate Theory for the Absorption and Scattering Properties of Soot. *Journal of Heat Transfer* 117(1), 152. (p. 48, 49)
- Farmer, J. and S. Roy (2020). A quasi monte carlo solver for thermal radiation in participating media. *Journal of Quantitative Spectroscopy and Radiative Transfer* 242. (p. 70)
- Farmer, J. T. and J. R. Howell (1998). Comparison of Monte Carlo Strategies for Radiative Transfer in Participating Media. In *Advances in Heat Transfer*. (p. 67)
- Farone, W. A. and M. J. Robinson (1968). The Range of Validity of the Anomalous Diffraction Approximation to Electromagnetic Scattering by a Sphere. *Applied Optics* 7(4), 643–645. (p. 41)

- Felden, A., E. Riber, and B. Cuenot (2018). Impact of direct integration of Analytically Reduced Chemistry in LES of a sooting swirled non-premixed combustor. *Combustion and Flame* 191, 270–286. (p. 57, 116)
- Feldick, A., A. Bansal, and M. Modest (2011). Variance Reduction Techniques For Monte Carlo Solution of Radiative Transfer in Hypersonic Flows: Hybrid P-1-Monte Carlo. (p. 69)
- Felske, J. D., T. T. Charalampopoulos, and H. S. Hura (1984a). Determination of the Refractive Indices of Soot Particles from the Reflectivities of Compressed Soot Pellets. *Combustion Science and Technology* 37(5-6), 263–283. (p. xiii, 28)
- Felske, J. D., T. T. Charalampopoulos, and H. S. Hura (1984b). Determination of the Refractive Indices of Soot Particles from the Reflectivities of Compressed Soot Pellets. *Combustion Science and Technology* 37(5-6), 263–283. (p. 39)
- Foster, P. and C. Howarth (1968). Optical constants of carbons and coals in the infrared. *Carbon* 6(5), 719–729. (p. 27)
- Franzelli, B., B. Fiorina, and N. Darabiha (2013). A tabulated chemistry method for spray combustion. *Proceedings of the Combustion Institute*. (p. 141, 171)
- Fredriksson, I., M. Larsson, and T. Strömberg (2009). Forced detection Monte Carlo algorithms for accelerated blood vessel image simulations. *Journal of Biophotonics*. (p. 69)
- Frenklach, M. and H. Wang (1991). Detailed modeling of soot particle nucleation and growth. *Symposium (International) on Combustion*. (p. 182)
- Gao, J., A. Hossain, and Y. Nakamura (2017). Flame base structures of micro-jet hydrogen/methane diffusion flames. *Proceedings of the Combustion Institute*. (p. 171)
- Geigle, K. P., M. Köhler, W. O’Loughlin, and W. Meier (2015). Investigation of soot formation in pressurized swirl flames by laser measurements of temperature, flame structures and soot concentrations. *Proceedings of the Combustion Institute* 35(3), 3373–3380. (p. xvi, 57, 116, 117, 118)
- Gigone, B., A. E. Karata, and Ö. L. Gülder (2019). Soot aggregate morphology in coflow laminar ethylene diffusion flames at elevated pressures. 37, 841–848. (p. 44, 127)
- Goody, R. and H. Yung (1995). *Atmospheric Radiation: Theoretical Basis*, Oxford University Press, (1995). (p. 24)
- Gülder, Ö. L., D. R. Snelling, and R. A. Sawchuk (1996). Influence of hydrogen addition to fuel on temperature field and soot formation in diffusion flames. *Symposium (International) on Combustion*. (p. 170)
- Guo, H., F. Liu, G. J. Smallwood, and Ö. L. Gülder (2002). The flame preheating effect on numerical modelling of soot formation in a two-dimensional laminar ethylene-air diffusion flame. *Combustion Theory and Modelling* 6(2), 173–187. (p. 170)
- He, Z., C. Dong, D. Liang, and J. Mao (2021). A weighted-sum-of-gray soot-

- fractal-aggregates model for nongray heat radiation in the high temperature gas-soot mixture. *Journal of Quantitative Spectroscopy and Radiative Transfer* 260, 107431. (p. 116)
- Hernandez-Perez, F., F. Yuen, C. Groth, and Ö. Gülder (2011). Les of a laboratory-scale turbulent premixed bunsen flame using fsd, pcm-fpi and thickened flame models. *Proceedings of the Combustion Institute* 33(1), 1365 – 1371. (p. 140)
- Hirschfelder, J. O. and C. F. Curtiss (1949). Theory of propagation of flames. Part I: General equations. In *Symposium on Combustion and Flame and Explosion Phenomena*. (p. 146)
- Hottel, H. and A. Sarofim (1967). *Radiative Transfer* (McGraw-Hil ed.). New York. (p. 24)
- Hovenier, J. W., K. Lumme, M. I. Mishchenko, N. V. Voshchinnikov, D. W. Mackowski, and J. Rahola (1996). Computations of scattering matrices of four types of non-spherical particles using diverse methods. *Journal of Quantitative Spectroscopy and Radiative Transfer* 55(6), 695–705. (p. 51)
- Howarth, C., P. Foster, and M. Thring (1966). The effect of temperature on the extinction of radiation by soot particles. *Proceedings of the Third International Heat Transfer Conference* 5, 122–128. (p. xiii, 28)
- Iacona, E., O. Penanhoat, P. Picot, O. Guignard, and J. Taine (2019). Radiation transfer modeling by a ray-tracing method and a CK or k approach. (p. 19)
- Ihme, M. and H. Pitsch (2008). Modeling of radiation and nitric oxide formation in turbulent nonpremixed flames using a flamelet/progress variable formulation. *Physics of Fluids*. (p. 140, 142)
- Intasopa, G. (2011). Soot measurements in high-pressure diffusion flames of gaseous and liquid fuels. (p. xviii, 170)
- ISF3 (2017). ISF3,international sooting flame (ISF) workshop website. (p. 96)
- Iskander, M. F., H. Y. Chen, and J. E. Penner (1989). Optical scattering and absorption by branched chains of aerosols. *Appl Opt* 28(15), 3083–3091. (p. 48)
- Iyer, S. S., T. A. Litzinger, S. Y. Lee, and R. J. Santoro (2007). Determination of soot scattering coefficient from extinction and three-angle scattering in a laminar diffusion flame. *Combustion and Flame* 149(1-2), 206–216. (p. xx, 168, 208, 209)
- Jacquier, S. and F. Gruy (2007). Approximation of the light scattering cross-section for aggregated spherical non-absorbent particles. *Journal of Quantitative Spectroscopy and Radiative Transfer* 106(1-3), 133–144. (p. 50)
- Jacquier, S. and F. Gruy (2010). Application of scattering theories to the characterization of precipitation processes. *Light Scattering Reviews* 5, 42. (p. 51)
- Jaure, S., F. Duchaine, G. Staffelbach, and L. Y. Gicquel (2013). Massively parallel conjugate heat transfer methods relying on large eddy simula-

- tion applied to an aeronautical combustor. *Computational Science and Discovery*. (p. 173)
- Jeans, J. H. (1917). The Equations of Radiative Transfer of Energy. *Monthly Notices of the Royal Astronomical Society*. (p. 15)
- Johnsson, J., H. Bladh, N. E. Olofsson, and P. E. Bengtsson (2013). Influence of soot aggregate structure on particle sizing using laser-induced incandescence: Importance of bridging between primary particles. *Applied Physics B: Lasers and Optics* 112(3), 321–332. (p. 53)
- Joo, H. I. and Ö. L. Gülder (2011). Experimental study of soot and temperature field structure of laminar co-flow ethylene-air diffusion flames with nitrogen dilution at elevated pressures. *Combustion and Flame* 158(3), 416–422. (p. 127)
- Joo, P. H., B. Gigone, E. A. Griffin, M. Christensen, and Ö. L. Gülder (2018). Soot primary particle size dependence on combustion pressure in laminar ethylene diffusion flames. *Fuel*. (p. 44)
- Joseph, D., P. Perez, M. El Hafi, and B. Cuenot (2009). Discrete ordinates and Monte Carlo methods for radiative transfer simulation applied to computational fluid dynamics combustion Modeling. *Journal of Heat Transfer* 131(5), 1–9. (p. 16)
- Juvela, M. (2005). Efficient Monte Carlo methods for continuum radiative transfer. *Astronomy and Astrophysics*. (p. 69)
- Kahnert, F. M. (2003). Numerical methods in electromagnetic scattering theory. *Journal of Quantitative Spectroscopy and Radiative Transfer* 79–80, 775–824. (p. 49)
- Kattawar, G. W. and G. N. Plass (1967). Resonance scattering from absorbing spheres. *Applied optics* 6(9), 1549–1554. (p. 33)
- Kennedy, I., C. Yam, D. Rapp, and R. Santoro (1996). Modelling and Measurements of Soot and Species in a Laminar Diffusion Flame. (p. 56)
- Kerker, M., W. A. Farone, and E. Matijevic (1963). Applicability of Rayleigh-Gans Scattering to Spherical Particles. *Journal of the Optical Society of America* 53(6), 758–&. (p. xiii, 40, 42)
- Konsur, B., C. M. Megaridis, and D. W. Griffin (1999). Fuel preheat effects on soot-field structure in laminar gas jet diffusion flames burning in 0-g and 1-g. *Combustion and Flame*. (p. 170)
- Koren, C., R. Vicquelin, and O. Gicquel (2018). Multiphysics Simulation Combining Large-Eddy Simulation, Wall Heat Conduction and Radiative Energy Transfer to Predict Wall Temperature Induced by a Confined Premixed Swirling Flame. *Flow, Turbulence and Combustion* 101(1), 77–102. (p. 175)
- Köylü, Ü. Ö. and G. M. Faeth (1992). Structure of overfire soot in buoyant turbulent diffusion flames at long residence times. *Combustion and Flame* 89(2), 140–156. (p. 44)
- Köylü, Ü. Ö. and G. M. Faeth (1993). Radiative Properties of Flame-Generated Soot. *International Geophysics* 115, 409–417. (p. 26, 41, 48,

- 127)
- Köylü, U. O. and G. M. Faeth (1994). Optical properties of soot in buoyant laminar diffusion flames. *Journal of Heat Transfer* 116(4), 971–979. (p. 48, 89)
- Köylü, Ü. Ö., G. M. Faeth, T. L. Farias, and M. G. Carvalho (1995). Fractal and projected structure properties of soot aggregates. *Combustion and Flame*. (p. 127)
- Köylü, Ü. Ö., C. S. Mcenally, D. E. Rosner, and L. D. Pfefferle (1997). Simultaneous measurements of soot volume fraction and particle size / microstructure in flames using a thermophoretic sampling technique. *Combustion and Flame*. (p. xix, 186)
- Lack, D. A., R. Bahreini, J. M. Langridge, J. B. Gilman, and A. M. Middlebrook (2013). Brown carbon absorption linked to organic mass tracers in biomass burning particles. *Atmospheric Chemistry and Physics* 13(5), 2415–2422. (p. 55)
- L’Ecuyer, P. and C. Lemieux (2016). Recent advances in randomized quasi-monte carlo methods. In *International Series in Operations Research and Management Science*. (p. 74)
- Lee, S. C. and C. L. Tien (1981). Optical constants of soot in hydrocarbon flames. *Symposium (International) on Combustion* 18(1), 1159–1166. (p. xviii, 28, 35)
- Lee, G. K. H., Wood, K., Dobbs-Dixon, I., Rice, A., and Helling, Ch. (2017). Dynamic mineral clouds on hd 189733b - ii. monte carlo radiative transfer for 3d cloudy exoplanet atmospheres: combining scattering and emission spectra. *A&A* 601, A22. (p. 216)
- Lefebvre, A. H. (1984). Flame radiation in gas turbine combustion chambers. *International Journal of Heat and Mass Transfer* 27(9), 1493–1510. (p. 5)
- Lemieux, C. (2009). *Monte Carlo and Quasi-Monte Carlo Sampling*. (p. 75, 174)
- Lin Xu, Y. and B. Å. S. Gustafson (2001). A generalized multiparticle Mie-solution: Further experimental verification. *Journal of Quantitative Spectroscopy and Radiative Transfer* 70(4-6), 395–419. (p. 50)
- Liu, C., Y. Yin, F. Hu, H. Jin, and C. M. Sorensen (2015). The Effects of Monomer Size Distribution on the Radiative Properties of Black Carbon Aggregates. *Aerosol Science and Technology*. (p. 55)
- Liu, F., J. L. Consalvi, P. J. Coelho, F. Andre, M. Gu, V. Solovjov, and B. W. Webb (2020). The impact of radiative heat transfer in combustion processes and its modeling “ with a focus on turbulent flames. *Fuel* 281(May), 118555. (p. 247)
- Liu, F., H. Guo, and G. J. Smallwood (2004). Effects of radiation model on the modeling of a laminar coflow methane/air diffusion flame. *Combustion and Flame* 138(1-2), 136–154. (p. 35, 56, 169)
- Liu, F., H. Guo, G. J. Smallwood, and O. L. Gulder (2002). Effects of gas and

- soot radiation on soot formation in a coflow laminar ethylene diffusion flame. (p. 56, 201)
- Liu, F., H. Guo, G. J. Smallwood, and Ö. L. Gülder (2003). Numerical modelling of soot formation and oxidation in laminar coflow non-smoking and smoking ethylene diffusion flames. *Combustion Theory and Modelling* 7(2), 301–315. (p. 36)
- Liu, F., K. A. Thomson, and G. J. Smallwood (2006). Effects of soot absorption and scattering on LII intensities in a laminar coflow ethylene/air diffusion flame. *CEUR Workshop Proceedings 211*, 27. (p. 43, 45, 55, 145, 150, 187, 194)
- Liu, F., C. Wong, D. R. Snelling, and G. J. Smallwood (2013). Investigation of absorption and scattering properties of soot aggregates of different fractal dimension at 532 nm Using RDG and GMM. *Aerosol Science and Technology* 47(12), 1393–1405. (p. 48, 91, 127)
- Liu, F., J. Yon, and A. Bescond (2016). On the radiative properties of soot aggregates - Part 2: Effects of coating. *Journal of Quantitative Spectroscopy and Radiative Transfer* 172, 134–145. (p. xiv, 26, 44, 45, 53, 55)
- Liu, J., H. M. Shang, Y. S. Chen, and T. S. Wang (1997). Analysis of discrete ordinates method with even parity formulation. *Journal of Thermophysics and Heat Transfer*. (p. 17)
- Lu, J., C. Lou, and H.-C. Zhou (2009, feb). Experimental investigation on soot volume fraction in an ethylene diffusion flame by emission spectrometry without optically-thin assumption. *Journal of Physics: Conference Series* 147, 012084. (p. 168)
- Malkmus, W. (1967). Random Lorentz Band Model with Exponential-Tailed S^{-1} Line-Intensity Distribution Function*. *Journal of the Optical Society of America*. (p. 21)
- Mandal, B. K., A. Sarkar, and A. Datta (2006). Numerical prediction of the soot and NO formation in a confined laminar diffusion flame without and with air preheat. *Proceedings of the Institution of Mechanical Engineers, Part A: Journal of Power and Energy*. (p. 170)
- Mattila, K. (1970). Interpretation of the surface darkness of a nebulae. *AAP* 9. (p. 26)
- Mätzler, C. (2002). MATLAB Functions for Mie Scattering and Absorption. *IAP Res Rep 2002-08* (July 2002), 1139–1151. (p. 33)
- McEnally, C. S., Ü. Ö. Köylü, L. D. Pfefferle, and D. E. Rosner (1997). Soot volume fraction and temperature measurements in laminar nonpremixed flames using thermocouples. *Combustion and Flame*. (p. xix, 186)
- McEnally, C. S., A. M. Schaffer, M. B. Long, L. D. Pfefferle, M. D. Smooke, M. B. Colket, and R. J. Hall (1998). Computational and experimental study of soot formation in a coflow, laminar ethylene diffusion flame. In *Symposium (International) on Combustion*. (p. 56)
- Megaridis, C. M. and R. A. Dobbins (1988). Soot Aerosol Dynamics in a

- Laminar Ethylene Diffusion Flame. *Symposium (International) on Combustion*, 353–362. (p. 43, 168)
- Megaridis, C. M. and R. A. Dobbins (1989). An Integral Solution of the Aerosol Dynamic Equation Including Surface Growth Reactions. *Combustion Science and Technology* 63(1-3), 153–167. (p. 26)
- Mehta, R. S., D. C. Haworth, and M. F. Modest (2010). Composition PDF/photon Monte Carlo modeling of moderately sooting turbulent jet flames. *Combustion and Flame* 157(5), 982–994. (p. 56)
- Mengüç, M. P. and R. Viskanta (1985). Radiative transfer in three-dimensional rectangular enclosures containing inhomogeneous, anisotropically scattering media. *Journal of Quantitative Spectroscopy and Radiative Transfer*. (p. 15)
- Min, M., C. P. Dullemond, C. Dominik, A. De Koter, and J. W. Hovenier (2009). Radiative transfer in very optically thick circumstellar disks. *Astronomy and Astrophysics*. (p. 69)
- Mishchenko, M. I., L. D. Travis, and D. W. Mackowski (2010a). T-matrix method and its applications to electromagnetic scattering by particles: A current perspective. *Journal of Quantitative Spectroscopy and Radiative Transfer* 111(11), 1700–1703. (p. 49)
- Mishchenko, M. I., L. D. Travis, and D. W. Mackowski (2010b). T-matrix method and its applications to electromagnetic scattering by particles: A current perspective. *Journal of Quantitative Spectroscopy and Radiative Transfer* 111(11), 1700–1703. (p. 50)
- Mobley, C. D. (1994). Light and Water : Radiative Transfer in Natural Waters. *Light and Water : Radiative Transfer in Natural Waters*. (p. 39)
- Modest, M. F. (1991). The weighted-sum-of-gray-gases model for arbitrary solution methods in radiative transfer. *Journal of Heat Transfer*. (p. 24, 25)
- Modest, M. F. (2003a). Narrow-band and full-spectrum k-distributions for radiative heat transfer-correlated-k vs. scaling approximation. *Journal of Quantitative Spectroscopy and Radiative Transfer*. (p. 26)
- Modest, M. F. (2003b). *Radiative heat transfer*. (p. xiii, 14, 16, 18, 21, 26, 28, 30, 31)
- Modest, M. F. (2003c). Radiative properties of metals. *Smithells Metals Reference Book* 115(May), 1–12. (p. 127)
- Modest, M. F. and H. Zhang (2002). The full-spectrum correlated-k distribution for thermal radiation from molecular gas-particulate mixtures. *Journal of Heat Transfer*. (p. 25)
- Mouton, T. (2014). *Analyse des processus de nucléation et de croissance des particules de suie dans des flammes par fluorescence induite par laser en jet froid appliquée aux hydrocarbures aromatiques polycycliques et par incandescence induite par laser*. Ph. D. thesis, Université Lille 1 Sciences et Technologies. (p. xiii, 35)
- Mueller, M. E., G. Blanquart, and H. Pitsch (2009). Hybrid Method of Mo-

- ments for modeling soot formation and growth. *Combustion and Flame*. (p. *xvii*, 89, 127, 128)
- Mueller, M. E. and H. Pitsch (2012). Large eddy simulation of soot evolution in an aircraft combustor. In *Western States Section of the Combustion Institute Spring Technical Meeting 2012*. (p. 140, 161)
- Mullins, J. and A. Williams (1987). The optical properties of soot: a comparison between experimental and theoretical values. *Fuel* 66(2), 277–280. (p. 26)
- Murphy, J. J. and C. R. Shaddix (2005). Influence of scattering and probe-volume heterogeneity on soot measurements using optical pyrometry. *Combustion and Flame* 143(1-2), 1–10. (p. 45)
- Nelson, J. (1989). Test of a mean field theory for the optics of fractal clusters. *Journal of Modern Optics*. (p. 48, 52)
- Nguyen, P.-D., L. Vervisch, V. Subramanian, and P. Domingo (2010). Multi-dimensional flamelet-generated manifolds for partially premixed combustion. *Combustion and Flame* 157(1), 43 – 61. (p. 150)
- OACI (2020). *Local Air Quality Technology Standards*. (p. 3)
- Oijen, J. V. and L. D. Goey (2000). Modelling of premixed laminar flames using flamelet-generated manifolds. *Combustion Science and Technology* 161(1), 113–137. (p. 140)
- Okyay, G. (2016). *Impact of the morphology of soot aggregates on their radiative properties and the subsequent radiative heat transfer through sooty gaseous mixtures*,. Ph. D. thesis, Université Paris-Saclay. (p. *xiv*, 43, 44, 45, 49, 50, 51)
- Ou, S. C. S. and K. N. Liou (1982). Generalization of the spherical harmonic method to radiative transfer in multi-dimensional space. *Journal of Quantitative Spectroscopy and Radiative Transfer*. (p. 15)
- Pagni, P. J. and S. Bard (1979). Particulate volume fractions in diffusion flames. *Symposium (International) on Combustion* 17(1), 1017–1028. (p. 27)
- Pal, G., A. Gupta, M. F. Modest, and D. C. Haworth (2015). Comparison of accuracy and computational expense of radiation models in simulation of non-premixed turbulent jet flames. *Combustion and Flame*. (p. 56)
- Palluotto, L. (2019). Quasi-Monte Carlo computation of radiative heat transfer in coupled Large Eddy Simulation of a swirled premixed flame To cite this version : Prédiction du transfert radiatif au sein d ’ une flamme prémélangée swirlée à l ’ aide d ’ une méthode Quasi-Monte. (p. 5)
- Palluotto, L., N. Dumont, P. Rodrigues, O. Gicquel, and R. Vicquelin (2019). Assessment of randomized Quasi-Monte Carlo method efficiency in radiative heat transfer simulations. *Journal of Quantitative Spectroscopy and Radiative Transfer* 236, 106570. (p. 67)
- Palluotto, L., N. Dumont, P. Rodrigues, O. Gicquel, R. Vicquelin, Q.-m. Carlo, M. Carlo, and Q.-m. Carlo (2019). Journal of Quantitative Spectroscopy & Radiative Transfer Assessment of randomized Quasi-Monte

- Carlo method efficiency in radiative heat transfer simulations. *Journal of Quantitative Spectroscopy and Radiative Transfer* 236, 106570. (p. 70, 73, 74, 75, 100)
- Paul, C., S. Ferreyro, D. C. Haworth, S. Roy, and M. F. Modest (2019). A detailed modeling study of radiative heat transfer in a heavy-duty diesel engine. *Combustion and Flame* 200, 325–341. (p. 57, 116)
- Paul, C., A. Sircar, A. Imren, D. C. Haworth, and S. Roy (2017). Modeling Radiative Heat Transfer and Turbulence-Radiation Interactions in Engines. pp. 1–6. (p. 57, 116)
- Peest, C., C. Schinke, R. Brendel, J. Schmidt, and K. Bothe (2017). Instrumentation-related uncertainty of reflectance and transmittance measurements with a two-channel spectrophotometer. *Review of Scientific Instruments*. (p. 69)
- Penndorf, R. B. (1962). Scattering and Extinction Coefficients for Small Absorbing and Nonabsorbing Aerosols*. *Journal of the Optical Society of America*. (p. 38)
- Pierce, C. D. (2001). *Progress-variable approach for large-eddy simulation of turbulent combustion*. Ph. D. thesis. (p. 140, 142)
- Pierce, C. D. and P. Moin (2004). Progress-variable approach for large-eddy simulation of non-premixed turbulent combustion. *Journal of Fluid Mechanics*. (p. xvii, 141)
- Pitsch, H., M. Chen, and N. Peters (1998). Unsteady flamelet modeling of turbulent hydrogen-air diffusion flames. *Symposium (International) on Combustion* 27(1), 1057 – 1064. Twenty-Seventh Symposium (International) on Combustion Volume One. (p. 150)
- Pitsch, H. and N. Peters (1998). A consistent flamelet formulation for non-premixed combustion considering differential diffusion effects. *Combustion and Flame*. (p. 150, 151, 152)
- Poinsot, T. (1992). Boundary conditions for direct simulations of compressible viscous flows. *Journal of Computational Physics*. (p. 145, 172)
- Purcell, E. M. and C. R. Pennypacker (1973). Scattering and Absorption of Light by Nonspherical Dielectric Grains. *The Astrophysical Journal* 186, 705. (p. 51)
- Puri, R., T. F. Richardson, R. J. Santoro, and R. A. Dobbins (1993). Aerosol dynamic processes of soot aggregates in a laminar ethene diffusion flame. *Combustion and Flame* 92(3), 320–333. (p. 45, 168, 207)
- Qi, S., Z. Sun, Z. Wang, Y. Liu, Y. He, S. Liu, K. Wan, G. Nathan, and M. Costa (2020). Effects of gas preheat temperature on soot formation in co-flow methane and ethylene diffusion flames. *Proceedings of the Combustion Institute* 000, 1–8. (p. 170)
- Ren, T. and M. F. Modest (2019). Line-by-line random-number database for Monte Carlo simulations of radiation in combustion system. *Journal of Heat Transfer*. (p. 20)
- Rivière, P. and A. Soufiani (2012). Updated band model parameters for H

- 2O, CO 2, CH 4 and CO radiation at high temperature. *International Journal of Heat and Mass Transfer* 55(13-14), 3349–3358. (p. 24, 88)
- Rodrigues, P. (2018). *Modélisation multiphysique de flammes turbulentes suitées avec la prise en compte des transferts radiatifs et des transferts de chaleur pariétaux*. Ph. D. thesis, Université Paris Saclay. (p. xviii, xvi, xvii, 22, 57, 89, 116, 117, 121, 128, 143)
- Rodrigues, P., B. Franzelli, R. Vicquelin, O. Gicquel, and N. Darabiha (2017). Unsteady dynamics of PAH and soot particles in laminar counterflow diffusion flames. *Proceedings of the Combustion Institute* 36(1), 927 – 934. (p. 57, 59, 141)
- Rodrigues, P., B. Franzelli, R. Vicquelin, O. Gicquel, and N. Darabiha (2018). Coupling an LES approach and a soot sectional model for the study of sooting turbulent non-premixed flames. *Combustion and Flame* 190, 477–499. (p. 96, 132, 161, 164, 178, 187)
- Rodrigues, P., O. Gicquel, N. Darabiha, K. P. Geigle, and R. Vicquelin (2019). Assessment of External Heat Transfer Modeling of a Laboratory-Scale Combustor: Effects of Pressure-Housing Environment and Semi-Transparent Viewing Windows. *Journal of Engineering for Gas Turbines and Power* 141(3). (p. 117)
- Rodrigues, P., O. Gicquel, B. Franzelli, N. Darabiha, and R. Vicquelin (2019). Analysis of radiative transfer in a turbulent sooting jet flame using a Monte Carlo method coupled to large eddy simulation. *Journal of Quantitative Spectroscopy and Radiative Transfer* 235, 187–203. (p. 56, 67, 70, 96, 97, 101, 129, 140, 161, 178)
- Rothman, L. S., I. E. Gordon, A. Barbe, D. C. Benner, P. F. Bernath, M. Birk, V. Boudon, L. R. Brown, A. Campargue, J. P. Champion, K. Chance, L. H. Coudert, V. Dana, V. M. Devi, S. Fally, J. M. Flaud, R. R. Gamache, A. Goldman, D. Jacquemart, I. Kleiner, N. Lacome, W. J. Lafferty, J. Y. Mandin, S. T. Massie, S. N. Mikhailenko, C. E. Miller, N. Moazzen-Ahmadi, O. V. Naumenko, A. V. Nikitin, J. Orphal, V. I. Perevalov, A. Perrin, A. Predoi-Cross, C. P. Rinsland, M. Rotger, M. Šimečková, M. A. Smith, K. Sung, S. A. Tashkun, J. Tennyson, R. A. Toth, A. C. Vandaele, and J. Vander Auwera (2009). The HITRAN 2008 molecular spectroscopic database. *Journal of Quantitative Spectroscopy and Radiative Transfer*. (p. 19, 20)
- Rothman, L. S., I. E. Gordon, R. J. Barber, H. Dothe, R. R. Gamache, A. Goldman, V. I. Perevalov, S. A. Tashkun, and J. Tennyson (2010). HITEMP, the high-temperature molecular spectroscopic database. *Journal of Quantitative Spectroscopy and Radiative Transfer*. (p. 20, 24)
- Saji, C. B., C. Balaji, and T. Sundararajan (2008). Investigation of soot transport and radiative heat transfer in an ethylene jet diffusion flame. *International Journal of Heat and Mass Transfer* 51(17-18), 4287–4299. (p. 36)
- Salenbauch, S., A. Cuoci, A. Frassoldati, C. Saggese, T. Faravelli, and

- C. Hasse (2015). Modeling soot formation in premixed flames using an Extended Conditional Quadrature Method of Moments. *Combustion and Flame*. (p. [xvii](#), [89](#), [127](#), [128](#))
- Samson, R. J., G. W. Mulholland, and J. W. Gentry (1987). Structural Analysis of Soot Agglomerates. *Langmuir* 3(2), 272–281. (p. [45](#), [127](#))
- Santoro, R. J., H. G. Semerjian, and R. A. Dobbins (1983). Soot particle measurements in diffusion flames. *Combustion and Flame* 51, 203–218. (p. [xix](#), [36](#), [186](#), [187](#), [188](#), [189](#), [190](#), [191](#), [192](#), [193](#))
- Santoro, R. J., T. T. Yeh, J. J. Horvath, and H. G. Semerjian (1987). The Transport and Growth of Soot Particles in Laminar Diffusion Flames. *Combustion Science and Technology* 53(2-3), 89–115. (p. [xviii](#), [167](#), [168](#), [169](#), [187](#))
- Schlup, J. and G. Blanquart (2019). Reproducing curvature effects due to differential diffusion in tabulated chemistry for premixed flames. *Proceedings of the Combustion Institute* 37(2), 2511 – 2518. (p. [150](#))
- Schnaiter, M., M. Gimmler, I. Llamas, C. Linke, C. Jäger, and H. Mutschke (2006). Strong spectral dependence of light absorption by organic carbon particles formed by propane combustion. *Atmospheric Chemistry and Physics* 6(10), 2981–2990. (p. [26](#))
- Schönfeld, T. and M. Rudgyard (1999). Steady and unsteady flow simulations using the hybrid flow solver AVBP. *AIAA journal* 37(11), 1378–1385. (p. [171](#))
- Selçuk, N. and N. Kayakol (1997). Evaluation of discrete ordinates method for radiative transfer in rectangular furnaces. *International Journal of Heat and Mass Transfer*. (p. [17](#))
- Siegel, R. (1987). Transient radiative cooling of a droplet-filled layer. *Journal of Heat Transfer*. (p. [xiv](#), [75](#), [76](#), [77](#))
- Smooke, M. D., R. J. Hall, M. B. Colket, J. Fielding, M. B. Long, C. S. McEnally, and L. D. Pfefferle (2004). Investigation of the transition from lightly sooting towards heavily sooting co-flow ethylene diffusion flames. *Combustion Theory and Modelling* 8(3), 593–606. (p. [56](#))
- Smyth, K. C. and C. R. Shaddix (1996). The elusive history of $m = 1.57 - 0.56i$ for the refractive index of soot. *Combustion and Flame* 107(3), 314–320. (p. [29](#), [36](#), [88](#), [126](#))
- Snelling, D. R., K. A. Thomson, G. J. Smallwood, and Ö. L. Gülder (1999). Two-dimensional imaging of soot volume fraction in laminar diffusion flames. *Applied Optics* 38(12), 2478. (p. [35](#))
- Sobol, I. M. (1976). Uniformly distributed sequences with an additional uniform property. *USSR Computational Mathematics and Mathematical Physics*. (p. [73](#))
- Sorensen, C. M. (2001). *Light scattering by fractal aggregates: A review*, Volume 35. (p. [48](#))
- Sorensen, C. M., J. Yon, F. Liu, J. Maughan, W. R. Heinson, and M. J. Berg (2018). Light scattering and absorption by fractal aggregates including

- soot. *Journal of Quantitative Spectroscopy and Radiative Transfer* 217, 459–473. (p. 46)
- Steinacker, J., M. Baes, and K. D. Gordon (2013). Three-dimensional dust radiative transfer. *Annual Review of Astronomy and Astrophysics* 51(1), 63–104. (p. 216)
- Steinmetz, S. A., T. Fang, and W. L. Roberts (2016). Soot particle size measurements in ethylene diffusion flames at elevated pressures. *Combustion and Flame* 169, 85–93. (p. 127, 128)
- Stull, V. R. and G. N. Plass (1960). Emissivity of Dispersed Carbon Particles*. *Journal of the Optical Society of America* 50(2), 121. (p. xiii, 28)
- Taine, J., F. Enguehard, and E. Iacona (2012). *Transferts thermiques, Introduction aux transferts d'énergie*. (p. 111)
- Tardelli, L., B. Franzelli, P. Rodrigues, and N. Darabiha (2019, 06). Impact of the Reaction Mechanism Model on Soot Growth and Oxidation in Laminar and Turbulent Flames. *Volume 4A: Combustion, Fuels, and Emissions*. V04AT04A055. (p. 140, 193)
- Tashkun, S. A. and V. I. Perevalov (2011). CDSD-4000: High-resolution, high-temperature carbon dioxide spectroscopic databank. *Journal of Quantitative Spectroscopy and Radiative Transfer*. (p. 24)
- Teng, S., V. Raman, M. E. Mueller, P. Selvaraj, and H. G. Im (2019). Effect of soot model, moment method, and chemical kinetics on soot formation in a model aircraft combustor. *Proceedings of the Combustion Institute* 37(1), 1065–1074. (p. 57, 116)
- Tessé, L. (2001). *Modélisation des transferts radiatifs dans les flammes turbulentes par une méthode de Monte Carlo*. Ph. D. thesis. (p. 70)
- Tessé, L., F. Dupoirieux, and J. Taine (2004). Monte Carlo modeling of radiative transfer in a turbulent sooty flame. *International Journal of Heat and Mass Transfer* 47(3), 555–572. (p. 174)
- Tessé, L., F. Dupoirieux, B. Zamuner, and J. Taine (2002). Radiative transfer in real gases using reciprocal and forward Monte Carlo methods and a correlated-k approach. *International Journal of Heat and Mass Transfer* 45(13), 2797–2814. (p. 56, 65)
- Tian, K., F. Liu, K. A. Thomson, D. R. Snelling, G. J. Smallwood, and D. Wang (2004). Distribution of the number of primary particles of soot aggregates in a nonpremixed laminar flame. *Combustion and Flame* 138(1-2), 195–198. (p. 26, 43)
- Tian, K., K. A. Thomson, F. Liu, D. R. Snelling, G. J. Smallwood, and D. Wang (2006). Determination of the morphology of soot aggregates using the relative optical density method for the analysis of TEM images. *Combustion and Flame* 144(4), 782–791. (p. 43, 44)
- Tien, C. L. and J. D. Felske (1977). The Use of the Milne-Eddington Absorption Coefficient for Radiative Heat Transfer in Combustion Systems. *Transactions of the ASME* 99(August 1977), 458–465. (p. 39)

- Van De Hulst, H. C. (1957). *Light Scattering by Small Particles*, Volume 1. (p. 33, 37)
- van Oijen, J., R. Bastiaans, and L. de Goey (2007). Low-dimensional manifolds in direct numerical simulations of premixed turbulent flames. *Proceedings of the Combustion Institute* 31(1), 1377 – 1384. (p. 150)
- Verhoeven, L., W. Ramaekers, J. van Oijen, and L. de Goey (2012). Modeling non-premixed laminar co-flow flames using flamelet-generated manifolds. *Combustion and Flame* 159(1), 230 – 241. (p. 150)
- Vicquelin, R., B. Fiorina, S. Payet, N. Darabiha, and O. Gicquel (2011). Coupling tabulated chemistry with compressible CFD solvers. *Proceedings of the Combustion Institute*. (p. 145, 172)
- Wang, A. and M. F. Modest (2007). Spectral Monte Carlo models for nongray radiation analyses in inhomogeneous participating media. *International Journal of Heat and Mass Transfer*. (p. 20)
- Wang, A., M. F. Modest, D. C. Haworth, and L. Wang (2008). Monte Carlo simulation of radiative heat transfer and turbulence interactions in methane/air jet flames. *Journal of Quantitative Spectroscopy and Radiative Transfer*. (p. 20)
- Wang, L., D. C. Haworth, and M. F. Modest (2005). A PDF/photon Monte Carlo method for radiative heat transfer in turbulent flames. *Proceedings of the ASME Summer Heat Transfer Conference 1* (January), 741–745. (p. 56)
- Wang, Y., A. Raj, and S. H. Chung (2013). A PAH growth mechanism and synergistic effect on PAH formation in counterflow diffusion flames. *Combustion and Flame*. (p. 141)
- Waterman, P. C. (1971). Symmetry, unitarity, and geometry in electromagnetic scattering. *Physical Review D* 3(4), 825–839. (p. 50)
- Weinert, D. W., T. G. Cleary, G. W. Mulholland, and P. F. Beever (2003). Light scattering characteristics and size distribution of smoke and nuisance aerosols. *Fire Safety Science*, 209–220. (p. 91)
- Widmann, J. F. (2003). Evaluation of the planck mean absorption coefficients for radiation transport through smoke. *Combustion Science and Technology* 175(12), 2299–2308. (p. 127)
- Wiscombe, W. J. (1980). Improved Mie scattering algorithms. *Applied Optics* 19(9), 1505. (p. 33)
- Witt, A. N. (1977). Multiple scattering in reflection nebulae. I - A Monte Carlo approach. *Astrophysical Journal Supplement Series*. (p. 26)
- Wood, K. and R. Reynolds (1999, November). A model for the scattered light contribution and polarization of the diffuse h-alpha galactic background. *Astrophysical Journal* 525, 799. (p. 216)
- Wriedt, T. and U. Comberg (1998). Comparison of computational scattering methods. *Journal of Quantitative Spectroscopy and Radiative Transfer* 60(3), 411–423. (p. 50, 51)
- Wu, B. and X. Zhao (2020). *Journal of Quantitative Spectroscopy & Radia-*

- tive Transfer Effects of radiation models on steady and flickering laminar non-premixed flames. *253*. (p. 169)
- Xu, Y.-l. (1995). Electromagnetic scattering by an aggregate of spheres. *Applied Optics* *34*(21), 4573. (p. 50)
- Xuan, Y., G. Blanquart, and M. E. Mueller (2014). Modeling curvature effects in diffusion flames using a laminar flamelet model. *Combustion and Flame*. (p. 161)
- Yang, B., B. Hu, and U. O. Koylu (2005). Mean soot volume fractions in turbulent hydrocarbon flames: A comparison of sampling and laser measurements. *Combustion Science and Technology* *177*(8), 1603–1626. (p. 43, 48, 228)
- Yang, P., K. N. Liou, M. I. Mishchenko, and B.-C. Gao (2000). Efficient finite-difference time-domain scheme for light scattering by dielectric particles: application to aerosols. *Applied Optics* *39*(21), 3727. (p. 50)
- Yon, J., A. Bescond, and F. Liu (2015). On the radiative properties of soot aggregates part 1: Necking and overlapping. *Journal of Quantitative Spectroscopy and Radiative Transfer* *162*, 197–206. (p. xiv, 26, 45, 53, 54, 88)
- Yon, J., F. Liu, A. Bescond, C. Caumont-Prim, C. Rozé, F. X. Ouf, and A. Coppalle (2014). Effects of multiple scattering on radiative properties of soot fractal aggregates. *Journal of Quantitative Spectroscopy and Radiative Transfer* *133*, 374–381. (p. 52)
- Yon, J., F. Liu, J. Morán, and A. Fuentes (2019). Impact of the primary particle polydispersity on the radiative properties of soot aggregates. *Proceedings of the Combustion Institute* *37*(1), 1151–1159. (p. 55)
- Yon, J., C. Rozé, T. Girasole, A. Coppalle, and L. Mées (2008). Extension of RDG-FA for scattering prediction of aggregates of soot taking into account interactions of large monomers. *Particle and Particle Systems Characterization*. (p. 52)
- Yoshikawa, T. and R. D. Reitz (2009). Effect of radiation on diesel engine combustion and heat transfer. *Journal of Thermal Science and Technology* *4*(1), 86–97. (p. 57, 116)
- Yurkin, M. a. and A. G. Hoekstra (2007). The discrete dipole approximation: An overview and recent developments. *Journal of Quantitative Spectroscopy and Radiative Transfer* *106*(1-3), 558–589. (p. 51)
- Yurkin, M. A., A. G. Hoekstra, R. S. Brock, and J. Q. Lu (2007). Systematic comparison of the discrete dipole approximation and the finite difference time domain method for large dielectric scatterers. *Optics Express* *15*(26), 17902–17911. (p. 51)
- Yusef-Zadeh, F., M. Morris, and R. White (1984). Bipolar reflection nebulae : Monte carlo simulations. *278*, 186–194. (p. 216)
- Zhang, Q., H. Guo, F. Liu, G. J. Smallwood, and M. J. Thomson (2009). Modeling of soot aggregate formation and size distribution in a laminar ethylene/air coflow diffusion flame with detailed PAH chemistry and an

- advanced sectional aerosol dynamics model. *Proceedings of the Combustion Institute* 32 I(1), 761–768. (p. 182, 192)
- Zhang, Q., M. J. Thomson, H. Guo, F. Liu, and G. J. Smallwood (2009). A numerical study of soot aggregate formation in a laminar coflow diffusion flame. *Combustion and Flame* 156(3), 697–705. (p. 36, 191)
- Zhang, Y. F., R. Vicquelin, O. Gicquel, and J. Taine (2018). Practical indicators for assessing the magnitudes of wall radiative flux and of coupling effects between radiation and other heat transfer modes on the temperature law-of-the wall in turbulent gaseous boundary layers. *International Journal of Heat and Mass Transfer*. (p. 67)

Titre : Simulation numérique et analyse du rayonnement thermique dans les flammes suitées : impact de la description des propriétés radiatives

Mots clés : combustion, suies, turbulence, rayonnement, modélisation, transferts thermiques

Résumé : Le rayonnement thermique lié aux particules de suies est un phénomène physique à modéliser dans les simulations numériques. En effet, le rayonnement dépend -entre autres- fortement de la taille des particules de suies, de leur morphologie, de leurs propriétés optiques. Dans la littérature, l'étude du rayonnement thermique des flammes suitées se base sur l'hypothèse de particules sphériques, bien qu'il soit aujourd'hui largement reconnu que les suies forment en réalité des agrégats complexes. Ce travail de thèse propose de considérer les suies comme de tels agrégats et d'analyser l'impact de modèles de rayonnement avancés (tel que le modèle RDGFA) sur différentes configurations. Ces modèles de rayonnement avancés sont intégrés dans un code précis basé sur une méthode Monte-Carlo permettant de résoudre l'équation de transfert radiatif et d'accéder aux quantités clés du rayonnement thermique. Des stratégies de calculs sont développées afin de réduire le coût de calcul associé aux méthodes Monte-Carlo tout en garantissant une grande précision.

Elles sont appliquées sur deux configurations turbulentes complexes : une flamme jet éthylène-air de diffusion, et une flamme swirlée non-prémélangée d'éthylène-air. Le modèle de rayonnement de suies RDGFA utilisé pour les flammes turbulentes est ensuite confronté à des données expérimentales obtenues sur des flammes laminaires afin de valider sa précision. Un calcul multi-physique couplé est réalisé sur la flamme laminaire éthylène-air de Santoro. Ce calcul couplé prend en compte à la fois la dynamique des suies, le rayonnement des particules, et le préchauffage de l'éthylène par les parois chaudes du brûleur sur laquelle la flamme est attachée. L'analyse du rayonnement thermique montre la capacité du modèle de rayonnement RDGFA à reproduire des données expérimentales avec fidélité. Enfin, une application basée sur la synthèse de signaux liés à la diffusion des particules de suies appliquée aux diagnostics expérimentaux sur la flamme de Santoro est proposée.

Title : Numerical simulation and thermal radiation analysis in sooted flames : impact of radiative properties

Keywords: combustion, soot, turbulence, radiation, modeling, thermal transfer

Abstract : Modelling soot radiation in CFD simulations is a challenging task as it strongly depends on particle size, morphology and optical properties. In the literature, all the studies related to thermal radiation in sooty flames are considering soot as spherical particles, although it is well admitted that they are clustering into complex aggregates. In this PhD work, an aggregate morphology for soot particles is considered and the impact of advanced soot radiative models (such as RDGFA) is assessed on several configurations. These models are implemented in an accurate code based on a Monte-Carlo approach, which solves the radiative transfer equation to retrieve key thermal radiation quantities. Numerical strategies are developed to reduce the computational cost due to the Monte-Carlo method while preserving a high accuracy. These strategies are applied on two turbulent flames: a diffusion coflow ethylene-air jet-flame and a swirled non-premixed ethylene-air flame.

The radiative model RDGFA is then compared with experimental data obtained on laminar flames to assess its accuracy. A multi-physics coupled calculation is performed on the diffusion laminar ethylene-air Santoro's flame. This coupled approach accounts for soot dynamics, radiation, and ethylene pre-heating due to the hot burner walls. The thermal radiation analysis demonstrates the capability of the RDGFA model to retrieve experimental data with a good accuracy. Finally, an application of based on the numerical synthetization of laser scattering signals due to soot particles is proposed and applied on Santoro's flame.